UNIVERSITÉ DU LUXEMBOURG

PhD-FSTC-2019-09

The Faculty of Sciences, Technology and Communication

DISSERTATION

Defense held on 15/02/2019 in Luxembourg
to obtain the degree of

DOCTEUR DE L'UNIVERSITÉ DU LUXEMBOURG

EN *Chimie*

by

Catherine Ging REYES

Born on 4 December 1990 in New York, N.Y. (U.S.A)

CONFINED IN A FIBER: REALIZING FLEXIBLE GAS SENSORS BY ELECTROSPINNING LIQUID CRYSTALS

Dissertation defense committee

Dr. Jan P.F. Lagerwall, Dissertation Supervisor

Professor, Université du Luxembourg

Dr. Anupam Sengupta, Chairman

Professor, Université du Luxembourg

Dr. Phillip Dale

Professor, Université du Luxembourg

Dr. Margaret W. Frey

Professor, Cornell University

Dr. Verena Görtz

Professor, Lancaster University

Confined in a fiber:
Realizing flexible gas sensors
by electrospinning liquid crystals

Catherine Ging Reyes

A dissertation
Defense: February 15, 2019

Colophon

This dissertation was typeset with LaTeX 2$_\varepsilon$ using the Overleaf-ShareLaTeX platform. It uses the *Clean Thesis* style developed by Ricardo Langner (`http://cleanthesis.der-ric.de/`). Additional minor typesetting modifications to this style were done by Catherine G. Reyes for this dissertation.

A permanent record of this dissertation can be found at:
`http://hdl.handle.net/10993/39533`.

This research was supported by funding from the European Research Council (ERC) (grant number: PE8 ERC-2014-CoG).

Acknowledgements

It sounds silly, but honestly, for the last several months I've purposely avoided writing this section of my thesis. It isn't that I find it difficult thanking and acknowledging the people who've helped me in arriving to this point, that part is very easy. However, I realize, now that I am writing this, that perhaps the real reason why I've avoided this section until the very end is because it is also the section that forces me to acknowledge the end of my time, officially, as an academic student.

Don't get me wrong, I am very happy and proud of what I've accomplished throughout the last six years I've been in graduate school, both from my time at Cornell and in Luxembourg. Though, it is a bit sobering to acknowledge that there will probably never be another moment in my life when I am allotted as much time to discover, learn, and fail with as much freedom as I've been given as while being a graduate student. I feel some sadness, but on the other hand, I am so happy to have had this opportunity because it is one that I know many wish they had.

In writing this thesis I also realized that there is still so much about the world, both in terms of science and society, that I still don't know. Actually, it's through the many conversations about nearly everything with Jan in the last four years that have helped me (finally) realize that it's ok to admit this as long as I am open to learning and giving new things (and people) a chance. I don't think I've ever met someone as happy to go to work everyday and learn something new while being calm under immense pressure as Jan. I hope I can remember to have as much patience in trying situations that I am sure to inevitably encounter in the future. Many thanks to Giusy as well who has always treated me with just as much kindness, generosity, and respect.

Thank you also Anjali, Rijeesh, Camila, Manos, Rao, Larry, Lionel, Vanessa, Paula and Urša for being around to share a few laughs and for teaching me new ways to think. Thank you Zory and Astrid for reminding me that work is still only one part, out of the many parts, that make up my life and for looking out for me when I least expect it. Thank you Shameek, my project successor, for once telling me that there is enough room in the world for many types of people to exist. These words help remind me that sometimes understanding someone's point of view does more good than arguing about how wrong or right they are. I also wish Nikolay continued success with his PhD work as well.

Daniel Siopa you have been my best friend in Luxembourg, and I am just so happy to have met you (all thanks to Phil and TP chem!). You've undoubtedly made work and social life immensely more joyful. I know we'll keep in touch in the future. Thanks Phil for always being supportive and for asking how my work was going even when at times I was reluctant to share. In hindsight, I realize it's because you care about my success.

Many thanks are also extended to the professional colleagues I've made throughout the years, who've also given me advice and support in various ways (sometimes serendipitously too!): members from the LCI at Kent State University, Nicholas Abbott and his group (now) at Cornell University, Dirk Broer and his group at T/U Eindhoven, Francesco Basoli from the Campus Bio-Medico University of Rome, and Peter Kaul and Lukas Pschyklenk from the Institute of Detection Technologies at the Hochschule Bonn-Rhein-Sieg.

I am also grateful for my friends from the past, who with their messages and Skype calls of support, have also gotten me through many moments. I admire you all for your strengths: Nidia, Helen, Minji, Vanessa Sanchez, and Angela. Many thanks to Margaret Frey for introducing me to Jan in the first place via email, as well as for continuing to be supportive in the research I've been involved in today.

Last, but certainly not least, I'm so fortunate to have three constant people in my life who've never once failed me, and who I know never will - my mother, father and brother. Through my successes and failures, through health and through every illness, they have always been there for me irrespective of the distance that separates us. Mom and dad, you may not have titles but you both truly are the living definitions of resilience, courage, selflessness and honor – qualities that not even the titled or wealthy can buy. I'm so grateful to have you mom, dad, and Dan. I owe you everything.

Catherine G. Reyes
January 2019

Abstract

Liquid crystalline phases (LCs) readily exhibit optical responsivity to small fluctuations in their immediate environment. By encapsulating LC phase forming compounds within polymer fibers through the electrospinning process (a fiber spinning method known for being a fast way of forming chemically diverse non-woven mats), it is possible to create functionalized LC-polymer fiber mats that are responsive as well. As this fiber mat can be handled macroscopically, a user can observe the responses of the mat macroscopically without the need for bulky electronics. This thesis presents several non-woven fiber mats that were coaxially electrospun to contain LC within their individual polymer fibers cores for use as novel volatile organic compound (VOC) sensors. The mats are flexible, lightweight, and shown to both macroscopically and microscopically respond to toluene gas. Such gas responsive mats may be incorporated into garments for visually alerting the wearer when they are exposed to harmful levels of VOCs for example.

Additionally, the interaction and re-prioritization of several electrospinning variables (from the chemistry based to the processing based) for forming the LC-mats are also discussed. The balance of these variables determines whether a wide range of phenomena occur during fiber formation. For instance, unexpected phase separation between the polymer sheath solution and the LC core can mean the difference between forming fully dried fibrous mats and wet/meshed films. A chapter is devoted to discussing the impact that solvent miscibility with an LC can have on fiber production, including also the effect that water can have when condensed into the electrospinning coaxial jet. The fiber shapes that the polymer fiber sheaths adopt (beaded versus non-beaded), as well as the continuity of the LC core, will influence the visual appearance of the mats. These optical properties, in turn, influence the mats' responsivity to gases and whether the responses can be macroscopically observed with or without additional polarizers.

During two types of gas sensing experiments - mats exposed to gas when contained in a cell, and mats exposed to gas diffused in ambient air without containment, we see that not all fibers within a mat respond at the same time. Moreover, different segments of the fibers within the same non-woven mat also show slightly different rates of response due to variations in fiber thickness, LC content, and whether the fiber cores had variations in LC filling (i.e. LC director twists, and gaps).

List of Original Publications

This dissertation is based on the results from the following publications.

1. **C. G. Reyes**, Anshul Sharma, and Jan P. F. Lagerwall. "Non-electronic gas sensors from electrospun mats of liquid crystal core fibres for detecting volatile organic compounds at room temperature." In: *Liquid Crystals*, **43** 13-15 (2016) pp. 1986–2001 <link>

2. Martin Urbanski[†], **C. G. Reyes**[†], JungHyun Noh, Anshul Sharma, Yong Geng, Venkata Subba Rao Jampani, and Jan P. F. Lagerwall. "Liquid crystals in micron-scale droplets, shells and fibers." In: *Journal of Physics: Condensed Matter*, **29** 133003 (2017) <link>

3. **C. G. Reyes**, and Jan P. F. Lagerwall. "Advancing flexible volatile compound sensors using liquid crystals encapsulated in polymer fibers." In: SPIE Conference Proceedings of Emerging Liquid Crystal Technologies XIII, **105550O**, (2018) <link>

4. **C. G. Reyes**, Jörg Baller, Takeaki Araki and Jan P. F. Lagerwall. "Isotropic-isotropic phase coexistence and spinodal decomposition in liquid crystal-solvent mixtures." `To be submitted: May 2019`

5. **C. G. Reyes**, and Jan P. F. Lagerwall."The impact of ambient humidity on coaxial Taylor cone formation while electrospinning liquid crystals with polymer solutions." `Manuscript in preparation`

6. **C. G. Reyes**, and Jan P. F. Lagerwall."Quantitatively determining the sensitivities of liquid crystal-polymer fibers mats to volatile organic compounds." `Manuscript in preparation`

Previous publications indirectly related to this dissertation:

1. **C. G. Reyes**, and Margaret W. Frey. "Morphological traits essential to electrospun and grafted nylon-6 nanofiber membranes for capturing submicron simulated exhaled breath aerosols." In: *Journal of Applied Polymer Science*, **134** 17, pp. 44759-73, (2017) <Link>

2. Nidia K. Trejo, **C. G. Reyes**, Vanessa Sanchez, Dorothy Zhang, and Margaret W. Frey. "Developing composite nanofibre fabrics using electrospinning, ultrasonic sewing, and laser cutting technologies." In: *International Journal of Fashion Design, Technology and Education*, **9** 3, pp. 192-200, (2016) <Link>

[†]Authors contributed equally to the paper

Contents

List of Figures

List of Tables

1

Introduction

If I wanted to tell you a story about how electrospinning was first discovered, then it would have to start in the 1600s when electro*spraying* was first observed by magnetism enthusiast, William Gilbert [1]. This is not a story about him, however, so it is sufficient to simply state that electrospraying is the process by which micro- and nano- sized droplets are continuously expelled, with decreasing size, from a charged fluid flowing under a constant potential. Electrospraying experiments were some of the first to demonstrate that the ionization of liquid by electrostatic forces was possible, and these experiments inspired the development of the electro*spinning* process (and preceded the formal discovery of polymers) some two hundred years later [2, 3].

Comparatively, electrospinning works in essentially the same way, but this time the potential is applied to a flowing polymeric solution, or melt [4], for the purpose of creating nano- and micro-diameter fibers (hence the change in suffix - "spinning", as for "fiber spinning"). So rather than droplets emitted, there is a continuously thinning and solidifying jet of polymer solution moving towards a grounded point. Upon reaching the grounded target the jet will have, ideally, finished solidifying into the micro- or nano- diameter sized fibers that make up a non-woven mat. The variables that control the process are many and rely heavily on figuring out how the polymer solution, under considerable elongational stress once in the jetting stage, is likely to be influenced by the electrostatic forces placed on it from the very high (kilovolt range) potential before drying into filaments.

Some would argue that before researchers at Akron university and MIT [5–7] in the late-1990s began reviving academic and industrial interest in it, the concept of electrospinning really began getting popular in the mid 1890s thanks to the growing synthetic textile industry. At the time, electrospinning was seen as a potential way of solving the ever rising demand for textiles that natural fiber industries could not keep up with [2]. Alternatively, there are also many who would argue that this process did not really make much of an impact on society at all apart from complementing current filter technology ([8]), and providing the occasional tissue scaffolds for regenerative medicine (i.e. Mimetix® scaffolds by the Electrospinning Company in the UK [9]). It is understated how profoundly important both of these examples are in modern society, but again, to those who are not personally familiar with situations where electrospun products are found, and that is probably a good number of people, the word and the concept of "electrospinning" are largely unheard of by the public. Those are just some perspectives to keep in mind about how old this concept is, and yet, how still relatively unheard of it is by many. Around the same time that the first electrospinning experiments were occurring though, another curious discovery was also happening in Prague.

The first *liquid crystal*(LC) phase forming compound was noticed by botanist Friedrich Reinitzer in 1888 while at the Prague German Technical University [10]. Funny enough, this was the exact same year when Charles V. Boys (in England) decided to conduct the first electrospinning experiment with sealing wax, and other viscous materials. No one at this time though realized that liquid crystal phases could be useful for anything until the late 1930s. It did not help

that the concepts of optical anisotropy and elasticity in liquids, were not yet fully agreed upon by the chemists and physicists at the time either. Although optical anisotropy* was known to occur in solids (like calcium carbonate crystals) since 1669, and though it was known that solids could sometimes be partially deformed and return back to their original shape (termed "elastic"), it was not easy for scientists to accept that melted organic compounds could form an intermediate phase between the liquid and solid states, one which could demonstrate these very same properties and be uncontaminated.

Derivatives of cholesteryl benzoate were the first of these organic compounds accidentally observed by Reinitzer to have these so-called "intermediate liquid and solid states" at well defined temperature ranges when either heated or cooled. Apart from being intrigued by the range of colors that these compounds displayed as they were cooled, for example, Reinitzer was surprised to find that they also showed a "milk-like turbidity, but [were] still fluid"† before more colors reappeared and the compounds finally crystallized into solid states. It was known that pure compounds could either freeze into solids or melt into liquids at precise temperatures, but any compound that appeared to do something different, as was conventionally believed, must have had impurities. Thus, the first argument against the existence of liquid crystalline states arose in the scientific community. Though basic polarizing optical microscopes (POM) existed since the 1800s, many chemists and physicists did not have them unless they specifically studied crystallography. Most of these devices were not equipped with heating stages either - which was crucial if one wanted to see a stable LC phase at a particular temperature under polarization.

The other main argument against LC phases had to do with their optical anisotropy and fluid-like properties. Normally, if a crystalline solid is melted it should immediately enter a fully isotropic state where the bulk sample of the liquid appears transparent and does not scatter light anymore. When presented with Reinitzer's LC phases, many scientists wondered how could a solid melt into this intermediate LC phase and still show a liquid that appeared to "shimmer" and refract light? To scientists back then, it appeared similar to that of Brownian motion seen for particles dispersed in isotropic liquids, but now it is known that it is because uniformly aligned sections of the LC phase fluctuate with thermal motion that they were able to see this "shimmer"-like effect in the sample. It only was after heating beyond this intermediate phase showing liquid and crystal-like behavior that the material then finally entered the transparently clear isotropic liquid state.

Even though it was not obvious then, now it is also known that there can be several types of intermediary liquid crystal phases formed within a single compound. Today we even know that LC phases can also form in mixtures of compounds that do not otherwise show LC phases individually on their own (these mixtures are called *lyotropic* LCs). Last but not least, once LCs started being confined between glass plates and studied under applied electric and magnetic fields (around the 1930s) we found out that the preferred molecular orientation in these phases (called the *director*) could be tuned by, and is acutely sensitive to, various forms of external stimuli apart from temperature. While this also meant that LCs were sensitive to volatile organic compounds (VOCs) as well, it was definitely the sensitivity to the electric fields that became useful for the LC displays we know and appreciate around us today.

*Further explained in the context of LCs in sec. 2.2.1.

†Taken from Reinitzer's letters to Otto Lehmann, in his attempt to convince Lehmann that he should study this "strange" phenomena. Reinitzer also knew that Lehmann was one of the few physical chemists around who had a polarizing optical microscope equipped with a temperature control stage who could study this further [11]. Today LC phases are still investigated in this manner.

So given what we know about the development of electrospinning and LCs throughout time, interestingly, if we compare the expectations of how useful researchers thought these two concepts would be for society, we would probably find that these expectations have managed to evolve oppositely. A crude, but plausible, interpretation of this idea is shown in the plot below, noting that both concepts were founded in almost the same year.

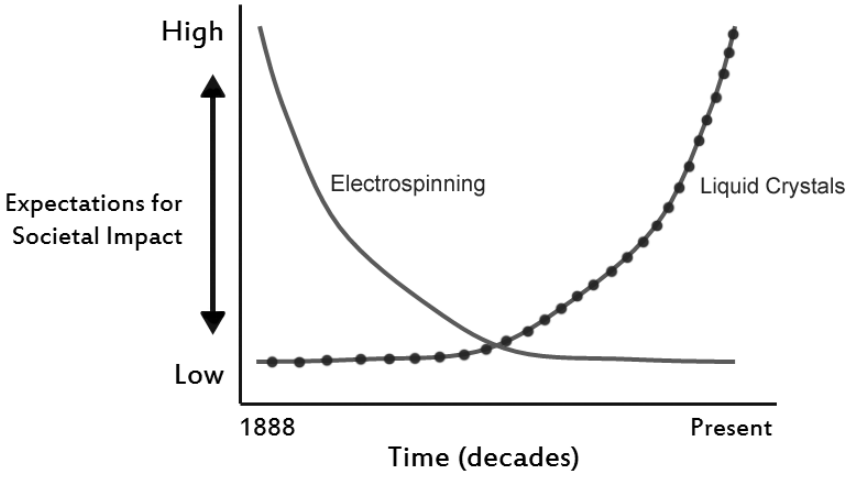

Every researcher who came across LC phases at first thought they were, at best, an interesting natural phenomenon, but no one then could have imagined that eighty years later society could benefit from them in the form of digital displays, and now, also windows with tunable transparency [12]. With electrospinning, in contrast, patents from textile industries and inventors were filed almost immediately after the initial process was demonstrated, but the approach mostly faded into scientific obscurity until academic interest in it was rekindled, also some eighty years later. In realizing that the trends for both concepts had opposing popularity, in the end perhaps it is not so surprising that it took almost another ten years (starting from 2008) for researchers to begin investigating what electrospinning with liquid crystals could look like. More so, since the combination of the two concepts is fairly recent, there are still plenty of unexplored questions pertaining to how LCs and polymer fibers can be optimally combined using the electrospinning technique to create multi-functional composite textile materials.

Thus, the story presented here is about the interactions arising between an LC confined within the polymer fiber structure, and the interactions between the polymer solvent and the LC, as the coaxial electrospinning process combines these substances together to form both beaded and cylindrical fibers in non-woven mats. It is also a story that examines the influence the spinning process has on the optics of the confined LC in individual fibers, and what these optical behaviors translate to macroscopically for a large scale fiber mat. LCs confined in glass capillaries with diameters several hundreds of microns thick have been studied before, but there are still many unanswered questions as to how the confinement in filaments changes when the space they enter is below the 5 μm diameter range. Moreover, what happens when that "glass capillary" has the freedom to bend and curl, and is porous? Or, when each filled filament contributes to the optics of a whole assembly? Ultimately, the consequences of changing optical behaviors and polymer-LC fiber confinement will affect how the macro-scale fiber mat will detect external stimuli, which in my case comes in the form of volatile organic compounds (VOCs).

With that in mind, the story of LCs confined in electrospun fibers for gas sensing will progress following the overview below. It will focus mainly on two protagonists: 4-Cyano-4'-pentylbiphenyl

(5CB) - the liquid crystal phase forming compound, and polyvinylpyrrolidone (PVP) - the polymer. This is their quest to unite harmoniously to create stable coaxial fibers while facing off the dangers of phase separation and degradation presented by encapsulation through electrospinning and "villains" in the form of water, ethanol, and toluene vapors. Hopefully, their unique story (although in some cases supporting characters, like nematic LC mixtures ROTN-403 and E7, will make minor appearances for comparison) will inspire others in continuing research on the complexities involved in the self-assembly of coaxially electrospun fibers with two (or more) channels containing LC phases and polymers.

1.1 Overview of chapters

Chapter 2

The relevant literature for understanding the results in this thesis regarding LCs, electrospinning fibers, and gas sensing using the two is discussed.

Chapter 3

My experimental protocols for LC-fiber mat formation and analysis. The reasons why these procedures, and setups were assembled in specific ways (from electrospinning to gas sensing) are also discussed.

Chapter 4

First Results Section: The question "What makes 'good' coaxially electrospun LC-polymer fibers?" is answered through a consideration of variables known to influence fiber formation during electrospinning.

Chapter 5

Second Results Section: "Why does LC-polymer electrospinning fail in high humidity?" Phase diagrams between the polymer solvent and the LC in the presence of water are examined to answer this question. During coaxial electrospinning the core fluid does interact with the sheath solvent, as well as water condensed from the air.

Chapter 6

Third Results Section: The encapsulated LC affects the scattering of the fiber mats. This influences how the reversible responses to gas are perceived macroscopically, from a qualitative standpoint. Some points on LC defects in the fibers are also discussed.

Chapter 7

Fourth Results Section: Quantitative data showing the sensitivity thresholds to which the LC-fiber mats respond to gas is examined. Two methods of vapor exposure and two methods for determining the gas concentrations were used.

Chapter 8

A summary of the main findings and an outlook on the opportunities for coaxially electrospinning LCs with polymer solutions to form LC-fiber mats for gas sensing.

2 Overview of relevant concepts

2.1 A primer on electrospinning

Electrospinning is the process by which micro- and nanofibers can be "spun" or extruded from a flowing polymer solution in the presence of an electric field. As mentioned in the introduction, the process is an approach to fabricating thin filaments inspired by the previous *electrospraying* method seen. The electrospraying method, in turn, was an approach of forming a continuous stream of droplets with progressively decreasing diameters from flowing Newtonian fluids, as well as low molar mass polymer solutions, through an electric field. The latter process has been implemented in many successful technological breakthroughs throughout the century, such as enabling large biomolecule ionization for mass spectrometry experiments [13], and enabling the propulsion of satellites [14, 15]*, for instance.

Electrospinning, while very popular in various research fields for enabling the integration of many types of chemical additives into fiber form in a quick way (faster than other types of fiber spinning techniques [17]), has mostly just been extensively integrated in certain industries involved with filtration [18], and biomaterial fabrication [19, 20]. While the properties that electrospun fibrous materials can offer are extensive - high porosity, increased freedom for altering fiber cross-section and morphology, ease of functionalization, high non-woven flexibility, and lightweight portability [21] - the electrospinning process is known to be difficult to standardize (if intended to be upscaled). Additionally, much of the physics and chemistry surrounding how different combinations of fluids (i.e. polymer solutions, liquid crystals, and other types of mixtures) behave when subjected to the process are still being explored.

What contributes to the difficulties in using the electrospinning process commercially is not that a fundamental understanding of the process is unknown. The challenges instead revolve around the fact that, in order to reproducibly and continuously electrospin the same quality fibers and fiber mats, the process requires the experimentalist(s) to keep track of several variables (at least nine primary ones) which can easily influence the material produced, or even *if* material is produced. For reference, a basic diagram of the experimental setup for a coaxial electrospinning case (in other words, for spinning one fluid within another) and the most crucial features seen is shown in Fig. 2.1. Further details on the precise setup used in this thesis for combining two fluids, like an LC and a polymer solution, are described in ch. 3 however.

*Dubbed as "colloid thruster" propulsion, the electrospraying process has enabled the very precise re-positioning of satellites through the micro-Newton forces generated from combining many spraying jets together since 1998 [14]. Currently NASA, in partnership with Lockheed Martin, plans to launch some of its first mini-satellites (weighing between 1 kg - 10 kg) that are solely propelled by these thrusters in 2020 [16].

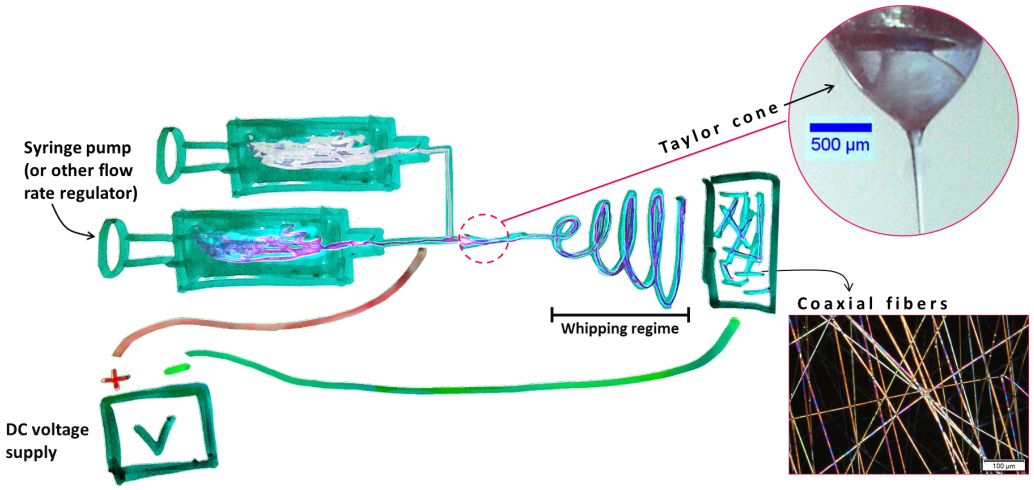

Fig. 2.1 – Sketch showing the most crucial elements of the electrospinning process seen with two co-flowing fluids. Two syringe pumps are co-flowed into an electric field generated in between the nozzle tip of one syringe, where the combined two fluids emerge, and a grounded collector, where the fibers are electrostatically deposited. The nozzle is charged with the positive end of a DC voltage supply and the ground end is connected to a collector. The potential applied to the solution contributes to charge repulsion within, which in turn opposes the solution's surface tension. When the surface tension is overcome by the electrostatic forces the fluid emerging will adopt a cone shape (the Taylor cone). A continuous fluid jet ejects from the Taylor cone apex with an ever decreasing diameter that flows towards the collector. The jet continuously narrows from the evaporation of solvent mid-flight, and from stretching due to electrostatic self repulsion along the jet. Last, the jet will eventually begin to helically whip about itself until finally reaching the grounded collector as solidified polymer fibers with a core of LC.

2.1.1 From droplets to a Taylor cone with a straight jet

For electrospinning to first start one needs to have a flowing polymeric solution. A solution that is not polymeric can also be used, but once the potential is applied the jet may break up into droplets of decreasing size. When this occurs one will be electrospraying droplets, rather than electrospinning fibers. Although the same Taylor cone feature (described in the caption of Fig. 2.1) develops once the potential is applied to the flowing solution, for both spraying and spinning, the molar mass influences whether there are enough chain entanglements in the solution to form filaments rather than droplets (or solidified beads). Since a non-polymeric solution lacks sufficient chain entanglements when the jet is expelled, the jet will quickly break down into droplets from the high amount of electrostatic self repulsion imposed by the potential. Thus, the chain entanglements of the solution are necessary for the jet to maintain a continuous fiber structure as it dries mid-flight and finishes solidifying into continuous fibers. The importance of chain entanglements in relation to polymer molar mass and the impact on electrospinning will be further discussed in detail in sec. 4.3.4.

Additionally, the solution that is chosen for electrospinning needs to constantly flow because once the jet expels from the Taylor cone the solvent will continuously evaporate, and contribute to mass loss, until it solidifies into fibers. Without a continuous supply of polymer solution from which fibers can form, the process will quickly halt once the initially emitted jet finishes drying. In a typical situation without an electric field imposed on a flowing polymer solution, the liquid

emerging from an orifice will eventually break up into droplets in order to minimize its surface area, and thereby surface energy, through the Plateau–Rayleigh instability [22].

The Plateau-Rayleigh instability helps explain why cylindrical columns of fluid break up into droplets with the same volume, but with overall smaller surface area than that of the starting fluid columns. Energy is required to create an interface between a flowing fluid and air. More energy is required to create a boundary with a large surface area than one with with a smaller surface area, thus, the fluid will assume a shape that minimizes the energy cost. This shape that satisfies this condition is the sphere, as opposed to a cylinder.

Plateau and Rayleigh both first witnessed and explained this phenomena once they realized that freely falling columns (streams) of water in air eventually break up into droplets when the column lengths exceed the diameter by over a factor of 3 [23–25]. More specifically, perturbations in a freely flowing column of fluid always exist. However, once these perturbations become large they can be mathematically analyzed as discretely periodic sinusoidal sections that define the maxima and minima in the fluid column. In other words, the radius of the fluid column no longer remains constant and it periodically expands and contracts depending on the rate at which the sinusoidal sections grow and decay. The pressure exerted at these periodic sections due to the surface tension of the fluid also changes. Eventually this changing pressure exerted on the fluid column causes spherical droplets with minimized surface area to pinch off.

Figure 2.2 illustrates how the surface tension of a liquid arises. Since the molecules at the surface of the liquid (orange) do not experience cohesive forces from the air at the liquid-air boundary, cohesive forces between neighboring liquid molecules on either side at the surface contribute to a net downward force over those molecules within the liquid below. This downward force causes the surface to resist being broken, and it is said that the molecules at the surface of the liquid are "under tension." By comparison, the liquid molecules located away from the interface within the bulk are not under tension since the forces acting on them from neighboring molecules cancel out.

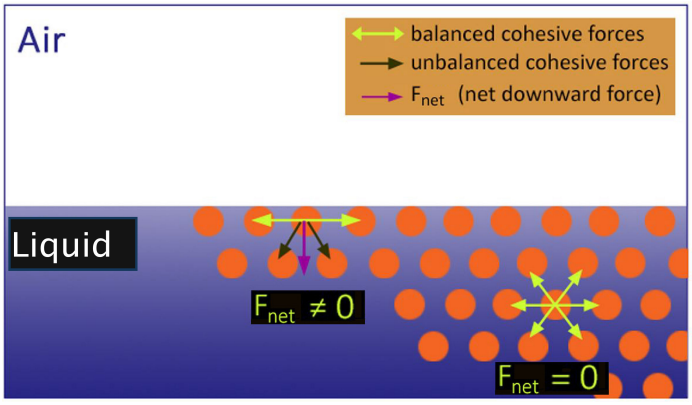

Fig. 2.2 – Sketch illustrating the origin of surface tension in a liquid.

The effect of the surface tension in holding the liquid together to minimize surface area when it is flowing as a stream becomes challenged by electrostatic forces when a potential is applied. Bugarski et al. [26] found that when high enough voltage is applied to a solution dripping from a cylindrical capillary, with droplets originally having radii larger than the capillary orifice, their radii will continue to decrease until a critical voltage is met. At this point, the electrical forces generated by charge separation from the potential applied to the flowing polymer solution will

be enough to overcome the surface tension of the solution and cause Taylor cone formation (shown in Fig. 2.1 for the coaxial electrospinning case). As described in ref. [5] the polymer solution drop which hangs from the orifice of a capillary before the potential is applied is held by a combination of the solution's surface tension and viscoelastic forces.

As mentioned earlier, a high enough potential induces charge separation between the positive and negative ions within the solution. According to Reneker and Yarin, the electrospinning process actually cannot occur if an excess of charged ions in the flowing solution have not been generated [5]. In charging the solution via application of the potential on the outer nozzle, electrons are allowed to transfer into the solution and aid in charge separation within. Reneker and Chun in ref. [27] estimated that the velocity at which these ions separate in solution when 10^5V/m was applied can reach to around 0.15 m/s. But note that their estimate was inferred from the mobility of sodium ions in water and the true value at the start of electrospinning will likely change based on several factors. Some of these factors can be whether organic or aqueous solvents are used, how well the polymer is dissolved in the solvents and its molar mass, and the distance from the interface between the charged nozzle and the solution. Interestingly, one may expect that perhaps the inner wall diameter of the nozzle, and its geometry can also play a role in Taylor cone formation from the perspective of enabling or hampering ion separation. Currently, this is an aspect that to my knowledge has not as of yet been explored in many electrospinning studies.

Once the electrostatic forces do overcome the surface tension of the solution, the Plateau-Rayleigh instability also becomes suppressed and the distortion of hanging solution droplets from the edge of the capillary into a conical shape called the Taylor cone is favored (named after Geoffrey Ingram Taylor who first observed its formation after applying a kilovolt potential to flowing organic solvents and water [28, 29]). Note that the conical shape has a larger surface area than that of the droplets that would originally pinch of the flowing solution stream were there no potential applied.

In electrospraying experiments this is the point where droplet break up would occur, since according to Rayleigh in ref. [30], there is a charge limit that droplets of a certain diameter can accommodate before breaking up further and further from the high amount of self repulsion present per drop. Since the polymer solution used here has chain entanglements, however, break up or "spray" will not occur when the jet from the cone is launched. The jet does, however, continuously reduce in diameter as it makes its way to the collector. Xu et al. measured this aspect by using a light beam to transmit the interference color patterns seen from thinning jets [5, 31] and confirmed that the straight segment of a launched jet could reduce down from 15 μm to 500 nm just before the jet begins to helically whip. Experiments have also shown that as the jet thins its velocity towards the collector will also increase, reaching over 10 m/s in some cases [21].

2.1.2 A straight jet becomes a whipping jet

It is at this point when, just as the jet is thinning, bending instabilities (Fig. 2.3a) arising from the self repelling surface charges within begin to dramatically influence the jet's motion. As the jet thins from solvent evaporation, the surface charges on the jet can become easily perturbed and so the distribution of forces acting on those charges can change, causing the jet path to move laterally and eventually form loops.

As shown in Fig. 2.3(a), assuming a line of uniformly distributed point charges in a small section of the straight jet, if there are no external perturbations acting on the jet then then the resultant net force acting on the central charge from the upper and lower charges is zero. In the case, the jet remains straight as the forces cancel out. However, if the jet is slightly perturbed, the forces acting on the central charge from the upper and lower charges (F_u and F_l) are slightly angled such that the resultant net electrostatic force on the central charge does not equal zero (Fig. 2.3b). This non-zero net force amplifies the perturbation of the jet causing it to bend. One bend leads to another in the jet and it continues propagating throughout the thinning jet. Stated by Reneker and Yarin when observing a typical polymer jet being electrospun - "A succession of three or more smaller diameter bending instabilities was often observed before the jet solidified. As a result, such jets acquired fractal-like configurations, and their length increased enormously as their cross- sectional diameter decreased to a fraction of a micron." [5].

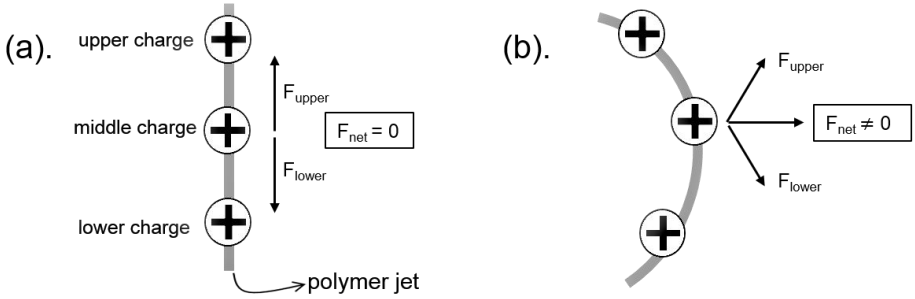

Fig. 2.3 – Sketches illustrating electrostatic forces from charges acting on electrospun jets with and without bending instabilities. If self repelling charges on the jet's surface are simplified to be consecutive point charges, then in (a), where the jet does not experience a lateral perturbation, forces from the upper and lower charges acting on the middle charge will have a net force equal to zero. However, if the jet is even slightly perturbed, the upper and lower forces from the charges above and below the middle charge will result in a non-zero net force that acts on the middle charge. This non-zero net force amplifies the lateral perturbation of the jet allowing the bending instability and helical whipping to propagate onward. (These sketches were reinterpreted from ref. [5]).

On the one hand, the rapid whipping motion of the jet may cause local surface charge density to lower, and one might expect the jet to slow down before landing onto the collector. However, one should also consider that as the jet is whipping and the solvent is evaporating, its diameter is also reducing substantially, and this causes an overall increase in local surface charge concentration. This also favors the onset of further secondary and tertiary bending instabilities in the jet to form as the jet whips. It is the competition between the Plateau-Rayleigh, the bending and other types of instabilities that determine how the jet helically whips and finally dries just prior to landing on the collector [21, 32].

Although seemingly trivial, it is these often overlooked aspects of electrospinning like the influence of the whipping instability on fiber diameter size, and the impact of nozzle geometry on charge separation, for example, that still require further studies, even though the origin of the instabilities (namely from the electric field and the surface tension of the solution) acting on the jet are well understood [5–7, 33]. Particularly when attempting to use the electrospinning technique to produce large scale fiber mats with uniform properties, and when attempting to spin with multiple types of fluids, these are the aspects about the process that may determine the difference between successful fiber formation or not.

2.1.3 Variables that influence the process

Let us return back to the nine main variables that govern the process. There are two main categories into which these fall into: those having to do with the chemistry of the fluids to be spun, and those having to do with how the process is carried out. In the chemistry category we have: (1). the polymer (its molar mass, and miscibility with solvents), (2). the solvent used to dissolve the polymer (its polarity, vapor pressure, and conductivity can also be important [34]), and (3). the chemistry of any additives (salts, surfactants, dyes...etc.) added to the solution made from (1) + (2). The viscosity and surface tension of the resultant polymer solution (made from combining variables 1, 2, and/or 3) are also critical factors but they emerge only after the final solution for spinning is made (this is why they are not categorized as main variables in this list). For the processing category there is: (1). the flow rate of the solution, (2). the applied voltage to the solution, (3). the nozzle geometry from which the solution flows out of, (4). the collector geometry onto which the dried fibers land, (5). the ambient conditions in the spinning area (temperature, relative humidity), and (6). the distance from the charged nozzle to the grounded collection source.

Since several of these variables are discussed in context to the formation of LC core-filled fibers within ch. 4 an evaluation of each will not be thoroughly described in this section. Here is an overview of what is covered in the chapter on LC-fiber production however: the aspects of the polymer solution (in terms of chain entanglements needed to create filaments) (sec. 4.3.4), the consequences of too high or too low applied voltage (sec. 4.2.1) with too low or too high fluid flow rate (sec. 4.3.1), the impact of changing the nozzle-to-grounded-collector distance (sec. 4.3.3) and collector type (sec. 4.3.3), and the impact of ambient humidity (sec. 4.4).

Although this list of variables may seem overwhelming, general working parameters for electrospinning several single component polymer solutions have already been well documented, at least from an empirical point-of-view [21, 35–37]. Modeling, or predicting, how fiber mat formation will proceed for a multi-component mixture using a setup under certain ambient conditions prior to conducting the actual experiments, on the other hand, remain currently under investigation by many [38, 39].

Typically, the most crucial of these variables to account for pertain to the chemistry of the solution, and the interplay that the flow rate and the applied potential have on this solution (also described in the second half of the review in ref. [40]). Most studies, for instance, have reported that reducing the flow rate while increasing the applied potential will aid in increased jet elongation as the more surface charges introduced into the solution, the more surface area they will require to distribute and cause the jet to elongate further as attraction to the grounded collector intensifies. The low flow rate, in turn, helps counteract the Rayleigh instability from dominating during Taylor cone formation.

When spinning multi-component mixtures, typically, previous polymer solutions that have been shown to form fibers on their own (before being mixed) is a good place to start. However, as is detailed in ch. 5, it is also helpful to be aware that unexpected phase separation can occur under certain conditions. Polymers containing high molar masses are generally desired for creating solutions as their polymer chains contribute to entanglements that can be stretched during the jetting stage without breaking up into droplets. This is not possible when non-viscoelastic Newtonian fluids are used.

Most issues regarding the reproducibility of an electrospinning experiment tend to arise when one does not know if the other parameters (e.g. ambient conditions, nozzle geometry and collector type) are inadvertently influencing the fluid system being spun. For instance, a hygroscopic polymer dissolved in a solvent that is also miscible with water is more likely absorb excess water during jet solidification and land wet on a collector when the ambient humidity in the spinning area is high, than a polymer which is immiscible with water but also spun from a water miscible solvent. In fact, this latter situation has been extensively characterized when electrospinning polystyrene (immiscible in water) with tetrahydrofuran and dimethylformamide (organic solvents miscible with water) [41, 42], and the former is a topic I discuss at length in regards to impacting the encapsulation of LC in polyvinylpyrrolidone (PVP) fiber cores (sec. 4.4).

Additionally, Kim and Lagerwall in a previous study [43] noticed that the moisture accumulated on a collector surface can also impact the cross-section morphology and outer structure of bi-component PVP-silicone oil fibers when they land. Meanwhile, several years prior to Kim's and Lagerwall's study Koombhongse et al. [44] believed that collector hydrophilicity or hydrophobicity were not likely to significantly influence electrospun multi-component fluid systems because for electrospinning single component solutions this attribute related to the collector was not documented as extensively at the time (compared to the effects of polymer molar mass, and applied potential). Such findings show us that variables previously not prioritized for electrospinning single component solutions may actually become more important for electrospinning multiple component solutions and that they could be worthy of further investigation.

2.2 What are liquid crystals?

As previously introduced, the term *liquid crystal* (LC) is often used to refer to a class of compounds, or structures, that have the ability to exhibit phases between that of an isotropic liquid and of a solid. What may seem confusing about the term to newcomers at first is that when certain organic compounds that form LC phases are discussed such as 5CB or 8CB, they are often referred to as being LCs themselves–something like "5CB is a LC that forms a nematic phase", for example, is commonly heard in the field. This statement is technically incorrect, as 5CB is not an LC per se, rather 5CB is instead an organic compound which forms a liquid crystalline phase that is nematic. Although used for brevity, such statements are potentially misleading because they suggest that "liquid crystals" can exist as single molecules. In reality, however, the term "liquid crystal" refers to a phase of many molecules that assemble together. Just like the more commonly known "liquid" and "crystalline solid" condensed phases which cannot exist unless there are many molecules (or atoms) that comprise them, neither can the liquid crystal phase. Although the structure and connectivity of an LC phase forming compound has certain defined features (the molecular structure should be anisotropic, and often has centers with rigid aromatic rings [45]), this structure is not otherworldly.

Additionally, two main classes of liquid crystals exist. This is because not all LC phases are formed by heating or cooling pure compounds. Mixtures of certain compounds in appropriate solvents (usually aqueous) can form LC phases as well and without solvent they cannot show LC phases on their own. For instance, 4-cyano-4'-pentylbiphenyl (5CB) is an organic compound that when heated or cooled exhibits one LC phase before reaching the solid or isotropic liquid state. It is also possible to have a solution containing amphiphiles, which do not form an LC phase

without solvent, but which can self-assemble to form micelles of various geometries with solvent (based on their packing parameter [46]). These micellar structures contribute to forming the LC phases observed in this case. So ultimately while the same LC phases can be found in various samples, they do not need to come from the same types of self-assembled structures. To make the distinction between the different ways in which LC phases are assembled, the former type, pure compounds that form LC phases when heated or cooled are called *thermotropic*, and the latter type, solutions of various compounds or macromolecular particles (micelles [47], carbon nanotubes [48], for example) that form LCs are called *lyotropic*. This thesis will only discuss the encapsulation of LC phases of the thermotropic category, and in particular just the nematic phase.

Before moving on to the particular ordering of the molecules that make up the nematic LC phase and how its elastic and optical anisotropy are characterized, it should be noted that as of 2003 [12] there are about 13 classes of LC phases which can be found in any number of combinations in various lyotropic and thermotropic based mixtures and compounds. The two most commonly experimentally encountered types of LC phases are summarized in Fig. 2.4. There is the class of smectic LC phases (i.e. SmC, SmA) and there are the nematic LC phases. While the smectic types have their individual molecules ordered in layers, such that the phases have one dimensional positional order in addition to long-range orientational order, a nematic LC phase lacks long-range positional order but has long-range orientational order instead.

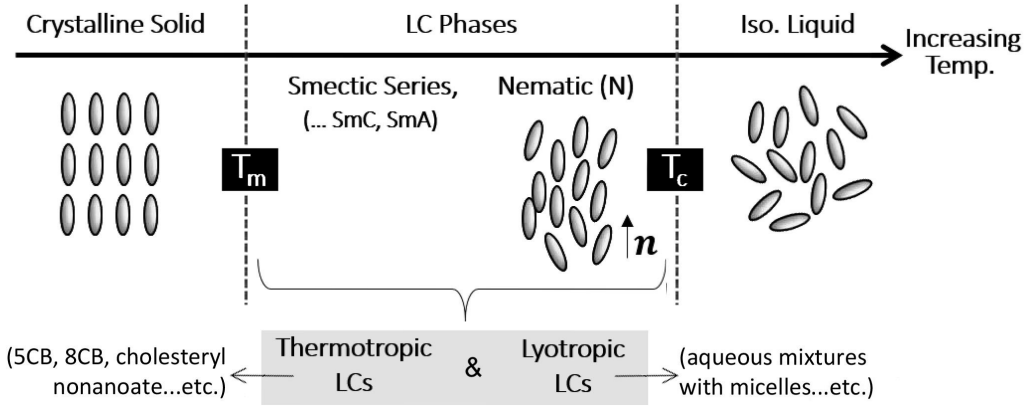

Fig. 2.4 – Sketch showing an example phase sequence for a substance developing one or more LC phases. At sufficiently low temperatures the substance will be in a crystalline phase. Heating further, the T_m is met, where the crystalline phase melts into an LC phase. There can be several - smectic phases, and the nematic phase, for example. The nematic phase is the least ordered until the T_c where it clears into the fully isotropic phase (without any long-range positional or orientational molecular order). The nematic phase is shown above in a 2D schematic containing rod-like molecules arranged without perfect intermolecular spacing but with a generally defined long-range order characterized by the director ($\mathbf{n}$). All LC phases fall into one of two categories, lyotropic or thermotropic, where lyotropic LC phases are formed by molecules or other entities (like micelles) mixed in solvents.

It is for this reason that a nematic phase will normally be located between the smectic phases (if a sample has this series) and the isotropic liquid state during heating or cooling. The nematic phase is the least ordered of all LC phases, but still breaks the rotational symmetry that characterizes isotropic liquids. The nematic phase is distinctly different from an isotropic liquid in that its molecules have long-range, mesoscopically noticeable, orientational order. The clearing

temperature (T_c), known as the temperature at which the nematic phase long-range orientational order breaks down on heating and the isotropic phase starts, as well as the melting temperature (T_m), the temperature which separates the solid crystalline phase from the lowest-temperature LC phase, both aid in characterizing the phase sequence of the sample as well as determining the extent of its responsivity to external stimuli.

In addition to LC phases being a class of soft matter, the latter defined as any condensed system which is easily deformable and exhibits high sensitivity to thermal fluctuations at room temperature (the energy of which is equal to Boltzmann's constant multiplied by temperature, kT) [49], each phase shows a characteristic optical texture defined by its molecular order that can be exploited for use as sensors (electrical, gas, thermal, pressure [12, 40, 50]), mediators for transport in biological systems, and displays [11], to name a few. By far the most successful application of these has been for display technology, but as will be briefly reviewed in sec. 2.3, the idea of using them for gas sensors is not unique.

To date, the difficulties in realistically implementing LCs in gas sensing devices have largely been due to non-trivial problems faced in enhancing their sensitivity, strengthening their selectivity, and confining them in "easy-to-handle" yet robust form factors. Often LC phase based gas sensors in the past have required the use of external electronic (or spectroscopic) equipment to characterize the response, and have been restricted to rigid, non-flexible confinements (i.e. glass cells, substrates) [40]. Hence a recurring theme throughout this thesis will be figuring out how to stabilize and completely encapsulate LC phases by coaxially electrospinning them in polymer fibers, and how these bi-component fibers contribute to the visualization of their responses to gases, as a mat and individually.

2.2.1 The nematic phase

As shown in Fig. 2.4 the nematic phase is characterized by having anisotropic molecules (here, depicted as rod-like, but which can also be disc-shaped [12]) with very short-range positional order but with long-range orientational order. The latter aspect, long-range orientational order, is a quality shared with that of a crystalline solid, but that is where the similarity ends as the nematic phase does not have lattice or grain boundaries in the same way some crystalline solids do. The average direction in which the individual rod-like molecules are ordered in the nematic phase is called the director (or, $\mathbf{n}$). In Fig. 2.4 the director next to the relatively (but not perfectly) aligned nematic phase molecules is shown pointing up ($\uparrow \mathbf{n}$), but actually the director is sign invariant.

For the image shown in Fig. 2.4, this means that $\uparrow \mathbf{n}$ is equivalent to $\downarrow \mathbf{n}$. The fact that the director is sign invariant suggests that all of the rod-like molecules in the nematic phase have as much probability of pointing upwards as downwards to make a symmetric phase. In reality, however, the actual molecules which can make up this symmetric phase, like 5CB molecules for instance, can be asymmetric. What is important is that the molecules that constitute the nematic phase, on average, will align in the direction parallel to the director along their long axis, and thus allow the nematic phase to have continuous rotational symmetry [49]. As a result of the sign invariance, one may come across the term "pseudovector" in various descriptions of the director [40].

The order parameter

The order parameter of the nematic phase, also known as the way in which the long-range molecular order of the nematic phase can be quantified [12, 40] and in general, the way to distinguish when the nematic phase begins and ends [51], can be defined using Eqn. 2.1.

$$S = 1/2\langle 3\cos^2\theta - 1\rangle \tag{2.1}$$

Here, the order parameter for the nematic phase (S) can range from [-1/2, 1] for θ values [0,π]. The angle θ is the magnitude of the deviation of the molecular long axis from the director ($\mathbf{n}$), shown in Fig. 2.5. The $\langle ... \rangle$ brackets denote that the orientations of all molecules in the nematic ensemble is averaged in three dimensional space. Although the angle ϕ (the azimuthal angle defining the direction of the deviation) in Fig. 2.5 does not explicitly appear in Eqn. 2.1, it is implicitly taken into account in the averaging.

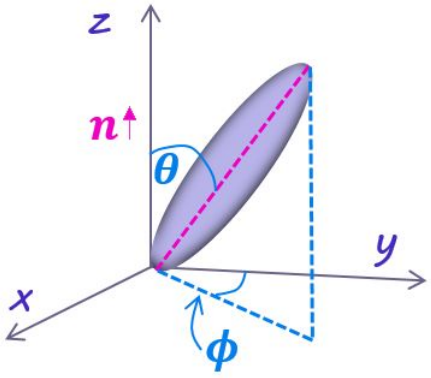

Fig. 2.5 – The parameters (angles: θ and ϕ) that define the orientation of a rod-like molecule in the nematic phase with respect to the director. Angle θ and ϕ are discussed in the main text in the context of explaining Eqn. 2.1, which defines the order parameter.

Experimentally, nematic phases have been shown to have S = 0.4 - 0.6 [12]. A nematic LC phase never achieves perfect order (S = 1). Moreover, the lower value (0.4) is observed when the nematic phase is closest to the nematic-isotropic transition (the clearing point), whereas the higher value (0.6) is the saturation value observed at low temperatures within the nematic temperature range. Additionally, it is rare to find S = -1/2, or a negative orientational order parameter, for a nematic phase since that would imply that the molecules are aligned perpendicular to the director, but it has been noticed to occur under specific circumstances[52–54]. What is more likely to be experimentally observed is the transition to when S = 0, when the nematic phase molecules have no orientational order like that of an isotropic liquid (Fig. 2.4). Since the transition between the nematic phase to the isotropic phase occurs discontinuously (S jumps from 0 to a non-zero value roughly = 0.4 [55, 56]) it is characterized as a first order transition [12].

The total free energy of the nematic phase

The characteristic free energy in the absence of external stimuli (F) of a nematic LC phase can be summarized as the sum of its free energy in the bulk state ($F_{elastic}$) and its free energy at a boundary or surface ($F_{surface}$). Equation 2.2 further elaborates on these contributions. Here,

$F_{elastic}$ is obtained by integrating the elastic energy density, $f_{elastic}$, over the volume (V) of the LC phase and $F_{surface}$ is obtained by integrating the corresponding energy density $f_{surface}$ over the LC phase surface (S). The term (F_0) in Eqn. 2.2 refers to all other contributions to the nematic phase free energy that are not defined in terms of effects at the boundary or in the bulk. These contributions to raising the free energy can be due to thermal effects or mechanical deformations, for example, but for simplicity they are grouped under term (F_0).

$$F = F_0 + \int_V f_{elastic} dV + \int_S f_{surface} dS \tag{2.2}$$

When the nematic phase contains a uniform director field, its minimum free energy state has been met and there are no deformations within the texture of the nematic phase. However, in subjecting the nematic phase to various types of confinement boundaries (e.g. between coated glass plates, or the cores of fibers), and external forces (e.g. mechanical shearing, electric or magnetic fields...etc.) the director may deform in a way that causes the energy expressed by Eqn. 2.2 to increase. Therefore, the total free energy (F) is a way of accounting for the cost of having the nematic phase adopt a particular configuration due to various forces imposed on it. The configuration that minimizes F is the equilibrium configuration, and can be used as a way of predicting how the director may distort given a certain type of confinement. Unlike solids that can experience distortions and have restoring *forces* to oppose the deformations generated in their lattice, distortions in the LC phase $\mathbf{n}$ (which, recall, is a function of all the molecules' orientations in time and space) are opposed through a restoring elastic *torque*. Note that this restoring torque does not occur in isotropic liquids.

When deformations throughout the volume of the bulk LC phase occur they can be described as superpositions of the director splaying, twisting or bending. Oseen and Frank characterized these elastic deformations as just that: *splay*, *twist*, and *bend*, in their influential works of the 1920s and late 1950s [11, 12, 40]. Thus, the contribution of elastic energy density in the bulk, $f_{elastic}$, can be seen as the sum of three terms preceded by the elastic constants: K_1, K_2, and K_3 representing splay, twist, and bend in the ground state nematic phase (as per Eqn. 2.3 and Fig. 2.6).

$$f_{elastic} = 1/2[K_1(\nabla \cdot \mathbf{n})^2 + K_2(\mathbf{n} \cdot (\nabla \times \mathbf{n}))^2 + K_3(\mathbf{n} \times (\nabla \times \mathbf{n}))^2] \tag{2.3}$$

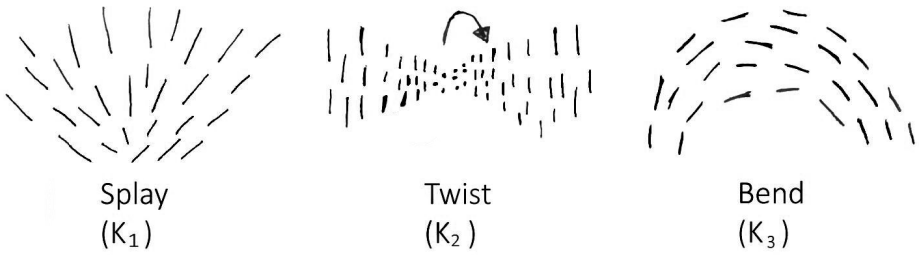

Fig. 2.6 – Sketch showing how the nematic director with pure deformations in splay (K_1), twist (K_2), and bend (K_3) would appear. All three of these deformations occur independently of each other and the LC director field can adopt any combination of them depending on the type of deformation. Note also that because all the terms are squared they all contribute to raising the elastic energy of the phase.

In general K_1, K_2, and K_3 tend to be in piconewtons, and for LC nematic phases formed from cyanobiphenyls they are similar in magnitude [57] (for 5CB: $K_1 = 5.2$, $K_2 = 2.9$, $K_3 = 6.8$ [58]). Although as seen with chromonic nematic LC phases formed from stacks of amphiphilic molecules in water stated above (and discussed in ch. 6) this is not always the case. As for the contribution of increased free energy due to confinement with well specified boundary conditions, $f_{surface}$, we need to take into account the contribution of the deformation of the director with respect to the preferred direction at the boundary. When an LC phase is confined against an interface, the interactions between the LC molecules and the surrounding phase will define one particular director orientation at the interface that minimizes the surface free energy density. Considering only the surface contribution, this is the orientation that the director takes at the interface. For instance, if the director field is perpendicular to the interface (we call this homeotropic), if it is parallel to the interface (it is called planar). In many instances, however, the combination of the shape of the interface and the preferred director orientation at the interface (referred to as anchoring) is incompatible with a uniform orientation in the bulk.

We thus often have a competition between $f_{surface}$ and $f_{elastic}$, where minimization of the former by necessity leads to an increase in the latter, and vice versa. While LC phases can adopt three types of orientations (planar, homeotropic, and tilted) at interfaces, one of these (planar) is most relevant for the nematic phase encapsulated within the polymer fiber cores discussed in this thesis. To see how the planar and homeotropic anchoring types alter the director when in contact with non-curved surfaces consider Fig. 2.7.

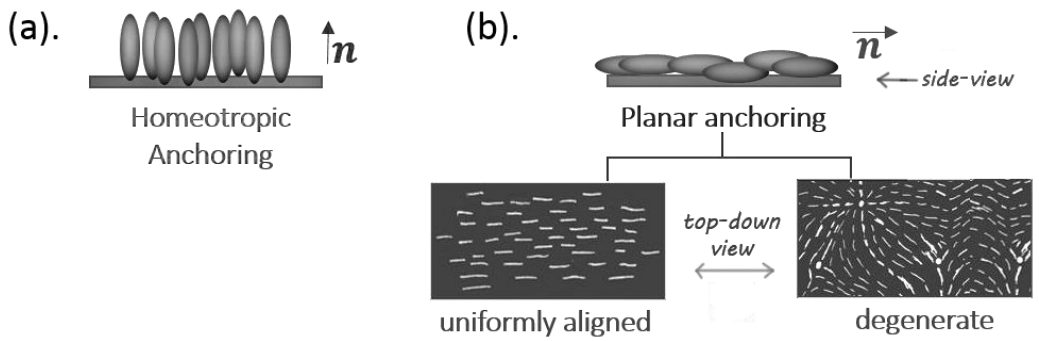

Fig. 2.7 – Sketch of the LC director on non-curved surfaces. When the molecules and director, $\mathbf{n}$, are perpendicular to the flat surface, we say that the sample has homeotropic anchoring (a). For the nematic phase, since the director is parallel to the optic axis, the optic axis is also perpendicular to the surface in (a). This has implications for how the phase appears when observed in the POM. When the director is within the plane of a flat surface it could be either uniformly aligned or "degenerate" (random orientation within the plane of the interface) (b). With a uniform director field the rod-like molecules (white lines) are arranged along the substrate's surface in a specific direction. A degenerate director will typically have several defects (white dots) showing where it has abruptly turned and changed direction.

What distinguishes planar anchoring from homeotropic anchoring is when the director changes from 90° to 0° with respect to the normal of the surface that the phase covers. Assuming there is a flat surface, if the LC phase molecules orient perpendicularly to it, Fig. 2.7(a), we say that the phase has anchored homeotropically to the surface. Likewise, if a particular two dimensional surface is coated or prepared in such a way that can promote the perpendicular alignment of the LC director field we can also say that the surface "promotes homeotropic phase anchoring." Alternatively, if the LC phase orients in the plane of the surface, Fig. 2.7(b), then the molecules

are planarly anchored. Most uncoated glass slides and polymer surfaces actually promote planar anchoring for LC phases, although there are exceptions depending on how they are prepared.

Additionally, there are two forms of planar anchoring that the phase can adopt - degenerate planar alignment, and uniform planar alignment. For the former, consider that just because the LC molecules lie in the plane of a surface this does not imply that the director must remain in a particular direction. The molecules are free to adopt any azimuthal angle while being in the plane, thus, this configuration is referred to as degenerate planar anchoring. The degeneracy in the director can be seen if the sample is observed from the top-down, where the director turns and curves in the plane of the surface - shown in the sketch of Fig. 2.7(b) as rods pointed in various directions with some defects areas. Experimentally, if a nematic phase with degenerate planar anchoring is observed through crossed polarizers in the polarized optical microscope (POM) one will see evidence of the turning director as *schlieren* ("brushes") and dark defects of varying strengths. However, degenerate planar anchoring differs optically from uniform planar anchoring, the latter which when viewed from the top-down in Fig. 2.7(b) will not show schlieren or defects in the director. This is because the director has been forced to align in a particular direction on the substrate from the way it was prepared or coated.

Mathematically, the surface anchoring coefficient (w) applied to the direction of the LC director, defined by (Θ, Φ), and the surface anchoring energy density contribution is found by Eqn. 2.4. The preferred director axis is called the *easy* axis–here one can say Θ_0, Φ_0. In Eqn. 2.4, the sum of the anchoring terms related to variations in Θ (i.e. w_Θ) and in Φ (i.e. w_Φ) describes how much work is needed per area (J/m^2) to make the molecules (and the director) deviate from its preferred easy axis to some new coordinate.

$$f_{surface} = f_\Theta + f_\Phi = [1/2 w_\Theta \sin^2(\Theta - \Theta_0)] + [1/2 w_\Phi \sin^2(\Phi - \Phi_0)] \tag{2.4}$$

Last, it is worth noting that the anchoring coefficients of the LC phase are temperature dependent. Thus, they will decrease as temperature increases. This inverse relationship exists because as temperature increases the nematic order parameter (S) decreases until the phase changes to an isotropic state [59].

2.2.2 Optical anisotropy of a uniaxial director

When applied to materials the term *anisotropy* refers to the directional dependence of properties found within a sample. This can mean anything from differences in the intramolecular distances of atoms in a crystal lattice, to differences in mechanical properties of a macro-scale structure that emerge from the direction in which the structure is measured. An example of the latter is seen in the way that different types of natural hardwoods are subjected to stress - the maximum compression stress before deformation is often seen "along-the-grain", or parallel to the long axis of wood fiber growth, wheres the minimum stress supported is seen during compression in the perpendicular direction [60].

However, an even more basic definition of something anisotropic is something that is the opposite of isotropic - the latter refers to a material that has the same properties, regardless of the direction or way it is measured. Here, the terms anisotropic and isotropic are used to refer to the differing optical properties of the nematic LC phase when it is observed under various conditions. Moreover, a consequence of a material having anisotropic properties is that optically it is also said to be *birefringent*. Birefringence can be generally described as the

difference between refractive indices for two perpendicularly polarized light rays passing through an anisotropic sample when viewed with a beam of light. A more detailed definition will follow below in the context of LCs.

Previously, it was mentioned that the T_c of an LC phase refers to the temperature at which the phase clears to an isotropic state. Here, while the molecules do not chemically transform, the long-range order of the self-organized nematic phase breaks down. At this point, it becomes an isotropic liquid, in all physical properties. An isotropic liquid, recall, has no long-range orientational order.

Since the individual molecules of 5CB already have anisotropy in their electronic polarizability, which differs along the axis from the short axis (perpendicular to the former), and since this helps the assembly into a nematic phase which has continuous rotational symmetry about the molecular long axis, we say that the nematic phase has an *optic axis* aligned parallel to the director. The optic axis is defined as the direction in the assembled phase along which light can traverse such that the phase appears isotropic. If a representative uniaxial ellipsoid is viewed along either its long axis, or short axis, as in Fig. 2.8, we see that the ellipsoid only appears isotropic (a circle which has full rotational symmetry) along the long-axis. If this representative sketch is extrapolated to consider the assembled nematic phase, with many molecules along the director, the same would be true. And in a more generic comparison, the rotational symmetry of the nematic phase mirrors that of the cross section of the uniaxial optical indicatrix as well (Fig. 2.8). The uniaxial nematic phase has two principal refractive indices ($n_{\parallel}$, and $n_{\perp}$) which affect how light interacts with it.

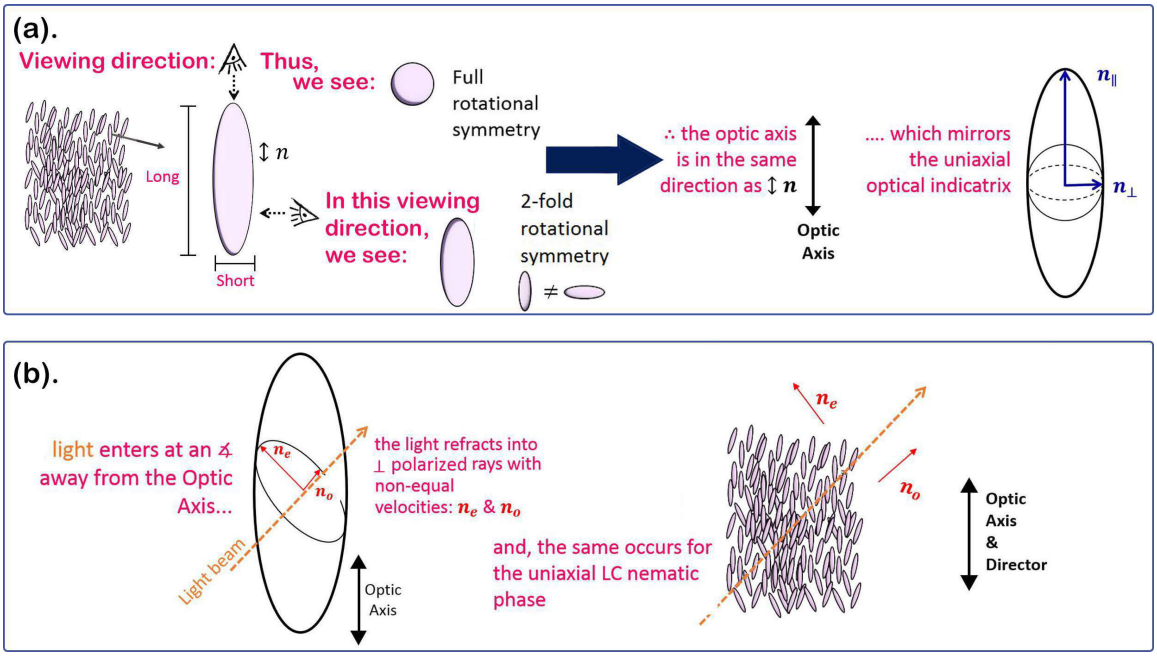

Fig. 2.8 – Sketches showing the reason why the uniaxial nematic phase has an optic axis that is parallel to the director in (a) using a model rod-like molecule as an example. The rod-like molecule does not give the nematic phase per se, but the self-assembly of several of these molecules gives the nematic phase. This then models that of the well defined uniaxial optical indicatrix (a). When the direction of the optic axis (and director) is known for the nematic phase, as light enters at a non-zero angle into the sample, it refracts into the extraordinary (n_e) and ordinary (n_o) waves through the medium (b).

Like in the uniaxial optical indicatrix model, if light enters the nematic phase at a non-zero angle, away from the optic axis (& director), it will refract into two individual ray components called the "extraordinary" and "ordinary" rays that are polarized perpendicular to each other (Fig. 2.8). Each are defined in terms relative to the principal refractive indices. The extraordinary ray may experience a portion of both $n_{\parallel}$ and $n_{\perp}$ (depending on the angle made between the optic axis and the direction of incidence for the light) giving rise to the refractive index: n_e, while the ordinary ray will always experience the refractive index $n_o = n_{\perp}$ only. The equations for calculating both as a function of the principal refractive indices are shown in Eqn. 2.5, where the angle α represents the angle between the optic axis and the propagation direction of incident light.

$$n_o = n_{\perp} \qquad \& \qquad n_e = \frac{n_{\parallel} n_{\perp}}{\sqrt{n_{\parallel}^2 \cos^2 \alpha + n_{\perp}^2 \sin^2 \alpha}} \tag{2.5}$$

Note, that if the incident light beam enters exactly through the optic axis ($\alpha = 0^{\circ}$) then the extraordinary ray (n_e) will also only interact with $n_{\perp}$ because it would be as if one were viewing an isotropic medium (like a perfectly symmetrical circle, Fig. 2.8) with complete rotational symmetry. Thus, the anisotropic quality and the "effective birefringence" of the sample, defined as (Δn), would be zero because: $\Delta n = n_e$ - $n_o = 0$.

Assuming a case where the incident light beam enters the nematic phase away from the director at a non-zero angle, however, birefringence would still be present because the extraordinary and ordinary rays traversing through the phase would be phase shifted relative to the distance they traveled through the sample by Eqn. 2.6, where Δ_s defines the magnitude of the phase shift. The constants d and λ refer to the distance traveled by the rays and vaccuum wavelength of the applied light, respectively.

$$\Delta_s = (\Delta n) d \frac{2\pi}{\lambda} = (n_e - n_o) d \frac{2\pi}{\lambda} \tag{2.6}$$

Especially when viewing our nematic phase between crossed polarizers in a microscope, the transmitted light that emerges once the extraordinary and ordinary light rays recombine after traversing through the sample is important for understanding how the bright colors of the nematic LC phase are observed microscopically (and for the optics ch. 6 in this thesis). Consider the situation in Fig. 2.9, for example, where unpolarized light initially traverses through polarizer # 1 that has a polarization axis of -90° then meets a sample containing a uniformly planar aligned nematic phase (just like the one shown in Fig. 2.7b) with its optic axis at a 45° with respect to polarizer # 1.

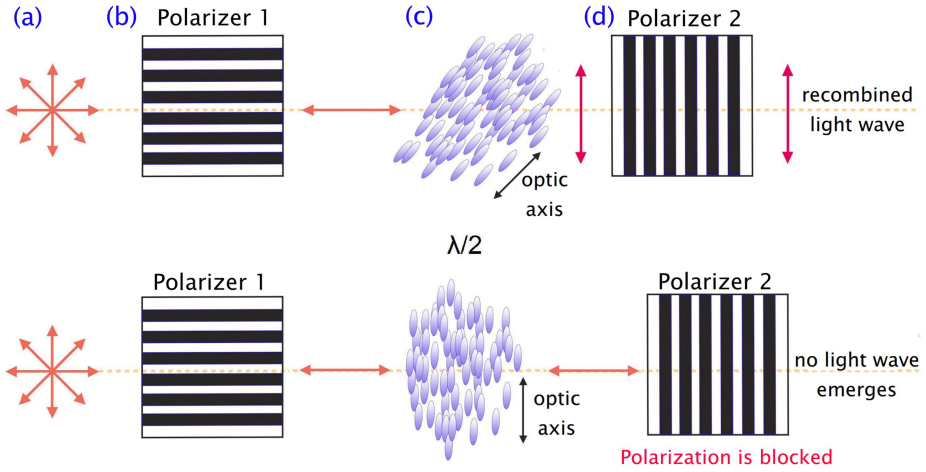

Fig. 2.9 – Sketch showing the dependence of the light transmitted, or not, through a uniformly aligned nematic sample with thickness and birefringence corresponding to the optical path length difference $\Delta\Lambda = \lambda/2$ when viewed through crossed polarizers in the POM. In the first row, unpolarized light from the back (a) passes through polarizer # 1 (b, with a polarization axis of -90°) before meeting the aligned nematic phase sample (c) with director (and optic axis) oriented 45° to the polarization of the light beam emitted from polarizer # 1. After the beam splits into the extraordinary and ordinary waves within the LC, and recombines after exiting the sample, the emerging light beam hitting polarizer #2 (d) has a linear polarization rotated 90°. This polarization matches that of polarizer #2 allowing it to pass through, and thus the sample appears bright. However, if the same nematic sample is rotated such that its optic axis matches the polarization of the light beam emitted from polarizer # 1 (bottom row), the resultant light beam will have the same polarization as before hitting the LC. The perpendicularly oriented polarizer #2 will block the light, and the sample will appear dark.

Since the light entering the phase at a non-zero angle will refract into the two ray components polarized perpendicular to one another (with n_e and n_o), the resultant light ray from those two recombining after exiting the sample may have a different polarization. The phase shift corresponds to a difference in effective optical path length between the two rays, that can be written as $\Delta\Lambda = \Delta_s\ (\lambda/2\pi)$. Depending on the magnitude of the phase shift (Δ_s), or optical path length difference, the polarization may be linear, circular or elliptical as illustrated in Fig. 2.10. An important example is the case where ($\Delta_s = \lambda/2$) where the polarization of the emerging beam is the mirror image of the polarization of the incoming beam with respect to the optic axis. This means that the light now has just the right polarization to go through polarizer # 2 shown in Fig. 2.9.

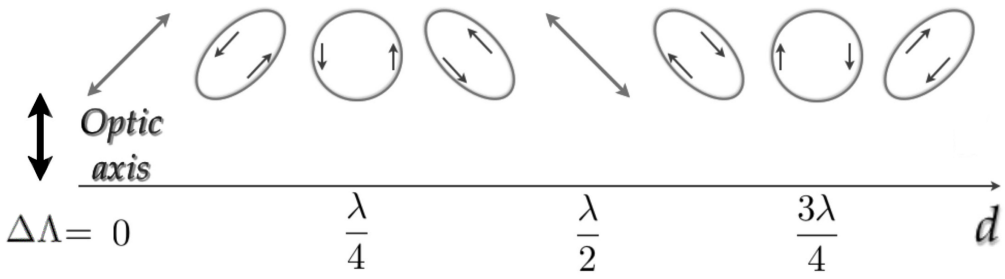

Fig. 2.10 – Sketch showing the general different types of polarizations of light possible with optical path length differences ($\Delta\Lambda$) from 0 to $3\lambda/4$ and increasing thickness (d) of sample. For linear incoming light, linear exit polarization occurs for $\Delta\Lambda = 0$, $\lambda/2$; circular for $\Delta\Lambda = \lambda/4$, $3\lambda/4$.

The phase shift and the resulting polarization change by the LC is relevant during polarized light microscopy (POM) analysis because when viewing a uniaxial anisotropic sample through crossed polarizers (polarizers[†] which are rotated by 90° with respect to each other) we can understand in which direction the optic axis (and for LCs, the director) is oriented based on the intensity of the light. A requirement for this phase shift to take place is that both the ordinary and extraordinary rays are excited by incoming light. If the incoming polarization is along the optic axis, only the extraordinary ray exists, and if it is perpendicular, then only the ordinary ray exists. Thus, in these two cases no change to the polarization can occur, and the sample will appear black between crossed polarizers.

The transmitted light which emerges from the second polarizer after the two rays have recombined after exiting the nematic phase will have a new intensity (I). The magnitude of this new I (Eqn. 2.7) will be dependent on the intensity of the initial light beam that remains after passing through the first polarizer (I_0), β which defines the angle between the analyzer and the director, and the amount of phase shift between the split rays upon passage through the nematic phase (Δ_s).

$$I = I_0 \sin^2 2\beta \sin^2 \frac{\Delta_s}{2} \tag{2.7}$$

While $\sin^2 2\beta$ describes the modulation in light intensity without a shift in color, $\sin^2 \frac{\Delta_s}{2}$ will describe the variation in polarization depending on the wavelength of incoming light (see Eqn. 2.6). Under the standard condition of white illumination, containing all visible wavelengths, the visible effect is a variation of color. Notice, that if $\beta = 90°$ or 0°, I becomes 0 and that for 45°, I is maximum. This represents the blocking and transmittance of light through the second polarizer when the uniformly aligned nematic phase was shown turned in Fig. 2.9. Thus, the sample has a 90° periodicity appearing dark when rotated at 0°, 90°, 180°, and 360°. This also means that even if the nematic sample is in degenerate planar orientation, wherever the director (defining the optic axis) happens to align with the transmission direction of one of the polarizers then the sample will appear dark in that area, even if other areas in the sample may appear maximally bright.

[†]When referring to the polarizers used in crossed polarizer analysis in the POM, the bottom polarizer closest to the stage is often referred to as a *polarizer*, while the top polarizer closest to the oculars is known as the *analyzer*.

Pictorially, the relationship between Δn, $\Delta\Lambda$ and interference colors observed is displayed in the Michel-Lévy chart (shown in Fig. 6.4 on pg. 118[‡]) named after Auguste Michel-Lévy who was a geologist and pioneered the use of the POM in studying minerals. Usually, if two of three components (out of interference color, sample thickness (distance the light waves traveled through the sample), and birefringence) are known, the third may be found by consulting the chart. In the chart, the interference colors seen are grouped by "orders" for every 550 nm of path difference. While the colors seen after the first order repeat themselves, eventually for high path differences ($\geq$ 4000 nm) and sample thicknesses, the colors become washed out. These higher order colors scatter as white because the waves transmitted will be a combination of many wavelengths.

Let us consider analyzing a nematic phase between crossed polarizers. While turning the sample (as in Fig. 2.8) can show where the maximum brightness and maximum darkness are, this is not enough for finding the direction of the optic axis if that is unknown. In the top image of Fig. 2.9, the nematic sample could have been rotated at $+45^\circ$ or -45° and it still would have appeared bright through crossed polarizers. To solve the ambiguity in the direction of the director, compensators, also called wave-plates, which are (generally) quartz wedges or quartz slabs of constant thickness can be inserted in between the sample and the microscope analyzer (polarizer # 2, in Fig. 2.9) to further add (or subtract) a certain value to (from) the optical path difference between the ordinary and extraordinary rays as defined within the sample. Of course, this depends on how the sample is oriented, but the compensator is always inserted at 45° with respect to one of the polarizers. Thus, with this fixed position, it becomes possible to determine whether the interference color observed after its insertion is the result of adding or subtracting the path difference of the phase plate, for instance , λ, in that particular direction.

[‡]The chart was placed in ch. 6 so that it could be referred to more easily when discussing the interference colors in the fibers.

2.3 Current status of VOC sensors

While the concept of VOC (volatile organic compound) sensing using LCs is not new [61–66], the idea of encapsulating LCs into electrospun fibers for VOC sensing is.[§] Given the ease of electrospinning to produce tangible fiber mats relatively quickly and the results of successful LC encapsulation in electrospun mats reported in 2008 [67] and in 2010 [68], the first report from Kim et al. in 2013 [69] proposed that electrospun LC fiber mats could be used as wearable sensors for showing responses to hazardous gases macroscopically and without the need for additional equipment. However, it was not until the results of several experiments, published in 2016 [70], that we knew the extent to which LC-fiber mats with different fiber morphologies, spun with varying configurations (aligned or random mats) could be used as VOC sensors and their relative longevity after use. The target gas used for LC-fiber sensing in this thesis was toluene as it is known to be a common byproduct found in many chemical industries and can readily distribute in air without being noticed.

While our experiments in testing the responsivity of LC filled fiber mats to toluene vapors were new, there were others who had used LCs for gas sensing using different form factors prior to us. Nicholas Abbott's group in Wisconsin (U.S.A) and and Dirk Broer's group in Eindhoven (Netherlands), for example, had experimented with using thin films of LCs using two separate techniques for gas sensing as well. What is common with both of their approaches is that their LC films were non-encapsulated (meaning they were open to ambient air from the top) and were on flat substrates. Table 2.1, modified from ref. [40], succinctly illustrates the state of the art from current non-textile and non-wearable "traditional" gas sensors to LC and non-LC fiber based sensors. It also introduces the major contributions made by both Abbott's and Broer's works.

[§]Note that much of this overview is a summarized version of the one I wrote in section 4.4.1. in Ref. [40].

Tab. 2.1 – Summary of state of the art (as of 2016) regarding portable and wearable gas sensing devices. The devices mentioned are grouped by type (with LCs, without LCs, fiber and non-fiber based) and with corresponding pros and cons for each. (This Table was adapted from ref. [40] with permission from IOP Publishing under the license: CC BY 3.0)

Sensing Device	Pros	Cons
Traditional Gas Sensors	Large variety commercially available & thorough understanding of functionality known [71]. Metal oxide (MOX) sensors: low fabrication cost, sensitive, wide selectivity range [72, 73]. Polymer sensors: low energy consumption, low fabrication cost, sensitive [72]. Carbon nanotube sensors: (fibers) high surface-to-volume-ratio, low cost, portable	MOX sensors: high energy consumption, unstable in uncontrolled environments [73, 74]. Polymer sensors: selectivity & long-term stability issues [75]. CNT sensors: high costs, reproducibility problems [76].
LC Based Gas Sensors	High sensitivity & selectivity demonstrated for many VOCs (Abbott's group tests: DMMP [77, 78], various nerve agents [79], and toluene [80]; toluene also tested by our group: [70], and Chang et al. [81]; chloroform tested by Dickert et al. [64]). Works w/ many LC compounds - dopants can ensure specificity, tested by Broer's group: [82]. Requires no electricity or power source to function - room temperature operation. Small devices possible. Chiral dopant sensors enable immediate detection by human sight (color change) [82].	LC sensors have issues with distinguishing specificity to nerve agents and other VOCs [69, 70, 79, 83]. Form factor challenge: requires flexible yet robust LC containment to allow exposure to environment. Many current solutions require polarizing microscopy analysis
Current Non-LC Wearable Gas Sensors	Conductive liquid / interdigitated electrodes for capacitive / resistive sensing: weavable into garments, some flexibility [84–86]. Inkjet printed CNT-based electrodes: fast, low-cost production, weavable into garments, coin cell batteries = good lifetime due to low power requirements	Electrodes: Reproducibility issues, time-consuming (& high coat) production for non-printed sensors [87].Capacitive/resistive response speed can be slow [84]. Read-out of sensing response requires further electronics. Sensing is limited (so far) to water vapor, sweat, and ammonia. Inkjet printed: form factor issue - not breathable or very reusable as they not true textiles but PDMS rubber films.[88], high cost
LC Gas Sensors in Fiber Form	Potential solution to form factor challenge: demonstrated function in non-woven mats [69, 70]. Response visible at room temperature, with/without additional optics [70]. Response and relaxation within seconds [70]. Long shelf life possible (minimum two months demonstrated [70])	Subject to production reproducibility issues [70]. Response function needs further investigation [69, 70]. Sensitivity & selectivity need further development [70]. Transition to more robust polymers needed to address washability & degradation issues

Platypus Technologies LLC in Wisconsin, headed by Abbott, successfully commercialized LC film based sensors for detecting gradual exposure to H_2S (hydrogen sulfide) gas via a quantitative readout. Though this sensor is separate from that which his research group has published, the availability of this type of commercial LC based sensor shows that there is industrial interest in the technology. Academically, the research regarding LC sensing that Abbott's group has done is based on the idea that anchoring changes within confined nematic phase LC films will be triggered upon exposure to the target gas. The anchoring change of the LC will be visually detectable as a change in birefringence of the confined LC film. His group found that when the thermotropic nematic phases containing cyanobiphenyls are doped with metal cation (Al^{3+}, Cu^{2+}, Na^{+}...etc.) perchlorate salts, the phases adopt homeotropic anchoring on glass surfaces. Optically the LC film appears dark. Then when this homeotropically aligned film is exposed to VOCs (mostly of the organophosphonate type) the anchoring of the phase changes to planar on at least one side [78, 79, 89–91] and the film then appears bright.

From the molecular perspective, before the VOC is introduced, the nitrile groups of cyanobiphenyl based nematic LCs become complexed to the perchlorate salt cations that are added in (the nitrile groups to the metal ions). Once the organophosphonate groups in the VOCs are introduced the complexed cations prefer the lone pairs of electrons to complex to on the phosphonate groups than the nitrile groups on the 5cb. Thus, when the films are exposed to the VOCs the response observed is the LC releasing its bond to the salts that allowed it to have homeotropic anchoring [79, 91]. Since the LC is no longer anchored by the salt to have a preferred orientation, the LC adopts planar alignment and appears bright. The salt complexed to the phosphonate groups of the VOCs does not show any birefringence, however, that is visible via the microscope at least. Organophosphonate groups are readily found in many chemical warfare agents, thus their detection by substrates supporting thin LC films have been of great interest. In a more recent study, described further in sec. 6.4.1, Abbott's group found that 5CB films, without the need for salts, can additionally show anchoring changes when they had hybrid anchoring (i.e. LC director is planar on bottom but homeotropic on top; LC is still open to air though) and exposed to toluene vapors [80]. In this last study, different types of surfaces were explored for carrying the LC films - polymeric and metal based (gold coated over glass) to see whether anchoring changes would still occur during toluene exposure, and they did.

Overall, the surface anchoring approach by Abbott's group offers a way of introducing selectivity, reversibility, and sensitivity for LC VOC sensors. The anchoring change approach was found to work with VOCs containing organophosphonate groups, provided that the films were also doped with metal perchlorate salts. However, one drawback is that one is not able to easily differentiate responses between several VOCs containing similar phosphonate groups because the dark to bright response seen is the same, the only difference being the time taken for the response to show. This is where the LC sensing approach by Dirk Broer's group can be advantageous. In the design by Broer's group thermotropic nematic LC films doped with chiral dopants, which are molecules that cause the nematic director to helically twist, can selectively reflect certain wavelengths. This means that a film containing the chiral dopant can have a certain color visible to the eye, and unlike in Abbott's films which are on the microscale order, these films can be macroscopically visible. Additionally, the dopant introduced can also be reactive to the desired target gas for sensing. This means these colored LC films can be highly selective to detecting CO_2, O_2, and water vapor, for instance, and can show macroscopically visible color changes as the responses [82, 92, 93]. Once all of the chiral dopant in the film finishes reacting with

the target gas the film was exposed to, the starting color of the film changes to show that the reaction ran to completion. In Han et al.'s [82] case the film starts as orange and then appears green after the dopant finishes reacting with CO_2 gas, for O_2 gas another film changes from green to yellow.

The only drawback in this approach, however, while solving the selectivity problem, is that the process cannot be reversed so that the original mat color before exposure is regenerated. Nor can the same mat be used again for detecting another gas. Depending on the application this may be beneficial, for detecting the level of absorption of these gases over time, but this can be a limitation if intended to be used as a visual detector for continuously monitoring changing exposure to the VOC as eventually the sensor would have to be replaced and cannot be reused once the dopant finishes reacting. Likewise, LC based sensors that rely on the phase change from nematic to isotropic [63, 64], and the fiber based ones proposed in previous studies [40, 69, 70, 83] (although beneficial in providing a flexible form factor, complete encapsulation of the LC for incorporation into other devices or garments, and reversibility) do lack selectivity. Two ways that could be employed to address the selectivity issue of the LC-fiber sensors will be addressed in the last chapter.

3

Experimental setups & protocols: From coaxial electrospinning to sensing VOCs

Rather than a generic experimental protocol for the analyses undertaken in this thesis, this chapter explains why certain setups (in particular, the electrospinning and gas sensing ones) were assembled in the specific ways they were, and why certain parameters were chosen for their operation. For those who do similar research, this chapter is meant to serve as a useful f.y.i. (for your information) guide. Additionally, the optimal settings from certain instrumentation used (FTIR, SEM, and DSC) are also described.

3.1 On electrospinning PVP fibers with a 5CB core

While there is such a thing as a generic type of electrospinning setup, that is, one which has all of the parts necessary to make the process work (e.g. a pump to flow a polymer solution, a high voltage unit, a collector) from my experience in building a few, visiting other labs which have some, and talking to others about making them, in practice the setups can be "as unique as snowflakes." This is because the *type* of nano- or microfibers one can electrospin can vary quite a lot.

Someone once told me that “we make all types of fibers here; various flavors for various purpose” when I was first introduced to electrospinning research. It is true that each modification to an existing setup adds an aspect that contributes to the final individual fiber morphology, and thus, contributes holistically to the type of fiber mat produced in the end.

Here, the interest is in forming solid polymeric microfibers with a core containing a non-reactive, oil-like liquid. To complicate matters further, this oil-like core fluid, while inert, is not always isotropic. It forms a room temperature liquid crystalline phase which must be easily distinguishable from the surrounding polymer sheath which contains it. As we rely on polarized optical light microscopy (POM) as the primary means of distinguishing key aspects of LC phases (e.g. anisotropy, director order, defects, birefringence), it is important that the fibers be easily mountable for detailed analysis onto a standard optical polarizing microscope stage. Another consideration is that the fibers, and fiber mat, should truly have the LC contained in its core, and not be leaking. This means that the LC should not be coating the outside of the individual fibers after being electrospun (more on the ideal fiber types is explained in context of the results in ch. 4).

3.1.1 Choice of liquid crystal & polymer solution

The combination of polymer solution and LC to be used already dictate whether or not the first point – easy differentiation of the LC core in the fibers via microscopy, can be realized. The polymer solution and liquid crystal combination I used was a solution of 12.5 wt.%

polyvinylpyrrolidone (PVP) in ethanol for the former, and 4-cyano-4'-pentylbiphenyl (5CB) for the latter. Their chemical structures are shown in Fig. 3.1.

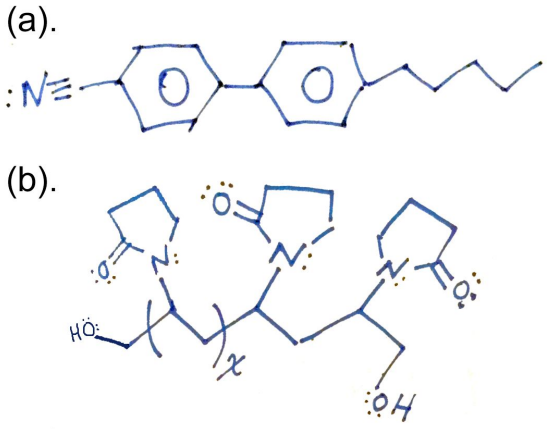

Fig. 3.1 – The basic chemical structures of the 5CB liquid crystal (a) and the PVP polymer (b) are shown. Although the two repeat units (of χ total repeat units) containing the lactam pendant group of PVP were drawn on the same side, this does not mean that synthesized PVP polymers are isotactic. Commercially sold PVP is usually atactic since it is synthesized via free radical polymerization to achieve molar masses up to 1 million g/mol using either hydrogen peroxide or AIBN (azobisisobutyronitrile) as initiators. Assuming hydrogen peroxide was used as the initiator in (b), the end-capping group on both sides should be (-OH) [94].

Liquid Crystal: 5CB

The nematic phase forming compound, 5CB, is by far one of the most commonly used throughout the community of liquid crystal researchers. This is because 5CB, although expensive (about $9 per gram), is readily commercially available (no custom synthesis required), is a low viscous liquid with density close to that of water at room temperature, is a single compound (unlike another popular nematic: E7, which is a mixture containing one terphenyl and three biphenyl compounds), and does not readily crystallize until around 18°C - 20°C. This compound does have a strong tendency to supercool, that is, it does not enter the solid phase until well below its melting temperature. This is actually beneficial for the purposes of electrospinning. We are interested in preserving the nematic phase during and after fiber formation to see how the vapor exposed fibers behave at room temperature. The 5CB used throughout the projects in this thesis was either bought from Synthon Chemicals GmbH or Yantai Xianhua Chem-Tech. Both were verified to have a nematic to isotropic transition between 35.7°C and 35.8°C.

Polymer Solution: PVP in ethanol

The PVP used for all polymer solutions has an average molar mass of roughly 1.3×10^6 g/mol, and was purchased from Sigma Aldrich. As a standard, anhydrous ethanol was also used for making the polymer solution, but 96 vol.% ethanol can be also used to yield similar spinning results. In general, it takes the same time (roughly 2-4 hours) to dissolve 12.5 wt.% of the PVP until it is macroscopically homogeneous in both anhydrous and 96 vol.% ethanol at a stirring rate between 500 – 600 rpm; no heating is necessary. It is possible to use either of the two ethanol types only if one is electrospinning the 5CB with the PVP solution in an ambient environment

with a relative humidity below 30%, and roughly room temperature conditions (25 °C ± 5 °C). The reason for this unique caveat is discussed in more detail in ch. 5.

Other than some fiber abnormalities that can result from electrospinning PVP in ethanol with 5CB at elevated humidity, in general this polymer was chosen to serve as the sheath because it forms fibers with very low optical birefringence. PVP is an amorphous polymer, and is unable to form strongly aligned chains that impart regions of semi-crystallinity on cooling unlike some Nylons (6, 6/6), and isotactic polypropylene (PP), for example. Although the electrospinning process itself naturally imparts a level of mechanical alignment longitudinally along the direction of extrusion, this overall form of alignment is too weak to give the PVP sheath significant birefringence. This means that the individual PVP fibers will not optically scatter as much light when viewed through crossed polarizers in the POM, and will not have competing birefringence with the LC phase forming compounds that are encapsulated within.

Additionally, through several experimental studies it was found that electrospun PVP fibers can have diameters ranging from 2 μm to 7 μm [69, 70, 95, 96]. The ability to form micron scale thick fibers with high optical transparency make using PVP as a sheath polymer suitable for detecting whether or not optically functional compounds are encapsulated correctly. In comparing (a). and (b). in Fig. 3.2 we see that the electrospun 5CB-filled PVP fibers in (b). are at least 2 orders more birefringent than the pure PVP fibers, which have polymer chains that are only weakly aligned..

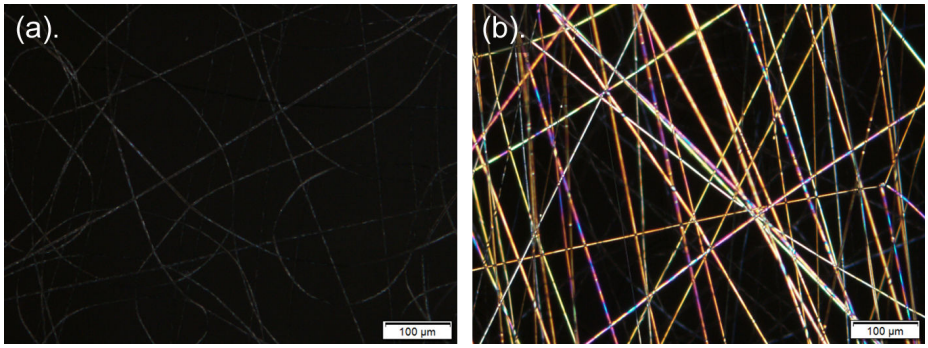

Fig. 3.2 – Crossed polarizer POM images comparing the qualitative difference in brightness seen in electrospun pure PVP fibers without 5CB in the cores (a), and with 5CB in the cores (b). The pure fibers show some brightness, however, the 5CB filled PVP fibers are considerably brighter, and exhibit higher orders of interference.

3.1.2 Coaxial needle setup for electrospinning

The coaxial needle used for co-flowing the PVP solution and 5CB liquid crystal together was fabricated in-house. The line diagram and photograph of the coaxial needle setup in Fig. 3.3 show how the individual components – tubes for flowing the PVP and LC, T-coupler, and stainless steel blunt-end cannula were fitted together, and how the final setup appears during use. The tube connections running from the microfluidics pressure based flow control system are also shown emerging from the tops of the vials because these provided the air flow needed to transport the liquids into the coaxial needle.

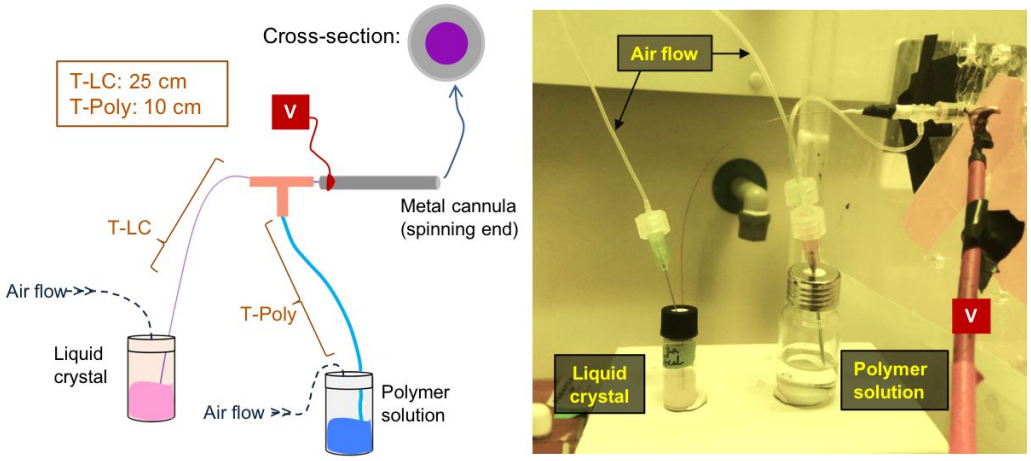

Fig. 3.3 – The coaxial needle setup used to electrospin the LC-PVP fibers with a photograph (right) showing the setup during an actual experiment. Air from the flow control unit discussed in sec. 3.1.3 is passed into the vials containing the polymer solution and LC. Over-pressurizing the vials causes the fluids to flow into their respective tubes in the coaxial needle setup. The total length of the tube that flows the LC ("T-LC") out of the coaxial setup was 25 cm. Note that this tube is inserted into one end of the T-coupler (shown in orange) and passes through the metal cannula. The total length of the tube that flowed the polymer solution ("T-Poly") was 10 cm. This tube only goes from the solution vial up to the T-coupler and does not pass through the metal cannula. The potential ("V" for voltage) is connected to one side of the metal cannula so that the co-flowing solutions can be charged before exiting the tip. The end of metal cannula cannot be seen in the photo because the wall of the spinning setup (Fig. 3.4) is covering that side.

For assembling the coaxial needle, a tube with a length of 25 cm for the inner capillary was placed through a T-coupler straight through to the end of the metal cannula. Then, a tube with a length of 10 cm was inserted through the opening of the T-coupler that is perpendicular to the openings where the inner capillary was passed through. This latter tube of 10 cm does not pass through the T-coupler all the way to reach the back end and instead is just inserted a few millimeters deep of the T-coupler opening. This tube serves to connect the polymer solution vial to the T-coupler. When the two ends of T-coupler are sealed, save for the last end that holds the metal cannula, the polymer solution will be able to flow throughout the T-coupler and out of the metal cannula. Meanwhile, the inner capillary will be responsible for transporting the LC from the vial through to the cannula end without mixing prematurely with the polymer solution throughout the T-coupler. If assembled and sealed correctly, the two fluids should come in contact for the first time at the end of the metal cannula.

While the line diagram of the coaxial needle setup in Fig. 3.3 shows a gap between the T-coupler and the metal cannula, this is merely just to illustrate that the inner capillary for delivering the LC (purple) should actually pass through all the way to the end of the metal cannula tip. In the actual assembly a gap between the T-coupling and the metal cannula should not exist at all. The metal cannula should be wedged into end of the T-coupler quite firmly and have a tight fit. To do this, a combination of heat-shrink tubes and Teflon tape were used together to fix the metal capillary and innner capillary to the T-coupler. Further details on the assembly process of the setup are described in the supplemental information of ref. [70].

As for the dimensions and types of tubes used for the coaxial needle setup, first, the inner capillary used was a flexible silica capillary with an inner diameter of 250 μm, outer diameter of 360 μm, and was purchased from www.bgb-shop.com (Part #: TSP-250350). The T-coupler used was of the "reducing" type (meaning that two openings side-by-side have the same inner diameter: 3.2 mm , while the middle perpendicular opening has a smaller inner diameter: 1.6 mm) and was made from polypropylene. The stainless steel blunt end cannula has a full length of 50 mm and an inner diameter of 0.70 mm, and an outer diameter of 1.10 mm.

A polytetrafluoroethylene (PTFE) tube with an inner and outer diameter of 0.8 mm and 1.0 mm, respectively, was used as the tube to transport the polymer solution from the vial (via attachment to an 18 gauge beveled point needle) to the T-coupler. Once the LC and the polymer solution were flowing together out of the metal cannula end, the voltage was applied to start the electrospinning process.The positive end of the voltage cable (red) is shown in Fig. 3.3 connected to a small section of the stainless steel cannula. This small area is a point on the steel barrel just before the T-coupler opening meets it.

Finally, the photo in 3.3 shows extra needles (with blue luers) connected to PTFE tubes that also extend from the LC and polymer solution vials. These connect to a pressure based flow control unit that was used to supply the air needed to over pressurize the vials and push the fluids into the coaxial needle setup. More details for why we used this approach to flow fluid rather than a typical syringe pump is described in sec. 3.1.3.

3.1.3 Camera, collector, & pressure based fluid flow

The line drawing in Fig. 3.4 represents the primary coaxial electrospinning setup which I designed and used for LC-PVP fiber production here. It is an evolution of the earlier set-up made by Eva Enz [97] (Fig. 3.7).

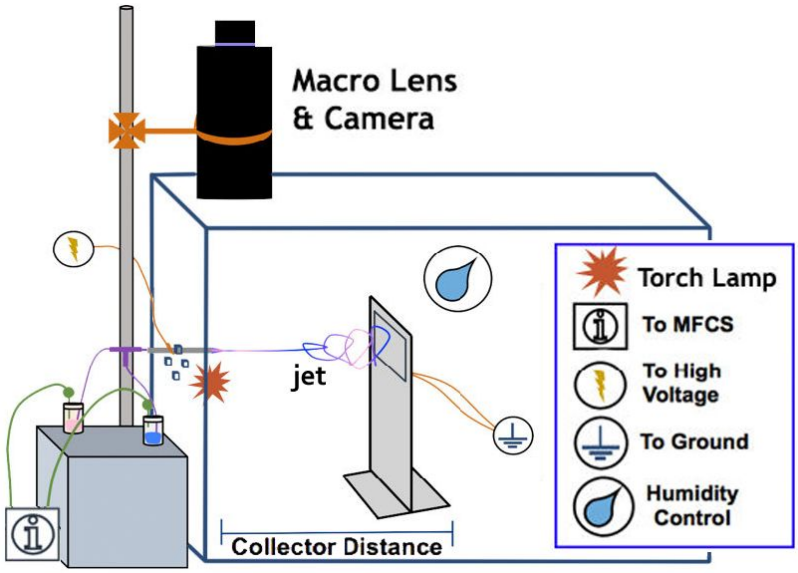

Fig. 3.4 – The line drawing of the coaxial electrospinning setup used to produce the fiber mats. Box dimensions are: 50 cm tall, 45 cm wide, and 45 cm long. The placement of the various components (see legend) are shown. The spinning takes place horizontally here.

Camera & attachments

The camera was mounted outside of the spinning box and directly positioned over the coaxial needle to film the Taylor cone jet during the electrospinning process. The digital camera used was from Zarbeco (model #: ZC-505-O2)*, and was attached to a macro lens with C-mount. This macro lens proved essential for capturing the liquid crystal core flow within the Taylor cone. Typically, an ideal PVP-ethanol Taylor cone will have a maximum tip to base length of about three millimeters, and even with the another fluid flowing within this cone, this part does not get much larger. It is difficult to see with the naked eye. The only way to be sure that the core remains consistently flowing within the Taylor cone of the polymer solution is to be able to see it during the process, and the addition of the macro lens helps immensely in this regard. It is also important to verify that the coaxial needle is not located too far from the focus of the macro lens as spinning other polymer solutions may produce a smaller Taylor cone than the one seen by PVP with ethanol. The distance from the bottom of the macro lens to the positioned coaxial needle was typically kept at 21 cm (Fig. 3.4).

For filming Taylor cones containing the birefringent LCs, an external torch lamp (brand: Fenix HL23) was attached to the inner wall of the setup in Fig. 3.4 and aimed towards the side of the coaxial needle. While using this lamp, along with turning the overall image brightness down while recording, it was possible to differentiate the intense scattering of the core fluid from the clear polymer solution.

Finally, to add one last reason why filming the Taylor cone during multi-core electrospinning experiments is highly beneficial - phase separation phenomena between the components can be readily observed. As discussed in ch.4 this had occurred with the two solid nematic compounds EBBA, and cholesteryl nonanoate. Both were individually dissolved in chloroform, and when mixed with the PVP-ethanol solution, they immediately began phase separating during electrospinning. Without the macro lens camera, this could not have been observed in the deformed droplets and deformed Taylor cones (shown in Fig. 4.6, pg. 58).

Collector

The main collector stand in this setup allows for the mounting of several types of smaller substrates for fiber collection. In addition to having the option of mounting the standard metal foil covered flat plate (usually copper or aluminum), this Nylon collector also has the option for height adjustment, and contains a large opening in the center (Fig. 3.5). This opening in the upper half of the collector stand allows various types of symmetrical metal frame collectors to be inserted which can be used for directing the alignment of the fibers deposited.

*In refs. [70, 98] the model # was mistakenly written as Z505-OR2, but in re-checking this number it turns out to be ZC-505-O2.

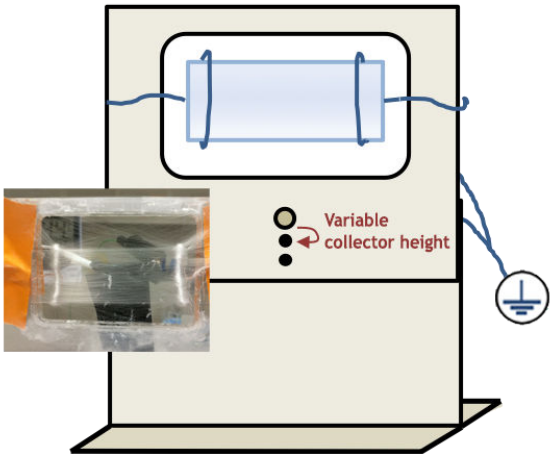

Fig. 3.5 – A diagram of the main collector stand used to hold grounded substrates (e.g. open wire frames, glass slides, aluminum foil sheets) for collecting coaxial LC-PVP fibers spun using the setup shown in Fig. 3.4. This diagram shows an example of a glass slide arranged with parallel copper wires (blue lines) and grounded in the back to collect aligned fibers horizontally. The inset photo shows an example of how an actual LC-fiber mat looks like after being spun onto this type of collector configuration.

Aligned fibers, as well as random fiber mats in a free hanging orientation can be gathered without destroying the individual filaments depending on how the metal frames, shown in the inset of Fig. 3.5, are designed. Typically, the metal frames were folded from bare copper wire (thickness: 0.4 mm), mounted onto the collector stand using insulating tape and connected in the back to the ground of the high voltage supply unit (Gamma High Voltage, model ES30P-5W). A good needle-to-collector distance for fiber formation using the PVP-5CB system is 10 cm, for example, given a constant applied voltage of 9kV. Other combinations of flow rate and applied voltage can be used, however, each must be experimentally verified if they work by observing the Taylor cone formation (discussed more in sec. 4.2 and sec. 4.3).

Using pressure based flow control rather than a syringe pump

A pressure based flow control unit (Fluigent, model MFCS-EZ, maximum pressure - 1034 mbar) was used for controlling the rates at which the LC and polymer solution co-flowed through the coaxial needle setup. The applied pressure used to flow the PVP solution and the 5CB during electrospinning was kept at 150 mbar for both fluids, unless otherwise stated. At most, the applied pressure for the LC never exceeded 200 mbar for producing the non-beaded fibers specifically. With the tube diameters and lengths shown in Fig. 3.3 150 mbar corresponds to 0.90 mL/hr for the PVP-ethanol solution, and approximately 0.55 ml/hr for the 5CB. When 200 mbar of pressure is applied to the LC it corresponds to a flow rate of 0.75 mL/hr.

A seeming disadvantage of using a microfluidics pump for the purpose of tracking the flow rate of our solutions is that we can only directly measure the applied pressure to a vial used for forcing fluid into our coaxial needle, rather than the flow rate of the fluid itself. A flow rate (mass or volume per unit time) is far more informative than a pressure value for the purpose of reproducibility, and an easy way to get the flow rate directly is to use a digital syringe pump.

However, there are three main reasons why the pressure based Fluigent unit is used as opposed to a traditional syringe pump. The first reason is that any sample container can be used. This avoids the need to fill samples into syringes (where large volumes of sample may be lost). Second, if temperature control is necessary for flowing fluids (particularly certain non-room temperature LCs) the fact that the container is well separated from any electronics makes this feature easier (and safer) to implement. Last, the response time after a pressure change is claimed (by Fluigent) to be dramatically faster than with syringe pumps. Indeed, at least one study shows that it can take up to an hour to get stable flow after a flow rate change using a syringe pump due to mechanical oscillations of the pump motor contributing to "periodic flow-rate and pressure fluctuations" [99].

To obtain a flow rate from our applied pressure readings we use the following method, first, apply the appropriate pressure to the flow the fluids into the needle setup as if one were to start an electrospinning experiment, and do not apply the potential (the coaxial needle setup should also be in the same position), second, place a vial directly below the dripping cannula and collect as much fluid that can drop in about 30 seconds, last, immediately weigh the vial. Repeat this process at least five times for each fluid (flowing the LC and polymer solution separately) to account for errors and average the masses. Using a high precision balance (up to five decimal points) also helps in estimating the precision. One should then have the mass of fluid that drips per 30 seconds, and can convert this to an approximate volume per hour.

One last point is that, if the coaxial needle setup tube and metal cannula sizes are changed, the flow rate of the fluids for the same applied pressures using the Fluigent control unit will also change accordingly as per the Hagen-Poiseuille relation (Eqn. 3.1). In the equation P refers to the pressure difference across the pipe, r is its radius, l is its length and η is the fluid viscosity. Thus, the fluid flow rate F scales by the fourth power of the pipe radius.

$$F = \pi P r^4 / 8\eta l \tag{3.1}$$

This also means that the very smallest nozzle in the coaxial needle design (usually the end where the fluids emerge) will determine the final flow rate of the fluid at the electrospinning stage.

3.1.4 Why space & ventilation actually do matter

Two other important aspects that many researchers overlook when starting to electrospin, or when deciding to alter their solution systems for electrospinning, are the necessity for adequate space and adequate ventilation. The former, while appearing trivial, can play a role in influencing the morphology of the individual fibers produced, and thus, the whole mat. Ample space is needed, for example, if one wants to electrospin large-scale, high surface area, uniformly thick fiber mats. For this objective, I mean fiber mats which can be meters long. It is not that a large amount of space work space is required for laying out the sheets during production, since a rotating drum, for instance, can be used in the place of a tall stationary collector to collect the same area of fibers while still having a smaller footprint.

Rather, what should be kept in mind is that achieving uniform fiber mat coverage for that larger collector will become more complex, thus will require more components to control, and this will inevitably take up production space. Fiber accumulation on a grounded collector will generally start off in one spot, and grow in size outward as this charged area on the collector becomes insulated with fibers. One fiber jet will be insufficient to cover all the sides of a wider

or taller collector, thus causing the center of the mat produced to have more fiber coverage than the sides (Fig. 3.6). Multiple arrays of needles for solution delivery to many areas of a large surface may be necessary [17, 100] and it these modifications that can take up the space. For instance, the space needed to account for the distance that many jets will need to achieve adequate solvent evaporation will contribute to the entire setup to function as intended. Moreover, insulating the area containing more needle arrays may require additional accessories as well.

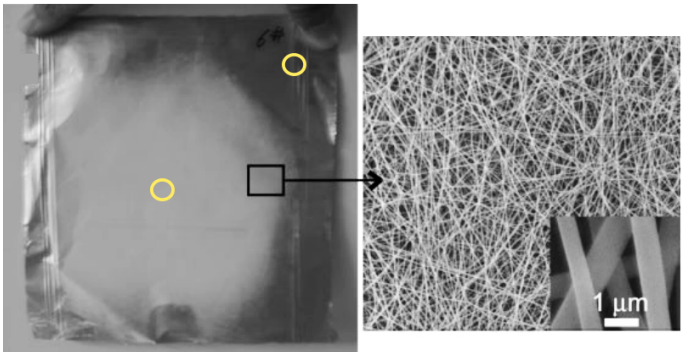

Fig. 3.6 – Example image of an electrospun fiber mat (left) with fibers that densely cover the center and spread radially outward over an aluminum collector. The sides and edges of the collector are qualitatively less denser in fiber coverage. This image was adapted with permission, from [101] John Wiley & Sons. Copyright © 2008 WILEY-VCH Verlag GmbH & Co. KGaA, Weinheim. Yellow circles were added by me to the image to indicate that the center of the collector has more fiber coverage than the outer edges.

Finally, as the electrospinning process relies on solvent evaporation to help form solidified uniform fibers as they land on the collector, it is recommended that the area directly surrounding the fiber collection space is not restricted, lest it leads to unexpected fiber morphologies with pores as described in Scalia et al. [102]. Fig. 3.7 shows a line drawing of the setup they used. The inset SEM images within Fig. 3.7 shows an example of 3 types of morphologies observed on individual fibers produced with this setup during the same electrospinning session. All spinning parameters were kept constant. It is also important to note that although humid environments are known to cause pore formation in some electrospun fibers, here the relative humidity at which the spinning took place was between 25% - 35% (quite low compared to [41]), and water is a solvent for PVP, unlike for polystyrene [41, 42] and poly(lactic acid) [103] polymers. So what could have caused the top most fiber (labeled α) to be porous, while the fibers below (labeled β and γ) to be solid?

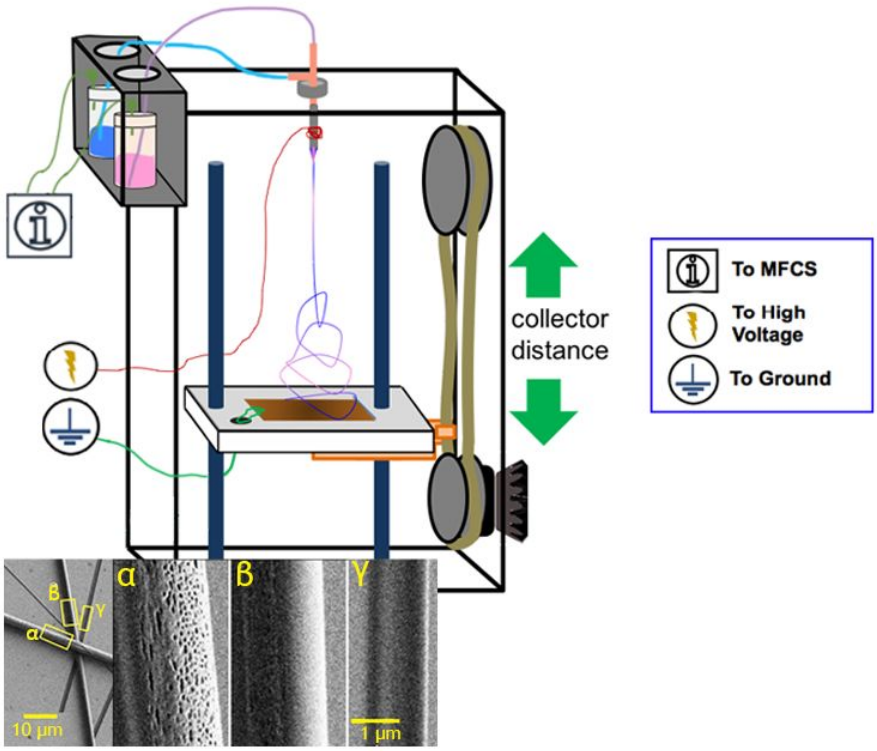

Fig. 3.7 – This is a diagram of the setup originally designed by previous members in Prof. Lagerwall's group and the image drawn here was re-created off of images I was permitted to take while using it before the setup in Fig. 3.4 was made. This box is about 30 cm tall, 17 cm wide, and 17 cm high. It has the main feature of allowing vertical collector distance adjustment via a gear pulley on the side. The inset SEM images showing the morphologies of three overlaid LC-PVP fibers produced using this setup (α - porous, β - rounded non-porous and γ - flat, non-porous) were adapted with permission, from [102] John Wiley & Sons. Copyright © 2013 WILEY-VCH Verlag GmbH & Co. KGaA, Weinheim.

The explanation given refers to the order of fiber deposition, and the inability of solvent evaporated in the small chamber to dissipate from the spinning area. This highlights the necessity for considering the second most overlooked aspect when assembling an appropriate electrospinning setup in addition to considering spatial requirements - it is the need for proper ventilation. For the study in Scalia et al. [102], the top-most fiber (α) came from a batch of electrospun fibers that deposited at a later stage than the batch of fibers that deposited at an earlier time (from which β and γ belonged to). Within the small chamber volume of about 0.003 m^3 (or, about two-thirds the volume of a standard bowling ball), the solvent that had already evaporated to produce the earlier batch of fibers had become far too saturated by the time that the fibers belonging to the later batch were collected. This solvent saturation could have led to the deposition of condensed solvent droplets onto the cooled dry surfaces of the top-most fibers, and caused the formation of pores.

While Scalia et al. do not specifically mention the time in which these fibers were produced, it is not unbelievable to think that the space used for fiber collection during electrospinning could become saturated with solvent vapor relatively quickly, particularly if the inside volume of the spinning area is small and has no proper ventilation. To highlight this point Wu et al. [104]

found a direct correlation between decreasing polymer jet diameter and solvent mass transfer from the jet to the surrounding air during electrospinning. They had found that spinning jets starting out with radii less than 1 μm could nearly completely dry (having roughly 98% solvent evaporation) in between 10 to 100 milliseconds [104]. For their case, while neither the effects of humidity nor temperature were taken into account, they did perform an experimental test by electrospinning PAN (polyacrylonitrile) with 88% DMF solvent (dimethylformamide) to test their model.

Considering that many studies claim that electrospinning in humid environments can alter fiber formation for a few polymer-solvent systems [21, 41, 105, 106], it is safe to assume that Wu et al.'s test occurred at low humidity and near room temperature conditions. Additionally, the vapor pressure of DMF is nearly 4 Torr at 25°C [107], roughly 10 times less than the vapor pressure of ethanol (45 Torr [108, 109]) at room temperature, used by Scalia et al. and myself for forming fiber mats here. The rate of DMF evaporation while electrospinning under ideal environmental conditions for the study by Wu et al. would have still been presumably slower than that of ethanol evaporation, and yet, sub-micron sized jets of PAN from the report by Wu et al. were still found to dry in fractions of a second.

For reference, the volume of my electrospinning box (Fig.3.4) was approximately 0.1 m^3 (dimensions: 45 cm width x 45 cm length x 50 cm height) and had roughly 30 times more empty volume than the setup used by Scalia et al. Furthermore, to ensure that the evaporated solvent did not oversaturate the atmosphere directly above the forming polymer jets during spinning, the entire electrospinning setup was used inside of a fume hood, elevated by ceramic posts (5 cm in height) to allow ample circulation of fresh air throughout.

Typically, it takes under 15 seconds to electrospin an LC-fiber mat with fiber coverage the size of a typical glass slide (75 mm by 25 mm) that is also thick enough to scatter ample light and appear white. Again, while the time spent spinning to produce mats this thick depends on the polymer solution and LC used, along with the other operational parameters relevant to electrospinning (sec. 2.1), I just mention these aspects to illustrate that solvent evaporation can be extremely fast during this process and fiber output can be quite high.

3.2 Setups used for LC-fiber mat VOC sensing

The two setups shown in Fig. 3.8 and Fig. 3.9 enabled the assessment of the coaxial fiber mat responses to volatile organic compounds (VOC) at the macroscopic and microscopic level. Both setups were designed and assembled in house. For this thesis, the organic compound vapors used for exposure were mostly toluene and acetone (to a lesser extent). These two organic solvents are very common byproducts in industries involved with textile dyeing [110, 111], vehicle maintenance [112], and cosmetic formulations [113, 114], to name a few. These gases can also be readily absorbed into the human body via respiration and dermal contact. Therefore, monitoring that the extent of workers' exposure to these vaporized organic solvents is not excessive is of great interest to the wider public [115].

The goal is to ultimately provide a means of detecting high exposure to these vapors using a way that is neither invasive, nor time/cost-consuming, yet accurate. Considering how LCs have been considered as good candidates for use as VOC sensors (sec. 2.3), if LCs could be integrated into fiber mats (which can be easily handled, and do not require electricity to operate) they

may be able to conveniently show the user when the ambient air is saturated with a harmful concentration of VOCs.

Thus, in order to obtain a more complete picture of how LC filled fibers produced here can respond to the vapors, the two previously mentioned setups were necessary so that I could uncover, first, how the LC-fiber mat responds holistically and macroscopically to the organic vapors it was exposed to, second, what happens to the LC in the cores of individual fiber strands at the microscopic scale, and third, how observations from the second point relate to the polymer sheath morphology of those fibers. Between these two goals I was hoping to answer questions like: Does the mat fall apart upon immediate exposure? Can I see evidence of the fiber mat responding to the vapors macroscopically? If so, are the responses reversible? What is the threshold response to the vapors? And can this threshold be tuned? While most of the answers to these questions are discussed in chapters 6 and 7, below describes how the setups were assembled to answer them.

3.2.1 Macroscopic responses to VOCs delivered to non-contained fiber mats

To determine whether the electrospun LC-fiber mats would be visibly responsive to organic vapors, we exposed our samples to vapors between macroscopic crossed polarizers approximately 20cm x 20cm in size (Fig. 3.8).

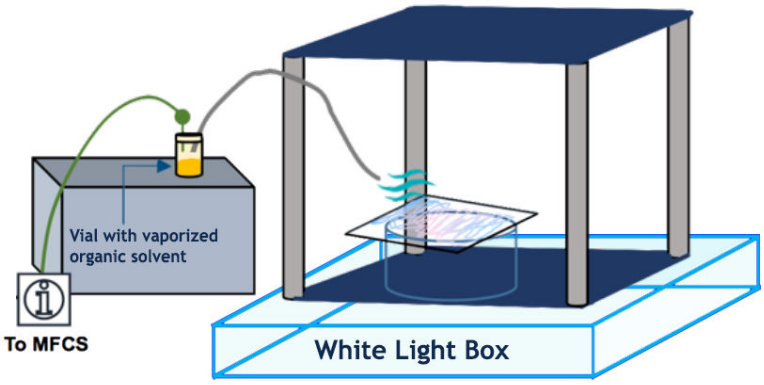

Fig. 3.8 – A diagram of the setup used to macroscopically analyze the responses of 5CB-PVP coaxial fibers to organic vapors. The microfluidics control system (MFCS) delivers air to a vial containing a small amount of organic liquid to be vaporized via a tube that is not in contact with the liquid. Then another tube, in contact with the liquid vapors, which also emerges from the vial, is guided to spread the vapors over the fiber mat sample. The fiber mat sample is kept in between the crossed polarizers over a light box for illumination. The VOC-induced change in scattering of the macroscale fiber mat can then be monitored.

To build this "macro-scope" sheets of linear polarizing film (*Alight Polarizers*) were cut and mounted at 90° to one another in an elevated frame with a spacing of about 5-6 cm. In ref. [70], some macroscopic images showing the vapor responses occurring in the fiber mats have light blue backgrounds. This is due to the fact that, at the time, the polarizing films used for building the macro-scope had wavelength-dependent polarization efficiency in the visible range, with lower absorption in the blue short-wavelength regime. Moreover, they had been attached to a frame with much wider spacing ($\geq$ 12 cm), thus, the amount of transmitted unpolarized light

from the room was much greater causing the contrast to decrease substantially. However this was soon corrected, and all macro-scope vapor sensing images shown in ref. [83], and in this thesis, have considerably better crossed polarized quality.

Note that although the quality of the linear polarizing films can always be better, when using crossed macroscopic polarizers attached to frames as was done here, since the frames will have openings on all four sides to allow sample insertion, there will always be some unpolarized ambient light that will enter the space between the polarizers. This causes the background of the crossed polarizers to appear very dark, at best, but not entirely black. Glass slides (75 mm by 25 mm) containing the fiber mats were placed in between the upper and lower polarizing films of the macro-scope frame. Finally, for getting the maximum contrast of the fiber mat, this entire macro-scope unit with the sample was placed over a white light emitting box.

To supply and flow the target organic gas to the fiber mat the microfluidics pressure based flow unit (the same one used for controlling the flow rates of the polymer solution and LC during electrospinning) was used. Fig. 3.9 shows that a septum covered vial containing 0.5 – 1 mL of organic solvent (toluene, or acetone) was connected to 2 inert PTFE tubes. One tube led to the flow unit (Fluigent, MFCS-EZ) that was responsible for supplying up to 200 mbar of air into the headspace of the vial. The other tube served as the organic vapor exposure tube, which would be responsible for delivering the vaporized organic solvent to the LC-fiber samples for sensing in between the polarizers. The fiber sample was not enclosed during exposure, thus, the vapor emitted from the exposure tube was allowed to freely saturate a large volume of air surrounding the fiber mat. Importantly, neither tube ends in the vial were allowed to touch the solvent at the bottom, or even the sides of the container. This was to avoid that any solvent in the condensed liquid phase be transferred out as droplets. This thesis analyzes the sensing experiments conducted with toluene vapors specifically.

While we were not initially able to find exactly what the vaporized toluene concentration produced inside of the vial was, nor what fraction of it was emerging from the exposure tube as we exposed the samples, we did grossly estimate that the vapor concentration saturating the air around the samples should not be greater than roughly 3%. Furthermore, while vapor concentration values inside the vial, or within the exposure tube, could not be found it was possible to estimate ranges of vapor concentration likely emitted nearest to the outlet of the exposure tube. These estimates were made possible by using the Dräger short-term exposure tube and pump setup.

The Dräger method of determining VOC concentration relies on drawing a sample of the target vapor into detection tubes fitted onto the hand held pump. The detection tubes each contain reactive analytes specific to the functional groups found in that the organic compound to be detected. When the analytes react with the vapor drawn in, the tube discolors proportionally to the concentration of vapor present. This semi-qualitative approach for determining VOC concentrations, when the fiber mats are not enclosed in a cell and exposed to vapors in ambient air by using the Fluigent pressure control unit, is further described in sec. 7.3. This method also helps describe another way the threshold response concentrations for the LC-fibers can be measured.

3.2.2 Microscopic responses to VOCs delivered to contained fiber mats

Another method for determining the threshold responses of the LC-fiber mats was through the microscopic setup shown in Fig. 3.9. This setup for observing local responses in individual fibers, which advantage of a microscope and a holding cell for containing the fiber mats and organic vapor. It was very much inspired by a similar setup used by our collaborators: Prof. Nicholas Abbott and his research group at the University of Wisconsin-Madison, USA (now at Cornell University in New York). As the Abbott group has worked with using LCs as sensors over a decade, I was able to see how they contained their LC films for sensing and then expanded on their design for specifically observing encapsulated LCs in fibers.

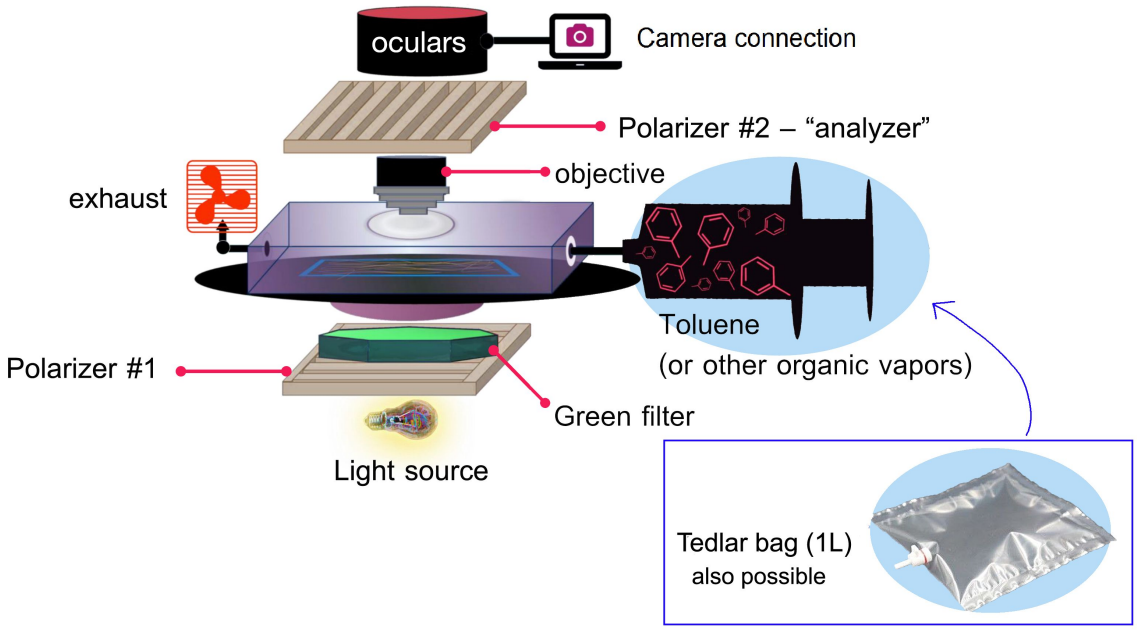

Fig. 3.9 – A diagram of the setup used to microscopically analyze the responses of 5CB-PVP coaxial fibers to organic vapors. Key components of a POM microscope are shown - the two polarizers in between the light source and the oculars, the stage, and an objective. On the stage, the metal cell for containing the coaxial fiber mats and the inserted organic vapors (discussed in sec. 3.2.2 and 3.2.2) is attached on one end to the exhaust (a suction pump - not shown) and to the container holding the mixed organic compound vapors. The container used to hold the vapors (here, toluene) can either be the syringe used to mix the air-VOC mixture, or an inert gas sampling bag (called a Tedlar bag). When the gas flows into the cell it can be contained by shutting off valves on either side of the metal cell (not shown), or allowed to pass through. The top of the cell has a glass window which allows us to observe the LC in the fibers undergo a phase transition (the response). For observing a uniform change in LC brightness, a green filter was used over the bottom polarizer so that the plane polarized light reaching the LC-fibers would be of a single wavelength. This allows a direct correlation of the light intensity, measured after the analyzer, to the change in polarization induced by the LC as explained in the main text.

In general, the way the process works is, the LC-fiber mat is added to the cell, the cell is closed so that it is air tight and placed under between crossed-polarizers in the microscope. Organic vapors can be introduced into the cell using one of two methods - either the inlet is connected to a 1L syringe (Hamilton, Model S1000 TLL - shown right of cell in Fig. 3.9), or a

vapor sampling bag made of Polyvinylidene fluoride (PVDF) (aka "Tedlar" bag) can be filled with the contents of the syringe and transferred to the cell using the push/pull lock located on the bag itself. An advantage of using the vapor sampling bags is that the vapor inside can be stored in a secure manner for weeks at a time without risk of contamination or leaking. Once the vapor holding cell with sample is attached to either the filled syringe, or the Tedlar bag, a region of interest can be chosen for observing the relative changes in LC brightness intensity via the POM as the sample is exposed to vapors.

A green filter (λ: 525 nm (bandwidth not specified) *Zeiss*) was placed over the bottom polarizer of the microscope so that the intensity changes could be tracked using a single wavelength of light. When we use white light, some wavelengths may experience a phase shift close to $\lambda/2$, leading to maximum intensity, whereas others may experience a phase shift near λ, thus not allowing any light to pass. Since the optical path length difference induced by the LC changes with VOC exposure, the intensity may thus increase for some wavelengths while it decreases for others. Only with monocrhomatic light can we get an unambiguous response.

Recordings of the fiber responses to the toluene vapor concentrations in the cell were done using a Canon EOS 706 camera. Consecutive sets of representative frames of the vapor-fiber responses were extracted from the videos. These green light filtered RGB images of the fibers were then batch converted to 8-bit grayscale by isolating the green channel portion using a "split channels" macro programmed in ImageJ 1.51s (NIH, USA <http://imagej.nih.gov/ij>). The images were run through a threshold algorithm to find the mean gray value changes in brightness versus time, and then normalized with respect to the mean gray values of the area before vapor exposure at highest brightness. The average area of observation possible using a 10x objective with the vapor cell was $\sim$ 488 μm x 868 μm. This area typically contains up to about 15 fiber segments. A Nikon LV100 polarized optical microscope with 10x objective was used for all microscopic vapor analysis experiments unless otherwise noted.

Vapor formulation & delivery method

Organic vapors of specific μM concentrations were formulated on the premise that adding micro-volumes of volatile solvents like toluene, or acetone, to the gas tight syringe would quickly evaporate at room temperature and create vapors of known concentrations within.[†] These vapors could then be transferred in a controlled way to the LC-fibers confined in the holding cell under the microscope for observation either using the syringe itself or the Tedlar bag[‡]. Microliter quantities of the target solvents (5 μL - 90 μL) were added into the 1L syringe at roughly room temperature condition: 22°C - 26°C, 28% - 32% relative humidity. The minute volumes were added using Eppendorf pipettes (purchased from Sigma Aldrich), but their error in dispensing volume was taken into account and the average mass of several droplets was used when calculating the final concentrations (further detailed in sec. 7.4). The liquids were left to evaporate in the sealed syringe barrel until the condensed liquid phase was no longer visible. For the larger volumes above 50 μL heat was sporadically added through the use of a heat gun to help evaporation occur faster, but this was just for a few bursts in the interval of ~1-2 minutes. The closed syringe with the volatile solvent was never left to constant heat.

[†]This method of creating VOCs was initially proposed by Kun-Ling Yang (from the National University of Singapore) during conversations in 2016.

[‡]The suggestion for using the inert Tedlar bags came from Peter Kaul and Lukas Pschyklenk (from the Hochschule Bonn-Rhein-Sieg University of Applied Sciences, Institute of Detection Technologies).

Finally, the point of choosing to report the vapor concentrations in terms of μM units rather than the commonly used ppm (parts-per-million) units is further discussed in sec. 7.2 which recounts the threshold sensitivities of the fiber mats to toluene vapors measured using the methods described in this section. To describe it briefly, the use of "parts-per" notation has become the common industrial practice of labeling fluid concentrations and it is inconsistent with that of IUPAC/P (International Union of Pure and Applied Chemists/Physicists) standards. Therefore, the possibility that these faux units may lead to misunderstandings in the way the measurements of quantities are interpreted becomes high. It is also a practice that has been adopted in academic papers and can also lead to errors in interpretation when reproducing results. Thus, for the vapors mixed via the method I presented here, a base unit which unambiguously states concentration such as the mole per liter (M) was used.

Holding cell for constant organic vapor exposure

Apparent differences in the vapor and sample holding cells fabricated for my project versus that of the one used extensively in the Abbott research group can be seen in Fig. 3.10.

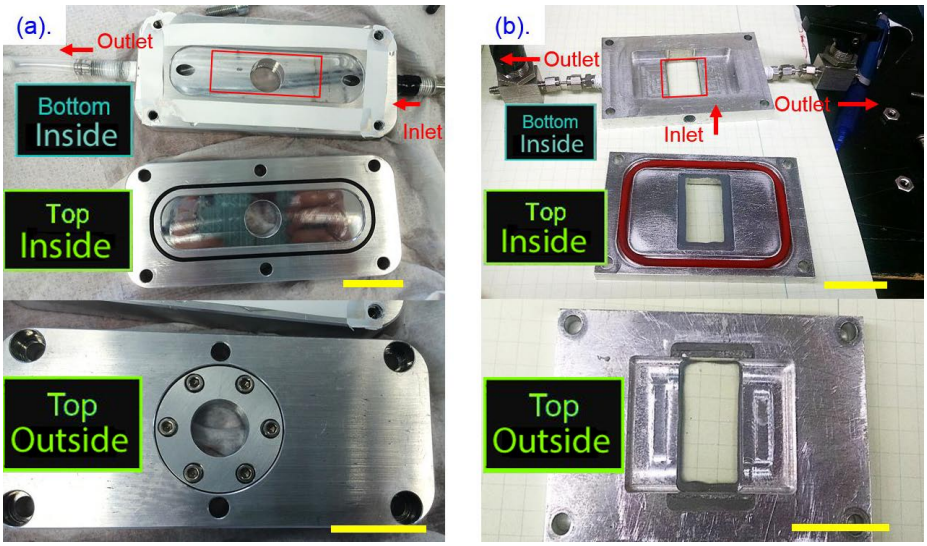

Fig. 3.10 – The sample holding cell used for quantitative POM based vapor exposure experiments in my work (a), and the one from the Abbott research group lab (b). I took the images in (b) myself (with permission) during an internship at Prof. Abbott's laboratory in Wisconsin-Madison. Scale bar: 3cm

Although both containers are made from aluminum, the cell fabricated in-house for my experiments, Fig. 3.10(a), is specific for containing the size of a typical glass slide covered with fibers. Since the fiber mats exposed for sensing are never more than a millimeter thick, the actual inner volume of the cell is quite small about, 15 mL, including the volume of the respective tubing at the inlet and outlet. The inset carved well in bottom inside of the cell where the glass slide with the fibers would sit (red rectangular outline) has a height of about 2.5 mm. This was chosen so that the distance of the samples from the POM objective would not add to difficulties in seeing the thin LC cores of the fibers, which usually have a diameter from 2 μm – 4 μm. In contrast, the Abbott cell, Fig. 3.10(b), has quite a large volume in the center for holding the glass sample. Usually they work with LC films several hundreds of microns wide so

the distance is not a problem. The total volume capacity of their unit is also small but they have two outlets as opposed to one, like mine.

A main difference is that their cell was intended for constantly flowing vapors over their LC films. This was done so that a response could be obtained as fresh vapor was exposed to the samples constantly, and then have the vapor immediately exit. In my cell, the goal was to contain the vapor of a specific concentration and see how the fibers respond when it's kept constant. It's also worth noting that my cell has removable glass windows located on the top and the bottom components of the cell to prevent the accumulation of any debris or dust after sensing experiments. They can be easily switched out as these windows are the dimensions of commercially standard cover slips. Though the addition of these windows holes add some stress when shaping the mold of the aluminum cell, the ability of the cell to hold air without leaking was tested several times by submerging it sealed into a bath of water. The outlet was closed and the inlet was attached to the air filled liter syringe. No air bubbles formed as I tried (and failed) to pump air through.

3.3 Optical microscopy & SEM measurements

3.3.1 Polarized optical microscopy (POM)

Both Nikon (LV100) and Olympus (BX51) optical polarizing light microscopes were used to analyze all samples (fibers, films, solution samples) containing any liquid crystalline material using bright-field contrast mode with and without the analyzer inserted. In particular, the Olympus microscope was used to characterize the presence of defects and the birefringence of the LC-filled PVP fibers in greater detail because its analyzer can be continuously rotated, and has a port for wave-plate insertion. All details on the importance of using crossed polarizers in characterizing the anisotropy of LCs is discussed in sec. 2.2.2. For recording the observations, a Canon EOS 760D was used, with a micrometer for adding the appropriate scale bars to images.

3.3.2 Scanning optical microscopy (SEM)

The need for a conductive coating

Because the PVP-5CB coaxial electrospun coaxial fibers are not conductive, to avoid the effects of *charging* during SEM imaging, the samples were coated with a thin film of gold. *Charging* is the term used in scanning electron microscopy to describe the situation when there are not enough electrons flowing from the top of the sample to the ground (the sample holder) as the electron beam of the SEM scans the sample. This causes an accumulation of charge on the surface of samples and results in an image that appears shifted with abnormal contrast, and blurriness. These artifacts make distinguishing features of a sample's surface difficult. It especially occurs with polymer and ceramic based samples, therefore, prior to imaging them a coating is usually necessary.

The Quorum Q150RS sputter coater used monitors the thickness of the deposited gold as a function of specified time. To reach a level of gold coating that is roughly equivalent to that used for the PVP-5CB fibers produced on glass slides in ref. [70], a deposition of gold between 6.8 nm to 9.7 nm is recommended at an applied current of 20 mA. This range corresponds to roughly between 180 and 240 seconds of time spent coating.

The ideal SEM parameters

Once the samples were coated, a JEOL (JSM-6010LA) SEM was used for imaging the sample morphology. The crucial parameters used for obtaining the most clear, and focused images possible were to have: a sample-to-lens working distance of 10 cm (maximum: 11 cm), the filament temperature held at 151°C, the accelerating voltage kept at 10 kV, and a spot size (SS) set to 50.

3.4 Other instrumentation used for characterization

3.4.1 Fourier Transform InfraRed Spectroscopy (FT-IR)

For documenting changes in chemical bonding, and the presence of other structures in our fiber mats a Nicolet iS5 laboratory FT-IR spectrometer with diamond crystal in ATR (attenuated total reflection) mode was used. The vibrational spectra of the samples were documented in terms of absorbance (y-axis) vs. vibrational wavenumbers ranging from 590 cm^{-1} to 4000 cm^{-1} (x-axis). Each sample measured was set to have 32 scans (meaning that the spectrometer's light beam passed through the sample 32 times in order to create the final spectrum shown). The resolution for the scans was also set to 4 cm^{-1}, which is the usual default setting for obtaining a meaningful spectrum of bond vibrations in liquids and solids. A higher resolution, such as 2 cm^{-1}, can also be used but since the molecules in liquids and solids are in more fixed positions than the molecules found in gases, the spectra produced will not be any more accurate. As a side note, for quantitatively probing the various transition energies in gases, lower resolution (between 0.5 cm^{-1} to 1 cm^{-1}) to get the finer details of the vibrational modes is usually recommended.

3.4.2 Differential Scanning Calorimetry (DSC)

DSC experiments for attempting to pinpoint the transition temperatures of coexisting 5CB-ethanol phases observed via POM experiments were performed with the help of Dr. Jörg Baller. Between 5 mg to 9 mg of liquid from six of the 5CB-ethanol mixtures were loaded into DSC aluminum pans and sealed tightly with lids at room temperature. The samples were analyzed using a DSC from Mettler Toledo with the heating and cooling program shown in Fig. 3.11, at the rate of 5 degrees per minute.

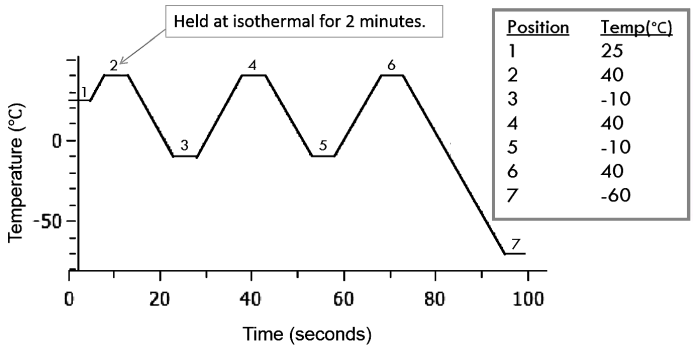

Fig. 3.11 – The DSC program for heating and cooling 5CB-anhydrous ethanol mixtures discussed in reference to the phase diagram presented in ch. 5.

In order to make sure that the weight% (and corresponding mol%.) fractions of 5CB did not change during the experiments, the six solutions beforehand were prepared by weighing out the 5CB and anhydrous ethanol fractions using a Sartorius MC1 research grade six digit balance.

The relationships used for finding the fractions of 5CB in the mixtures are indicated in Eqn. 3.2 and Eqn. 3.3, where n refers to the number of moles of the compound found by dividing its measured mass m (in grams) by its molar mass (grams/mol).

$$mol.\%5CB = \frac{n_{5CB}}{n_{5CB} + n_{ethanol}} \times 100 \tag{3.2}$$

$$wt.\%5CB = \frac{m_{5CB}}{m_{5CB} + ma_{ethanol}} \times 100 \tag{3.3}$$

After the experiments, the weight % of the solutions in the pans were rechecked to make sure that they were within experimental error and to know whether ethanol had evaporated. Reference pans containing only ethanol were first weighed before and after pressing to make sure that the contents would not evaporate as well.

4

Analyzing 5CB encapsulation & coaxial fiber formation via electrospinning

This first results chapter describes in detail how several variables for forming LC filled PVP microfibers via the coaxial electrospinning method using the setup discussed in ch. 3. Alterations in flow rate, and differences in ambient humidity, for example, can dictate how the morphology of the core-sheath fibers spun can change from being cylindrical to beaded.

Knowing how the evolution (or devolution, in some cases) of a solution's Taylor cone can change throughout the process is also valuable. While images of the Taylor cone are usually not included in most electrospinning papers, because its typical shape has been described extensively by Reneker [5], Yarin [32], Taylor [28], and others [116] for single polymer solutions, for the case of coaxially electrospinning multiple fluids, we cannot assume that these solutions will co-flow predictably. Successful coaxial electrospinning requires that the core fluid is incorporated into the jet, but sometimes the core fluid does not deform into a cone. Instead it forms a spherical droplet that never reaches the jet. If the core fluid is successfully incorporated into the jet, there is also the possibility it could experience break up from the high flight velocity of the jet (up to 10 m/s) [117] and elongational strain rates ($\geq 10^3$/s) [118] that the process induces. This is where tuning the various processing and solution parameters, such as core flow rate and the solvent chosen, for instance, play a role in "good" fiber formation.

The final section demonstrates that the core fluid introduced together with the polymer solution for coaxial electrospinning matters a great deal, as the miscibility or immiscibility of the fluids can change depending on ambient conditions, leading to a disrupted Taylor cone. A poor Taylor cone can finally result in poor core fluid encapsulation, and likewise, poor fiber and fiber mat formation.

4.1 What are "good" LC-core, polymer-sheath fibers?

It is crucial to recognize when the individual fiber cores of coaxially electrospun core-shell fibers are adequately filled, when they are not. There are more stresses on a solidifying bicomponent jet during coaxial electrospinning than there are for a solidifying single component jet (from the differing fluid properties in the core), and it is possible that a bicomponent jet can collapse mid-flight causing the fibers formed to lack an adequate amount of core fluid. As the encapsulation of very optically birefringent, room temperature nematics are the primary focus of this thesis (and not the encapsulation of other fluids), checking the level of core filling is made relatively easy using the POM.

As was mentioned in ch. 3, distinguishing microfibers filled with LC through the POM is especially easy if the polymer chains within the fiber sheath do not align themselves into semi-crystalline regions during spinning, and remain in a fairly amorphous glassy state. It means we need not concern ourselves with the potential issue of polymer birefringence significantly

interfering with that of the LC in the fiber cores during observation. Though true that polymer is as asymmetrically stretched while solidifying mid-flight towards the collector, any minor birefringence that results as a consequence of this stretching is not significant.

It is also worthwhile mentioning that distinguishing high levels of encapsulation in micro- and nanofibers can also be less straightforward at times, and may require several additional spectroscopic (e.g. FTIR, EDX) or thermogravimetric methods (e.g. DSC) for verification if SEM/TEM analysis shows questionable findings. For instance, when viewed through the light microscope with only plane polarized light, coaxial fibers may appear to have clear sheaths with darker cores across the centers [119, 120]. However, at times it is difficult to tell whether the centers are dark because the sides of the polymer sheath are a slightly thicker than than center and protrude slightly more outwards, or because there actually is another material truly encapsulated within the fibers causing the center to scatter more than at the edges. It is possible for electrospun fibers to buckle into flattened ribbons upon landing onto the collector [44]. They can have either "dog-bone" or elliptically flattened non-circular cross-sections visible through SEM inspection. Sometimes even the coating of the collector, such as whether it is hydrophobic or hydrophilic, can impact the cross-sectional shape of the landing fibers as well [43].

Some key factors to consider when encapsulating fluids, and in particular LCs, are listed in Table 4.1. Of these four important criteria for obtaining "good" coaxially electrospun LC-core, polymer-sheath fibers using PVP in ethanol and 5CB, criteria # 1, # 3, and # 4 can be applied to producing any core-sheath fiber containing any core fluid. Although steps should be taken to ensure that the core fluid is continuous throughout the solidified fiber, depending on the core fluid used it may, or may not be as birefringent as 5CB.

Tab. 4.1 – Four criteria to ensuring the production of "good" coaxially electrospun LC-core, polymer-sheath fibers using PVP in ethanol. Ideal and non-ideal examples of how the features described in the "criteria" column appear are shown. Images (1) and (2) in row 2 of the "non-ideal" column have scale bars that are 50 μm. Image (1) is of pure electrospun PVP fibers viewed through crossed polarizers, they are barely birefringent. Image (2) shows the crossed polarized image of an area containing PVP fibers with very little LC in the cores (appearing like bright dots). Both are non-ideal cases of no, or poor, LC core filling. Row 3 (non-ideal column) shows electrosprayed LC-PLA beads. *(see footnote info. on next page)

Criteria	Ideal	Non-Ideal
Taylor cone is predictable, reproducible, & visible	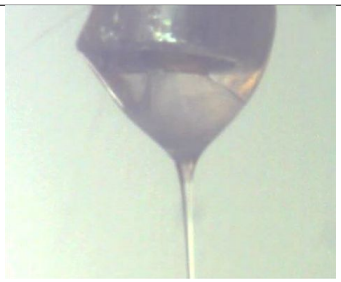	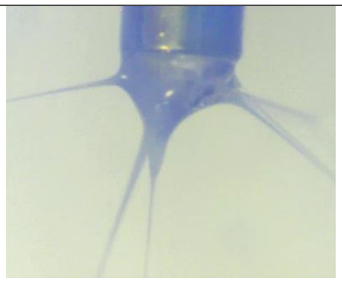
Core is continuous & significantly birefringent in all fibers	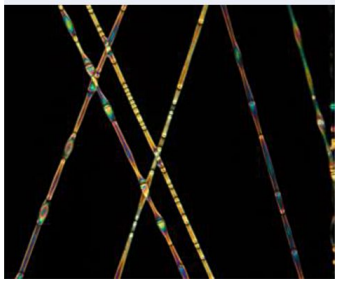	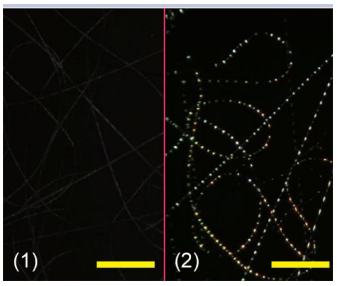
Filaments only – No polymer beads	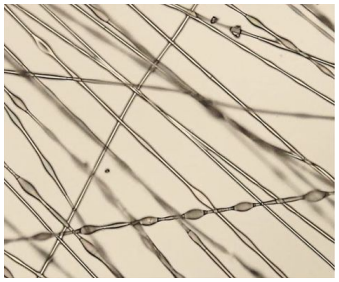	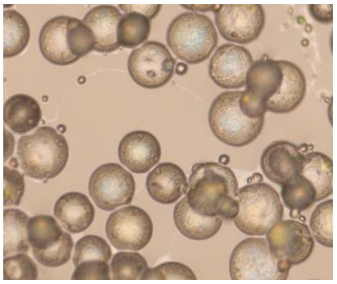
Ensure core containment (i.e. no smearing, leaking, or dripping)	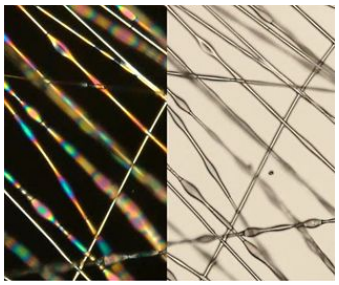	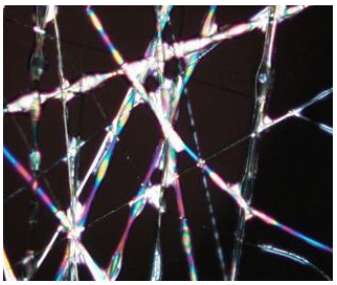

4.1.1 1. Taylor cones are predictable, reproducible, & visible

Although a stable and visible Taylor cone (Table 4.1, row 1: "ideal" column) in that of itself is not evidence that fiber formation is occurring at the end of the jet (the electrospraying process shares the same geometric feature), it is nevertheless the first feature seen in the process that can indicate one is off to a good start.

The presence of the Taylor cone indicates that at least the surface tension of the fluid/(s) flowing from the needle tip are at a state in which they are being counteracted by the electrostatic forces from the applied potential. It also indicates that the potential is at least high enough to initiate charge repulsion within the solution by creating an excess of surface charges [21]. Because the surface tension has been overcome, the Rayleigh instability has been suppressed, thus, rather than immediate fluid break up occurring, if the camera is directed past the cone's apex we see the fluid extend as a sub-micrometer jet towards the ground. For the solution to maximize its surface area under the accumulation of excessive charges the solution will always jet outwards. During this, the jet solidifies as the organic solvent evaporates. If the jet fails to extend outward and immediately breaks into droplets, then filament formation does not occur (i.e. the electrospraying process has initiated, rather than the "spinning" one).

Taylor cones formed by Newtonian solvents (water, methanol, acids ... etc.) and complex non-Newtonian mixtures (i.e. polymer solutions) may be stationary features, but they are never completely static or immobile [121]. Significant charges through the ions displaced in the solution are always in motion and impact the cone geometry in subtle ways. This is one reason why even though Taylor's initial prediction that a half angle of 49.3° was necessary before jetting to start [28], does not entirely describe the full extent of cones seen experimentally (in practice, half angles from cone apices were found to vary between 32° - 46° [32, 122], and additionally some cones have more curvature than others [121]). Taylor never took into account that the dielectric properties of the solutions being charged can vary, or that ionic transfer constantly occurs. More on this in the context of coaxial Taylor cones is discussed in sec. 4.2.

When initiating the electrospinning process we attempt to confirm that the cone's stability over several seconds is also consistent (Fig. 4.3) when other processing parameters (flow rate, collector distance, ambient conditions...etc.) are constant. If the cone geometry significantly alters, or constantly fluctuates at any given moment (i.e. it forms multiple jets as shown in Table 4.1, row 1 - "non-ideal" column), or appears to flatten, then it usually indicates one of two things. First, it could mean that the solution properties altered in some way; for example, chemically – some solvent from the bulk solution has evaporated, if the vial was not sealed or stored properly, or the aggregation of any additives present has occurred and affected the flow rate. Or second, the environment changed in some way. The Taylor cone may no longer be reproducible due to a difference in the evolution of the electric field surrounding the cone and the jet area that occurred. Most often this can occur with changes in temperature and humidity conditions. The latter factor is a recurring issue with consequences explored in sec. 4.4 and in ch. 5.

*The image of the electrosprayed polymer beads was taken by summer intern, Aditi Naik, who I supervised during the summer of 2015. The polymer solution used to produce the beads was 7% by mass polylactic acid (PLA) in a solution of 3:1 (volume ratio) chloroform:acetone.

4.1.2 2nd: Continuous cores & significant birefringence in all fibers

To decide whether significant LC encapsulation was successful during coaxial LC-core polymer-sheath electrospinning, the birefringence of the collected coaxial fibers should be noticeably and significantly higher than that of the pure, non-core filled polymer fibers (Table 4.1, row 2). The "ideal" image in row 1 of Table 4.1 shows PVP fibers that have up to two orders of interference colors visible from the 5CB core encapsulated within when viewed through crossed polarizers using the POM. This level of interference colors are not at all present in the images (1) and (2) of the corresponding right-side "non-ideal" column. Instead, image (1) shows that the pure, non-core filled PVP fibers appear almost black under crossed polarizers.

Polyvinylpyrrolidone is a linear polymer with a large, repeating pendant group (the γ-lactam). This side group contributes to the polymer chains favoring entanglement far more readily than other polymers (like polypropylene, or Nylons) which do not have bulky side groups [94, 123]. Increasing the amount of bulky side groups in a large molar mass polymer has the effect of decreasing the flexibility of the polymer chains since the side groups are more likely to become sterically hindered [124]. Since the γ-lactam groups also do not contribute to the formation of intermolecular bonds, like Nylon or even atactic poly(vinyl alcohol), domains of crystallinity are prevented from forming within the PVP polymer chain network. Topologically, PVP shares a similarity with polystyrene which also has a pendent group (the vinyl benzene) that inhibits crystalline domain formation below its glass transition temperature (Tg) (for PVP: 150 °C – 180 °C). This similarity will relate to chain entanglements necessary for avoiding electrospraying in sec. 4.3.4. Also, since the electrospinning jet experiences evaporative cooling [106, 125], it is highly unexpected that there will be enough thermal energy present to allow significant rotation or vibration to occur in the PVP chains to enable the growth of semi-crystalline regions.

Moreover, PVP is usually commercially sold as atactic since it can be inexpensively synthesized via free radical polymerization without the use of a catalyst, the latter is sometimes used to influence the stereochemistry of polymerizing chains [94]. As PVP is hygroscopic and prone to make brittle films when processed via melt extrusion it is also a polymer that is most often used for pharmaceutical coatings requiring biodegradability [94, 123]. Thus, it makes sense that the optical scattering and birefringence associated with crystalline structures will not be present to a large degree in fibers electrospun purely from this polymer, and a birefringent material like 5CB encapsulated can be easily distinguishable through POM analysis. Image (2) in Table 4.1, on the other hand, shows an area of a separate PVP fiber sample that was filled with a very small amount of 5CB. While the specific impact of 5CB core flow rate on the morphology of the LC-PVP fibers produced will be discussed later, the image here is used to emphasize the differences in the birefringence between completely filled LC fibers with a continuous LC core ("ideal" column), unfilled fibers (image 1) and sparsely filled LC fibers (image 2). While the Rayleigh instability of the polymer sheath solution may have been suppressed by the applied voltage, if the flow rate of the LC core is too little, Rayleigh breakup of the core fluid will also occur.

4.1.3 3rd: Only filaments are present, no beads

The third row of Table 4.1 compares one plane polarized light micrograph of fibers, and another of polymer spheres that can also result when attempting to electrospin. Though from an administrative health perspective a "fiber" can be defined as any structure with a length ≥ 5 μm,

and a length to diameter aspect ratio $\geq$ 3:1 such that staple fibrils can be included (like those from asbestos), the types of fibers we aim to produce should be at least several centimeters long and have aspect ratios approaching infinity. Centimeters because that typically covers the length ranges of the collector substrates on which the fibers get deposited on during the electrospinning process. Clearly, if structures seen on the collector have very length to diameter aspect ratios closer to one, and are not connected or conjoined (like beaded fibers are), then most probably the polymer solution has broken up too early into the jetting stage and began electrospraying beads instead.

If the chosen polymer-solvent system lacks a high enough molar mass, or is not concentrated enough in the solvent, it will not have the necessary amount of chain entanglements needed to sustain a continuous jet while carrying the excessive surface charges imposed onto it by the applied potential [126]. Rather, immediately after the formation of the Taylor cone (a feature that emerges as a result of the solution attempting to balance excessive charge buildup with its own surface tension), a discontinuous jet containing droplets will be expelled. The surface charges accumulated onto those expelled droplets will then continue to drive the subdivision into more droplets until all of the solvent has evaporated, and the polymer content within has solidified into micro- and nano-sized spheres onto the grounded collector. Although predictions based on chain entanglement theory can indicate the likelihood of certain polymer solutions producing filaments or beads and beaded filaments based on their molar mass (discussed in sec. 4.3.4), the situation complicates itself when co-flowing with another substance.

4.1.4 4th: Polymer sheath encapsulates all core fluid, no leaks

Finally, making sure that the polymer sheath has remained fully intact to encapsulate the fluid (Table 4.1, row 4) determines whether the fibers can be reliable for analyzing unique features (i.e. phase separated parts, LC alignment defects) and applications (i.e. volatile organic vapor sensing). After production, the coaxial LC-PVP fibers can be immediately examined via POM ad they should not appear as they do in non-ideal image of Table 4.1 row 4, that is, with birefringent core fluid coating over the filaments formed. The point, after all, is form coaxial filaments that can encapsulate the low molar mass compound so that the latter can be utilized as a non-woven, macroscale, free-standing mat. Certainly, it is possible to "pull out" stable fluid filaments from certain complex bulk substances, like columnar liquid crystal phases [127], and have them suspended for several hours at a time, but this example is completely different from the types of LC coaxial fibers formed here. Moreover, the former is not meant for handling as one would typical textile fibers. Thus, for achieving the fully polymer sheath encapsulated LC fibers, it is important to know when the polymer sheaths have completely solidified. In this case, the term *solidified* refers fibers that are geometrically and individually distinguishable from one another, and those which have not merged to create a film-like structure.

While evidence of the core leaking, or poor sheath solidification is difficult to observe during electrospinning process, apart from evaluating whether or not the Taylor cone forms, it is very obvious to see evidence of it having occurred once the collected sample is inspected under crossed polarizers in the POM. The "non-ideal" image in row 4 of Table 4.1 shows birefringent PVP fibers, but this time with significant LC that has leaked out and spilled over and around the filaments. it is noticeable from seeing that at nearly all of the points where the fibers cross one another, there are highly birefringent white blotches present in between. In some areas, there

even appear to be some fibers laying over the spilled LC on the substrate beneath. Compared to the "ideal" image on the left, all of the filaments (though some have beaded morphology) do not have excess fluid sitting in between, or coating over them. All these fibers also have far more uniform lengths and diameters as well compared to those shown in the "non-ideal" column.

Typically, electrospun fibers that have poorly solidified in flight will usually appear as a 2d-mesh on the collector. This has been discussed by Reneker and Yarin in refs.[5, 128] where they mention that segments in the whipping jet (if not dry enough prior to landing) can merge together such that they "conglutinate" into partially solidified ribbons. Different segments of the whipping jet, they experimentally showed in [128], can cross one another if their momentum happens to be high enough to ignore their respective repulsive Coulomb charges. The surface tension of the crossing fluid segments can then cause the segments to merge and "loops" of wet merged fibers can deposit onto the collector.

With more solvent, or non-evaporating fluid present within the jet (like for the coaxial spinning case) the more likely it is that wet segments can merge in flight and land conglutinated as Reneker [5, 44], and I have also observed (Fig. 4.1). As shown in the SEM image in Fig. 4.1(C), the conglutination of the wet polymer with the core fluid is in the form of flat, uneven ribbons with a wrinkled texture that indicates non-uniform drying. This drying probably only took place after buckling onto the collector upon landing.

In contrast, dry electrospun fibers will deposit in layers onto the grounded collector, and the sheaths of the fibers overlaid on top will not mesh or join with those below them. For this reason, when observing the sample under the microscope some fibers will appear out of focus as some may be on different layers in the vertical z-axis. This is the case for at least 3 or 4 of the fibers shown in the plane polarized light micrograph in the "ideal" column for row 4 of Table 4.1. This implies that at least the bottom-most layer of fibers solidified enough to encapsulate the LC core fluid such that the core was not able to leak. Had it done so, the leakage would have interfered with the solidification of the subsequently deposited upper fiber layers. Polymer wrinkling or signs of deformation from uneven drying are largely absent as well (Fig. 4.1d).

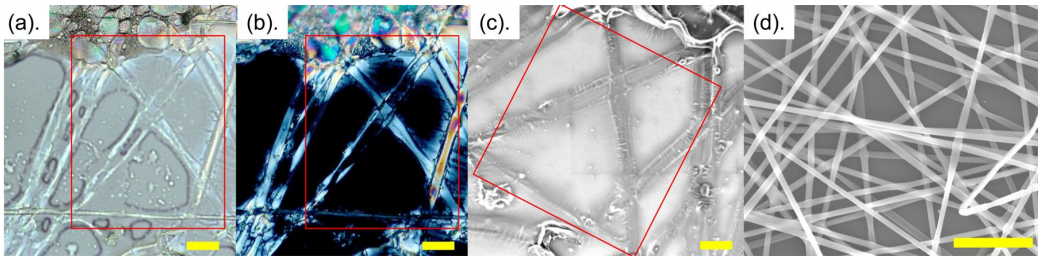

Fig. 4.1 – Electrospun areas showing poor and ideal coaxial fiber morphologies. If the coaxial jet still has a significant amount of solvent prior to landing on the collector, or if the LC flow is too high, the coaxial fibers accumulated will appear flattened and wet, shown in the plane polarized light, crossed polarized, and SEM images (a), (b), and (c), of the same area, respectively. In (a) - (c) the "fibers" formed within the red outline appear wet with both solvent and LC. Though the outlines of the fibers are visible through the POM images, the SEM image (c) shows that distinct filaments did not form. Image (d) shows proper non-beaded coaxial fibers formed by comparison. Scale bars: 30 μm.

Finally, poor core encapsulation particularly for the low molar mass LC case, is prone to occur when either one of two conditions are met: first, if the flow rate of the core LC fluid exceeds that of the polymer sheath to the point where the LC saturates the Taylor cone and disrupts

the electrostatic repulsion in the polymer solution, or second, the flow rates of the core and sheath fluids are not altered, but there is poor solvent evaporation due to a substantial increase in ambient humidity during spinning. Sometimes increasing the applied potential can work to counteract the effect of increasing the core LC fluid rate in the polymer solution, but as shown in sec. 4.2.2, whatever coaxial fibers that are produced will still be highly irregular and wet for the most part.

For the second situation, discussed in more detail in sec. 4.4, if the relative humidity in the spinning area is quite high, meaning $\geq 60\%$, the solvent used in the polymer solution is completely miscible with water (such as ethanol used here), and the polymer itself is hygroscopic (like PVP), then there is also the possibility that excess moisture can condense along the solidifying jet, and prevent filament solidification to encase the core fluid within. Since the whipping jet during electrospinning dries via evaporative cooling, excess atmospheric water vapor surrounding a water soluble polymer can enhance the probability of conglutination occurring during the whipping/deposition stage on the collector [5, 44].

4.2 All about Taylor cones

4.2.1 Tuning Taylor cones by applied potential & flow rate

Although the formation of Taylor cones during electrospinning and electrospraying experiments have been thoroughly described, starting from Taylor's and Zelany's initial empirical reports [28, 29, 129], uncertainties among theoreticians still remain regarding which models can best describe how the cone forms and, importantly, how it remains stable throughout time. Since Taylor's and Zelany's initial observations, there have been far more experimental observations reporting that variations of cones that can exist. The morphological shapes vary from appearing strictly triangular with straight sides and a sharp apex, to those that have more curved sides before the tip. In Taylor's initial experiments in forming the single-cone jet, Taylor proposed that the cone required a half angle of at least 49.3°, from the apex to the base, for it to remain stable and produce a continuous jet [29].

A more unified theory by Kalayci et al. [130] was later developed in 2005 which accounted for the roles that solution viscosity, surface tension, conductivity, charge/mass transfer, and solution velocity have on the formation of the cone. Kalayci et al. knew that the conductivity of the solution influenced the rate of charge separation within the solution during spinning, but they did not expect the flow of current measured from the grounded electrode to decrease once the polymer solution flow rate was increased [130]. They hypothesized that this may have been due to the fact that a higher flow rate would cause more solvent to evaporate into the surrounding air, and therefore, the air became more ionized through charge transfer. This led to an insufficient amount of separated charges in the flowing solution that could generate a force countering the solution's surface tension. So since the surface tension could not be countered, then Taylor cone and jet would fail to form.

Experimentally, this makes sense as a study by Barua et al. [116] has shown that while electrospinning a solution containing polyacrylonitrile, the Taylor cone half-angles can vary from about 23° to 47° if the flow rate of the solution is changed from 0.6 mL/hr to 2 mL/hr. The applied potential (15 kV) was kept the same throughout, however. Figure 4.2 reproduced from

their article shows that the types of cones seen for this flow rate range can be grouped into four types regimes where the fiber production changes as well. At flow rates closer to 2 mL/hr either a wide cone with intermittent drops, or one that is completely dripping is seen (regimes 1 and 2). For regimes 3 and 4 they ultimately noted that cones tuned to have half-angles between 32° and 45° were actually most reliable for creating continuous and dry electrospun fibers.

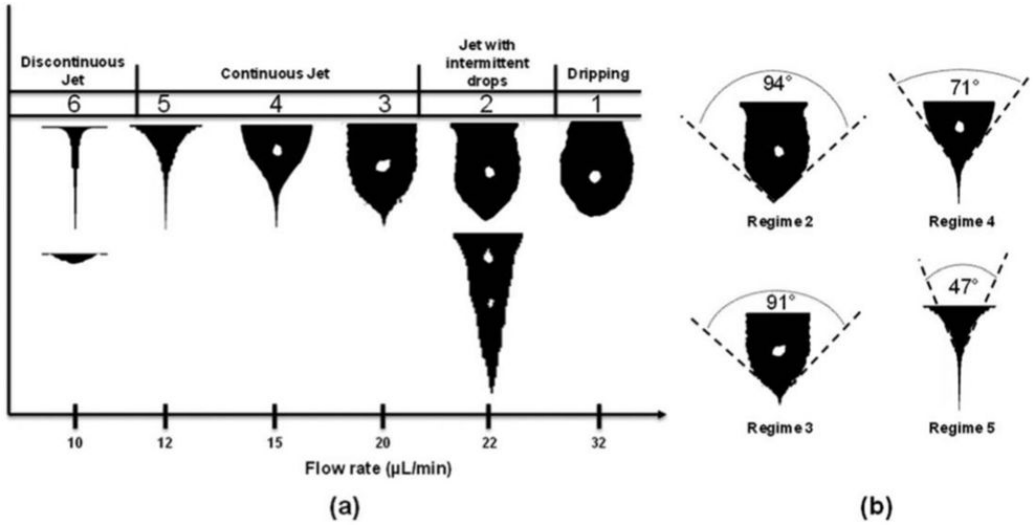

Fig. 4.2 – The figure above was reproduced from ref. [116] with permission, from John Wiley & Sons. Copyright © 2015 WILEY-VCH Verlag GmbH & Co. KGaA, Weinheim. This diagram shows an example of the best polymer (polyacrylonitrile) solution flow rate regimes for spinning continuous, non-broken fibers under a constant applied potential. It shows four spinning regimes where the Taylor cone shapes (the full-angles made from the cone apices) can change when the polymer solution flow rates are increased from 10 μL/min (0.6 mL/hr) to 32 μL/min (1.92 mL/hr). In the original text Barua et al. refer to the dotted lines depicting the angles measured in the four cone examples in (b) as *half- angles*, but as their figure shows they are actually full-angles. The actual half-angles at regimes 2, 3, 4 and 5 would then be: 47° (i.e. 94°/2), 45.5°, 35.5°, and 23.5°, respectively. In regimes 1 and 2 the polymer solution constantly dripped and continuous fiber formation was not possible. Regimes 3-4 yielded the formation of continuous filaments, while in spinning regimes 5-6 produced broken, shorter filaments.

For coaxially electrospinning two fluids, as in my work, quick measurements of the outer sheath cone half-angles in Fig. 4.3(c) and (e) show that the values are roughly 38.2° and 43.7°, respectively. Incidentally, the cones shown in Fig. 4.3(c) and (e) are also ideal in producing dry and continuous, non-beaded fibers as well. The flow rates of the core 5CB fluid in both cases are lower (roughly 0.5 mL/hr) than that of the polymer solution (closer to 0.9 - 1 mL/hr) as well, showing that if the core fluid within a coaxial jet is non-reactive with the polymer sheath solution and can be contained within the outer cone, the electrospinning process proceeds as if there were no core flowing within.

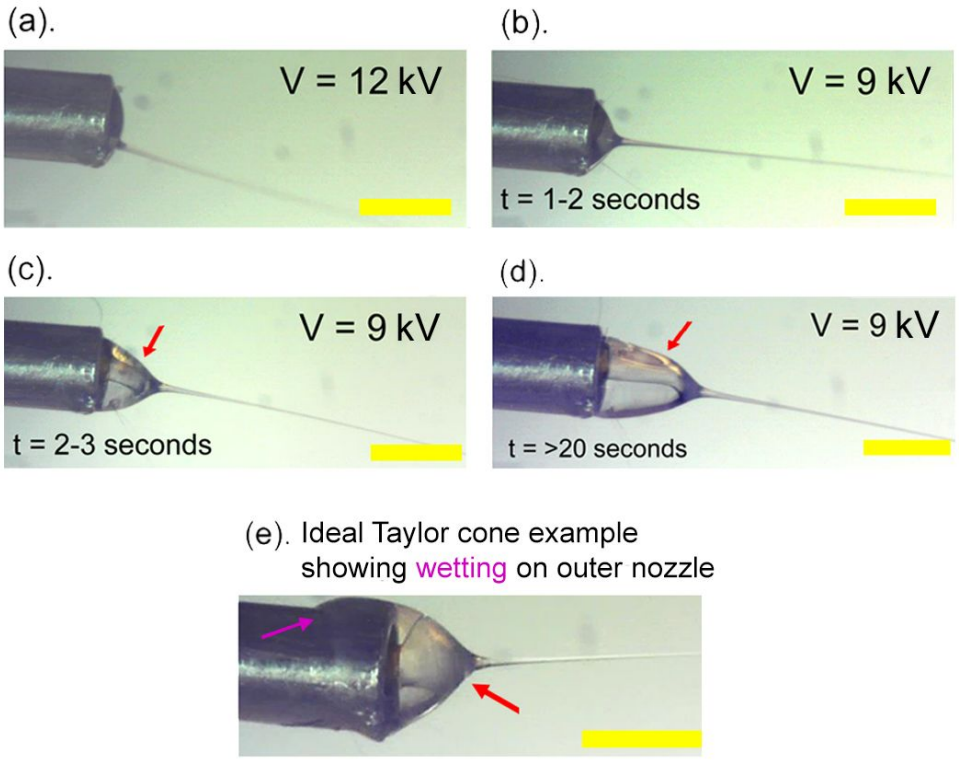

Fig. 4.3 – The evolution of a stable coaxial Taylor cone and jet containing 5CB in a PVP-ethanol solution is shown when the applied potential is slightly varied. Red arrows indicate where the LC can be visibly seen in the cone with respect to the polymer sheath solution. In (a). the applied voltage is too high and the cone is not visible. This cone half-angle is roughly equal to 80°, and does not produce continuous fibers. Turning the voltage down slightly, and within a few seconds, an ideal coaxial TC, confirming that the LC is flowing into the polymer jet is observed in images (b) and (c). The TC will eventually become elongated, (d), if left undisturbed for several seconds due to the accumulation of charges on the now insulated collector containing several layers of fibers over each other. Wetting of the capillary can also occur while the polymer solution is flowing, shown in (e), but at least for the PVP-ethanol polymer solution, this was not found to dramatically influence the formation and visibility of an ideal coaxial Taylor cone. Scale bars: 1.1 mm.

Interestingly, 4.3(b)-(d) also show that even when the applied potential and flow rates of the two fluids have been tuned, there is still a time component that dictates the stability of the Taylor cone. After several seconds of spinning (>20) there will be a charge accumulation on the grounded collector from the many fibers landing. Although this charge accumulation may be small, it is enough to decrease the influence of the electric field on the cone. In turn, this makes the cone progressively extend outward until it finally starts to drip (not shown).

4.2.2 Other coaxial Taylor cone complications

Sometimes it is assumed that increasing the flow rate of the LC and increasing the applied potential, in order to suppress the onset of the Rayleigh-Plateau instability, will lead to the production of highly filled LC-polymer fibers. Most of the time, however, this approach tends to fail. The suppression of the Rayleigh instability will not work when the charged outer solution

is engulfed by the inner fluid which has a totally different phase, and chemistry, than that of the outer solution, hence the LC flow rate must never be so high, compared to the polymer solution flow rate, that this happens. The outer solution is aqueous so at least charge and ionic movement throughout it will be much faster than if the inner solution (which is an oil like fluid) is coating the latter. The pendant drop at the tip of the coaxial needle will immediately break down in semi-gelled webs of polymer with drops of core LC fluid coating over and in between (Fig. 4.4). The fiber mats that result from the broken up Taylor cone will appear more like a spider web than a non-woven textile mat (Fig. 4.5), and clearly, the LC will not be encapsulated within the polymer fiber cores.

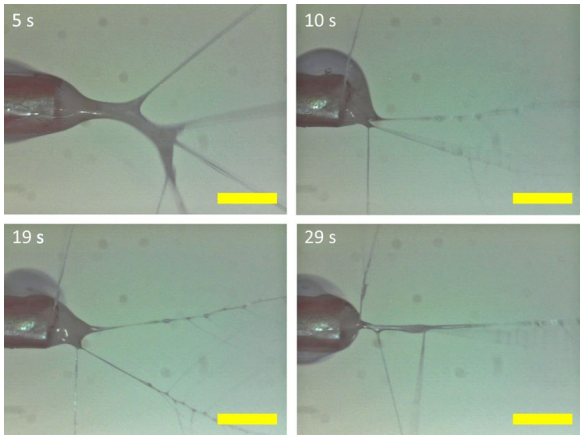

Fig. 4.4 – Evolution of Taylor cone instability immediately seen within the first 29 seconds when trying to couple high inner LC flow rate (roughly 5 times higher than that of the outer PVP sheath solution), with high applied voltage in attempt to prevent Rayleigh instability break up of the jet caused by the high volume throughput of the core. The ambient humidity during spinning was 24%, the temperature - 23°C. Scale bars: 1.1 mm

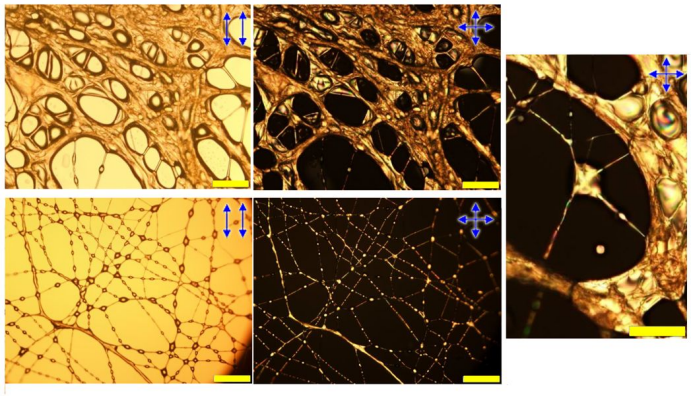

Fig. 4.5 – POM images (with and without crossed polarizers) of highly intertwined, branched and non-continuous webs produced from the Taylor cones shown in Fig. 4.4. These fibers show that not all LC is encapsulated; some LC droplets are between the fiber branches. Scale bars: 100 μm

Lastly, if certain LC-solvent mixtures are co-flowed within the same outer sheath solution phase separation within the Taylor cone can disrupt the spinning process. Demonstrated in the

images of Fig. 4.6 are two instances of when using a non-room temperature, nematic phase forming solid (EBBA), and a non-room temperature, cholesteric phase forming solid (cholesteryl nonanoate) mixed in chloroform are not compatible for co-electrospinning with PVP and ethanol as the sheath solution. In (a), a PVP in ethanol sheath solution was co-flowed with a core solution containing EBBA (N-(4-Ethoxybenzylidene)-4-butylaniline) in chloroform. In images (b) - (d), the same PVP in ethanol solution was co-flowed alongside a core solution containing cholesteryl nonanoate in chloroform. Both EBBA and cholesteryl nonanoate are solid powders at room temperature, and both can form LC phases when heated (EBBA: only a nematic phase, cholesteryl nonanoate: a nematic and cholesteric phase). They both need organic solvents to act as their "carriers" for flowing during electrospinning, chloroform was arbitrarily chosen due to its miscibility with the solids.

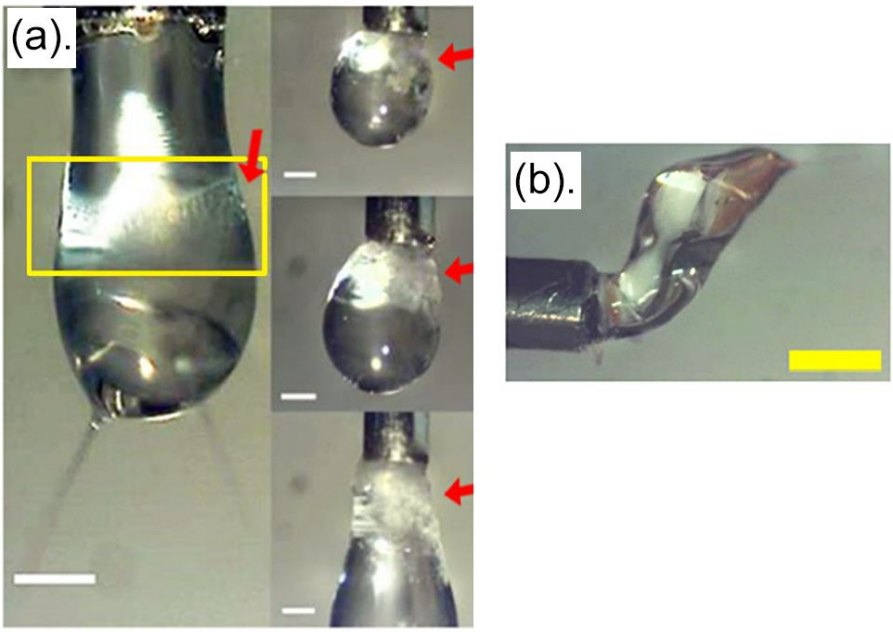

Fig. 4.6 – Three extreme cases of non-ideal coaxial Taylor cones drying, and undergoing phase separation and precipitation during electrospinning are shown in (a) - (e). All example cones contained LCs as the core fluid and all were unsuccessful in producing well defined coaxial fibers. The solution drop containing EBBA (a) stiffened (red rectangle outline) as it attempted to form the Taylor cone and extend outward. The red outlined area of the drop shows wrinkle streaks of the LC and polymer solution beginning to separate. The solution drop containing the cholesteryl nonanoate in (b) - (d) on the other hand immediately precipitated out. (Images (a) - (d) were adapted from ref. [40] with permission from IOP Publishing under the license: CC BY 3.0). Finally, image (e) shows another extreme case of a polymer solution beginning to gel and stiffen while forming the TC, in this case, it is a polystyrene-dimethylformamide mixture co-flowed with 5CB as the core. Here, the cone part takes on an "s" cobra-like shape because as the flowing outer sheath gelled, the inner core was still able to flow, and push the gelling polystyrene sheath tube further outwards. Yellow scale bar: 1.1 mm; white scale bars: 0.5 mm.

Both cholesteryl nonanoate and EBBA are insoluble in water, and both mixtures were attempted to be spun in an environment with humidity greater than 25%. Once the mixtures began to co-flow with the PVP solution, the pendant drops containing the LCs, chloroform, and the

PVP-ethanol mixture, begin to distort the formation of stable Taylor cones in different ways. The EBBA solution causes the Taylor cone to gel and stiffen (shown by the PVP sheath wrinkling in Fig. 4.6a) before the EBBA precipitates out. Meanwhile, the cholesteryl nonanoate solution precipitates out immediately from the Taylor cone before the Taylor cone finishes forming (Fig. 4.6b-d). While it was known that both EBBA and cholesteryl nonanoate are insoluble in water, I expected that this attribute would make spinning these two LCs in highly humid environments work even better. I thought this lack of miscibility would translate to the formation of drier coaxial fibers. Moreover, it was later noticed that while EBBA is soluble in ethanol, cholesteryl nonanoate is not.

Given the attempt to spin these solutions with PVP and ethanol, what most likely occurred for the cholesteryl case is that once the spinning process began, as ethanol is miscible with chloroform, the cholesteryl may have begun to phase separate out as ethanol from the PVP sheath solution entered into the core. As the ethanol began evaporating from the sheath during jet formation water from the humid atmosphere must have condensed into the jet, then this water could have been responsible for causing this particular LC to immediately precipitate out.

Another likely scenario is that a chloroform, ethanol and water mixture could have also entered into the core of the coaxial jet and caused LC precipitation. The latter is possible given that ethanol is miscible with water and chloroform. Of course since PVP is also miscible with all three of these solvents, it does not aid in solidifying the fibers formed much either. For EBBA, the same process is to have likely occurred, however, with the important difference being that when EBBA interacted with the developing ethanol-water mixture, it did not instantly come out of the solution because it is miscible with ethanol. Instead, as more water would have continued to condense inside of the Taylor cone it would have eventually begun causing the EBBA in the core to begin phase separating, even though the water-ethanol mixture would continue to keep the polymer solubilized.

This issue of ambient humidity playing a role in altering, and sometimes completely disrupting the coaxial electrospinning process is further discussed in the next chapter. Ultimately, it plays a crucial role in helping to understand why certain LC core fluids may not always produce viable coaxial LC-polymer fibers, and likewise LC-polymer fiber mats.

4.3 After the Taylor cone forms: A look at LC-fiber morphology

4.3.1 Regulating the core flow rate, sheath flow rate is constant

Table 4.2 shows the experimentally applied pressures, and the flow rates they correspond to, for flowing the 5CB while coaxially electrospinning. These flow rates were calculated specifically for this coaxial needle using the core and sheath tube dimensions previously described in sec. 3.1.2. The mass fraction of PVP in ethanol used throughout this thesis was 12.5%, and its approximate density was measured to be 0.88 g/mL (rounded to ~0.9 g/mL) using a Sartorius five decimal point precision balance (at near room temperature conditions 21°C - 24°C).

In order to simplify the number of variables which needed accounting for during the coaxial electrospinning experiments, typically either one of two standard flow rates was used for flowing the PVP polymer solution: 0.9 mL/hr (which experimentally corresponded to an applied pressure of 150 mbar), or 1.1 mL/hr (applied pressure: 200 mbar). Moreover, the results in Table 4.2

Tab. 4.2 – The flow rates of 5CB were estimated by weighing the amount of 5CB dripping from the coaxial needle when several pressure values were applied to its vial using the microfluidics unit (sec. 3.1.3). The drops of 5CB collected within 2 minutes under each applied pressure value were weighed. This process was repeated five times for each pressure value and the average mass of 5CB was calculated. The error corresponds to the drift in mass values before averaging. The average mass values, with the density of 5CB (≈1.02 g/mL), were used to calculate the flow rates for the 5CB (in mL/hr). Inner capillary dimensions: outer diameter = 360 μm, inner diameter = 250 μm, tube length = 25 cm (Fig. 3.3 in ch. 3).

Applied pressure to LC vial (mbar)	**Estimated flow rate of 5CB (mL/hr)**
100	0.36 ± 0.1
150	0.55 ± 0.1
200	0.75 ± 0.2
250	0.97 ± 0.2
350	1.11 ± 0.3
450	1.38 ± 0.3

were gathered by flowing 5CB through the inner capillary of the coaxial needle setup placed in the same orientation as if I were to start the electrospinning process. Instead of applying the voltage to the outer metal cannula, however, a two mL vial was placed under the tip to catch the falling 5CB droplets. This vial was weighed every two minutes on the precision balance to obtain the mass of LC gathered, per unit time, for each applied pressure setting. This process was repeated at five times for each pressure value listed, and the mass values averaged. Finally, since the density of 5CB is highly disputed throughout the literature - reported to range from as little as 1.008 g/mL [131, 132] to as high as 1.1 g/mL [133] at room temperature, the calculated average flow rates listed in Table 4.2 have some small errors associated with them.

We can determine how well the method of using a microfluidics pressure based flow unit works for flowing non-volatile, liquid crystalline fluids based on how the flow rate data from Table 4.2 fits to the Hagen–Poiseuille equation (Fig. 4.7). Using the applied pressure (p) and flow rate data (F) the viscosity (η from Eqn. 3.1) can be solved for. Here, the viscosity parameter is found through the slope of the linear curve when the original equation is rearranged (i.e. $\eta = \pi \Delta P r^4 / 8 / l / \phi$). Assuming there is no pressure loss due to the vials slightly de-pressurizing from the tubes inserted through their septa, for low pressure differences from about 100 mbar to 250 mbar (or $1 \cdot 10^4$ to $3 \cdot 10^4$ Pa), the fitted viscosity of 5CB was 0.034 Pa·s. As shown in Stefan Schymura's thesis [134] the experimentally measured viscosity of 5CB at approximately room temperature is about 0.03 Pa·s, in good agreement.

Additionally, if the Hagen–Poiseuille equation is fitted to all six of the experimentally established flow rates, including the higher last two pressure values, we find that the viscosity increases up to about 0.042 Pa·s. Nevertheless, despite some pressure loss and slightly lower than expected flow rates for 5CB, at elevated pressures applied to the 5CB, distortions in the formation of the Taylor cone still occur. Rayleigh breakup of 5CB in the fibers still occurs for applied pressures well below that of the PVP solution.

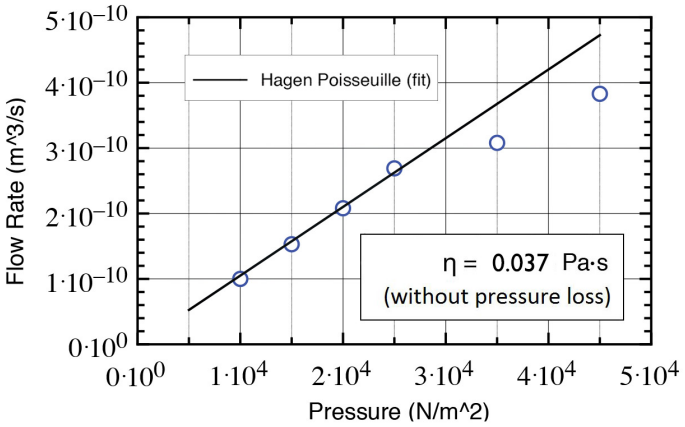

Fig. 4.7 – Plot of 5CB flow rates vs applied pressures (blue open circles). The Hagen–Poiseuille equation (Eqn. 3.1) is fitted to the data in order to solve for the viscosity of 5CB. The equation fits best to the first four pressure values. Since flow rate should linearly scale with pressure drop under the conditions of laminar flow, the flow rates calculated for the last two pressure values (corresponding to 350 and 450 mbar) are too low due to some loss in pressure at the inlets of the LC vial. The viscosity of 5CB found from this fitting is 0.0365 Pa·s, rounded to 0.37 Pa·s.

For nearly all of the coaxial electrospun fibers shown in this thesis, however, the applied pressure values to the vials containing LC were kept at roughly 150 mbar, which roughly corresponds to a flow rate of 0.5 mL/hr. This is roughly equal to half of the flow rate of the PVP solution. In order to see how the the LC core filling and the final fiber morphology change when the LC flow rate is increased to beyond and below the typically used flow rate value, POM images of several mats produced with the same polymer solution flow rate were compiled in Fig. 4.8.

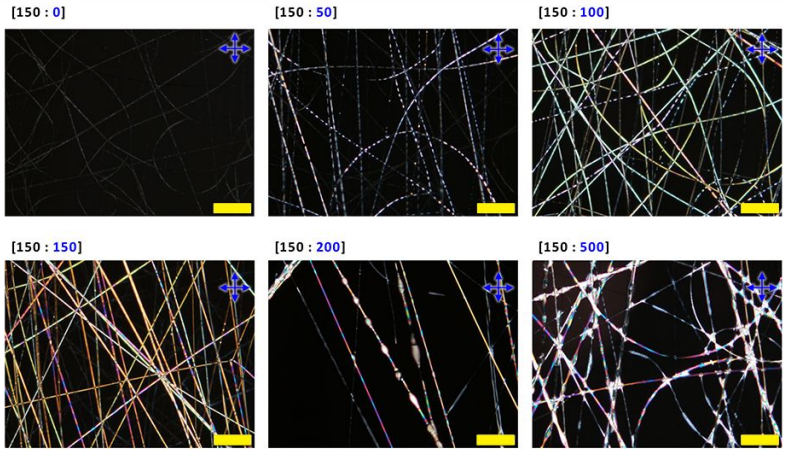

Fig. 4.8 – Coaxially electrospun PVP fibers containing differing amounts of 5CB filling in the cores according to the flow pressures applied to the LC in Table 4.2. The blue values in brackets correspond to the experimentally LC applied pressures (0 mbar - 500 mbar; 0 mL/hr - $\geq$ 1.4 mL/hr), while the applied pressure for the polymer solution was kept constant at 150 mbar (~0.9 mL/hr). Scale bars: 100 μm

Core flow rates that are too low (50 mbar; $\leq$ 0.3 mL/hr) will produce fibers that still non-beaded, and fully dry, but the LC within the cores will be broken up into several birefringent

drops within the sheath "tube". At too high of a flow rate (above 450 mbar; >> roughly 2 mL/hr) the LC core will coat the outside of whatever fibers are produced and pool around it, ultimately leading to a poorly solidified LC fiber mat with little LC encapsulated.

We can consider that both of these phenomena are predominantly driven by the interactions between the inner fluid's surface tension, and the outer fluid's viscous drag. This was final conclusion made by Utada et al.'s study [135] which examined two different types of dripping-to-jetting transitions observed when oils of different viscosities are co-flowed in water through microfluidics channels. Although it is not possible to visually see how electrospinning fluids in a coaxial jet are separating in air as the spinning proceeds, the break up of the core fluid into droplets, the core fluid beading, and the core pooling out of the polymer solution all manifest themselves in the fibers that get collected at the end of the process (like those shown in Fig. 4.8). The microfluidics approach can at least be used to explain why these events may occur during the straight jet stage of the electrospinning process. First, Utada et al. found that if both of flow rates of the inner and outer fluids are low, dripping of both inner and outer fluids will occur due to the Rayleigh instability taking over for both.

However, if the outer fluid flow rate is optimized to be much greater than that of the inner fluid, such that the inner fluid droplet size becomes the same diameter as the nozzle tip (or larger), then the inner fluid will transition from dripping to jetting within the fast flowing outer fluid. However, this jetting is short-lived because the core fluid jet downstream will become thinner and thinner from the shearing forces applied onto it from the faster moving outer fluid surrounding it. The surface tension of the inner fluid is not completely suppressed at this stage since it is the cohesive forces between the molecules that are holding the jet together and allowing it elongate. Eventually this jet will break off into droplets as the Rayleigh instability is no longer suppressed and the "viscous drag" (termed by Utada et al.) from the outer fluid becomes too high. It is this viscous drag from the outer fluid that finally overcomes the surface tension of the core fluid [135].

When applied to the case of electrospinning, in the straight jetting regime a low LC flow rate may still be a jet, as the surface tension of the outer sheath solution is the one that is primarily being lowered by the applied voltage and that of the core. However, at some point once the straight jet starts to enter the vigorous whipping regime during the drying stage, the drag of the outer fluid which is also cooling from the outside inwards, will probably also contribute to forcing the core LC droplets apart in the fibers when the core liquid's elongational viscosity is much higher than that of the outer.

For the inner core fluid to pool at the end of a jet it would conversely have to mean that the velocity of the inner fluid is much larger than that of the outer fluid. This causes the inner fluid to form an ever widening jet. The high shearing that the faster inner fluid experiences against the slower moving solution surrounding it causes the inner fluid to slow down and widen [135]. In the coaxial electrospinning case, this may apply to a certain degree at the earliest stage of the jet for the formation of the beaded fibers, which can be formed with a very high flow rate of the LC core relative to the flow of the sheath solution around it. However, the polymer sheath is also solidifying during spinning, so eventually, unlike Utada et. al's results in the micfluidics setup, the inner core fluid will not have the chance to widen into large drops at the end of the jet. As the jet is drying during spinning it is also elongating during the whipping stage from the build up of charges. At most, if the sheath does not prematurely rupture, the sheath will expand

outwards to create pockets or "beads" that can accommodate a larger volume of LC through the continuous fiber.

Last, one good example where high filling of the LC core can be especially useful is for creating colorful fiber mats using a chiral nematic mixture (Fig. 4.9b). The chirality imposes a continuous twist of the director, such that the optical properties of the LC vary periodically. If the period p is on the order of light wavelengths, $\lambda \approx 400$ nm in the LC, selective reflection of a narrow wavelength range around $\lambda = p$ occurs [12]. The result seen is strongly irridescent colors. Here we produced such a chiral nematic phase by doping a room temperature nematic mixture (ROTN-403) with the chiral dopant CB15 (initially shown by Eva Enz [97]). In this case, with an adequate flow rate of these mixtures, selectively reflecting colorful mats can be successfully electrospun.

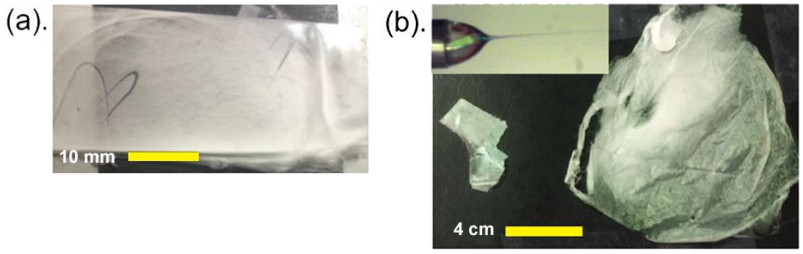

Fig. 4.9 – Two fiber mats coaxially electrospun with a nematic LC (a), and a green wavelength selectively reflecting chiral nematic LC (b) are compared. The Taylor cone with the PVP-ethanol sheath solution and the green selectively reflecting LC core flowing into the jet is also shown in (b). The glass slide (2.5 cm x 7.5 cm) in (a) contains the randomly oriented fiber mat with just 5CB as the core fluid. In (b), the macroscopic mat selectively reflecting a greenish color wavelength is spun using a mixture of ROTN-403 doped with 42% chiral dopant (CB15) by mass.

The drawback however in making such mats is that during spinning once the center area of the mat becomes too saturated with fibers, it tends to scatter more and appears white due to how thin the microfibers are. This differs from just surface dyed fibers, which although colored, will not reflect specific wavelengths of color when viewed under crossed polarizers. One final thing about the LC-filled PVP fibers is that while they can be handled up to a certain point, unfortunately, they are quite hygroscopic. They will degrade in about 3-4 months time if left under ambient conditions containing 30% - 45% relative humidity; sooner, if the humidity is higher.

4.3.2 Two types of LC-PVP fibers can be formed

The two types of coaxial fibers that can be successfully electrospun with this PVP-ethanol-5CB system are those with beaded morphology, and those which are mostly cylindrical without beads (further referred to as "non-beaded"[†]).

Generally, core continuous beaded 5CB-PVP fibers are usually easier to produce than core continuous non-beaded 5CB-PVP fibers (when optimal conditions, such as low relative humidity

[†]I do not use the term "cylindrical" because it implies that all the fiber cross-sections are always completely circular. However, sometimes the fiber lengths do slightly narrow and widen over long distances. In this sense, it is better to call these fibers "non-beaded" rather than entirely "cylindrical."

and room temperature, are maintained). This is because, experimentally, it is easiest to see what happens to the Taylor cone immediately after increasing the LC core flow rate too much. At worst, Rayleigh breakup within the LC flooded cone will occur, and the jet will no longer be stable. The LC flow rate during spinning when this happens then becomes our upper limit threshold for how much core fluid can be released before the break up of the jet occurs. If the LC core flow rate is adjusted to a value just below this limit, that will still allow fiber formation, then more often than not the fibers that are produced are beaded. Again, because the flow rate of the outer sheath fluid would still be lower than that of the rate of the core fluid, beaded fiber formation will occur as the core fluid tries to pool in the fiber (sec. 4.3.1). Tuning the LC flow rate to be lower for producing continuously filled non-beaded fibers requires more effort because we still want to avoid having so little LC within the jet that Rayleigh break up of the LC inside the fibers occurs as well.

The most effective ways to re-affirm the core consistency of the fibers, and the polymer sheath thickness of the filaments produced (both beaded and non-beaded) is by examining their cross-sections as shown in Fig. 4.10(a-b), via SEM. A quick procedure to ensure that the fiber cores do not completely collapse on themselves prior to imaging is to remove a bundle of fibers using tweezers and gently place them onto the edge of a conductive tape coated SEM stub having a 45° tilt angle. When placing the fibers onto the stub, they should not be pressed so that they completely flatten against the stub surface, lest the cores get severely deformed.The vacuum of the SEM will siphon out the tiny volumes of liquid crystal that are present in the core exposed fibers, thus we will only see the textured polymer sheath surrounding the hollow core where the LC once was.

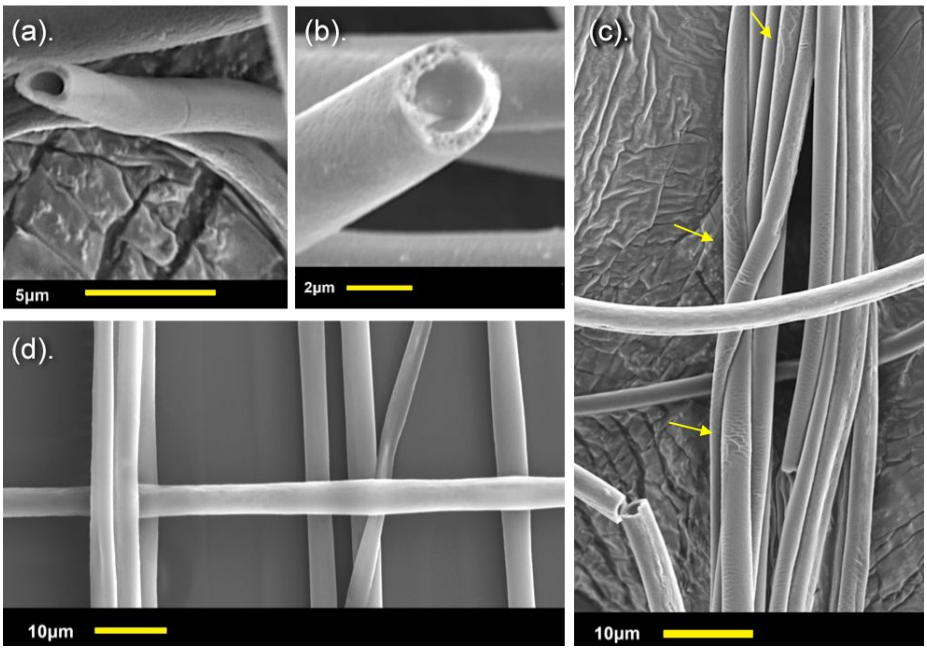

Fig. 4.10 – SEM images of non-beaded 5CB-PVP fibers electrospun with a smaller LC flow rate than the polymer solution at room temperature and relative humidity below 30%. Two examples of fiber cross-sections from the same sample (a-b), and several fibers intertwined (c-d) are shown. Fibers gathered in a bundle in (c) tend to have more wrinkles on the surface (yellow arrows) than those non-beaded fibers laying without being wound around others (d).

After having compared the cross-sections of several coaxial fibers seen via SEM, the typical core diameter for non-beaded fibers electrospun tends to take up roughly 60% to 80% of the whole fiber diameter. For instance, the two fibers shown in Fig. 4.10(a-b) have total diameters: 2μm, and 1.75μm, respectively, and their cores take up about 1.5μm. As the fibers are non-beaded, their widths are also more constant for the entirety of their lengths even if many individual filaments have wound around one another (like those in Fig. 4.10c). Many of those intertwined fibers tend to have textured surfaces showing roughness and wrinkling, but it is also possible to find non-bundled, non-entangled fibers with porous cavities as well (Fig. 4.10b). Likewise, it is also possible to obtain coaxial 5CB-PVP fibers without any surface texture at all (Fig. 4.10d).

One possible reason for this difference in surface texture may be simply that the more filaments landing on top of, and near to, one another forces them to adopt twisted configurations as they finish drying. For instance the configuration of how the fibers collected in Fig. 4.10(c) is very different from how they collected in Fig. 4.10(d) as the latter group contains fibers that are not just straight and are curved around each other. In fact, the only filament in Fig. 4.10(c) that does show signs of wrinkling and texture is the one that appears to be twisting around the middle second vertical fiber from the left.

Moreover, the reason why this type of wrinkling and roughness does not tend to appear on pure PVP electrospun fibers when they land twisted on the collector is because they lack the cores of fluid adding stress on the polymer sheath from the inside out. More than 50% of these coaxial fibers is comprised of the liquid crystal component and this contributes to a very thin polymer sheath, which during the process of evaporative cooling that occurs during electrospinning, will easily exhibit signs of micro-cracking if deformed while landing (i.e. like if the fiber has intertwined with several others).

The level of wrinkling and texture becomes more apparent when the fibers become beaded, and even more, so after they have been used for sensing when exposed to organic vapors. Section 6.4.2 continues the discussion of fiber deformation and wrinkling since movement of the LC in the fiber cores contributes to more of these deformations in the polymer sheath. For now though, it is clear from cross-section images of the fibers that the ratio of polymer sheath to liquid crystal core for these fibers is overall significantly less than for the non-beaded fiber types. Protruding sections in the beaded fibers can range from being 1.5 times up to 3 times wider than the non-beaded sections, as shown in Fig. 4.11(a-b). For that one highlighted filament in Fig. 4.11(a) the non-beaded sections are roughly 3.5 μm wide and the largest beads are 10.5 μm.

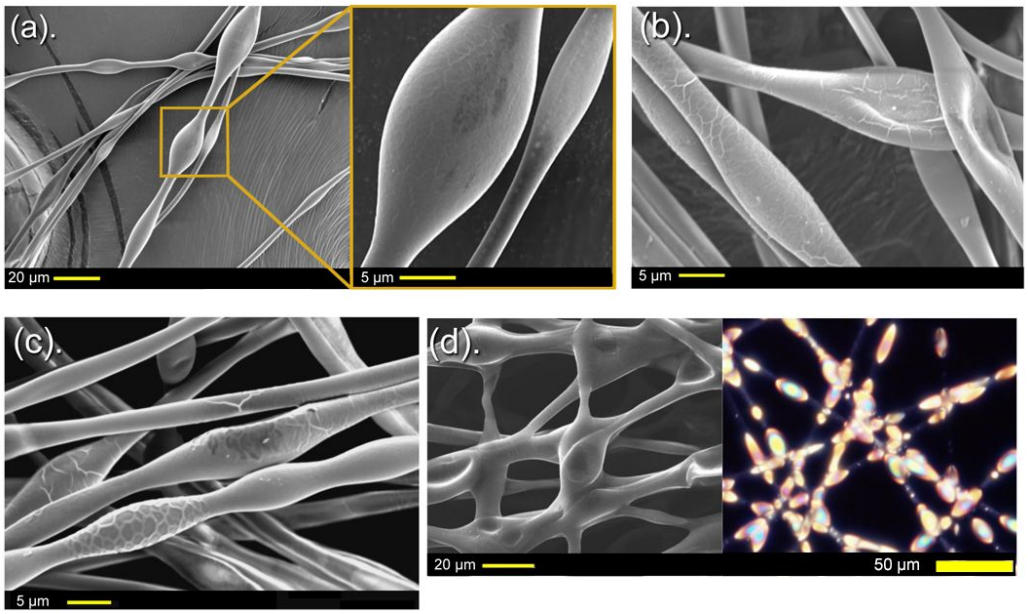

Fig. 4.11 – SEM images of several beaded coaxial 5CB-PVP fibers, electrospun with LC flow rate greater than than the polymer solution flow rate at room temperature and relative humidity below 30%. The beaded sections of theses fibers can be similar in size, or up to three times as wide as the non-beaded portions separating them (yellow outline in (a)). Beaded portions have thinner sheaths compared to the non-beaded parts. Wrinkles and cracks (b-c) are more visible at these points where higher volumes of LC exist. The thin sheathed beads can flatten more easily (b-c). If merged, (d), LC accumulates at the merged beaded points rather than being distributed evenly throughout the filaments.

Furthermore, while not shown in this image set, from a cracked fiber bead visible in Fig. 4.12 the sheath thickness, compared to the core diameter, is significantly thinner than the sheaths found for non-beaded coaxial fibers. The outer diameter of the bead itself is about 15.5μm wide, but the sheath itself is at most only a few hundred nanometers thick on all sides surrounding the center core. This means that the core diameter takes up at least 95% of the space in the bead, if not more.

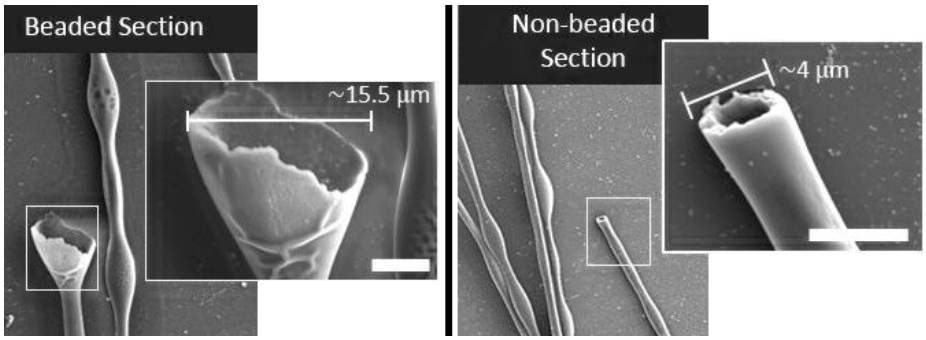

Fig. 4.12 – The SEM images of two cracked 5CB-PVP beaded fibers showing their core spacings. The beaded sections (right) tend to have sheaths considerably thinner than the sheaths surrounding the non-beaded sections in the fibers (left). For the beaded part, the core diameter is largest and the sheath is very thin, at most a few hundred nanometers or so. This is unlike the non-beaded section of the fibers, which shows that the sheath is roughly a micron thick around the core diameter.

The non-beaded sections in the beaded fibers also tend to have sheaths with similar thicknesses as those of the non-beaded fibers in general. In the representative image in Fig. 4.12, the non-beaded section in the fiber is 3.5 - 4μm wide, but the core itself is about 2.5 μm wide. This leaves almost 1 μm of polymer interface between the surrounding air and the LC core on all sides of the coaxial fiber where there are no beads present. This is important to know for vapor sensing tests discussed in ch. 7, as the amount of LC present in the fibers and how thick the sheaths are will reflect how fast the vapor penetrates the fibers to interact with the LC for creating a response.

Finally, if a crude extrapolation based on the combination of the sheath-to-core measurements found for both types of beaded and non-beaded fiber types electrospun is made, a 1.05 mm long beaded PVP filament could potentially have up to 5 times more core volume to contain liquid crystal than a non-beaded filament of the same length. To make this calculation, the following assumptions were made: (1). the non-beaded filament has a core diameter that is 80% of the total fiber diameter, and that this core diameter does not taper in size throughout the filament's length (experimentally, the latter issue sometimes occurs and can be LC flow rate dependent), (2). that the number of beaded sections and non-beaded narrow sections in the beaded filament are equal and that their lengths are constant (i.e. equal bead spacing), (3). that the beaded sections are three times as wide as the non-beaded sections, (4). that all cores in the beaded sections have diameters that take up 95% of the total outer bead diameter, and (5). that the size of the beads are geometrically similar to prolate spheroids with only two lengths for the major and minor axes.

Perhaps, if a beaded fiber has flattened beads, like those that appear almost like red-blood cells (i.e. biconcave disk-like with flattened centers) such as the one in Fig. 4.11(b), the volume of the core might decrease substantially, but then again if the bead expands outwards in width rather than height it could make up for the difference. In any case, while these assumptions are unlikely to remain constant for actual fibers collected with long lengths, the volume difference found for estimated core sizes in both the beaded and non-beaded types puts into perspective the level of LC filling volume difference that could exist between these fiber types.

4.3.3 Ensuring non-leaking & non-merged coaxial fiber formation

Vary the distance between the nozzle & collector

Apart from maintaining a constant voltage and flow rate throughout the spinning process, one can further ensure that solidified filaments are obtained by choosing the optimal collector distance from the charged nozzle sustaining the Taylor cone. Too short of a distance (usually less than 5 cm) will not provide the adequate space needed for the jet to dry into a filament before it impacts onto the collector. This can result in the collection of wet gel-like streams rather than solid fibers as the whipping regime the jet endures is shortened, and the whipping sections of the jet are likely to impact and merge with another before landing [32] (Fig. 4.1(a-c) with the 5CB shown as well).

In Fig. 4.1, with the electric field kept the same with the ground at 7 cm, the fibers produced are still quite wet and leaking. At 10 cm and 15 cm uniform, but thinner, fibers are formed and all are dry without LC pooling out. At 15 cm, there is a slightly higher proportion of fibers with less continuous LC filling in the cores. Finally, at 20 cm the crossed polarizer and plane polarized light POM images show that there are fewer fibers collected and also fewer fibers containing the LC within. All other spinning parameters were kept constant for these fibers produced in Fig. 4.1. When spinning horizontally, too long of a distance (usually more than 15 or 20 cm) may reduce the electric field strength to sustain the whipping motion in the charged jet. Gravity will also start to pull the jet downwards with greater horizontal distances. It is possible that one can avoid this issue by spinning vertically however.

The changes in the morphology of the fiber mats produced while increasing the collector distance from the charged nozzle tip for electrospinning LC-fibers are shown in Fig. 4.13. Even at at a distance of 7 cm, the LC filled fibers produced are already much thicker, and less dry than those produced with the collector just 3 more centimeters further away. Recall that the LC core fluid is neither contributing to the mass loss of the jet during solvent evaporation, nor adding charges to the jet to help it induce whipping. This means we need to account for polymer sheath solidification being slightly slower than it otherwise would be without the core fluid encapsulated within, and it would need a further distance so that the whipping envelope can finish evaporating. Moreover, too high of a distance (20 cm) can cause the filling of the LC core to break up if not adjusted in parallel to the movement of the collector (this relates back to considering the ratio between outer sheath flow rate and inner core flow rate discussed in sec. 4.3.1. As the solution jet becomes thinner, the constraints of the radius may cause the LC core to become discontinuous.

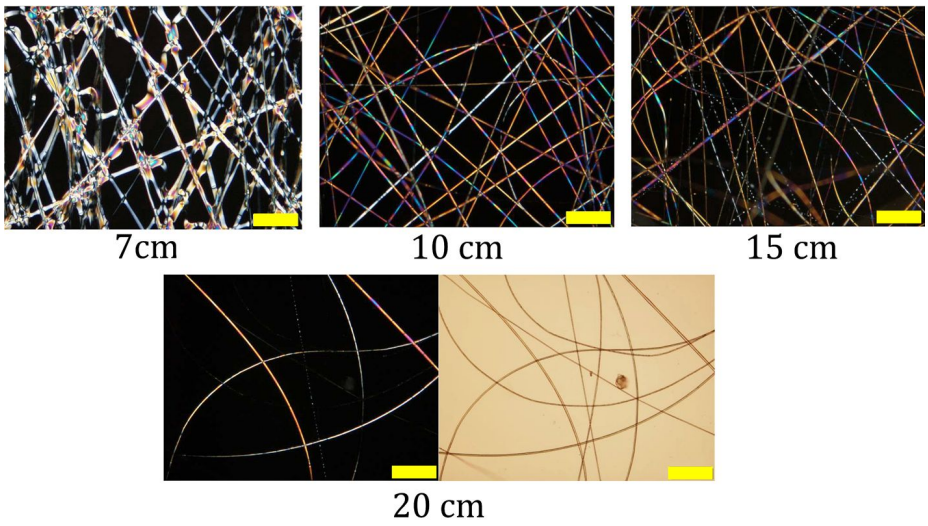

Fig. 4.13 – Crossed polarizer POM images show the optical changes in coaxial 5CB-PVP fibers spun with nozzle-to-collector distances from 7 cm to 20 cm. (LC:Polymer flow rates - 0.55 ml/hr:0.9-1.0 ml/hr; applied voltage to nozzle - 9 kV; temp.:relative humidity - 24 °C:25%). Scale bars: 100 μm

Theron et al. [136] and Thompson et al. [137] found that the charge density in a solution jet will decrease exponentially as the distance from the nozzle to the collector increases due to the fact that as collector distance increases the electric field diminishes in strength. Lower charge density in the solution jet means that fiber formation will be hindered as the effects of surface tension will dominate. Apart from distance, the other physical parameter that can play a role is the direction of electrospinning, that is, spinning with the solution jet in the direction of gravity or perpendicular to gravity. While not many studies exist exploring the impact of this often overlooked parameter, a higher distance with a horizontal spinning setup (jet perpendicular to the direction of gravity) will produce less fibers for the same area (Fig. 4.13) as the jet eventually curves downward in its path. On the other hand, for near-field electrospinning, that is, electrospinning to collect highly directional fibers using a nozzle-to-collector distance less than a few millimeters, the collector distance becomes one of the top three most important variables that influence the system next to the size of the nozzle diameter, (in the micrometer range), and the applied voltage (below one kV) [138].

Use non-traditional collectors

"Non-traditional" collectors such as those that are porous (e.g. metal wire frames, and mesh grids) can be used in the place of solid smooth substrates like glass slides and metal foils in order to collect drier fiber mats. A mat of randomly oriented freely hanging 5CB-PVP fibers can be made by using a circular copper metal frame (Fig. 4.14c). The charged fibers from the jet attract to random points on the frame to discharge onto, causing the fibers to gradually build up across one another in the center of the frame with their ends electrostatically held onto the ends of the frame. It is also possible to control the orientation and distribution of the fibers across porous collectors as well (Fig. 4.14a-b), where conductive parallel "rods" guide the positively charged whipping jet to distribute filaments across back and forth to create a mat of aligned

fibers. Using metal grids, or any other mesh pattern connected to the ground, will result in the production of fiber mats with a complementary pattern of the mesh.

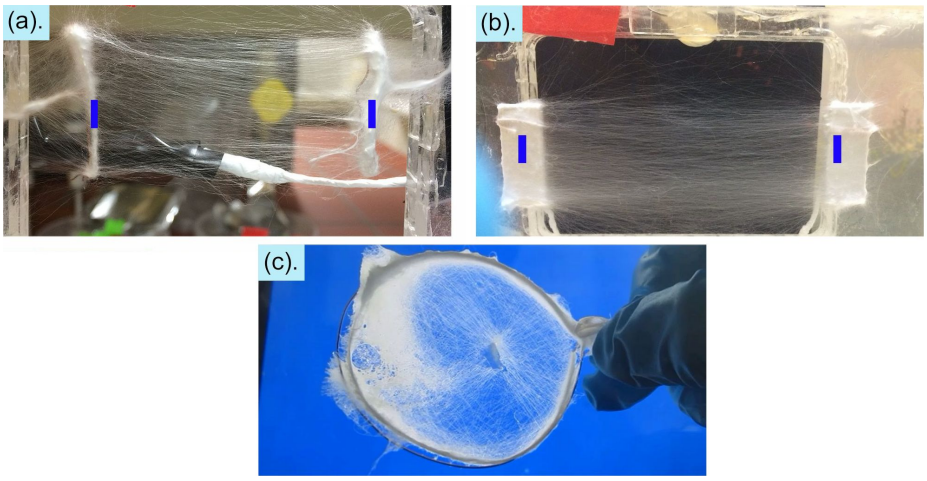

Fig. 4.14 – Using copper wires as separated rods (a), or to fashion circular frames (diameter: 6cm) (c), freely hanging substrates without a surface underneath can be used to collect electrospun fibers. These collectors can be placed in the larger opening of the collector stand in the setup (sec. 3.1.3). A separate wire in the back of the circular frame in (c) leads to the ground of the high voltage box. For (a), the parallel copper rods are separated by about 6.5 cm (the space between the two blue rectangles). In (b) the electrodes are just small rectangles of folded aluminum foil taped to the sides of the stand 9cm apart, the wires to the ground are attached from the back. Fibers collected in (a-b) are mostly align parallel, in (c) they have a random orientation. The circular frame in (c) is an image adapted from [70] with permission from Taylor & Francis under the license: CC BY-NC-ND 4.0.

For all these cases, but particularly for the collectors which collect fully free-hanging mats, the layers of fibers deposited do not lay flat. This means that any residual solvent has a more of a chance to evaporate in all directions around the fibers due to higher surface area exposed to ambient air. Solvent evaporation is not only limited to proceeding in the direction opposite to the part that is against a non-porous, solid substrate because there is no substrate supporting the fiber mat. When the fibers are collected in this way, we avoid having to contend with potentially collapsed fibers flattening into ribbons [44], as there is no impact from the substrate to add stress onto the drying fibers as they land. Additionally, residual solvent contained within the drying fibers will not seep or "wick" onto the substrate, which could impact the drying of fiber layers that deposit later.

4.3.4 Chain entanglements ensure fiber formation

There are least two main competing processes to consider when trying to determine whether electrospraying or electrospinning will occur for a solution. There is first the competition between polymer solution concentration (or, likewise, polymer molar mass) and the surface charges accumulated in the jet during solvent evaporation. The higher the polymer concentration, or molar mass, the more entanglements between the polymer chains will develop during solvent evaporation and this in turn prevents electrospraying (i.e. the subdivision of the jet into droplets) while stabilizing the geometry of the polymer as it dries mid-flight. If there are not enough entanglements in the solution, then the accumulated surface charges in the fluid "win" and

droplet subdivision will continue to occur until finally the droplets will have dried into nano-sized polymer beads [126, 139].

The second aspect to consider is the fact that the electrospraying/spinning process is, in essence, exothermic. The fluid jet continuously loses thermal heat to its surroundings in order to solidify into either beads or fibers. The rate of solvent evaporation will also play a significant role in limiting the droplet and/or the fiber diameter size since the drying will hamper further charge accumulation over the solidified polymer surface [126]. As the latter aspects regarding solvent evaporation rate and charge distribution are more complex to experimentally measure, here, only the role of polymer chain entanglements in determining spinnability will be considered.

In the absence of a predictable model that can gauge whether certain polymer solutions have the right amount of chain entanglements needed to form fibers during electrospinning, a study conducted by Shenoy et al. [140] concluded that for eight polar and non-polymer solutions, at least 2.5 entanglements per chain would be required so that only fibers without any beading from spraying would result during electrospinning. Shenoy et al. calculated this value by considering that the number of chain entanglements in a polymer melt (n_e) is defined as the ratio between the polymer's critical molar mass (M_c) to its entanglement molar mass (M_e) [141–145].

This section re-considers Shenoy et al.'s equations for finding the theoretical number of entanglements necessary to obtain beaded and non-beaded fibers for the PVP solution used in these experiments. It also compares whether the regimes suggested by the plot obtained predict the same polymer solution concentrations leading to beaded fiber and non-beaded fiber formation seen experimentally. Moreover, the number of entanglements necessary for polystyrene fiber formation are also re-calculated and also compared to independent experiment data obtained. This comparison allows us an opportunity to evaluate the extent of the role played by the chemistry of the polymer and solvent during fiber formation by electrospinning.

Defining the chain entanglement equation

The parameters M_c and M_e come from considering the conformation of polymer chains from a rheological perspective. The critical molar mass is defined as the mass where a polymer's zero shear viscosity (η) makes a significant upturn in the slope of Fig. 4.15(a). For most polymers with low molar mass $\eta \propto M$, however, once a polymer reaches a certain molar mass the proportionality alters such that $\eta \propto M^{3.4}$ [142]. Since this upturn in slope was seen for many polymers, regardless of their monomer chemistry, it was hypothesized to emerge from the increased number of chain entanglements present within polymer melts with high molar masses above a certain value.[‡]

[‡]Experimentally, researchers found that this value tends to fluctuate between 3.4 and 4.6 for some linear polymers actually [146]. However, for polymers containing many branches or "star-like" architecture it can deviate much more [147–149].

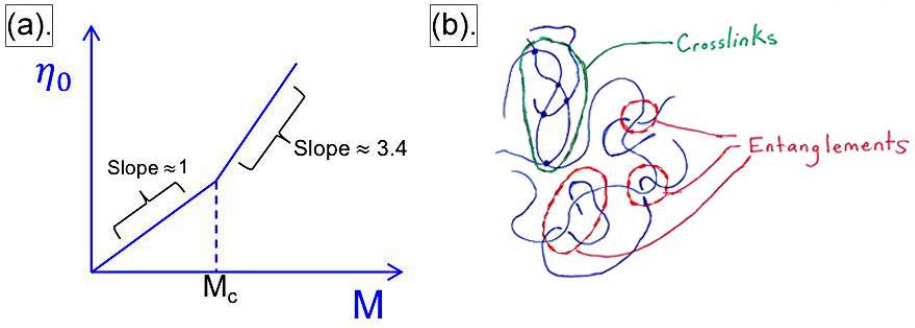

Fig. 4.15 – General plot showing the dependence of zero shear viscosity (η) on molar mass (M) of a polymer melt (a), and entanglements (b). A linear correlation between the viscosity of polymers having molar masses lower than a certain critical value (M_c) will exist [141–145]. After the critical molar mass, the relationship deviates such that $\eta \propto M^{3.4}$, causing the slope to increase. Experimentally this has been found to be the case for several linear polymers in the melt [144, 145], and for highly concentrated linear polymers in good solvents. The viscosity increase is due to high molar mass (or concentration) that facilitates an increased number of physical chain entanglements present (b) [142, 143, 150]. Entanglements are different from chemically bonded cross-links (green text in (b)).

For this simplified discussion "chain entanglements" refers to the loops a polymer chain makes when intertwined with another neighboring chain in a random manner (Fig. 4.15b). Covalently bonded cross-links, for example, are those that introduce extra bonds to link polymer chains together (e.g. the heating of natural rubber polymers with sulfur to create sulfur cross-links), and they are permanent unless destroyed. In contrast, entangled polymer chains slide in and out of entanglement junctions if sufficient energy is added. Longer polymer chains will take much longer than shorter chains to move out of entanglements and this parameter of time (often referred to as $\tau_{\text{relaxation}}$) influenced Pierre-Gilles de Gennes, Masao Doi and Sam Edwards to expand the quantitative theory between the number of chain entanglements (n_e) by introducing the "reptation tube model."

Returning to M_e now, a polymer's entanglement molar mass (first defined by Ferry [145], Colby et al. [146] and Fetters et al. [144]) refers to the average molar mass of polymer chains present in between the junctions that are entangled. M_e actually relates to the ideal random-walk polymer chain model as it turns out to be $\propto (\rho^{-2} \cdot [< R^2 >_0 /M]^{-3})$, where ρ is the polymer density, and $[< R^2 >_0 /M]$ is the mean squared end-to-end distance of the unperturbed polymer chain divided by the melt molar mass [144]. Moreover, M_e values for several polymers can be found experimentally according to the relationship: $M_e = 4/5 \cdot [\rho N_a KT/G^0{}_N]$, where N_a is Avogadro's number, K is Boltzmann's constant, T is the temperature in Kelvin, and $G^0{}_N$ is the plateau modulus (usually found by applying an oscillatory stress and strain to the polymer via dynamic mechanical analysis (DMA) measurements).

Experimentally, the value of $G^0{}_N$ describing the "rubbery plateau" region is seen in a log plot of the polymer's relaxation modulus (G) versus log time (t) for a very small step strain [144, 151–153]. Finally, the $4/5$ coefficient comes in from de Gennes', Doi's and Edwards' tube model expansion mentioned earlier [152, 154, 155]. Having now M_c and M_e, Bueche theorized that the ratio of these values would correspond to the number of entanglements (n_e) that would cause the upturn in the viscosity vs. polymer molar mass slope (Fig. 4.15a).

This idea that entanglements influence polymer melt and solution viscosity is relevant for electrospinning and electrospraying because the same ratio between M_c and M_e is applicable for polymer solutions such that: $n_{e_{soln}} = M/M_{e_{soln}}$. In other words, the number of entanglements in a concentrated polymer solution ($n_{e_{soln}}$) is equal to the ratio of the polymer molar mass (M) to the molar mass of entanglement of the solution ($M_{e_{soln}}$). The critical molar mass is not used here because it is assumed that the polymers used for electrospinning alreadt very high molar masses such that $M >> M_c$ and have viscosities well into the upturned slope region described in Fig. 4.15(a). A dilution factor (ϕ) is also applied to take into account the presence of solvent influencing the molar mass (M) of the polymer melt such that the relationship: $M_{e_{soln}} = M/\phi$, where ϕ refers to the volume fraction of polymer in solvent [140]. Granted, this only works if we assume: (1). the polymer is in a good solvent and that non-solvent or bad solvent effects (like gelation, or crystallization) do not occur, (2). the concentration of the polymer is high enough such that chain overlapping is guaranteed.

To summarize, to find the number of entanglements in a polymer solution ($n_{e_{soln}}$) that could be possible given a certain molar mass (M) and solution concentration (ϕ) we can use equation 4.1. The molar mass for (M) is usually taken as the weight average molar mass value (M_w) for polydisperse polymers. Given three important assumptions: (1). that several electrospinning results noting the concentrations resulting in bead formation and fiber formation, exist for several linear polymers exist, (2). that solution concentration and polymer molar mass impact fluid jets the most, and (3). that rheological parameters (like M_e, and G^0_N) for many linear polymers have already been determined, we can hypothesize that semi-empirical plots predicting the relative regions of bead and fiber formation for electrospun polymer systems on the basis of concentration and molar mass can be accurately computed using 4.1.

$$n_{e_{soln}} = M/M_{e_{soln}} = (\phi M)/M_e \tag{4.1}$$

Predicting the polymer solution concentrations that produce beaded and non-beaded electrospun fibers

While Shenoy et al. calculated these plots for at least eight solutions as mentioned before, they actually made a minor mistake regarding their results for solutions containing polystyrene in tetrahydrofuran (THF) in their Fig. 1 of [140]. They mistakenly assumed that Fetters et al. [144] did not already take into account the tube model coefficients that were proposed previously by de Gennes, Doi and Edwards. In reality, Fetters et al. had already incorporated them into their calculation of G^0_N, which Fetters et al. then also experimentally measured just to make sure their calculation was a reasonable estimation [144, 152]. So the mistake Shenoy et al. did was to use a value of M_e for polystyrene that was about twice as high than it should have been, because they multiplied the tube model coefficients (again) to the M_e values Fetters et al. found.

This error was corrected by recalculating the polystyrene solution plot shown in Fig. 4.16, and this plot now indicates that bead formation for a solution containing 190,000 g/mol polystyrene in THF will likely occur when there are roughly $\leq$ 2.5 chain entanglements present for solutions containing polymer mass fractions $\leq$ 18%. This is opposed to Shenoy et al.'s original result which indicates that beads without fibers will most likely be seen up until a slightly higher

solution mass fraction (20%). Likewise, from my revised plot, beaded fibers for this molar mass of polystyrene are predicted to form if solutions have entanglements between 2.5 - 4 (as opposed to 2 - 3.5 in Shenoy et al.), corresponding to polymer mass fractions between 20% and 30%.

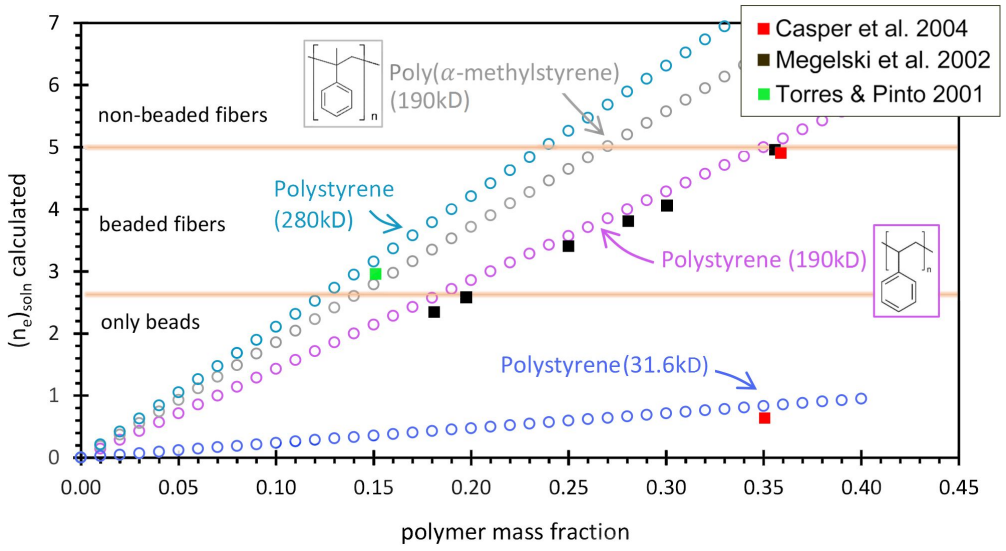

Fig. 4.16 – A plot showing the mass fractions of polystyrene in THF that are most likely to produce beads, beaded fibers, and non-beaded fibers according to the number of entanglements ($n_{e_{soln}}$) calculated for each molar mass using Eqn. 4.1. The molar masses (g/mol) of polystyrene used in Eqn. 4.1 were 31.kD, 190kD, and 280kD. For comparison, to show that that monomer chemistry does not contribute to the chain entanglements, the M_e value for poly(α-methylstyrene) with a molar mass of 190kD was found and $n_{e_{soln}}$ was also calculated for the same mass fraction ranges. The abbreviation "kD" used in the plot refers to kilodaltons (1 kD = 1000 g/mol). The square symbols refer to independent studies that have confirmed seeing particular morphologies (beads, fibers, or both) after electrospinning the solutions containing these polymer mass fractions (Casper et al. [41], Megelski et al. [106], Torres et al.[156]).

Non-beaded fibers should exclusively form from solutions with polymer mass fractions above 30% ($\geq$ 5 entanglements, as opposed to $\geq$ 3.5 in Shenoy et al.). Although at first glance the change in the number of entanglements between my result and that of Shenoy et al. (between 0.5 and 1) appears insignificant, their error in using an overestimated M_e can carry over for predictions made on the types of fibers to be expected when using other polymers that follow a similar topology to that of polystyrene (i.e. a linear carbon chain with repeating bulky side groups). Not all of the M_e values for such polymers have been tabulated, one of those is actually PVP which is further discussed below.

In order to divide the regions of expected beads, beaded fibers, and non-beaded fibers, the empirical data was used from the results of other electrospinning studies. The experimental data acquired from Megelski et al. [106] that extensively described the results of spinning various mass fractions of 190,000 g/mol polystyrene in THF were first used (blue squares, in Fig. 4.16). If the polystyrene molar mass is theoretically increased in Eqn. 4.1, while keeping all other values the same, a steeper sloped curve emerges (for polystyrene that is 280,000 g/mol in Fig. 4.16). This indicates that lower mass fractions should give a higher number of entanglements which is expected. It also indicates that with more entanglements made for lower mass fractions of high molar mass polymers, the non-beaded fiber regime during electrospinning is achievable earlier on.

Likewise, decreasing the molar mass will produce a flatter curve (e.g. 31,600 g/mol). This implies that if the molar mass of the polymer is too low, then there could be potentially no concentration range (at least up to 40% polymer mass fraction) that would be able to produce the number of entanglements needed to form non-beaded fibers at all. Indeed, it would seem like this could be believable as there is one report by Casper et al. [41] that mentions attempting to spin a 35% mass fraction of low molar mass polystyrene (31,600 g/mol) in THF and failing to achieve fibers at all in the presence of various levels of ambient humidity.

If such curves are as reliable as Shenoy et al. have suggested, it would certainly take out the guess work of considering which polymer solutions to use if we wanted to electrospray beads or spin fibers. Finally, it would mean that the polymer topology, or architecture, matters more to forming the entanglements needed in electrospinning than the actual chemistry of the monomer functional group, as shown with the curve of poly(α-methylstyrene) in Fig. 4.16, which almost matches that of a higher molar mass polystyrene despite having an extra methyl group attached suggesting that similar spinning results, if it could be dissolved in THF, should be expected. Equation 4.1 does not take into account functional group size, but something interesting to see is if steric hindrance could play a role in entanglement formation and subsequent electrospinning, however, this outside of the scope of this thesis. So far though, there have only been a few other sources (indicated by the colored squares in Fig. 4.16) which had independently electrospun these molar masses of polystyrene using THF without indicating prior knowledge of Shenoy et al.'s study.

So far while the results acquired from independent sources follow the trends predicted by Fig. 4.16, with regards to the study by Casper et al. [41], there is no way though that it explains the pore formation that occurs in the polystyrene fibers and beads produced in high ambient humidity. From Lu et al.'s study [42], we now know that pores appearing on the surface of and within the cores of the polystyrene fibers are really due to the combined effects of solvent and ambient humidity during spinning. If a solvent more volatile than water, like THF, is used at high humidity, pores will only develop over the polystyrene fiber surface. Since the spinning jet will have cooled down considerably as a result of the evaporation of the THF, the water vapor will have condensed on the surface of the dried cooled fibers rather than entering into the cores. Since polystyrene is insoluble in water the droplets condensed on the surface will create indents or "pores" on the fibers when they finally evaporate.

Changing the solvent to one that is less volatile than THF, like dimethylformamide (DMF), will additionally contribute to internal pore formation as this solvent will not evaporate as quickly as THF, giving the water vapor from the humid environment a chance to enter into the solidifying jet. Both THF and DMF are also water soluble. Most importantly though, neither the plot, nor equation 4.1 actually take the formation of these types of surface features (i.e. surface pores, cross-sectional pores, wrinkles) into account.

Figure 4.17 shows the relevant mass fraction-entanglement curves for PVP using 13,400 g/mol for M_e.[§] Since M_e for PVP, as mentioned previously, was not able to be found in the literature by neither myself, Shenoy et al., nor Munir et al. [158], Shenoy et al. first decided to estimate M_e by assuming that it behaves similarly to polystyrene when it entangles at high molar mass

[§]The two commonly used molar masses I'm most familiar with are plotted: roughly 1,300,000 g/mol, used in this thesis, and 43,000 g/mol, used extensively in ref. [157]

given its topology.[¶] However, since Shenoy et al. in [140] made the mistake of using a larger value for M_e than necessary for their polystyrene entanglement plot, instead of using 16,800 g/mol as they did, I used 4/5 of this value (13,440 g/mol). This is because Shenoy et al.'s M_e polystyrene estimate had mistakenly multiplied 5/4 to the value that Fetters et al. [144] and Larson et al. [152] originally had.

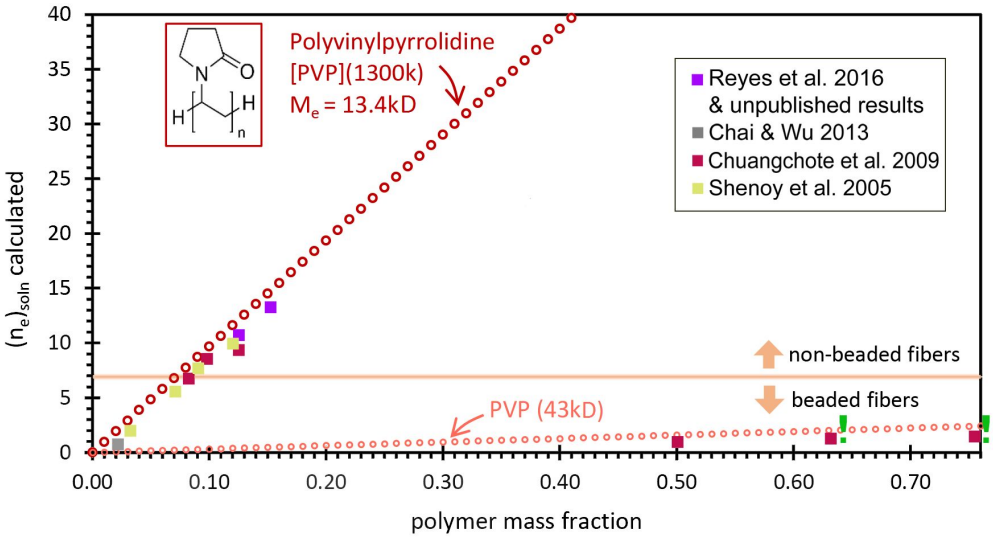

Fig. 4.17 – A plot showing the PVP mass fractions in ethanol that are most likely to produce beaded fibers, and non-beaded fibers according to the number of entanglements ($n_{e_{soln}}$) calculated for each molar mass using Eqn. 4.1. The molar masses (g/mol) of PVP used in Eqn. 4.1 were 1300kD and 43kD. The abbreviation "kD" used in the plot refers to kilodaltons (1 kD = 1000 g/mol). The square symbols refer to independent studies that have confirmed seeing particular morphologies (beads, and beaded fibers) after electrospinning the solutions containing these polymer mass fractions (Reyes et al. [70], Chai and Wu [160], Chuangchote et al. [157], Shenoy et al. [140]). Unlike for the similar plot of polystyrene shown in Fig. 4.16, few experimental data existed showing just the production of PVP beads alone, thus the transition between acquiring just polymer beads alone and beaded fibers may be very small actually. The two green exclamation points near the two square symbols for the 43k PVP indicates that the solutions containing 50% and roughly 64% PVP did not produce beaded fibers as was expected by the plot, but instead produced non-beaded fibers.

In order to be more accurate, however, the unperturbed end-to-end distance squared ($[< R^2 >_0 /M]$) of the PVP in a theta-solvent would probably need to be calculated such that it could then be used in the equation relating M_e to M, as proposed originally by Fetters et al. in refs. [144, 161]. Despite these estimations used for M_e though, the results describing which mass fractions to expect beaded fiber and non-beaded fiber formation in Fig. 4.17 are in close agreement with the experimental electrospinning results seen for these PVP molar masses in ethanol. Just like the issue with polystyrene above though, the affects of humidity, much less the affect of core filling for the coaxial fiber spinning case cannot be predicted using this plot and molar mass data alone. As we've seen from my results in ref. [70], and in sec. 4.3.2 above, electrospinning PVP with LC in the cores can result in beaded fibers at both low and high

[¶]Apparently there are many reports suggesting that attempting to analyze PVP in its melt form (without solvent) for getting an experimental M_e value is very difficult as it quickly degrades at temperatures past its glass transition and has poor flow properties[123, 159].

ambient humidity. At low humidity beaded segments can form when the core fluid is quite high, and the sheath bulges in an attempt to accommodate the incoming mass flow, while at high humidity the beads occur as a result of condensing water vapor mixing with evaporating ethanol. Experimentally, we've seen that for a 12.5% mass fraction of roughly 1,000,000 g/mol PVP in ethanol, with no other additives added, with a core LC flow rate that is smaller than that of the sheath, if the humidity is higher than 30%, beaded fibers will reproducibly and consistently form, regardless of the other parameters used.

Ultimately, while the discussion surrounding the influence of polymer molar mass on chain entanglements gives us a rough guide of what solution mass fractions can likely result in filaments and beads electrospun or sprayed, it is clear that for coaxially electrospinning these same polymer solutions with other fluids, the results will quickly deviate from the curves plotted above. As there will be an appreciable difference between the fraction of sheath solution that will take up entirety of the jet in a coaxial case versus the non-coaxial case, this will evidently reduce whatever entanglements are forming in the polymer segment to begin with. Additionally, the interface between the drying polymer sheath alongside the core fluid may also contribute to differences in the rate of solvent evaporation, particularly if the core may be partially soluble with the solvent that the polymer was dispersed in. Coupled with possibility that the ambient humidity during electrospinning may increase, and that solvent evaporation from the jet may be hindered by the surrounding water vapor, we can imagine that environment really can contribute to the quality of the core-sheath fibers produced.

4.4 When the ambient humidity matters

4.4.1 Does humidity alter the electrospinning of pure PVP?

In considering the impact that humid environments can have on a drying solution jet during electrospinning, the heavily cited study by De Vrieze et al. [162] will be referred to for specifically addressing the morphology of PVP fibers electrospun from ethanol in water vapor saturated air at 23 °C. In the environments with humidity ranging from 20% to 45%, a 10% (by mass) solution of PVP in ethanol was successful in producing uniform non-beaded fibers (nozzle-to-grounded-collector distance: 12 cm, potential: 10kV). However, at 60% relative humidity (RH) the PVP fiber mat produced contained only fused and flattened filaments. De Vrieze et al. reasoned that this dramatic morphological change was due to the fact that "the PVP-ethanol solution absorbs ambient water during electrospinning [and]...at higher humidity the absorption of water does not allow the drying process [to complete] during the time of flight of the polymer solution jet" [162]. Thus, this results in the deposition of a "fused-fiber" polymer film on the collector. While at first the reasoning by De Vrieze et al. seems to make sense if one considers that water and ethanol are entirely miscible and that PVP is a hygroscopic polymer, there are some aspects particular to the evaporation of ethanol in humid atmospheres and the jet drying process in electrospinning that they may have overlooked in their explanation.

Before moving to those points, however, first consider the results shown in Fig.4.18 showing the electrospun pure PVP fibers obtained while electrospinning in environments with a relative humidity between 27% and 65%. Probably the most straightforward observation is that unlike De Vrieze et al. neither beaded, nor meshed/"fused" fiber mats wre obtained when these

PVP-ethanol solutions were spun in the presence of excess moisture up to 65%.[‖] Interestingly, while the PVP fibers spun at 55% RH on glass appeared as though they might have gotten slightly meshed, SEM imaging of the same area revealed that although the fibers do appear to be flattened, the individual filaments in the mat were still able to stack over each another without fusing with the fibers below. The fibers spun at 65% RH were collected in a free-hanging manner and not on a substrate. These began showing signs of fiber webbing occurring. However, this level of meshing compared to the fused film De Vrieze et al. produced at 60% RH was significantly lower.

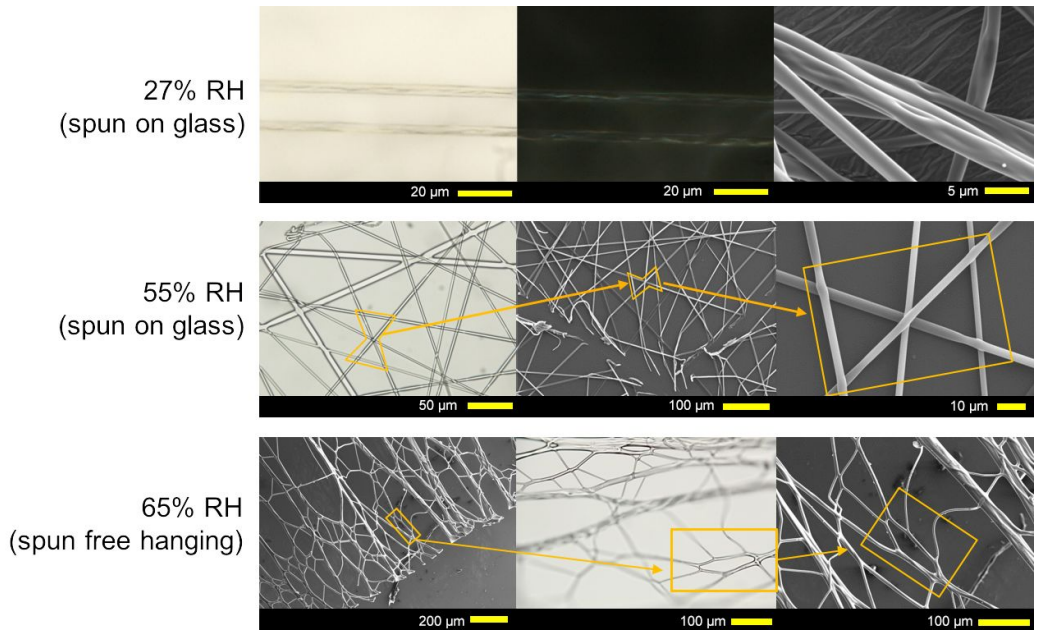

Fig. 4.18 – Pure PVP fibers electrospun from solutions containing 12.5% PVP (molar mass ~1,300,000 g/mol) in anhydrous ethanol in environments with varying humidity (RH) levels. Similar results are obtained using PVP dissolved in slightly diluted ethanol (e.g. 96 vol.%). The fibers produced in 27% RH and 55% RH conditions were spun onto glass slide substrates, while the fibers produced in 65% RH conditions were spun onto a wire frame without a surface (so the fibers could freely hang). Images shown are from either the same, or similar, areas seen through the POM and SEM.

In fact, it is only when I increase the humidity in the spinning box to about 70% when a higher level of fiber meshing occurs to the point where the fibers appear indifferentiable. The point in making this comparison with De Vrieze et al.'s study is to show that just because one is electrospinning a certain polymer solution in the presence of increased relative humidity, it does not mean that fiber production will automatically fail due to the polymer solvent's miscibility with the water vapor in the air. Slight changes in collector type used and polymer molar mass can make major differences without having to change the chemical functionality in the solution by adding salts or other compounds.

Finally, the last two aspects I think De Vrieze et al. overlooked relate to this issue of water-ethanol miscibility in humid environments, and the drying process of the jets during electrospinning. Although they are correct in stating that the vapor pressure of water increases

[‖] I had used anhydrous ethanol for the PVP solution spun to make the fibers shown in Fig.4.18, however in repeating the experiments using slightly diluted ethanol (96% by volume) I also obtained fibers that looked similar.

in the atmosphere as the relative humidity increases, when it comes to ethanol evaporation in humid environments, we have to consider what happens in non-humid, normal room temperature environments. Recall that the mixing of water and ethanol at room temperature is highly exothermic and is not volume-additive [163]. Adding 1 volume unit of ethanol to 1 volume unit of water will not exactly give 2 volume units of an ethanol-water mixture, it gives a slightly less volume (i.e. ~1.9 volume units) accompanied by a measurable increase in the temperature of the mixture with noticeable bubble formation. While the thermodynamical reasons for this difference in volume will not be discussed,** it is relevant in mentioning because it shows that the interaction of ethanol and water is already quite complex at the molecular level without having the added variable of ambient humidity to contend with.

In comparing the change in surface area (mm^2) of several alcohol droplets placed in environments with humidity ranging from 0% to 100%, Law et al. [165] saw that at first, the rate of alcohol evaporation in the humid environments above 72% actually increases for a short time before finally slowing down. The droplet diameters of the alcohols observed ranged from 1.00 mm to 1.8 mm, and the rates of "normal" evaporation (defined in terms of surface decrease per time) for droplets of methanol and ethanol in atmospheres with 0% RH were .012 mm^2/s and ~0.006 mm^2/s, respectively. In an environment containing 72.5% RH the rate at which the ethanol droplet evaporates remains higher, roughly 0.008 mm^2/s, within the first 100 seconds before tapering below 0.006 mm^2/s. If the surrounding air is 100% saturated with water vapor, then the evaporation rate increases still, twice as much in fact, then tapering to 0.007 $mm^2/$ within the first 100 seconds. This trend was extracted originally from Fig. 9 in [165] using a third party plot data extractor.††

For the case of methanol, the rate of evaporation is only faster for the first 30 seconds or so in 100% RH, the fastest rate being 0.02 mm^2/s. So contrary to the belief that ethanol should evaporate slower in humid environments from the initial exposure, there is a small time window of about 2 minutes in humid atmospheres where the rate of evaporation is actually accelerated. This is because as excess water vapor enters the surface of the alcohol drop the mixing causes exothermic heat to be released. This heat released aids in the evaporation of more ethanol content until the droplet becomes saturated with water [165]. Using equations of heat and mass transfer adopted from known equations for droplet vaporization and combustion, Law et al. also modeled their experimental data acquired for the methanol droplet evaporation to have decent qualitative accuracy in the end (quantitatively, however, their model did suffer in showing slightly slower evaporation rates).

Moving back to electrospinning PVP-ethanol solutions now, since De Vrieze et al. saw their fibers merge into a wet film after spinning at 60% RH, they probably assumed that the reason why was because ethanol could not evaporate from the solution jet and that the film formed probably contained the ethanol left behind. However, given Law et al.'s findings, it is more likely that the ethanol did actually entirely evaporate, and the fused-fiber film was wet from excess water absorbed during exchange of ethanol and water occurring at the jetting stage. De Vrieze et

**Studies have postulated that the heat released from water and ethanol mixing has to do with the flexibility of the water hydrogens to form two types of H-bonds differing in energy that help weaken adjacent water bonds leading to a rearrangement of the number of ethanol molecules that can be accommodated in between water molecules [163, 164].

††The program used was: WebPlotDigitizer, found at https://automeris.io/WebPlotDigitizer/ - free-ware and guides through the process of data point extraction from image files containing x-y, ternary and other types of plots.

al. also did say that the mats were spun for 2 minutes each as well, and that also happens to be roughly the same amount of time at which Law et al.'s ethanol droplets were seen to evaporate faster than if they were in non-humid environments. In this sense, this changes the proposed model for thinking about how humidity could impact fiber formation during electrospinning.

For the case of spinning with a water miscible solvent and a water miscible polymer, the evaporation of the solvent does occur but the water may simultaneously replace it and cause the drying polymer to re-swell before it lands on the collector. The entire jet cools down as it dries, so perhaps the key then to getting fiber formation for this case is rather to electrospin a high molar mass of polymer for a shorter period of time so as to be able to collect the initial filaments that form before the solvent exchange with condensing water finishes.

Again while the PVP fibers I produced in Fig. 4.18 were from a solution with a higher polymer molar mass these fibers were collected on average in the first 10-20 seconds of applying the 9kV potential. A quick look at the FT-IR data acquired for pure PVP and coaxial 5CB-PVP fiber mats in Fig. 4.19 shows that the hydroxide stretching group on the left is due to water, not the presence of ethanol. In fact, producing PVP and 5CB-PVP fiber mats purely devoid of some water present is nearly impossible, even if the fibers are successful in solidifying uniformly without fusing.

Last, for the case of coaxial 5CB-PVP fiber formation, while spinning in an environment with relative humidity above 30% beaded fibers were always produced.[‡‡] If the humidity was increased further past 50%, while keeping all other parameters constant, no fibers formed at all. At this point, the Taylor cone constantly drips unless the 5CB is replaced with another LC or removed entirely (shown in Fig. 4.20). Reasoning out why this occurred actually became the focus of ch. 5. However, the last two sections below will briefly describe the extent of the effects ambient water vapor had on coaxial fiber and Taylor cone formation.

4.4.2 Ethanol-water content of 5CB-PVP coaxial fibers

Although it is possible for pure PVP fibers to be electrospun from ethanol without forming beaded sections, even when spun in humid environments, FTIR spectroscopy data indicates that residual water (not ethanol) is the solvent left behind when pure PVP fibers and 5CB-PVP coaxial fibers are spun in high humidity. In Fig. 4.19(a) the absorbance peaks (in arbitrary units) of the PVP-ethanol polymer solution (green curve) are plotted against the wavenumber frequency (in cm^{-1}) and stacked alongside the spectra obtained for: deionized water (gray curve), pure PVP fibers electrospun without an LC core (orange curve), coaxial 5CB-PVP fibers electrospun at low humidity without being dried afterwards (blue curve), coaxial 5CB-PVP fibers spun at low humidity with drying (yellow curve), and coaxial 5CB-PVP fibers spun at 48% RH without being dried (purple curve). In Fig. 4.19(b) the corresponding spectra of pure 5CB (red curve), anhydrous ethanol (pure EtOH - yellow curve), and the 12.5% (by mass) PVP-ethanol polymer solution prior to spinning the fibers analyzed in plot (a) are shown for comparison.

[‡‡] All other parameters are kept the same, i.e. LC : Polymer flow rates - 0.55 ml/hr : 0.9-1.0 ml/hr; applied voltage nozzle - 9 kV; temperature - 24$^{\circ}C$; see sec. 3.1.1 for further solution details.

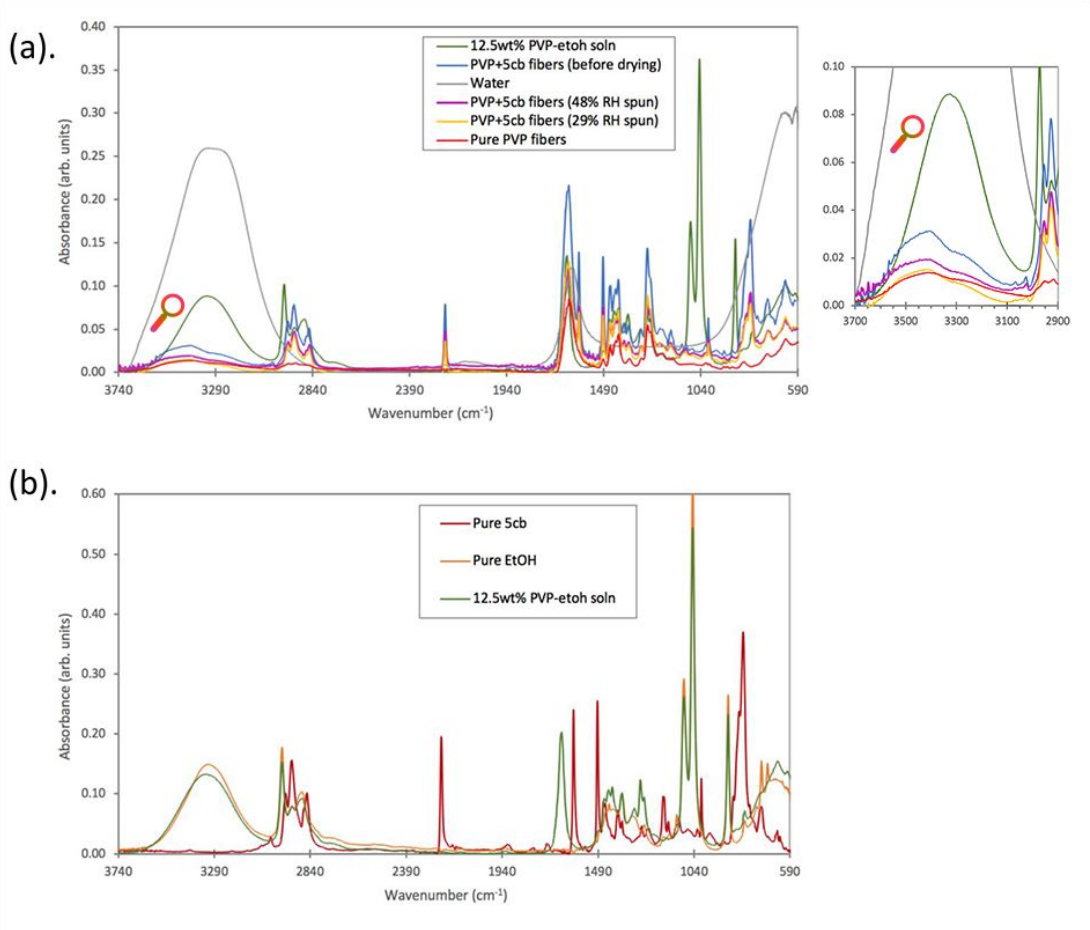

Fig. 4.19 – FT-IR spectra of pure PVP fibers, and 5CB-PVP fibers spun in environments with different relative humidity (RH) compared to the spectra of pure 5CB, anhydrous ethanol (Pure EtOH), deionized water, and the 12.5% (by mass) PVP-ethanol polymer solution. A close-up of the region showing the curves at 3290 cm^{-1} is shown on the right side.

The major areas of interest in Fig. 4.19(a-b) are: the broad peak at roughly 3290 cm^{-1}, the sharp peak just to the right of 2390 cm^{-1} (at 2220 cm^{-1}), the sharp peaks directly to the left of 1490 cm^{-1} (from 1610 cm^{-1} to 1664 cm^{-1}), and finally the sharp peaks at 1040 cm^{-1}. Looking at the spectra of the the liquids first before moving on to the fibers, in plot (b) that the PVP-ethanol solution (green curve) I used for electrospinning shares the similar molecular vibrations as the pure anhydrous ethanol (yellow curve). The two most defining peaks for all primary carbon alcohols are the broad absorbance peak around the 3000 cm^{-1} - 3500 cm^{-1} region, and the sharp split peak near the 1040 cm^{-1} - 1050 cm^{-1}. The former is due to hydroxide group (R-OH) stretching vibrations, further enhanced by hydrogen bonds within the liquid, while the latter peaks are caused by the asymmetric stretching of carbon-carbon-oxygen (C-C-O) bonds [166, 167].

While both of these peaks overlap one another almost exactly in plot (b) for pure ethanol and the PVP-ethanol solution, the one peak between these two fluids that is the outlier is the one at roughly 1660 cm^{-1} present in the PVP-ethanol solution (green curve), and to the left of the 1490 cm^{-1} region. This sharp peak is only shared by water (the spectra of which I also experimentally obtained and plot as the gray curve above in group (a)). In fact it is this peak,

which corresponds to the two oxygens bending in a scissor-type motion in a water molecule, along with the broad hydroxide stretch near 3000-3500 cm^{-1} that all alcohols share, are the two most defining vibrations observed for water. Water was already present in the PVP-ethanol solution even before I had started electrospinning with it.

At the moment that the FT-IR spectra was acquired, the PVP-ethanol solution had been freshly made using anhydrous ethanol. It is doubtful that the small amount of water which had entered was due to condensation from the air, otherwise, the same peak within the anhydrous ethanol IR spectra would have developed. Rather something which I, and probably others who have performed electrospinning experiments with PVP, had overlooked is that PVP readily absorbs moisture from the atmosphere with prolonged exposure. Actually, depending on its molar mass it can absorb up to 40% [94, 123].

A study by Bhattacharya et al. [168], where thin films of PVP containing tracer particles were exposed to increasing ambient humidity for 30 minutes, showed that the plasticization of the PVP films were enough, to allow for significant particle movement (both rotational and translational) throughout the polymer network. Granted, though this study had used PVP with a molar mass only 4% of the one I had used for my solutions (40,000 g/mol vs. 1,000,000 g/mol), it nevertheless presented evidence that moisture absorption is relevant for PVP based materials. To avoid water from entering any future PVP-alcohol solutions made for electrospinning, it would probably best to store the PVP pellets in desiccators flushed with nitrogen before use.

However, moving on to Fig. 4.19(a) comparing the FT-IR spectra of the pure PVP and coaxial 5CB-PVP fibers spun, it is rather noticeable that all of the fiber samples, regardless if they were originally spun in the presence of low RH (29%) or slightly higher RH (48%), dried in the oven (~60 °C) for a few minutes after spinning or not, contained at least some amount of water in the end (seen again by the presence of both the hydroxide stretch, and the oxygen-hydrogen scissor peaks). Conversely, what was common in all the fiber spectra in (a) this time is that the ethanol was not present. Now it is the asymmetric C-C-O stretch at 1040 cm^{-1} (green curve) that is the outlier.

As an added bonus we can also tell from the IR spectra that for the coaxial fibers 5CB was also successfully encapsulated. Pure 5CB (red curve,(b)), apart from showing the broad peaks in the 2840 cm^{-1} region (that define the saturated and unsaturated carbons in the alkyl chain and the aromatic rings) shows the very sharp peak at roughly 2220 cm^{-1} (just to the right of 2390 cm^{-1} indicated in the x-axis). This peak in the middle of the spectra defines the asymmetric carbon-nitrogen triple bond (the nitrile group in 5CB). Note that if the carbon triple bond would have either been di-substituted symmetrically on both sides it would not have had an absorption peak present. Likewise, if the triple bond was not connected at the terminal end of the molecule its peak intensity would have decreased substantially [169, 170]. Nevertheless, neither PVP, water, nor ethanol on their own have this feature, and yet it is present for all of the spectra for the coaxial fibers containing 5CB in (a).

4.4.3 Other nematics tolerate humidity while coaxially electrospun, not 5CB

So how does the water present in the electrospun coaxial PVP fibers affect the encapsulated 5CB? While the low humidity (below 30%) does not appear to have any visible consequences when encapsulating 5CB in the PVP solution jet, and the fibers that result do not appear to be fused or beaded despite containing small amounts of water (discussed above), once the humidity

rises past 30% obtaining beaded fibers becomes unavoidable. Additionally, at an even higher vapor content (above 50%) the act of coaxially electrospinning PVP-ethanol solutions with 5CB becomes impossible.

From the snapshots showing the progression of the Taylor cone within the first 33 seconds before and immediately after the potential is applied to the co-flowing solutions, Fig. 4.20(b), we see that the cone attempts to form but breaks down into several jets. Rather than forming a constant and symmetrically defined cone (as the pure PVP jet does, Fig. 4.20(a)), the appearance of the this gel-like "blob" of 5CB-PVP-ethanol hanging at the nozzle with multiple jets emerging from it is similar to the coaxial jet when the 5CB flow rate, and the potential are both very high (Fig. 4.4).

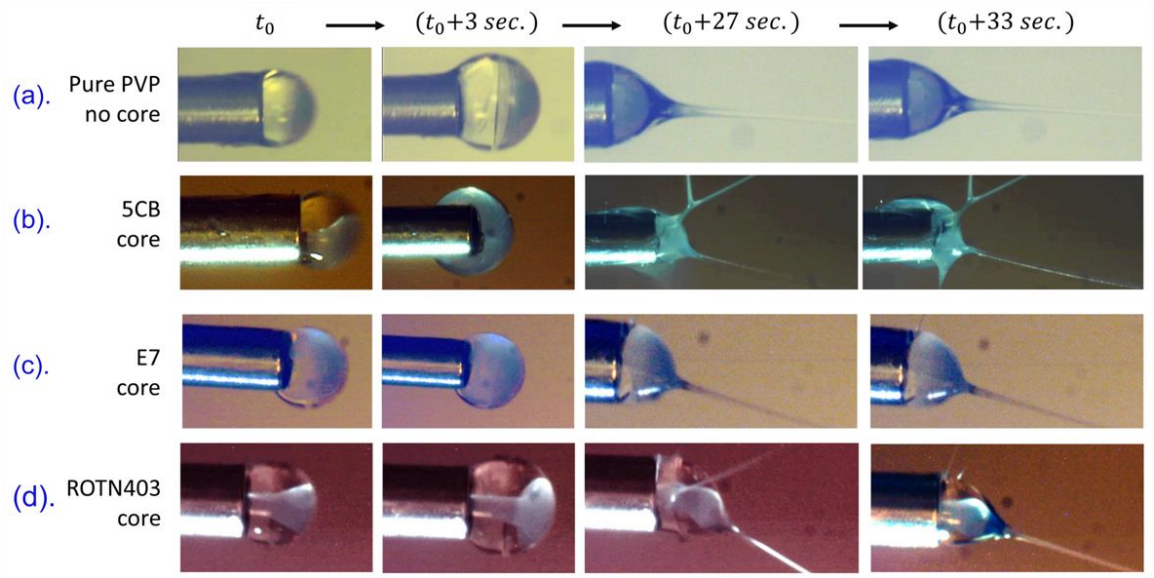

Fig. 4.20 – Screen-shots showing the first 33 seconds of Taylor cone evolution observed while attempting to electrospin pure PVP fibers, and PVP fibers with a 5CB core, an E7 core, and ROTN403 core in an environment with relative humidity ~63%. The LCs are shown as the bright fluids within the clear polymer solution. None of these images were artificially colored (see sec. 3.1.3 for filming details). The variable t_0 designates the time point at which a drop was seen to emerge from the coaxial needle containing the polymer solution, or polymer solution and LC. It took about 3 seconds before each drop could fall. However, the droplet containing 5CB slightly wets the outer edge of the capillary more noticeably than the other LC filled droplets just before falling. The images until 3 seconds were just before the voltage was applied to start the electrospinning process and before Taylor cone formation. The outer diameter of the needle tip is approximately 1.1 mm.

The major difference between the situation discussed in sec. 4.2.2 and here, however, is that even altering either the voltage or flow rate does not make a visible difference is stabilizing the cone's geometry. For instance, lowering the potential in order to minimize the accumulation of excess charges in the solution so that the jet will not branch out in multiple directions only leads to excessive dripping. Decreasing the content of 5CB co-flowing alongside the PVP solution, in turn, helps to prevent the dripping, but in the end if the 5CB content is too low poor or no filling is present it defeats the whole purpose of spinning coaxial 5CB-PVP fibers in the first place.

As shown in the first crossed-polarizer POM image in Fig. 4.21 5CB-PVP fiber formation was not possible from the distorted Taylor cone shape shown in Fig. 4.20(b). Although in the

crossed-polarizer image it looks like filaments were produced, as was discussed in sec. 4.1.4, these are merely ribbons of gelled polymer that managed to land on the grounded collector surface with 5CB coating them. As water is also a solvent for PVP, and not for 5CB (in fact 5CB adopts a planar alignment against water), it is more than likely that while electrospinning at this humidity level, water rapidly condensed into the PVP-ethanol drop. Recall, that the polymer solution may have already had some residual water to begin with as was seen in the FT-IR spectra above, and so, with the contribution of elevated humidity, its concentration further increased.

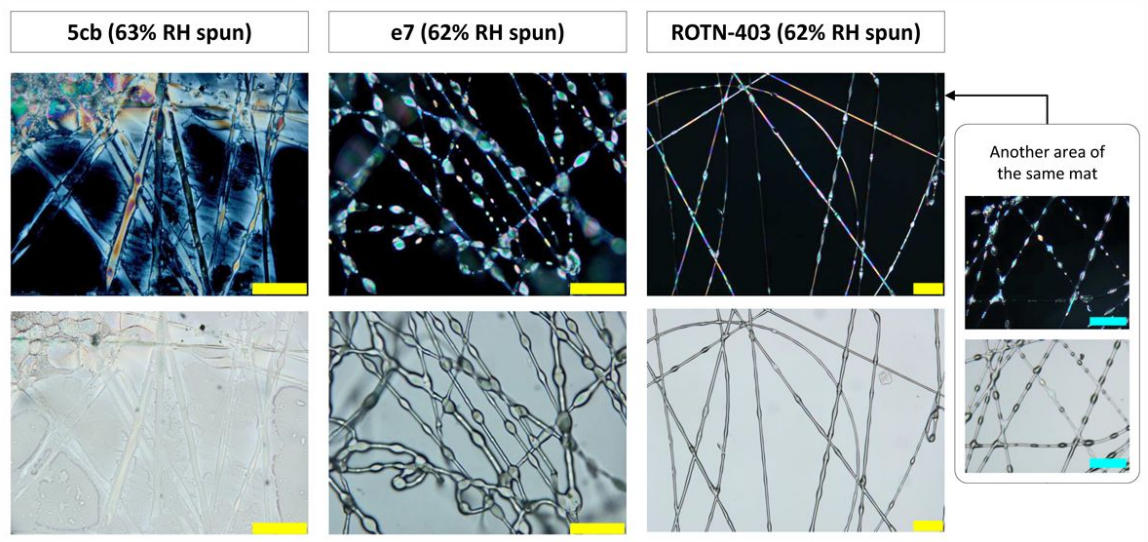

Fig. 4.21 – POM images taken in plane polarized light (bottom row), and through crossed polarizers (top row) of coaxial LC-PVP fibers electrospun in environments with 62% - 63% RH. The LCs used as core fluids for encapsulation for each sample were different but all three shared a nematic phase - 5CB (pure compound), E7 (compound mixture), ROTN-403 (compound mixture). Solid coaxial fiber formation was not possible for 5CB at this RH, while beaded fibers were instead formed when using E7 and ROTN-403 as the core fluids. For ROTN-403 a variety of fibers with small beads (less than 5 μm wide), no beads, and large beads were produced. The yellow and blue scale bars are 50 μm, and 100 μm, respectively.

The increased composition of water in the ethanol-PVP solution will not alter the solubility of the PVP, but instead will alter the solubility of 5CB. This change can be qualitatively seen if, instead of co-flowing 5CB with the PVP-solution, other thermotropic nematic liquid crystals like E7 and ROTN-403 are used as core fluids. From the dripping observed at t_0 seconds to the moment at which the 10 kV potential is applied to the nozzle, if the spread of the birefringent LCs within the clear polymer solution drops and jet are compared, 5CB fills the entirety of the volume that the polymer solution takes up (Fig. 4.20b-d). The LCs ROTN-403 and E7 are both thermotropic nematic mixtures. This means that they are each comprised of different compositions of biphenyl and other molecules that contribute to forming the nematic LC phase at room temperature. They are helpful in using as substitutes for 5CB because not only are they probably comprised of 5CB (E7 being comprised of roughly 50% 5CB), they are also inert and share very similar flow properties as 5CB at room temperature.

It was quite unexpected, however, to see in both Fig. 4.20(c-d), and in Fig. 4.21 that at even at high humidity coaxial nematic LC fibers could form from both E7 and ROTN-403. Moreover,

for ROTN-403 the initial droplets containing both the LC with polymer solution always remained clearly divided, and the coaxial Taylor cone formed for ROTN-403 remained quite stable without showing signs of fluctuation or distortion. Although beaded fibers were still formed in the end, the the beaded filaments were for the most part filled and solid. The difference in fiber and Taylor cone formation between 5CB and ROTN-403 are stark contrasts with E7 being the intermediate between the two.

Seeing these differences already just in the initial stages of electrospinning using 5CB, E7 and ROTN-403 imply two important aspects regarding coaxial LC fiber formation through electrospinning. The first is that even though the LC core may appear to be immiscible with the polymer solution's solvent, due to the former being an oil-like alkane, with 5CB this is not the case. Second, in particular for 5CB, there has to be some non-trivial interaction occurring with the miscibility of ethanol, water, and 5CB in these solutions that also affects the Taylor cone geometry, which does not occur when other similar biphenyl LCs are used. Since the 5CB-ethanol-water miscibility becomes relevant to influencing stability of the 5CB-PVP fibers, even before they can be used for organic compound gas sensing, this became focus of my next investigation.

5

LC core & polymer solvent miscibility: Unexpected phase separation

5.1 Results overview & recap

The previous chapter ended with the conclusion that if the parameters are well tuned, then one should be able to coaxially electropsin either beaded or non-beaded "ideal" 5CB-core PVP-sheath fibers. Fibers produced from stable Taylor cone jets, which do not mesh or leak upon landing, are fully solidified, and which have a high degree of encapsulated fluid. Furthermore, the ideal coaxial fibers do not have small aspect ratios, instead, their lengths should roughly span the distances of the substrates used to collect them (these can easily go up to several centimeters) without showing breakage.

The last point in ch. 4 was that the ambient humidity actually does play a crucial role in determining if ideal coaxial 5CB-core PVP-sheath fiber formation is possible during electrospinning, despite the fact that even if PVP-ethanol solutions are spun on their own (in environments with up to 65% RH) ideal fibers are produced without showing meshing, swelling, or Taylor cone break-down. This is unlike the results seen for coaxial systems containing 5CB in particular.

Other thermotropic LCs (E7, ROTN-403) electrospun with PVP and ethanol are also not miscible with water either, so initially it was expected that high humidity would not influence the core filling during jet formation. However, there are significant differences in whether stable Taylor cones and fibers are formed depending on the LC used. Though E7 and ROTN-403 are mixtures containing cyanobiphenyl functional groups like 5CB, both of these nematic mixtures still yield fibers (although beaded) with the same PVP-ethanol solution used, and show stable Taylor cones. With 5CB, a stable Taylor cone and uniform fiber formation are nearly impossible to obtain. Moreover, 5CB strongly wets the coaxial needle when 5CB flows in contrast to all the other reference cases.

Water condensation into a Taylor cone jet during electrospinning is something we should expect to happen if either the polymer or the solvents are also miscible with water. The important contribution from Law et al. [165] is that the exothermic mixing of ethanol with the condensed water vapor from a humid atmosphere plays a role in initially speeding up ethanol evaporation (contrary to intuition). Thus, electrospinning with LCs as core fluids is not a trivial process of merely finding components that immiscible with each other to co-flow.

This chapter presents miscibility observations and phase diagrams showing that there is a partial miscibility between 5CB and the ethanol used in the PVP sheath solution during coaxial electrospinning. This miscibility also becomes exacerbated when there is excess moisture in the air. Last, the impact that phase coexistence in these mixtures (5CB-ethanol, and 5CB-ethanol-water) can have during the coaxial electrospinning process is discussed since it alters fiber formation.

5.2 Considering the miscibility of three nematic LCs in ethanol

Although the densities of the pure nematic 5CB compound, and the two nematic mixtures E7 and ROTN-403, are very similar and close to 1.0 g/cm^3, their clearing temperatures are very different. While 5CB has a clearing point of 35.5°C, the mixture E7, which is roughly comprised of 50% 5CB, transitions from nematic to isotropic 58°C.* Finally, while few literature data exist on the clearing temperature for ROTN-403, as it is no longer commercially synthesized, its clearing point roughly occurs at 81.5°C. Previous theses using this LC have also reported this value as well [97, 134].

In general, observing higher LC-phase-to-isotropic transition temperatures usually indicates that the compounds are larger in size. For instance it could mean that the compounds may have a higher number of heterocyclic rings, aromatic hydrocarbons, and/or aliphatic chains attached. The increased presence of these diverse functional groups can indicate that more energy, for the same volume of LC phase assembled, should be required to disrupt non-covalent molecular interactions (e.g. π-π stacking, hydrogen bonding) that help keep the phase together. This is why the mixtures, although containing similar biphenyl structures as the pure 5CB compound, need to be heated to much higher temperatures before their nematic phase can clear to the isotropic phase.

Furthermore, attempting to dissolve these compounds in certain polar protic solvents (like water or dilute acetic acid, for instance) at room temperature may also be difficult. Due to the complexity of the functional groups present the solvent chosen would have to promote a combination of both polar and non-polar interactions in order for the LCs to fully dissolve. This is why the situation can become more interesting when short aliphatic chain alcohols are introduced, as they can be considered to function as amphiphilic solvents to some extent. Their aliphatic end(e.g. methyl-, ethyl-, isopropyl- groups) can interact with the non-polar constituents of the LC compound, while the hydroxide end can interact with the more polar constituents (e.g. nitrile groups, esters, carboxylic acids, and even phenols). If we mix 5CB in anhydrous ethanol, these are the interactions that are likely to have taken place at near room temperature conditions (21°C - 23°C) since the liquid crystal appears to fully dissolve (Fig. 5.1). The aliphatic five-carbon chain end interacts with the ethyl- group, and the biphenyl-nitrile end with the hydroxide group. For the particular experiment shown in Fig. 5.1, the ratio of nematic liquid crystal to solvent used was 1:5 (200 μL : 1000 μL). For the other two biphenyl nematic mixtures at room temperature, E7 and ROTN-403, anhydrous ethanol does not appear to be non-polar enough to solubilize the nematic phase completely.

*Experimentally, since the clearing points of LC compounds will tend to drift depending on their purity, different samples of 5CB for example can show clearing points that range from 35.5°C - 35.8°C when measured using the DSC or the temperature control stage at very slow (0.1°/minute) heating rates. For example, the 5CB used for experiments throughout this thesis had a clearing point of 35.8°C, and was still considered to be pure. The clearing pattern observed through the microscope when the nematic-to-isotropic transition occurs can also indicate purity.

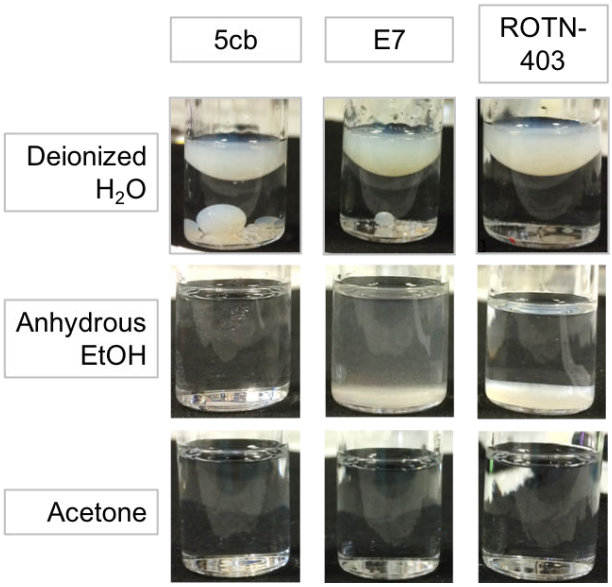

Solvent	Empirical Parameter of Solvent Polarity*
Water (H_2O)	1.000
Methanol (MeOH)	0.762
Ethanol (anhydrous EtOH)	0.654
Dimethylformamide (DMF)	0.386
Acetone	0.355

Fig. 5.1 – The miscibility and immiscibility of three types of room temperature nematic LCs (5CB, E7, ROTN-403) in three common solvents (deionized water, anhydrous ethanol, acetone). While 5CB is a single component room temperature nematic, E7 and ROTN-403 are both multi-component mixtures that are nematic. Approximately 200 μL of LC were added to 1 mL of solvent to observe the qualitative difference in solubilities. The results seen correlate to the semi-empirically derived normalized polarities for common solvents listed on the right side table (compiled from the solvatochromic data listed by Reichardt [171]). Here, water has the highest polarity (1.000), while acetone the lowest (0.355).

However, if we add the same quantities of E7 and ROTN-403 to a slightly more non-polar solvent than anhydrous ethanol, acetone for instance, as shown by the relative solvent polarity table (Fig. 5.1) we should expect that both nematic mixtures easily mix, and experimentally this is what does occur.[†] While it is difficult to compare the polarities of the three nematics, since two of them (E7 and ROTN-403) are mixtures, and one (E7) contains roughly 50% 5CB, it is safe to assume that both would require a solvent that is at least 30% less polar, with respect to water, to fully dissolve unlike 5CB which can dissolve in a solvent that is slightly more polar. In particular, the ease with which 5CB dissolves in anhydrous ethanol compared to the other two room temperature nematics in Fig. 5.1 is also apparent microscopically.

Fig. 5.2 demonstrates successive time lapse screen-shots of what happens when 5 μL of each nematic LC (5CB, E7, and ROTN-403) are exposed to a 5 μL drop of ethanol. The screen-shots are representative of how fast the ethanol droplet begins to dissolve the LC drop within the first 18 seconds of exposure. All images were taken in bright field mode with crossed polarizers to visualize the LC. In the first two rows containing 5CB, the ethanol drop immediately begins to dissolve the nematic phase 4 seconds after landing on the surface (holes in the nematic texture develop, along with the changing brightness) by 18 seconds.

[†]The normalized relative solvent polarity values in the table of Fig. 5.1 come from the appendices of Christian Reichardt's *Solvents and Solvent Effects in Organic Chemistry* [171].

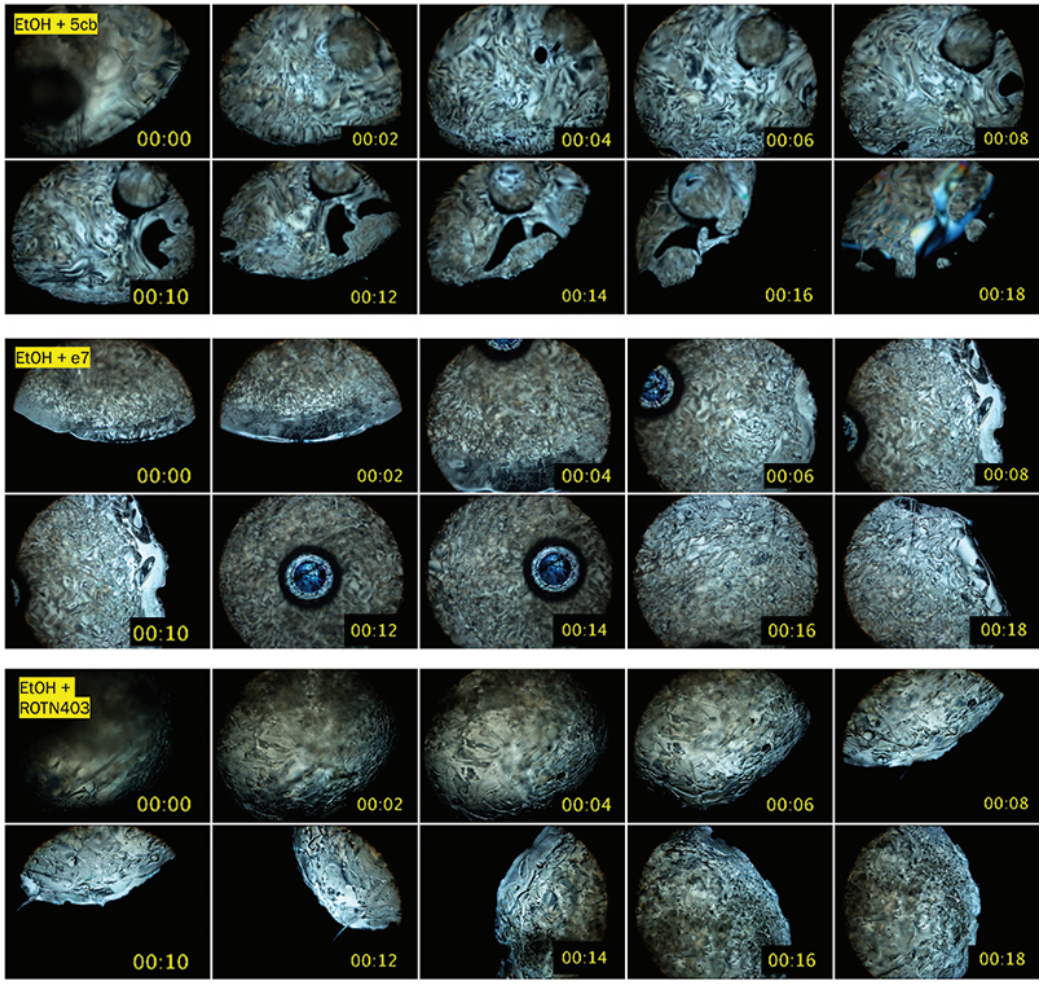

Fig. 5.2 – Micro droplet of ethanol added to 5CB, E7 and ROTN-403 viewed through crossed polarizers via POM. The screen-shots depict different areas of the LC micro droplets (center, and sides) for the first 18 seconds after adding the drop of ethanol. The ethanol droplet either dissolves the nematic phase of the LCs immediately (5CB), partially (E7), or has no effect (ROTN-403). For all three cases, the experiments went on longer than the 18 seconds recorded. This figure shows the immediate reaction of the LCs to very small volumes of ethanol.

Conversely, when the ethanol drop is added to E7, it appears to only just partially dissolve the nematic phase (as shown by the interference color change in and around the diameter of the drop at 6 seconds). Although for most of the time period recorded, the droplet looks suspended within the nematic phase without drastically clearing most of it, E7 still is comprised of roughly 50% 5CB, and this means that at least some portion of it should have been dissolved. There could be more dissolution occurring where the droplet is, seen at 12 and 14 seconds, compared to the rest of the nematic volume, and the phase separation visible was not as prominent as it was for the 5CB.

For the ROTN-403, the ethanol drop does not appear to cause any sort of phase separation to occur, as there was no visible decrease in the volume of the nematic phase observed. It seemed as though when dropped over the nematic area, the ethanol drop preferred to wet the glass around it, rather than LC itself. There was no part in the LC where the dissolution of the nematic texture was visible. Furthermore, using 96 vol.% ethanol, another common laboratory

solvent, gives the same patterns of dissolution observed microscopically for the same volumes of LC used. At this point, since similar observations as those in Fig. 5.2 were seen using the aqueous ethanol, it would be reasonable to assume that if we attempted to characterize the macroscopic miscibility of 5CB in this slightly diluted ethanol in the same manner as shown in Fig. 5.1, we'd probably obtain results similar to the anhydrous ethanol case. However, as will be seen in the following sections, this assumption was very wrong.

5.2.1 Isotropic-Isotropic phase coexistence emerges in 5CB-ethanol mixtures

A brief note on terminology before beginning the discussion on the types of phase separation seen in the various 5CB-ethanol mixtures. The term "aqueous ethanol" used throughout the rest of this chapter is defined as slightly diluted anhydrous ethanol having 4 vol.% water. Essentially, the "aqueous ethanol" used here is really just 96 vol.% ethanol. Thus, when referring to mixtures containing 5CB and 96 vol.% ethanol I will simply state, for example, that "the mixture has 10 mol.% 5CB in *aqueous* ethanol". I do this to easily differentiate between the mixtures containing anhydrous ethanol and those containing water without having to repeatedly state "96 vol.%" every time I refer to the latter.

In general, the study examining phase separation in aqueous ethanol and 5CB mixtures was motivated by following reasons: first, due to the impact of the humidity on coaxially electrospinning the 5CB-PVP-ethanol system, the contaminant that interests us the most for controlling is water, and second, many lab-grade ethanol bottles sold are also 96 vol.%, thus issue with working with these commercial bottles is that there is uncertainty regarding whether other contaminants in addition water are present. Figure 5.3 best illustrates the issue for 5CB that can arise when mixing it with aqueous ethanol. While the nematic mixtures ROTN-403, and E7 again show phase separation occurring between nematic and isotropic liquid phases, the mixture with 5CB now shows an unexpected split isotropic-isotropic coexistence. To my knowledge, this is the first time that the coexistence of two compositions of the same isotropic phase, for a mixture containing 5CB and aqueous ethanol, has been experimentally observed to occur at near room temperature conditions.

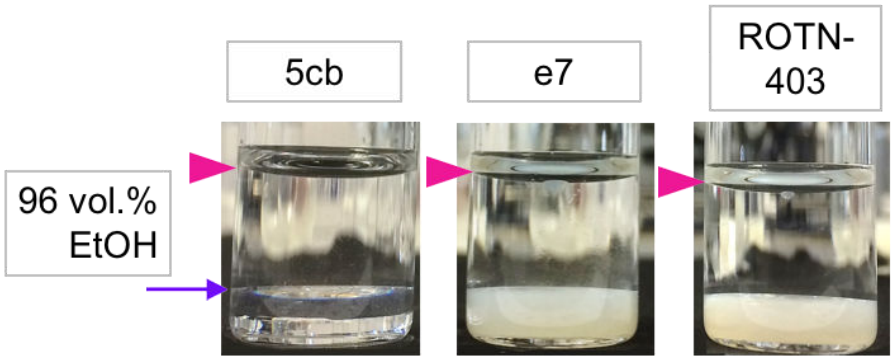

Fig. 5.3 – Isotropic-isotropic phase coexistence emerges for 5CB in aqueous ethanol at room temperature conditions (21°C - 25°C). The other biphenyl based LCs, E7 and ROTN-403, are show insolubility in this slightly water diluted solvent, and their nematic phases remain intact at the same temperature conditions. The pink arrows for each vial point to the level of meniscus of total solutions, while the purple arrow near the vial containing 5CB points to the meniscus of the second isotropic phase in coexistence with the first. The two isotropic phases in coexistence for the vial containing 5CB do not differ in optical or structural properties, they are actually the same isotropic phase but with differing concentrations of 5CB in each part. The ratio of LC to solvent used was the same as shown in Fig. 5.1, 1:5 (200 μL : 1000 μL), as were the types of vials (2mL capacity).

The upper and lower isotropic portions seen in the vial simply have different fractions of 5CB and solvent present, and at room temperature for several fractions of 5CB, the two do not homogeneously mix. Furthermore, adding 5CB to the mixture results in the bottom isotropic layer increasing in volume relative to the top layer (Fig. 5.4). The macroscopic mixtures showing various 5CB concentrations in each ethanol type are shown in Fig. 5.4(a-b). The vials in Fig. 5.4(a), containing mixtures of 5CB in anhydrous ethanol, never show isotropic-isotropic coexistence occurring at room temperature. Furthermore, it is only when the fractions of 5CB in the vial are above roughly 75 mol.% that the nematic phase actually nucleates completely (95 mol.%). For this series of mixtures, there are only the following phases/coexisting phases ever seen: the homogeneous isotropic, and the isotropic-nematic phases.

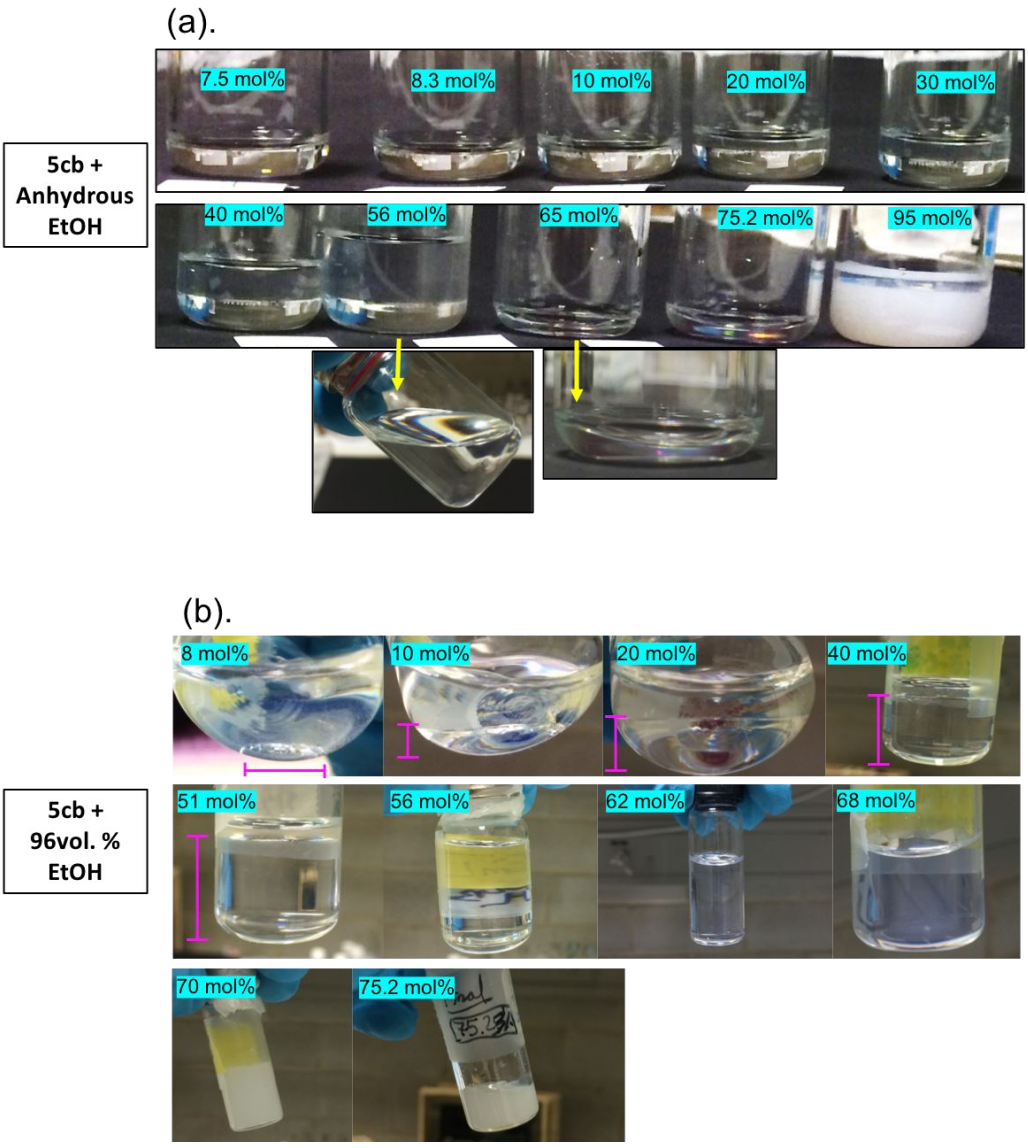

Fig. 5.4 – Bulk mixtures with fractions of 5CB ranging from 7.5 mol.% to 95 mol.% in anhydrous ethanol (a), and from 8 mol.% to 75 mol.% 5CB in aqueous ethanol. These mixtures shown were made volumetrically for visualizing the emergence of any coexisting phases macroscopically. The vials shown in (a) are 2 cm in diameter, while the narrower bottles in (b) are roughly 1.5 cm in diameter. The purple scale shown in (b) visually indicates the approximate size of the 2nd isotropic phase that formed relative to that of the rest of the mixture as the fraction of 5CB was increased from 8 mol.% to 51 mol.%. For vials containing $\geq$ 56 mol.% 5CB in (b) the separation between the two isotropic phases was no longer seen.

Conversely, the vials in Fig. 5.4(b), containing mixtures of 5CB in aqueous ethanol, continually show the isotropic-isotropic coexistence starting from about 8 mol.% 5CB to 51 mol.%, or so. At roughly 56 mol.% 5CB the mixture shows a single homogeneous, clear isotropic phase, while at higher fractions of 5CB (62 mol.% and 68 mol.%) the homogeneous isotropic phase begins to have a bluish tinge. For mixtures containing 5CB in aqueous ethanol, the nematic phase finishes nucleating completely at roughly 75 mol.% 5CB at room temperature.

Compared to the mixtures made with anhydrous ethanol in Fig. 5.4(a), the extra water in the aqueous ethanol mixtures definitely help in promoting the nematic phase to develop at considerably lower concentrations of 5CB present. To sum up the number of the phases/coexisting phases seen, we have four (the isotropic-isotropic phase, the homogeneous isotropic phase, the isotropic-nematic phase, and the homogeneous nematic phase).

Note that the mixtures in the vials shown in Fig. 5.4(a-b) were made volumetrically using micro-pipettes. To obtain these targeted concentrations the densities of 5CB, anhydrous ethanol, and the aqueous ethanol were approximated according to literature values for the temperature range between 21° and 23° (mimicking that of the laboratory in which they were prepared most closely). For 5CB, a value of 1.022 g/mL was used, approximated using the relevant 5CB density references mentioned in sec. 4.3.1, and the data from the plot in Deschamps et al. [172]. For the anhydrous and the 96 vol.% ethanol, the values 0.790 g/mL and 0.806 g/mL were used, respectively. Both were found from plotting the density versus temperature values in refs. [173] for the aqueous ethanol, and [174], for the anhydrous ethanol. The approximate mol.% fractions of 5CB in each of the vials were found using the densities of each component, the volumes successively added to the vials, and their molar masses,

Moreover, since it was later noticed that preparing the mixtures gravimetrically using the masses of the components instead (described in sec. 3.4.2) yielded more accurate values for the calculations of the mol.% fractions of 5CB, some of the mixtures were re-analyzed for heating and cooling experiments using both the POM and DSC. However, during the POM analysis of the coexisting phases, discussed further in sections 5.3 and 5.3.1, although the transition temperatures differed at times between the mixtures prepared gravimetrically versus those prepared volumetrically, the textures of the nucleating isotropic and nematic parts of the phases were exactly the same.

Finally, incrementally adding micro-liter amounts of water to the mixture containing 20 mol.% 5CB in anhydrous ethanol allowed me to relatively pinpoint where the start of the two phase isotropic-isotropic region should start at room temperature (Fig. 5.5). The only reason why I chose the 20 mol.% mixture for water addition is because the volume of this particular mixture already occupied a considerable portion of the vial, and so seeing the formation of the isotropic-isotropic meniscus line macroscopically would be simpler. In fact, it takes about 30 μL of deionized water for the split isotropic phase to form, and this corresponds to roughly 1.4 vol.% of water present. Adding higher volumes of water causes the overall mixture to start becoming cloudy, almost as if the nematic phase would start nucleating, but the isotropic-isotropic phase coexistence remains present.

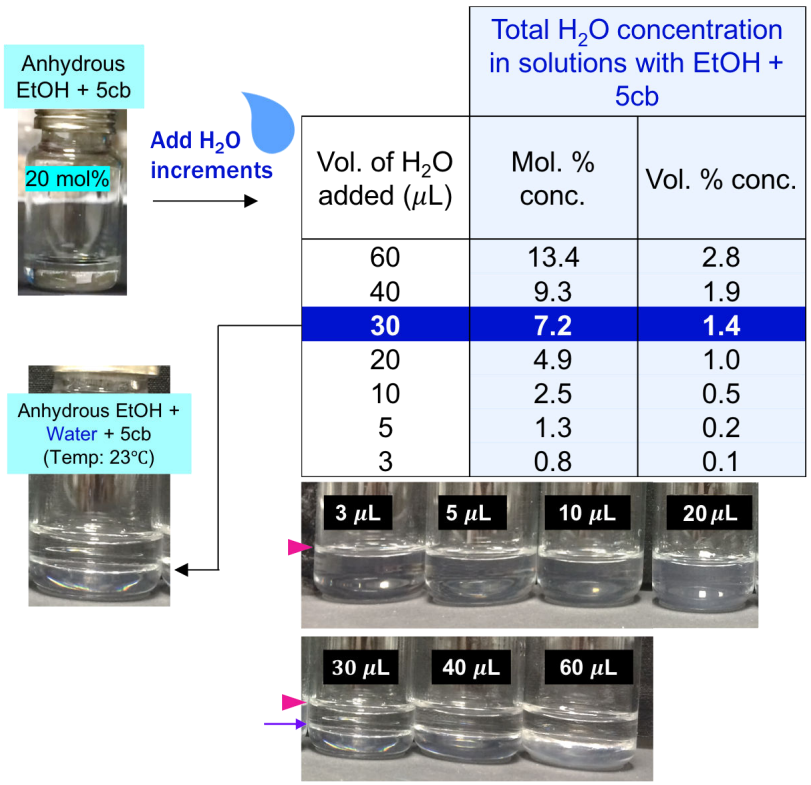

Vol. of H_2O added (μL)	Total H_2O concentration in solutions with EtOH + 5cb: Mol. % conc.	Vol. % conc.
60	13.4	2.8
40	9.3	1.9
30	**7.2**	**1.4**
20	4.9	1.0
10	2.5	0.5
5	1.3	0.2
3	0.8	0.1

Fig. 5.5 – Incremental volumes of water (ranging from 3 μL to 60 μL) were added to solutions containing 20 mol.% 5CB in anhydrous ethanol to reproduce the isotropic-isotropic phase separation seen at room temperature for the 5CB-aqueous ethanol mixtures. This phase separation occurred once 30 μL of water was added. The purple arrow shows the position of the second meniscus line. All other vials with the pink arrow show only one meniscus.

This makes sense because adding more water to the mixture should decrease the miscibility of ethanol with the 5CB present, effectively diluting the ethanol. In turn, this should cause the LC to prefer to aggregate with more of its own molecules and start to planarly anchor against the more water rich areas.

Have coexisting isotropic phases already been seen in 5CB mixtures?

Though there were two studies that previously reported similar results to this observation, they were not quite the same as the isotropic-isotropic coexistence seen here. The first, from Yamamoto and Tanaka [175] described the formation of a "transparent nematic" phase, which appeared isotropic during POM characterization, but actually proved not to be as disordered as they originally thought. In their case, another nematic-like phase in their mixtures containing 5CB, water, and surfactant formed thanks to the development of inverse micelles just below the isotropic-nematic transition temperatures of the mixtures. Since the inverse micelles did not aggregate below the isotropic-nematic transition temperature of 5CB, the mixture optically appeared transparent as if it had no order at all. However, DSC analysis on their mixtures indicated that there was some short range 5CB ordering between the inverse micelles - one that was not long-range enough to be called "nematic", but still very present despite macroscopically appearing transparently isotropic.

In our case, our mixtures do not have the possibility of forming inverse micelles, or micelles for that matter, as no surfactants were used at all in our mixtures. And though ethanol can be considered to be a "short amphiphile" from its alkyl non-polar chain and polar hydroxide groups, it will still dissolve the hydrodrophic end of the 5CB "oil" eliminating any chance of micelle formation. Rather, the isotropic-isotropic coexistence we see is due to a difference in fractions of water-ethanol solvent relative to 5CB present, and the interactions between the water and ethanol being slightly more preferred over those between the ethanol and 5CB.

The second study, from Serrano et al. [176], which just recently appeared in early 2018, described an isotropic-isotropic phase coexistence occurring between methanol and 5CB. While at first it would appear that Serrano et al. also saw a split isotropic coexistence in their mixtures, their study did not consider a variety of important factors that our work elucidated during this analysis. One main point they do not discuss is the possibility of water playing a role in causing that separation at room temperature. For ethanol, adding roughly 7 mol.% water to a mixture already containing roughly 20 mol% (Fig. 5.5) will play a significant role in preventing the homogeneous miscibility of 5CB in anhydrous ethanol at room temperature. This mol.% of water also physically corresponds to roughly 30 μL of water being added.

Though Serrano et al.'s study concerns 5CB-methanol mixtures, water can still readily dissolve in this alcohol (arguably much faster than even for ethanol as its polarity level is slightly higher) and the potential consequences this could have had on the nucleation of the 5CB nematic phase in their system was not discussed. Another factor we quickly noticed that Serrano et al. overlooked was the extent to which the super-cooling nature of 5CB contributes to the formation of phases which can be metastable at certain low temperatures and for certain fractions of 5CB present - again, another important point if trying to track the precipitation of the nematic phase from this solvent. Lastly, concentration gradients in our samples during analysis became important to consider as well. Though these former points will be discussed in the following sections describing the phase diagrams for our mixtures, first we should see the extent to which isotropic-isotropic coexistence is possible at room temperature for several fractions of 5CB in anhydrous and aqueous ethanol.

Before discussing a slice of the ternary phase diagram containing ethanol and water with 5CB, however, first the phase diagram of the 5CB in anhydrous ethanol is analyzed to get a starting idea of what the miscibility looks like before water is added.

5.3 The isobaric phase diagrams of 5CB-ethanol mixtures

5.3.1 Case 1: 5CB in anhydrous ethanol

To construct a phase diagram for 5CB in anhydrous ethanol[‡] new mixtures noting the actual masses for each component were re-created. Molar fractions were calculated using Eqn. 3.2 on pg. 45, rather than using a density calculation. Though the volume based mixtures (Fig.5.6a) had slightly different molar concentrations than the mass based mixtures (Fig.5.6b), the phase separation for both mixture sets followed the same qualitative trend.

These mass based mixtures were filled into capillaries placed in the temperature control stage, and were heated and cooled several times during POM observation to obtain transition

[‡]Merck #108543 - Ethanol for Molecular Biology (GC purity $\geq$ 99.8%)

temperatures for the first phase diagram (Fig. 5.9). Later, DSC experiments confirmed that the transition temperatures obtained through the POM studies were not quite as accurate (for reasons discussed on pg. 104). This led to the refinement of the first phase diagram proposed to another version that was later submitted for publication (discussed further on pg. 104) .

The first interesting aspect observed was that mixtures containing low fractions of 5CB ($<$ 50 mol.%), on heating, displayed transition temperatures to the fully isotropic phase that were below 0°C (Fig. 5.6b, on pg. 98). Additionally, these mixtures with low 5CB fractions also never showed purely nematic phases when cooled, instead they either showed coexisting nematic-isotropic ($<$ 9.9 mol.%), or nematic-isotropic-isotropic $\left[18.6 \text{ mol.\%}, 29 \text{ mol.\%}\right]$ phases. Mixtures containing higher mol.% fractions of 5CB had clearing points that steadily raised in temperature, with the highest one analyzed being 25°C for a mixture containing roughly 95 mol.% 5CB in anhydrous ethanol.

The second most striking aspect noticed was that, for the most part, both mixtures containing low and high fractions of 5CB, when cooled down to negative temperatures (roughly, -7°C and lower) would again nucleate isotropic droplets. But even in mixtures containing fractions of 5CB near 77 mol.% 5CB, for example, which also showed the presence of a full nematic state, at sub-zero temperatures would show isotropic droplets nucleating in front of a nematic background. In fact, the blue "bubble" symbol next to several 5CB fractions in both Fig. 5.6(a) and (b) indicates which mixtures had these isotropic droplet clusters emerge, with the droplets themselves usually being around 10μm in diameter (representative POM images below Fig. 5.6(a).

Although at first appearing like air bubbles, this idea was quickly ruled out when it was seen that they remained constant after cooling was stopped, and clustered in chains that moved with the background nematic π wall disclination lines. For the set of mixtures with 5CB fractions in the interval $\left[18.6 \text{ mol.\%}, 29 \text{ mol.\%}\right]$, these droplets would emerge in front of a background that already had an isotropic-nematic phase coexistence. Thus, for these mixtures we saw what appeared to be the coexistence of two isotropic phases plus a nematic phase; three phases in total at equilibrium! Making sense of this aspect in a phase diagram would be challenging for the reason that Gibbs phase rule does not allow it.

Finally, the third aspect observed gave a clue as to how the phase diagram should look. Particular to samples analyzed from mixtures containing roughly 20 mol.% 5CB, on cooling, spinodal decomposition between an isotropic-isotropic phase was observed to occur at roughly -4°C. This was also quite unexpected as it actually seemed to contradict the macroscopic observations of the bulk 5CB-anhydrous ethanol mixtures previously shown in Fig. 5.4(b). The appearance of an isotropic-isotropic coexistence, similar to the one visible in the bulk mixtures containing ethanol, 5CB, and water at room temperature, and at a depressed temperature, already became an indication that the phase coexistence between 5CB and pure ethanol would not be as straightforward as imagined. Moreover, it indicated that the miscibility gap region for the 5CB-anhydrous ethanol mixtures could actually be very similar to the one seen for the 5CB-aqueous ethanol mixtures. Thus, the spinodal decomposition of the two isotropic-isotropic states is further described in sec. 5.3.1.

(a).

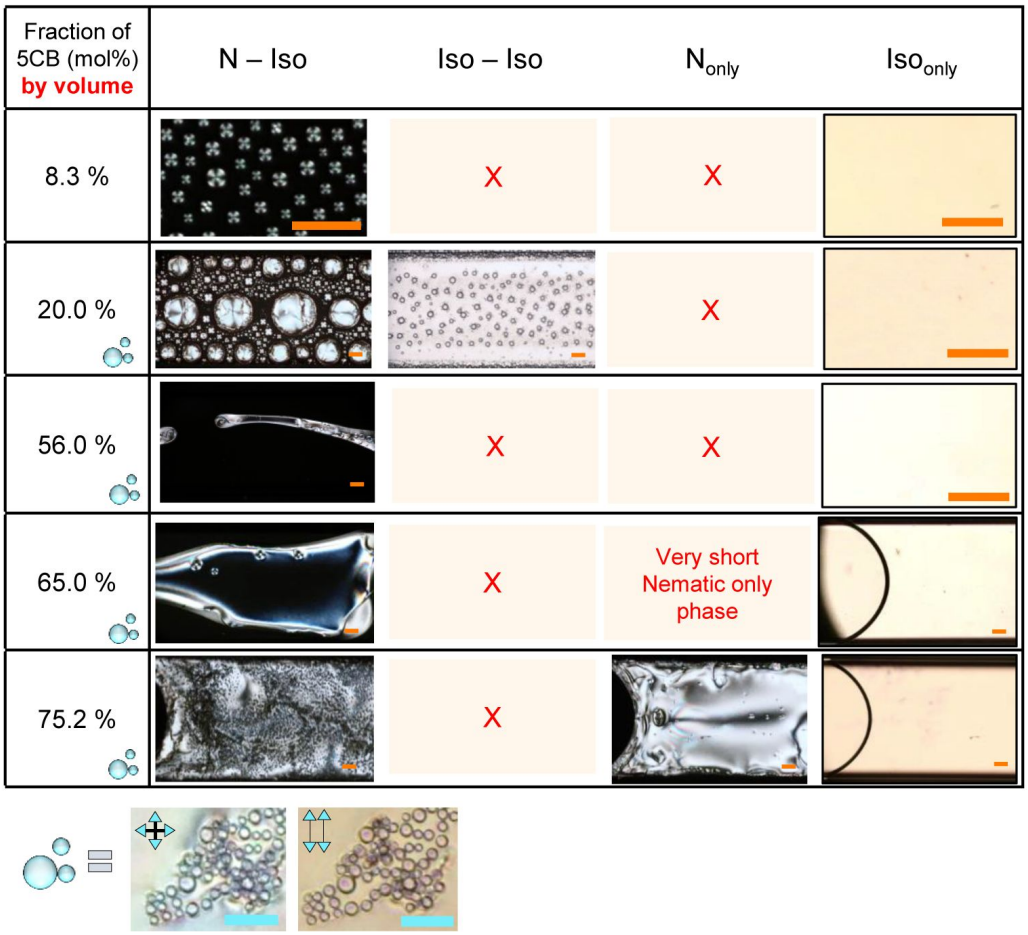

(b).

Fraction of 5CB (mol.%) by mass	N – Iso	Iso – Iso	N_{only}	Iso_{only}
9.9 %	✓	X	X	✓ -8 °C
18.6 %	✓ (also N-I-I)	✓	X	✓ ~ -3°C to 0°C
29.0 %	✓ (also N-I-I)	✓	X	✓ ~ -3°C to 0°C
49.8 %	✓	X	Short lived Nematic only phase	✓
77.2 %	✓	X	✓	✓
95.0 %	X	X	✓	✓

Fig. 5.6 – Four regimes of phase coexistence were observed microscopically with and without crossed polarizers for fractions of 5CB in anhydrous ethanol. Some also showed nucleation and growth of isotropic droplets below $0°C$, indicated by the drop icons. Scale bars: 150 μm (orange), 50 μm (blue)

So, taking what we knew of how several LC-ethanol mixtures underwent phase separation for a series of temperatures between roughly -20°C and 25°C and after an extensive literature search on what was theoretically known about how LCs mixed with isotropic solvents [177, 178], and other LCs [179, 180] *could* phase separate, and how mixtures containing LCs with polymer *do* phase separate in practice [181, 182], it was possible to realize that the regions of separation and co-existence we saw at these temperatures followed a partial miscibility curve for two fluids having a UCST (upper critical solution temperature). In particular, the theoretical phase diagram proposed by Araki and Tanaka for a thermotropic liquid crystalline compound mixed with a purely isotropic solvent should apply most closely to our case (Fig. 5.7).

There, we see the existence of 3 key regions: a UCST point (or *critical point*) above which the mixture's components are homogeneously and completely miscible (the "isotropic phase"), the existence of miscibility gap below the USCT where the "spinodal line of phase separation" is indicated within the binodal lines separating the isotropic state (isotropic-isotropic coexistence), and the diagonal region, on the right called "spinodal line of I-N transition", which overlaps with the miscibility gap curve and indicates the onset of the nematic phase.

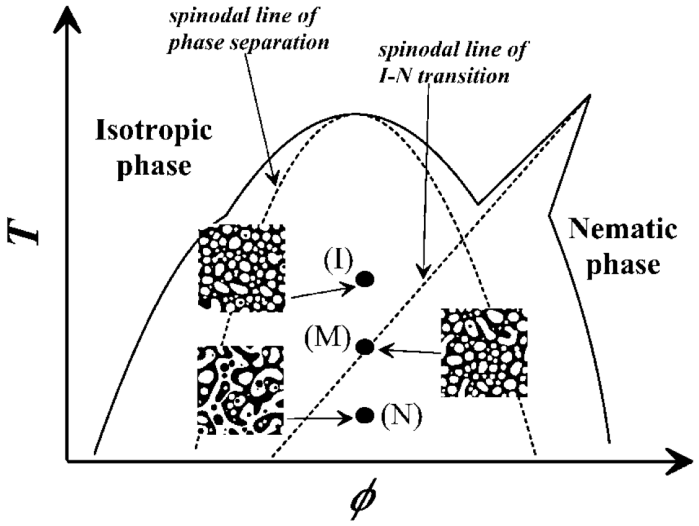

Fig. 5.7 – The theoretical isobaric (ϕ - component fraction vs temperature) binary liquid phase diagram proposed by Araki and Tanaka in [177] for a mixture containing LC and isotropic solvent. The regions (I), (M), (N) refer to the isotropic-isotropic phase, the metastable isotropic-isotropic-nematic state and the nematic-isotropic phase, respectively. This image was reprinted with permission obtained from ref. [177] (Fig.1). Copyright (2018) by the American Physical Society.

Normally, in either polymer-solvent or polymer-polymer mixtures, if a miscibility gap between the two occurs, one would get, at most, the presence of two stable regions. These regions are known the "one-phase" and "two-phase" regions, or, if we applied this to Araki's and Tanaka's curve in Fig. 5.7, it means just the region outside the USCT point (one-phase) and the region below the USCT point (two-phase) would have the possibility of existing at equilibrium for a certain temperature, component fraction, and pressure range. There is no incoming "nematic" right side. The special thing about Araki and Tanaka's theoretical binary liquid phase diagram, and similarly, our experiment based diagram, is that we do have the LC which at some temperature will eventually transition from an isotropic state to another stable phase (the nematic phase) when the fraction is high enough. In order to do that, since none

of the components are undergoing a chemical reaction, the right side of the diagram (where the "spinodal isotropic-nematic transition" line starts) will have to remove fractions of the isotropic-isotropic coexistence occurring on the left side.

How this separation proceeds is illustrated in the diagram shown in Fig. 5.8, which borrows Araki's and Tanaka's model to show an example of how the experimentally observed isotropic-isotropic coexistence seen in a 5CB-anhydrous ethanol mixture progresses to a nematic-isotropic one. For a mixture containing a 5CB fraction less than 50 mol.%, marked by the orange triangle, and at a temperature within the miscibility gap region, then two coexisting isotropic-isotropic phases develop either through nucleation and growth, or spinodal composition (a). This is because while the triangle point indicates the overall composition of the mixture, the actual composition of the coexisting phases at this very point is defined according to the horizontal orange tie lines that extend to the region's limits (as per the lever rule). Lowering the temperature (T) will effectively move the tie-lines such that they will eventually coincide with the new phase area containing the nematic phase. Since the nematic phase can only nucleate when enough material from an isotropic region is removed, we see a metastable area (b) showing the isotropic droplets in the sample are increasing in 5CB richness and gradually turning nematic.

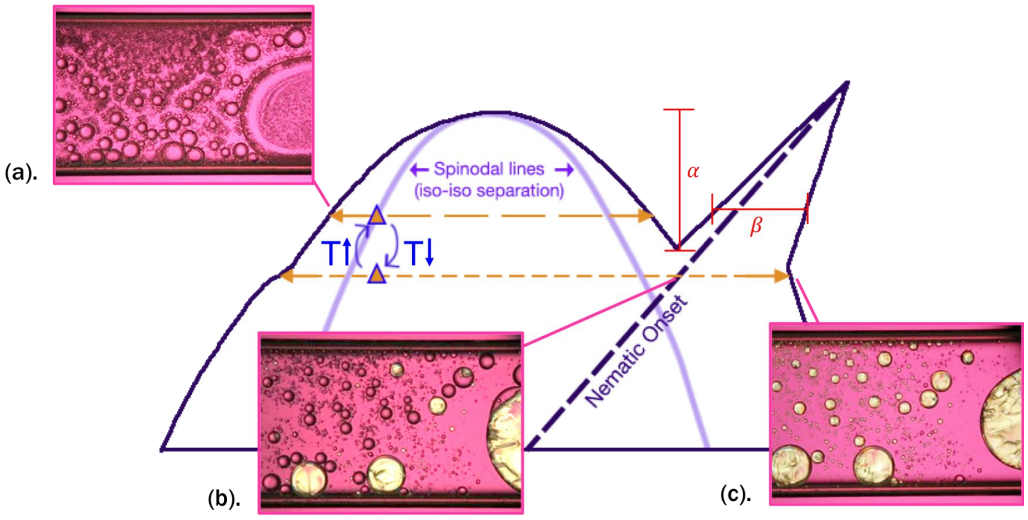

Fig. 5.8 – The progression of isotropic-isotropic coexistence to isotropic-nematic coexistence in 5CB-anhydrous ethanol mixtures is shown using Araki's and Tanaka's theoretical model with the experimentally observed transitions from the filled capillaries. A mixture containing a low fraction of 5CB is cooled (triangle) from an isotropic-isotropic coexistence (a) to a temperature (T) where isotropic droplets begin transitioning to the nematic phase (b). This causes the phase coexistence to move from the miscibility gap on the left to the right side of the overlapping diagram containing the nematic part. The coexistence will end at the equilibrated state where nematic droplets are now suspended in one isotropic background (c). The height (α) and width (β) defining the nematic region separating the left isotropic-isotropic region changes depending on the solvent used. The capillaries shown are 100 μm thick, and were viewed via crossed polarizer POM with a λ wave-plate (this is why the isotropic background appears magenta).

While not marked by Araki and Tanaka originally, it is assumed that this overlapping diagonal the "nematic onset" line will likely be the place where this conversion of one of the isotropic regions to a nematic region starts. This is because when the conversion is complete we arrive

to the final plausible coexistence of one isotropic phase (end of left tie line) with one nematic phase (end of right tie line). Experimentally, this can have the appearance of the latter being droplets dispersed in a uniform background of the former (Fig. 5.8c). Additionally, from altering the type of ethanol used it was noticed that the width (β) and height (α) defining the onset of the nematic region, relative to the parabolic miscibility gap region on the left, also changes (discussed further in sec. 5.3.2).

Note that Gibbs' phase rule describing the maximum degrees of freedom for a multi-component system is still be obeyed if the system's phases are indeed at thermal and mechanical equilibrium [183]. The degrees of freedom for a system can also be thought of more simply as the maximum # of "choices" one has for varying a parameter (usually: temperature, pressure, or component fraction) that defines the system without causing the number of phases present to change. Gibbs' phase rule (Eqn. 5.1) states that (F), our "# of choices", or "degrees of freedom", is equal to the number of non-reactive components (C) in the system subtracted from the number of phases (P) present plus 1.

$$F = C - P + 1 \tag{5.1}$$

Originally the phase rule uses plus 2 at the end, but for our case we assume one variable, pressure, is kept constant throughout our experiments. This means that this variable has been constrained from the start, and that there is only the option to vary, at most, the two variables of component fraction and temperature.

Taking a closer look at Fig. 5.7 the phase rule is indeed obeyed throughout. In the isotropic only phase, we have: 2 components (5CB, ethanol) minus the 1 phase plus 1 (Eqn. 5.1) which gives 2 degrees of freedom. We have the option of varying either both temperature and component fraction while still maintaining this isotropic phase at constant pressure. Entering into the miscibility gap where we get nucleation and growth, or spinodal decomposition, phase separating our ethanol-rich isotropic phase from our 5CB-rich isotropic phase (Fig. 5.8a), the maximum degree of freedom is equal to 1 while keeping pressure constant (2 components minus 2 phases plus 1). The same still remains true when the coexistence transitions to the isotropic-nematic state as well; there is one degree of freedom (Fig. 5.8c).

Does our POM based phase diagram follow Gibbs Phase Rule?

The only time when a phase coexistence would break the phase rule would be if 3 phases or more were in coexistence. More than 3 phases gives a negative degree of freedom value which physically does not make sense, so this is immediately rejected. With 3 phases and at constant pressure, however, the equation becomes: 2 components minus 3 phases plus 1 which is 0 maximum degrees of freedom. This would imply that our proposed phase diagram should have a triple point at some exact specific temperature and 5CB mol.% fraction where the 3 phases are observed in coexistence (much like water which has a triple point at 6.11 mbar and 0°C [184]). However, the problem is that while some mixtures have three phases in coexistence (i.e. nematic-isotropic-isotropic, Fig. ref5.6b) they tend to span an interval of temperatures. Thus, these phases are not in equilibrium at a single point.

This is the subtle, yet important issue that emerges when we compile our phase diagram base solely off of POM capillary experiments, even when the component fractions are rigorously accounted for using gravimetric analysis (Fig. 5.9). Even though mixtures are not under great confinement (they are in 100 μm uncoated glass capillaries as opposed to 10 μm coated cells),

because the volume examined is still quite large there are unavoidable concentration gradients that develop as the capillaries are heated and cooled. For this reason Fig. 5.9 has the added region called "Nematic-Isotropic" which is not present in Araki's and Tanaka's theoretical diagram, but which allows the final transitions observed experimentally in the POM before reaching the "isotropic only" phase to make sense.

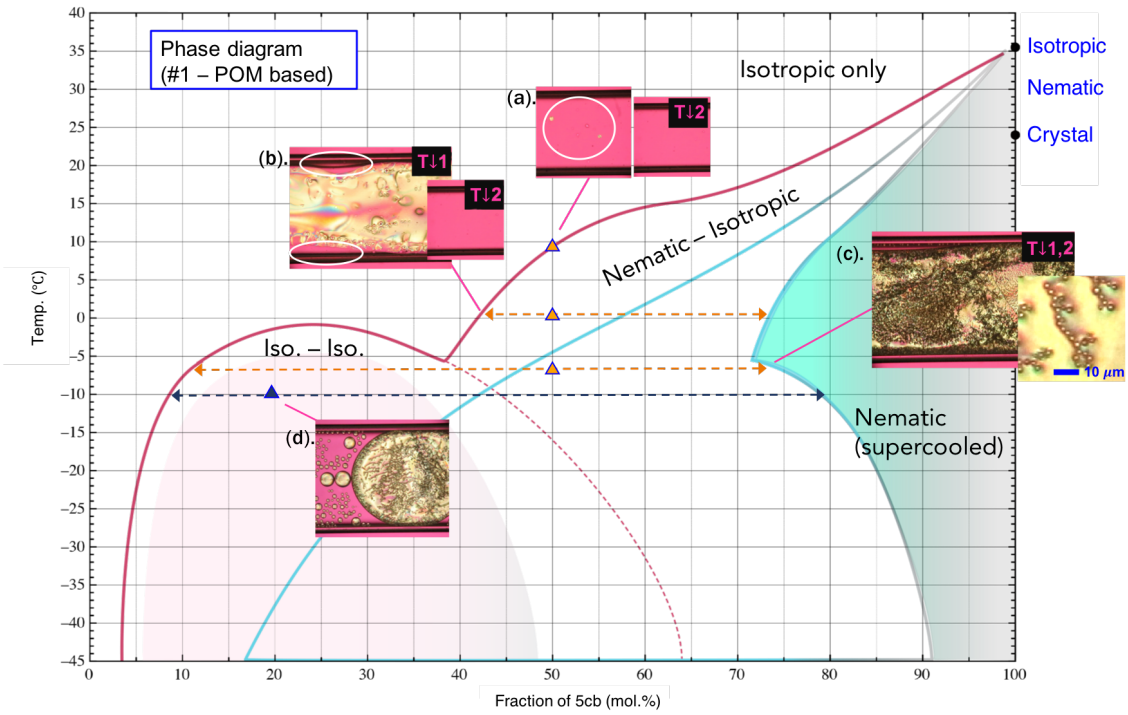

Fig. 5.9 – The first attempt in devising a 5CB-anhydrous ethanol phase diagram based on POM temperature experiments on mixture filled capillaries. The mixtures used were the ones prepared gravimetrically shown in Fig. 5.6(b). Example experimental images showing the coexisting phases for two mixtures points (blue and orange triangles - 49.8% and 18.6% 5CB) are shown in (a-c) and (d). Images (a-c) show how the phases appeared when cooling the 49.8 mol.% 5CB mixture twice (T ↓1 and T↓2). Due to concentration gradients in the sample, obtaining repeatable transition temperatures was not always possible. This was the main reason for the differences in the phase types seen between T↓1 and T↓2 in (a-b). Image (c) repeatedly showed the expected coexistence between one nematic and isotropic state (the nucleated isotropic droplets being the isotropic part). However, the 18.6 mol.% 5CB mixture had a coexistence of three phases (nematic, isotropic background, and isotropic droplets) which was repeatedly seen, but is contrary to Gibbs' phase rule.

The issue is that since we've designated that a nematic-isotropic metastable region has the possibility of existing here, it implies that 3 phases could coexist (nematic-isotropic-isotropic), and that directly conflicts with Gibbs phase rule.

A screen-shot of a mixture containing 49.8 mol.% 5CB cooled down to roughly 0°C the first time (T↓1) shows that there is a mostly birefringent nematic phase that still contains some isotropic areas. While this could be an allowed case of "nematic-isotropic" coexistence because there are also a few boundary lines present (white circles) that show yet another isotropic part separated in Fig. 5.9(b), it counts as "nematic-isotropic-isotropic" instead. The issue is that even if cooling is stopped, the features do not settle out into a homogeneous nematic phase, and it gives the impression that the 3 phases are in coexistence at an equilibrium state. Moreover, if

the solution is cooled again for the second time (T↓2) from the isotropic state, at 0°C again instead of there being the 3 phase coexistence like before, there is only one isotropic phase seen. The same was observed at the start of the mixture cooling as well in Fig. 5.9(a) after it was heated from negative temperatures. At this point it should have been in an only isotropic phase, however, nematic droplets were still present.

In the negative temperature region, for both the 18.6 mol.% and 49.8 mol.% mixtures, isotropic droplets develop after the nematic region formed as well in Fig. 5.9(c-d). These droplets, along with the inconsistency in the phase transition temperatures seen after repeated heating and cooling trials, all stem from the non-homogeneous mixing and concentration gradients forming within the capillaries. Recall that the first phase separation seen, the isotropic-isotropic coexistence for mixtures containing low fractions of 5CB on the left side, is just comprised of different ratios of 5CB to ethanol. One isotropic part is rich in ethanol, and the other is slightly richer in 5CB, but both are the same isotropic phase. When cooling down, or heating up, diffusion between the two isotropic phases will occur but not evenly across all areas of the filled capillary. One side, for example, may have more droplets that are ethanol rich than the other. For this reason, some isotropic droplets (and also depending on their size) might take longer to change into a nematic state than others when cooling down. Likewise, when heating up, nematic droplets in one area can remain present longer than in another despite Gibbs' phase rule indicating that the sample should have already entered the single homogeneous isotropic phase (Fig. 5.10).

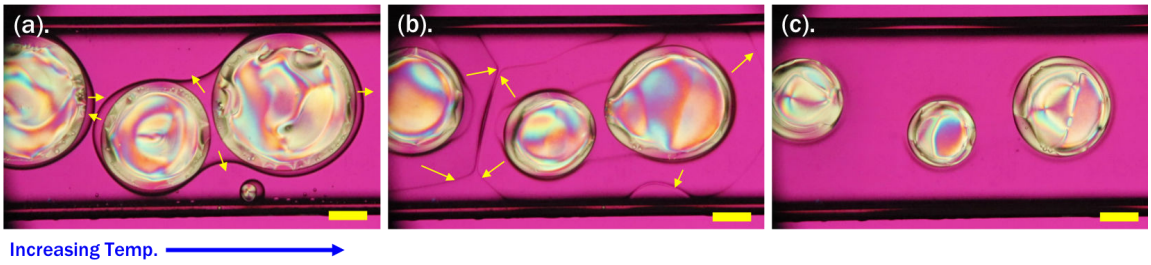

Fig. 5.10 – Screen-shots showing an example of nematic domains left over once all the isotropic-isotropic domains coalesce. For low fractions of 5CB in anhydrous ethanol the isotropic-isotropic state should be the last regime seen before reaching the homogeneously isotropic state. However because our sample has many concentration gradients present, uniform diffusion between the phases do not occur and sometimes the nematic state can still end up coexisting with an isotropic phase before reaching the single isotropic state (c). In (a) the nematic begins shrinking as it gives fractions of 5CB to form the second isotropic phase shown by the yellow arrows extending out from the boundary. After the two isotropic phases have meshed in the background (b), the nematic domains still remain but become progressively smaller until they too disappear. Scale bars: 200 $/mu$m, viewed through crossed polarizers with λ plate.

Through the microscope we cannot differentiate between the ethanol rich isotropic states and the 5CB rich isotropic states because both appear transparent. Thus, it is not possible to visibly see how the diffusion between the two isotropic media is progressing. In general, however, without further mechanical or thermal agitation diffusion in liquids takes a long time because the process is essentially governed by the molecules' random walks and collisions with other surrounding molecules (the results of Brownian motion [185]). Indeed, if the diffusion of non-reactive particles in a medium are viewed as discrete small steps taken from their point of origin, in one dimension, the probability of finding them at some distance follows that of the one

dimensional random walk (the very same model used in describing the ideal random polymer chain end-to-end distance) [186]. As such, there is a lower probability of finding the molecule further away from its starting point after less time elapsed than at a closer distance.

Using the DSC data to reduce the uncertainty from concentration gradients

In an attempt to account for the fact that observing three phases in coexistence during capillary heating and cooling experiments carried out in the temperature control stage and observed via the POM most likely means that the mixtures are not fully equilibrated, it was decided that using the DSC to obtain more concrete values for the phase transition temperatures would help. Note that while the POM investigations are instrumental in defining the types of phase coexistence that can occur at various temperatures qualitatively, for quantitative determinations of transition temperatures they are difficult to reproduce. Unlike the sample sizes needed for DSC pans (at least 5 mg or so), for observing phase separation phenomena in the ethanol-5CB mixtures via the POM at least several hundred milligrams would be used in order to visually see the components. Thus, because of the large disparity in the volumes of material used it becomes more likely that concentration gradients develop throughout the sample from non-uniform mixing during phase coexistence transitions.

The revised, final, experimental phase diagram reflecting the transition temperatures observed for mixtures containing 5CB and anhydrous ethanol using the DSC data is shown in Fig. 5.11. There are two main features to notice: first, compared to the POM based diagram in Fig. 5.9 the isotropic-isotropic regime has shifted slightly higher in temperature and now the whole isotropic-isotropic regime in general on the left side has become wider pushing the nematic-isotropic coexistence further right and narrowing it more, second, the eutectic point close to roughly 55 mol.% 5CB is present. The relevant mixtures observed in the DSC were comprised of 15 mol.%, 28 mol.% and 50 mol.% 5CB in anhydrous ethanol. The cooling peaks observed for the 15 mol.% and 28 mol.% mixtures were clearly overlaid, and as the samples were heated and cooled repeatedly this feature appeared to be very reproducible at this temperature. It is most likely that while cooling the two mixtures after entering the isotropic-isotropic regime at this point both immediately begin to nucleate the nematic phase at once by going through the eutectic point at 0°C. Finally, the DSC traces also show that for the 28 mol.% and 50 mol.% mixtures, there are also sharp, reproducible peaks that occur at which should indicate the rapid spinodal decomposition occurring between the isotropic-isotropic states and the isotropic-nematic.

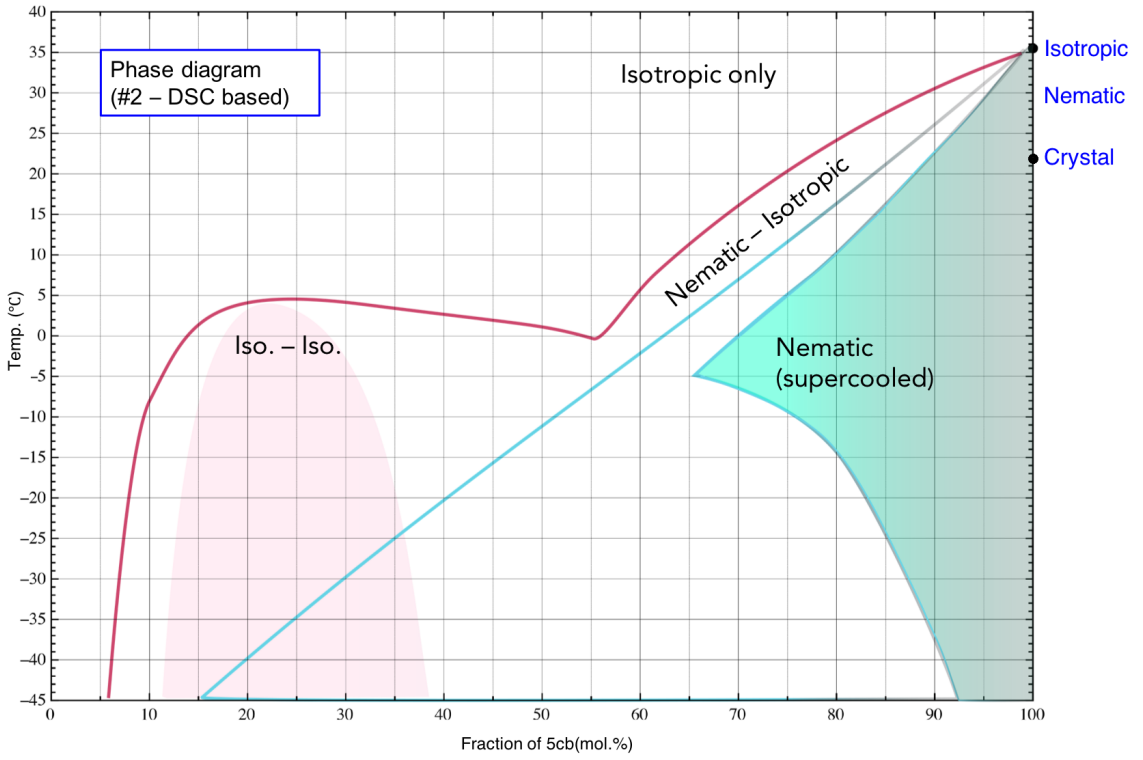

Fig. 5.11 – Our final attempt at devising a 5CB-anhydrous ethanol phase diagram based on DSC temperature experiments using smaller mixture volumes. The mixtures used were the ones prepared gravimetrically described in Fig. 5.6(b).

Isotropic-isotropic spinodal decomposition

Finally, to end this section before moving on to the slice of the ternary 5CB-aqueous ethanol phase diagram in sec. 5.3.2, evidence of the isotropic-isotropic spinodal decomposition of a 20 mol.% solution of the mixtures containing only 5CB and anhydrous ethanol was captured (Fig. 5.12).

Recall, that spinodal decomposition is defined as a point (at a certain temperature and overall component fraction) where the components of an initially homogeneous mixture immediately become unstable and rapidly separate into two stable coexisting phases. It is distinct from phase separation occurring by nucleation-and-growth because during spinodal decomposition the fluctuations that occur in component fraction are much larger and occur at once. Rapidly recurring concentration fluctuations between components (A) and (B), for example, immediately result in an overall negative free energy [187, 188]. Because the system is unstable to begin with, the infinitesimal component fluctuations between (A) and (B) never settle out. As such there is no energy barrier needed to overcome. If component (A) separates out from (A+B), component A just immediately separates. This causes the free energy to raise. Thus, experimentally, when spinodal decomposition occurs it is clearly recognized as a process of component separation showing an interdigitated texture, and is very much unlike the cluster formation seen from nucleation and growth.

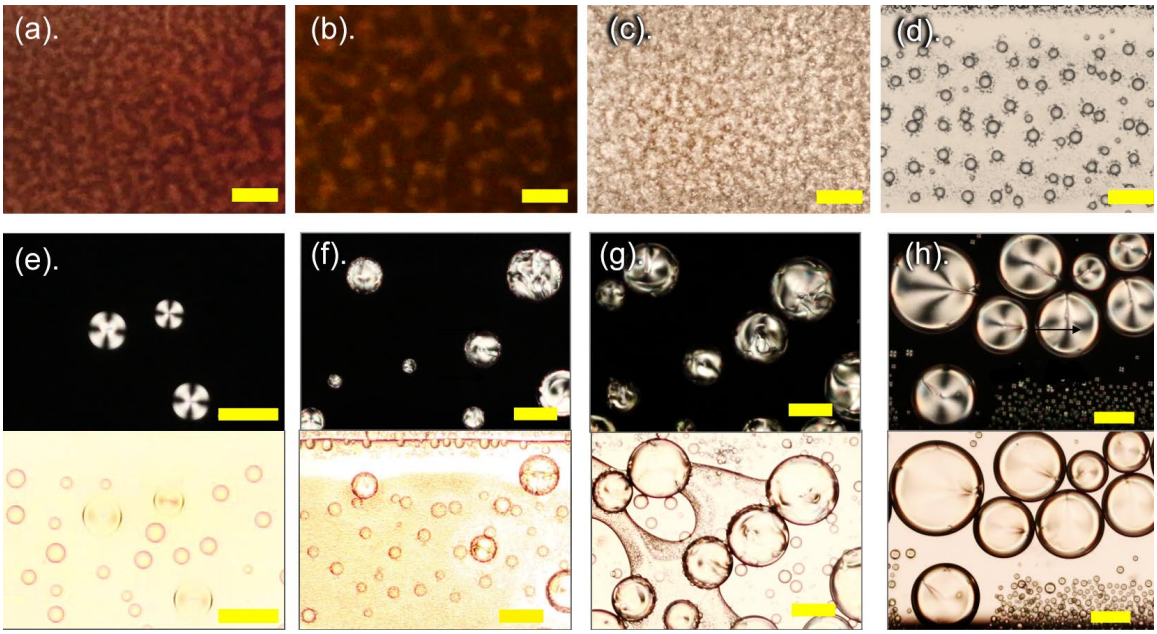

Fig. 5.12 – Screen-shots of spinodal decomposition between the two isotropic phases occurring for a volumetrically prepared 20 mol.% 5CB in anhydrous ethanol mixture while cooling. Interdigitated phase separation characteristic of spinodal decomposition was visible in (a) - (c). Nucleation and growth, within the isotropic-isotropic coexistence state appears to take over momentarily in (d), before the nematic phase begins in to emerge in (e). Cooling was slowly continued until all of the background isotropic was consumed to form the nematic droplets (h). The nematic radial droplets were 10 μm to 100 μm in size, while those preferring planar alignment had diameters $\geq$ 150 μm (f - h). The last image (h) ends with a coexistence between one nematic and one isotropic phase. Scale bars: 100 $/mu$m.

Phase separation by nucleation and growth happens gradually as small fluctuations between component fractions occur back and forth (e.g. between A and B), settle out uniformly, and then fluctuate again until finally a large enough fluctuation causes the nucleation of one of the components (A, for example) to some critical size. This nucleation of component (A) from the homogeneous background (A+B) then drives the diffusion of more component (A) to continue separating out of the mixture until several nucleated particle-like clusters of (A) have grown apart. At the end of nucleation and growth there is nucleated component (A) suspended in a uniform medium containing (B).

In Fig. 5.9 we originally had marked the UCST point of the miscibility gap curve on the left as occurring at exactly at 20 mol.% 5CB. This was because the volume based mixture shown in Fig. 5.12(a) showed clear evidence of isotropic-isotropic spinodal decomposition occurring at once in the interdigitated texture expected from theory [189, 190]. However, after observing the cooling patterns of the mass based solutions containing 5CB fractions at 18.6 mol.% and 29 mol.%, and seeing that spinodal decomposition also seemed to initially occur in these solutions (Fig. 5.13), it was decided that the USCT should be slightly broader and shifted to the right to reflect some error due to the presence of concentration gradients (Fig. 5.9).

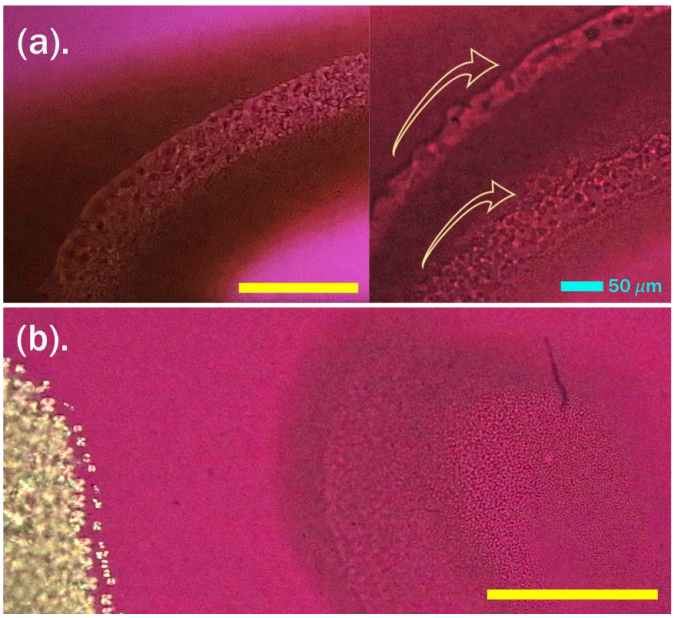

Fig. 5.13 – Spinodal decomposition was also observed to occur for gravimetrically made mixtures containing 18.6 mol.% 5CB (a), and 29 mol.% 5CB (b), in anhydrous ethanol while cooling from the single isotropic state. Due to the concentration gradients present in the samples the texture is not uniform across all areas. In (a), spinodal separation begins in the curved dark areas and quickly coarsens out (magnified in the right image with arrows pointing to the area) giving way to many isotropic droplets. In (b), nematic droplets nucleate on the left (unexpectedly) while the isotropic-isotropic spinodal decomposition occurred on the right. The sample in (b) sometimes started nematic nucleation and sometimes did not, this inconsistency was due to the concentration gradients in the sample. Yellow scale bars: 200 μm, viewed through crossed polarizers with λ plate.

Once the cooling was stopped at the first site of the interdigitated texture in Fig. 5.12(a), the coarsening of the separated isotropic-isotropic phases continued in images (b-d). Eventually the nucleation and growth nematic droplets began and the analyzer was inserted to view their formation between crossed polarizers. Interestingly, many of the nematic droplets that began nucleating started off with radial alignment, as if they were being anchored homeotropically (Fig. 5.12e), and then once reaching diameters larger than about 150 μm they appeared as planar (f-g). It may be similar to the case described by ref. [191] that showed that bulk elastic energy ($f_{elastic}$) of the droplets scales linearly with the droplet radius, while surface energy $f_{surface}$ scales with the surface anchoring energy multiplied by the droplet radius squared. Thus, for small droplets as shown here in planar anchoring conditions radial alignment is preferred since it is a small contribution to the surface energy. However, apart from observing this peculiar feature of phase separation causing both radial and planar nematic droplets being formed, this was not studied further.

Finally, evidence of the background isotropic being engulfed to form the nematic phase was seen by repeatedly inserting and removing the analyzer to view the sample with and without cross-polarizers. Particularly in Fig. 5.12(f) the boundary lines of one isotropic state are seen connecting several of the growing nematic droplets. This area of isotropic fluid distinguished by the boundary lines eventually ends up shrinking smaller and smaller until eventually it is

non-existent. In its place is just the previous isotropic background, and the nematic phase in droplets (Fig. 5.12h).

5.3.2 Case 2: 5CB in aqueous ethanol

This section now evaluates the mixtures containing aqueous ethanol and 5CB. Note that a slice of the ternary phase diagram containing ethanol, water, and 5CB is presented here as the water mol.% fraction was not varied. A qualitative overview of the phases in coexistence seen for the mixtures containing 5CB and aqueous ethanol is shown in Fig. 5.14, as was shown in Fig. 5.6 previously for 5CB and anhydrous ethanol. One of the differences between the sequence of the coexisting phase regimes from the two figures is that for the 5CB-aqueous ethanol mixtures there is a more clearly noticeable presence of the isotropic-isotropic coexistence starting from low 5CB molar concentrations (starting from roughly 8 mol.%) all the way until about 50 mol.%.

All isotropic-isotropic phases appeared stable when heating towards the isotropic only state. Additionally, a similarity shared with the 5CB-anhydrous mixtures is that both sets always showed the presence of isotropic droplet nucleation when concentrations between 18 mol.% - about 77 mol.% were cooled to negative temperatures. Apart from the isotropic-isotropic coexistence emerging at lower 5CB concentrations in the aqueous mixtures than for the anhydrous ones, one would assume that the phase diagrams for both are quite similar from only just comparing Fig. 5.14 and Fig. 5.6. However, this is not true. While the phases qualitatively seen are the same, quantitatively, the phase diagrams are offset by several degrees of temperature.

As seen previously in the macroscopic mixtures (Fig. 5.4 on pg. 93), the isotropic-isotropic phase coexistence that occurs for the aqueous ethanol mixtures is visible at room temperature (unlike that for the anhydrous mixtures) and in particular, mixtures containing fractions of 5CB between 20 mol.% - 30 mol.% tend to not fully clear to the isotropic only phase until above the known clearing temperature of even pure 5CB (35°). A slice of the ternary phase diagram containing water is proposed in Fig. 5.15 reflecting these features. Moreover, while it seems as though the it is mainly the left side of the diagram (the isotropic-isotropic region) that increases well above room temperature, the right side showing the nematic-isotropic coexistence narrows somewhat to reflect the observation that the supercooled nematic only phase will nucleate slightly sooner with fractions of 5CB ~60 mol.% rather than at ~77 mol.% (Fig. 5.4).

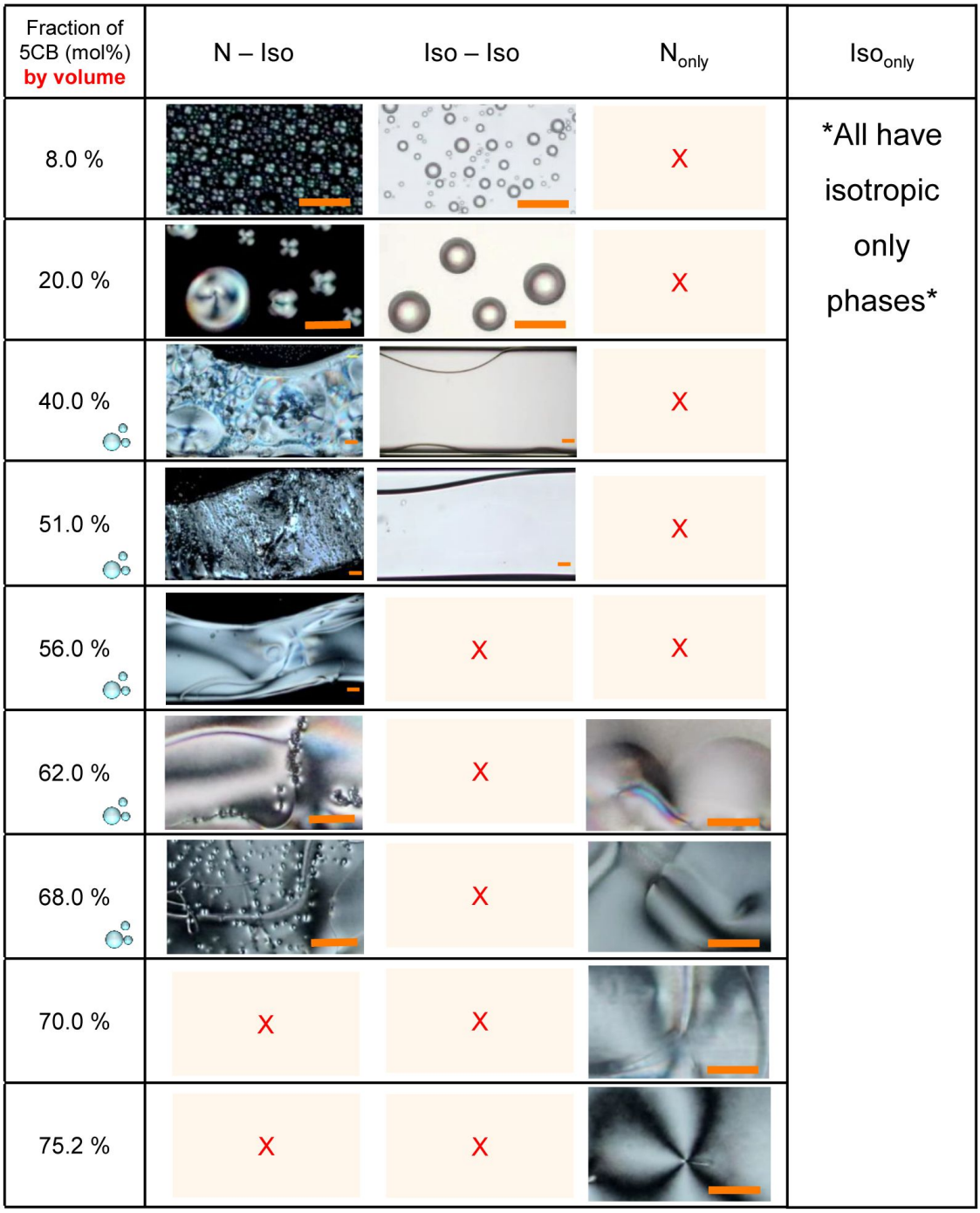

Fig. 5.14 – Four regimes of phase coexistence (N-I (nematic-isotropic), Iso-Iso (isotropic-isotropic), N_{only} (nematic), and Iso_{only} (isotropic)) were observed microscopically with and without crossed polarizers for mixtures containing 8% to 75% mol. of 5CB in aqueous ethanol. Qualitatively, the emerging phases are the same between both mixture sets prepared gravimetrically and volumetrically. This summary of phases is for capillaries containing solutions from the bottles in Fig. 5.4(b). Again, certain mixtures also showed isotropic droplet nucleation below $0°C$, noted by the blue bubbles. Scale bars: 150 μm

Recall, that with the aqueous mixtures nematic phases without isotropic coexistence were also seen to form macroscopically at ~75 mol.% 5CB while for the anhydrous mixtures, the nematic only phase was not macroscopically visible until the vials containing nearly 100 mol.% 5CB. (The slice of the ternary phase diagram shown in Fig. 5.15 is still preliminary. Complementary DSC experiments will be performed in the near future to improve the quantitative reliability).

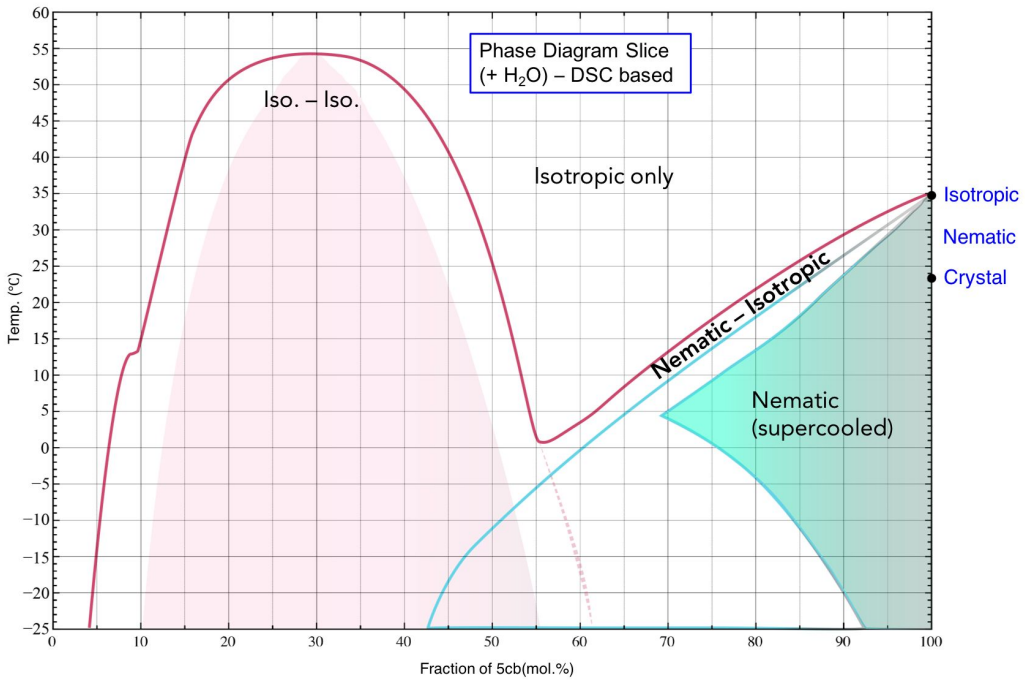

Fig. 5.15 – Slice of the isobaric ternary phase diagram for mixtures containing various mol.% fractions of 5CB in aqueous ethanol. Again, this phase diagram was constructed based off of the mol.% fractions of new mixtures created that took into account the actual masses of the 5CB and aqueous ethanol obtained from the micro-liter volumes pipetted, and the DSC data. Qualitatively, again, they share the same regions of coexistence shown macroscopically in Fig. 5.4(b). Surprisingly, the addition of a small percent of water (4 vol.%) to dilute the anhydrous ethanol has the profound affect of shifting the whole isotropic-isotropic coexistence (left-most region including the binodal and spinodal) upwards by several degrees when the aqueous ethanol is mixed with 5CB in similar concentrations as for the anhydrous case. The right-most region of the curve including the nematic-isotropic coexistence is by comparison much thinner than for the anhydrous ethanol mixture case as the onset nucleation of the nematic phase is accelerated somewhat by the water present.

5.4 How this influences the electrospinning process

5.4.1 Spinning 5CB-PVP-anhydrous-ethanol in normal conditions

First, let us consider what occurs while electrospinning in the "ideal no-water" situation, given the phase diagrams derived in Fig. 5.11 and Fig. 5.15 for the 5CB-anhydrous ethanol case and the 5CB-aqeuous ethanol case, respectively. According to the 5CB-anhydrous phase diagram, at temperatures roughly close to room temperature (25°C ± 5°C), and without humid conditions (i.e. excess water condensed into the Taylor cone), we should expect to be in the right side of

the diagram–the nematic-isotropic coexistence regime. Experimentally, this is what is visibly seen during a normal, non-Taylor-cone distorted, electrospinning experiment using anhydrous ethanol and 5CB. The coaxial Taylor cone forms at a predictable 9 - 10 kV range with a PVP solution flow rate at roughly 1.1 mL/hr, and a 5CB flow rate close to 0.5 mL/hr (for my coaxial needle setup). More importantly the Taylor cone remains stable without breaking down into multiple jets, excessive dripping or polymer stiffening (Fig. 4.3).

Since 5CB supercools so strongly that is also what allows us to see it scatter as it enters the center of the Taylor cone and into the emerging jet. Moreover, the supercooling is what enables us to flow it so easily at temperatures near to 22°C when it should have, technically, solidified into a crystal. Once the evaporative cooling of the spinning jet begins to occur at a higher rate, presumably right when the whipping instability starts, it is possible that the temperature of the jet can lower down to as low as 0°C such that the jet would be in the isotropic-isotropic regime. However, I doubt would affect the fibers formed so much because by this point, the PVP sheaths would have largely solidified and rarely any ethanol solvent would remain for a miscibility gap to form between ethanol and 5CB (as per the FTIR data discussed in ch. 4). Another point to remember is that the 5CB is not a solvent for PVP either, so no interactions would occur between these two components here.

5.4.2 Spinning 5CB-PVP-aqueous-ethanol

At low humidity

Since electrospinning 5CB with a PVP solution containing aqueous ethanol (96 vol.%) at room temperature and relative humidity conditions below 30% gives us non-beaded fibers, and between 30% - 45% generally gives us beaded fibers, it suggests that some water condensation is still acceptable for the system to work. Recall that the FT-IR spectra of several 5CB filled fibers spun, on pg. 81, revealed that water adsorption on the fibers could not be 100% prevented. According to the slice of the ternary diagram in Fig. 5.15, for the normal room temperature, non-elevated humidity case, our Taylor cone is most likely in the regime where the coexisting isotropic phases are emerging simultaneously with the nematic phase. The presence of coexisting isotropic phases at room temperature suggests that right when spinning starts the solvent from the sheath has already begun entering the core, while the core has simultaneously started entering the sheath. However the jet does not break down because the rate of these processes occurring may be quite fast before the jet starts rapidly cooling and the 5CB-ethanol miscibility enter the right side preferably: the nematic only regime.

At high humidity

Alternatively, the moments when the jet and Taylor cone break down occur are at high ambient humidity when an excess of water vapor from the atmosphere enters. If the humidity continues to be elevated we could reasonably expect the left side of Fig. 5.15 to continue increasing upwards, such that eventually it may become the opposite of the anhydrous case, where the coexisting isotropic phases are preferred rather than a nematic only phase. If this scenario occurs then not only does more condensed water mix with the ethanol in the sheath, but this mixture of water and ethanol can act as a suitable convoy for trapping 5CB and bringing it outwards to further interfere with the stabilization of the cone and jet. This means that Taylor cone formation is delayed and Rayleigh instability will be favored leading to drop formation. Thus,

multiple uncontrollable jets will emerge because charge separation in these droplets will be too non-uniform for the Taylor cone to equilibrate. Ultimately, the result of these interactions would end up appearing as was seen and discussed in sec. 4.4 of ch. 4.

6

The ground state optics of 5CB-PVP mats impact their responses to VOCS

6.1 Results overview & recap

Assuming coaxial 5CB-PVP fiber formation is successful and mats that are not meshed or leaking are produced, their optical properties should be considered especially if they will be used as visual sensors. In sec. 2.2.1, the optics of thermotropic nematic LCs were discussed for the most general case, thin films of the LC with defined constant thickness in rectangular glass cell confinement with specific anchoring conditions (homeotropic or planar). The director (n), which defines the average molecular orientation of the bulk LC, helps us differentiate the transitions of several LC phases was also defined. However, how n can orient when confined in a non-beaded or beaded porous fiber only a few microns wide is not entirely the same as for the rectangular glass cell case.

Knowing that n is sensitive to variations in surface anchoring and confinement, and that external factors such as processing and environmental conditions (ch. 4, ch. 5) influence the filling of the LC in the fiber core, as well as the formation of the outer sheath, areas of non-uniform director alignment ("twists") arising from deformation during the electrospinning process may develop. These fluctuations in director alignment are important because they ultimately impact how the macroscopic optical properties of the LC-fibers can change when exposed to external stimuli, in our case for making flexible gas sensors.

In this chapter I will discuss some of these optical consequences (director alignment changes like twists, differences in fiber mat brightness) that result when confining 5CB within the PVP microfibers. Moreover, how some of these features contribute to visualizing the responses in the fiber mat sensors from a qualitative perspective will also be analyzed starting from sec. 6.4.

6.2 The LC director confined in fibers

6.2.1 The LC core contributes to coaxial fiber mat birefringence

In addition to contributing to high individual fiber birefringence seen at the microscopic level, the optics of 5CB within the individual PVP fibers also influences the level of macroscopic scattering seen from the assembled non-woven mats when observed macroscopically between crossed polarizers (Fig. 6.1). Although when compared in ambient light two fiber mats (one containing fully dried, non-beaded, LC-PVP fibers and the other containing just pure PVP fibers) appear to look exactly the same (Fig. 6.1a), if the mats are both analyzed through macroscopic polarizers (using the "macroscope" - sec. 3.2.1) their optical differences are quickly noticeable. For both types of fiber mats collected in two different ways—with the individual fibers uniformly

aligned and unaligned "random", clearly the amount of light passing through the analyzer after entering the mats is intensified from just the presence of the birefringent 5CB core.

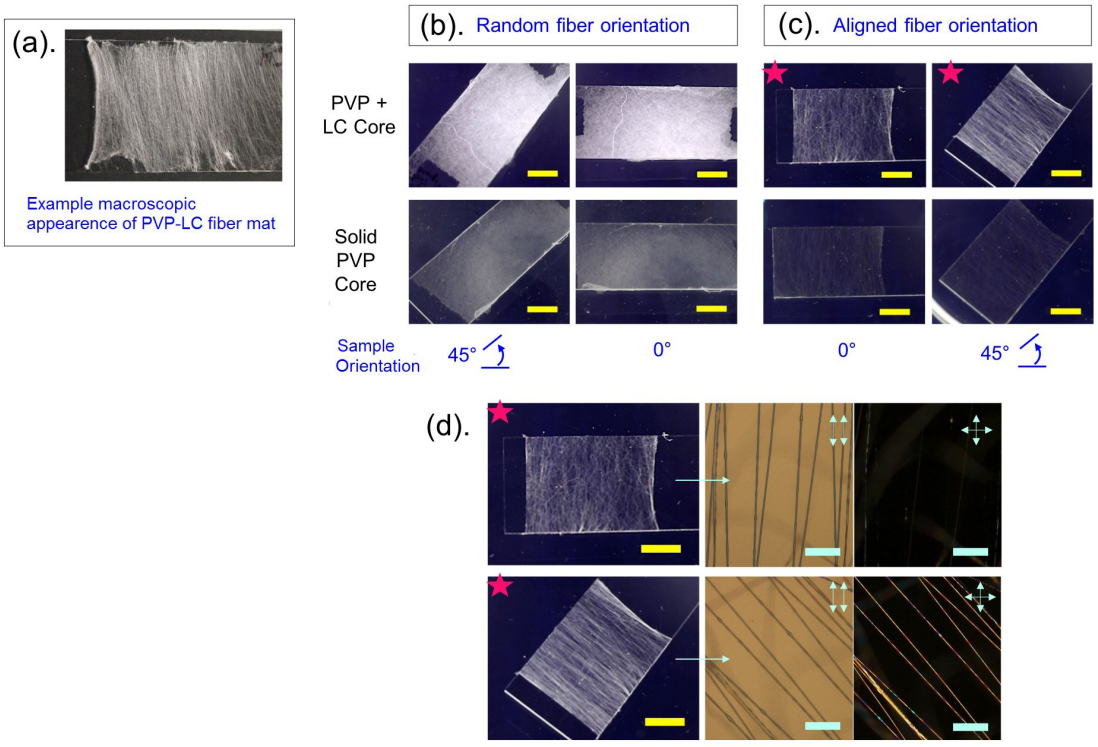

Fig. 6.1 – The qualitative differences in overall mat brightness between LC core filled PVP fiber mats (top row in b and c) and pure PVP fiber mats (bottom row in b and c) when viewed between macro-scale crossed polarizers are shown. However, when viewed macroscopically without the polarizers in ambient light the LC filled fiber mats (a) still appear white just like the non-filled, pure PVP fiber mats do. Between crossed polarizers though the difference in mat brightness between the LC filled sample and the pure polymer sample is visible depending on whether the individual fibers were collected randomly (b), or in an aligned manner. The samples were also rotated between 0° and 45° to see any changes in appearance. If the aligned 5CB-PVP fiber mat (designated by the pink star) is observed at the 0° and 45° positions through the POM with and without crossed polarizers the periodicity of the LC birefringence within the fibers is also visible (d). Scale bars: 10 mm (yellow), 50 μm (light blue)

Recall from ch. 4 that pure electrospun PVP fibers are optically transparent due to the polymer's inability to organize its chains in a highly ordered manner which ensures that the fibers produced exhibit an isotropic glassy state, even when rapidly stretched during the electrospinning process. In fact, when viewed through the crossed polarizers in the POM with the λ wave-plate inserted, the pure PVP filaments do not show any sign of chain alignment when rotated 360° on the stage. However, were there a considerable level of chain alignment (or crystalline regions) present in these pure fibers, upon rotating the fibers, there would be a periodic alternation of color, always different from the pink background of the λ-plate itself. This would depend on whether the polymer chains align mainly along or mainly perpendicular to the optic axis of the λ-plate, and is known to occur for several types of filaments for example, which due to their shape, are also anisotropic (e.g. asbestos [192])

Moreover, particular to the aligned LC filled fiber mat shown in Fig. 6.1(c) is the feature of the bright-dark alternation that the mat displays when rotated with 90° periodicity. Recall that this is a feature that was transferred over to the macro-scale mat from the anisotropic nature of the LC adopting planar alignment with the fiber cores. When the aligned mat is turned to either one of the positions parallel or perpendicular to the bottom macro-scale polarizer (that is, either 0° or 90°) it will dim in brightness, and when turned to the 45° position, it will be maximally bright. Looking more closely at the individually aligned fibers in this mat through crossed polarizers in the POM reveals that the confined 5CB in the fibers behaves in generally the same way as it would if it were in the previously mentioned uniformly aligned planar cell (Fig. 6.1d). However, not all of the fibers in this mat are dark for the same orientation. If they were then when turned to the 0° position the brightness of this mat should be quite identical to that of the pure PVP fiber mat, and yet it is not. At the 0° position the aligned 5CB-PVP fiber mats still appears brighter than the pure polymer aligned mat.

The reason this occurs is because during the electrospinning process, and handling of the fiber mat, not all of the LC filled fibers land perfectly parallel on the collector. While there is an average fiber alignment perpendicular to the two parallel grounded electrode plates, there is a certain variation in orientation around this direction for individual fibers. Thus, since the 5CB director confined within will also, for the most part, follow the long axis path of the fibers in planar alignment, through crossed polarizers, these non-aligned criss-crossing fibers will still contribute to increasing the brightness of the mat before the whole sample is rotated to its maximum brightness point at 45°. This is a macro-scale optical aspect that is unique to the aligned and filled LC-fiber mats because of the form factor in which the LC is confined in - a flexible, 2 μm - 4 μm thin, "capillary" which is layered among others of the same kind that can freely entangle or disentangle within the non-woven textile mat. Therefore, the movement of some individual filaments can also alter the optical appearance of the sample mat as a whole.

Lastly, notice how the 5CB-PVP fiber mat which doesn't contain predominantly aligned fibers (the randomly oriented one, Fig. 6.1b), when rotated between crossed polarizers, does not appear to have a reduction in brightness. This time this mat behaves most similarly to the previously described cell containing the nematic phase with either the degenerate director. The major difference here is that rather than the optical effect being due to the director which is randomly oriented within the plane of the cell, the individual fibers, each containing a mostly uniformly aligned director, are oriented in random directions in the mat such that when one fiber goes dark under crossed polarizers, other ones above or below it positioned at even slightly different angles, will not. Thus, the grouping of many of these LC filled fibers together in different orientations can make it appear as though the entire mat is not changing in total scattering intensity to the eye when it is rotated 360° between crossed polarizers, even if individual fibers are changing in brightness intensity at the microscopic level.

For observing the effect that gas sensing will have on visualizing the macro-scale responses of the mats these attributes are important because depending on how the mat is oriented, and whether it contains aligned or mostly random oriented fibers, it can affect how fast the overall visual scattering change is perceived. More on this will be discussed in sec. 6.4 of the next chapter.

6.2.2 A closer look at individual fibers

The rotation guide shown in Fig. 6.2 will help in visualizing the angles at which several of the fibers in this section were analyzed. The chart goes only from 0° to 180° because upon turning the samples a full 360° the same optical features in the fibers were seen again after the 180° point, with the only difference being that the image is upside down..

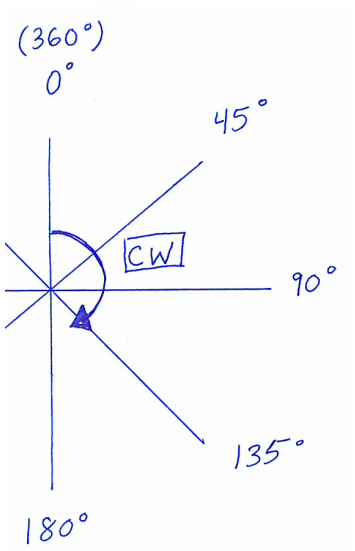

Fig. 6.2 – A simple guide showing the rotation pattern taken for analyzing the birefringence and defects in the electrospun 5CB-PVP coaxial fibers between crossed polarizers in this chapter. Unless otherwise noted in the text, the default direction chosen was clockwise (CW) starting with the vertical position designated as 0° and ending in the anti-parallel position at 180°.

Although the director in most non-beaded 5CB-PVP fibers will align along the long axis of the fibers, shown in the close-up of two filaments from an aligned sample in Fig. 6.3, even the slightest modulations in fiber thickness will result in noticeable changes in birefringence and interference colors. Even though both of these fibers are from the same mat, and both have roughly the same aligned orientation, if looked at closely using the λ wave-plate and at a higher magnification one of these fibers has slightly bulging sections unlike the other (Fig. 6.3, 0° orientation). The fiber containing the white circle outlines, which highlight where the bulges are, contains bulges that become even more noticeable once the fibers are turned to the 45° position because the interference color in the bulges at these points appears brownish-purple while the rest of the filament has a yellow character, when observed without the λ-plate. The fibers at the 45° orientation are also parallel to the direction of the optic axis of the inserted λ wave-plate.

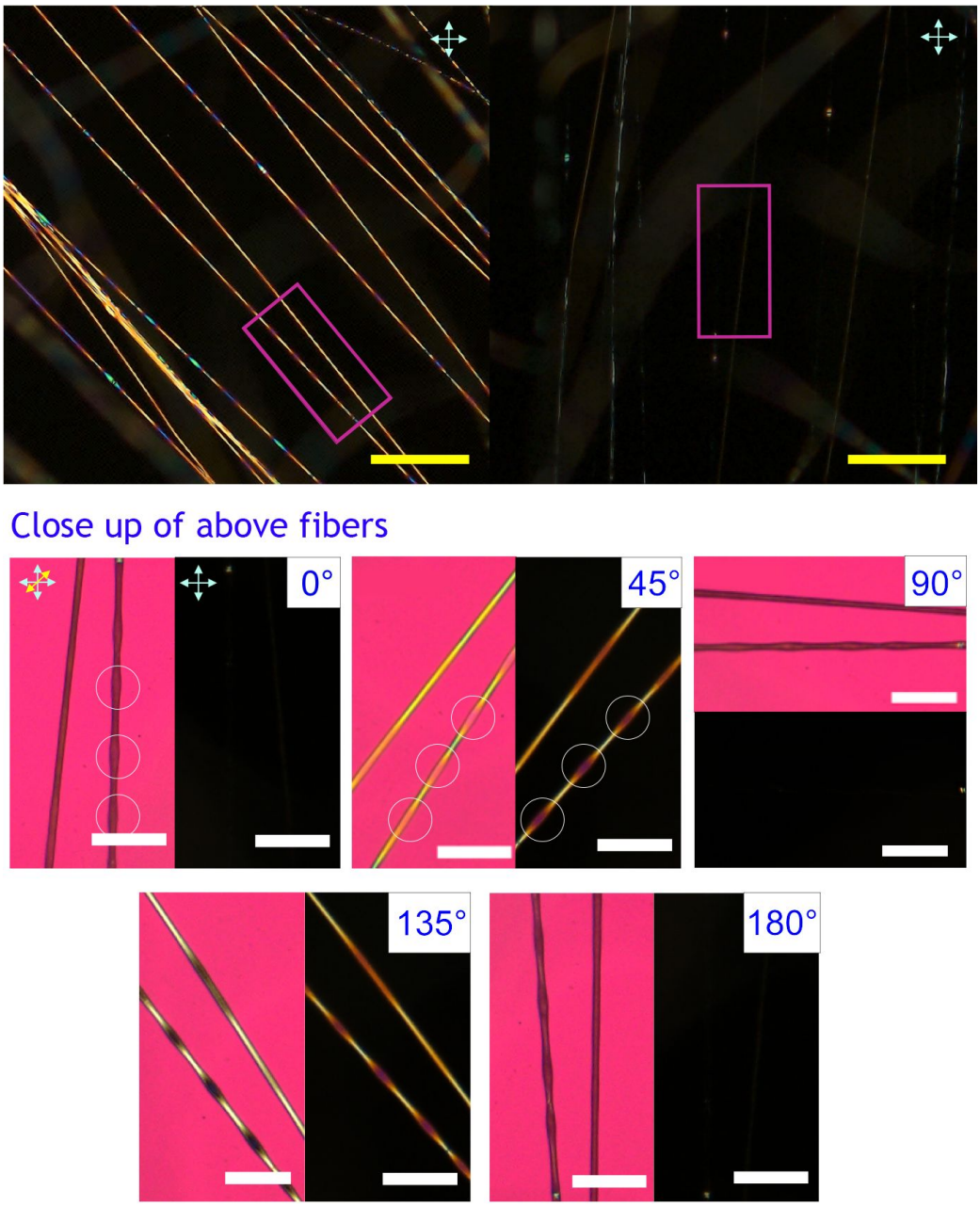

Fig. 6.3 – The close-ups of two aligned 5CB-PVP fibers (purple outline in the top images) when rotated between 0° and 180° through crossed polarizers with and without the λ wave-plate inserted. These two sections of fibers (one with slightly more bulges than the other) show that even minor variations in fiber thickness contribute to differences in interference color within fibers produced within the same sample. See main text for analysis using the Michel-Lévy chart. Scale bars: 50 μm (yellow), 20 μm (white)

Using the Michel-Lévy chart in Fig. 6.4, it can be seen that the 530 nm wavelength from the λ plate added to the birefringence of the 5CB core. This is based on the assumption that both fibers start off by showing 1st order yellowish white (thin fiber parts) and purple (bulges) interference colors, respectively. To confirm the starting assumption consider the rotation of the sample to the 135° position. Once the sample is rotated for this orientation we see that with the wave-plate inserted, the non-bulging sections turn almost white/gray, while the bulging sections purple sections take on a dark blue/black color. This black appearance shows that the optical retardation of the 5CB core is approximately equal in magnitude to that of the λ-plate, thus about 530 nm.

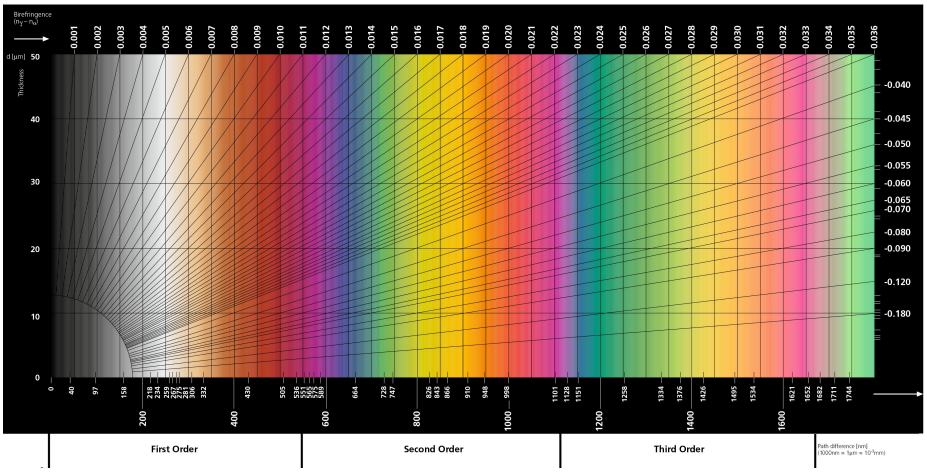

Fig. 6.4 – An adapted version of the Michel-Lévy Interference Color & Birefringence Chart.*It shows the first, second and third order of interference colors seen in a thin anisotropic sample. The x-axis has the optical path difference (or, "retardation") in nanometers between the extraordinary and ordinary rays passing through the sample. The sample's thickness values are the y-axis in increments of 10 μm (from 0 μm to 50μm). The birefringence values start on the top of left-side of the chart, continue to the right and down the y-axis on of the chart's right side (values end at 0.18). After confirming the interference color seen in a sample between crossed polarizers, and determining its order group, the intersecting line that joins the sample's thickness where its interference color is can be traced diagonally upwards to find the birefringence value.

This is corroborated by the fact at the 45° position, the purple bulges in the fiber appear orange-pink when wave-plate is inserted. This color is found just to the left of the 2nd order purple in the Michel-Lévy chart and informs us that the retardation of the core in the bulges is slightly less than 530nm. Since we know from the extensive literature on 5CB that its birefringence at room temperature is around 0.2 [193, 194], we can estimate that the core diameter in the bulges shown in Fig. 6.3 should be close to 2.5 μm (2500*0.2=500nm).

Interestingly, while the POM images in Fig. 6.3 show examples of filament areas containing a uniformly aligned director, the majority of the 5CB-PVP non-beaded fiber mats that are electrospun actually show many local points along individual fiber lengths that are filled with what at first sight appear to be defects (Fig. 6.5). They are easy to confirm when the samples are observed through the POM because at every 90° rotation, while the majority of the filaments

*The original chart was donated by Carl Zeiss Microscopy GmbH to Wikimedia Commons here: `https://commons.wikimedia.org/wiki/File:Michel-L%C3%A9vy_interference_colour_chart_(21257606712).jpg` under the creative commons license code: cc-by-sa-2.0.

become extinct, the "defect" areas remain a bright white, or sometimes colored yellow, green, or red (Fig. 6.5).

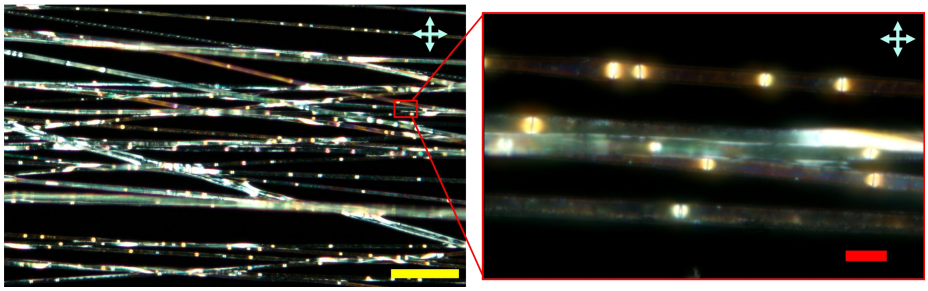

Fig. 6.5 – Crossed polarizer POM images show that nearly all of the non-beaded, aligned 5CB-PVP fibers contain brightly spotted defects within the fiber cores. Rather than seeing the lengths of the fibers become black when at the 90° position (a sign that the director is completely uniformly aligned along the length of the fibers), the fibers exhibit multiple bright yellow, white and pink spots scattered throughout. A close up of one region of these fibers on the right reveals that these bright spots tend to also show a black vertical defect line in the center. Even if the entire sample is rotated by 360°, these bright areas never become dark. Scale bars: 100 μm (yellow), 10 μm (red)

Figure 6.6 shows a closer examination of three of these types of bright spots appearing in separate fiber strands. It is evident that they can appear at various locations throughout the fibers and they are also the most noticeable when the entire mat is oriented perpendicularly to either one of the polarizers. This sample is also the same mat as the one examined earlier in Fig. 6.3, and the filaments with uniform director field shown were just from the lower regions of two fibers. This also reveals that electrospinning 5CB within PVP can result in fibers that can have *mostly* uniform director alignment, but that not all fibers, and especially within all areas of the same filament, need to have the same director configuration throughout. Although this does not mean that the director will adopt dramatic conformational changes that are visible for a large area, such as the likes of twisted directors in chromonic lyotropic liquid crystal mixtures which show long range director twists over hundreds of microns under crossed polarizers [195, 196], the mere fact that these areas are even seen when 5CB is not expected to support this level of director change, even when confined in a thin cylinder, is surprising enough.

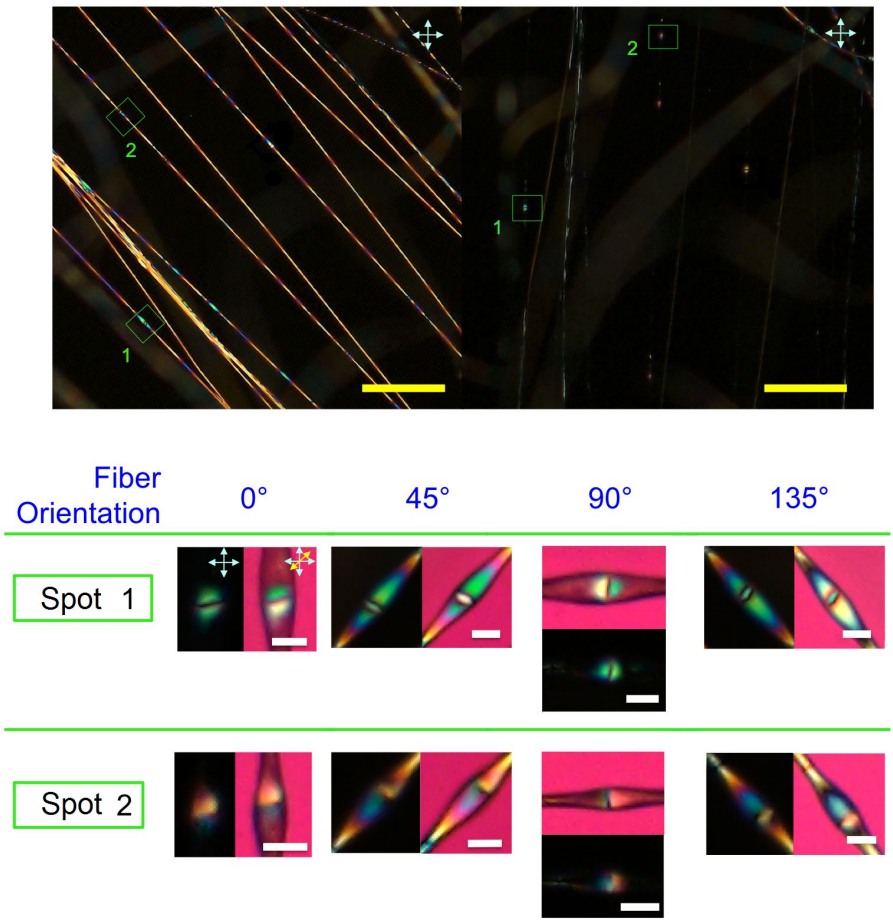

Fig. 6.6 – Although many fibers in the sample shown in Fig. 6.3 do not have these spots, some fibers in the mat have a few. When the mat is turned to 0° or 90° these areas appear as bright, non-darkening spots. They (Spots 1 and 2, here) indicate small regions where the 5CB director is not uniformly aligned, and most likely twisted, with respect to other fiber areas that have gone dark. Scale bars: 50 μm (yellow), 4 μm (white)

As the crossed polarizer images of Spot 1 and Spot 2 at the 0° orientation in Fig. 6.6 show, the defects can either have a black line perpendicular to the fiber's width (Spot 1) or just be indicated by the presence of the illuminated spot without the black line going through it (Spot 2). In both cases the bright spot demonstrates that the director at the position has adopted a twisted configuration. In rotating the sample such that Spots 1 and 2 are turned a full 360° we see that while the surrounding area outside of their centers modulates in brightness as expected, these spots never go extinct, just as we would expect for a nematic with a twisted director configuration. Since there will always be some part of the sample where the director is neither parallel nor perpendicular to the polarizer, thus some birefringence effect is always seen.

Upon viewing Spot 1 through crossed polarizers with the 530 nm wave-plate inserted, the green area below the black line immediately turns white whereas the are above remains green. If the director configuration were the same above and below the black line then this asymmetry in color should not occur. After turning the fiber so that it is 45° and parallel to the direction of the λ-plate optic axis, the spot turns back to green save for a white spot that remains in the

center. It is challenging to consult the Michel-Lévy chart for this case, since it assumes a uniform optic axis orientation, whereas here the director within the fibers is clearly twisted. Determining whether the director abruptly changes configuration in Spot 2 is a little more difficult, and indeed, when inserting the λ-plate we don't see the same distinctly asymmetric response as in Spot 1.

So to summarize - we have several locations in the 5CB filled PVP fibers where deviations from the uniform director field along the fiber can spontaneously arise. Sometimes the bright spots are present with a black line in the center. The two remaining questions which will be explored in the next section are: for the case of electrospun 5CB filled fibers, does the presence of bright spots indicate that the director field twists in small regions of the fiber? And, if so, why does 5CB - an achiral, non-chromonic nematic develop a director twist in the first place?

6.3 The spontaneous emergence of a local twisted director

Achiral, non-chromonic nematic LCs like 5CB are not known to adopt twisted director configurations when confined. In general, thermotropic nematics, particularly those of "# cb" cyanobiphenyl type (5CB, 6cb ...etc.) have elastic constants that are all very similar in magnitude (for 5CB, K_1=5.2 pN, K_2=2.9 pN and K_3=56.8 pN) [57, 58]. Therefore, it becomes too costly for the phase to minimize its free energy by specifically adopting a long range twisted director configuration. The splay, twist and bend terms are all positive and minimize the free energy of the LC so that it does not have defects.

However, a complete description of the free energy includes the saddle-splay term (K_{24}) which relates to surface curvature. Even when K_{24} (the saddle-splay constant) for 5CB was initially measured it was still found to have a similar value to K_2 (roughly 2.9 pN) [197]. So for the most part, its role in helping to decrease the total bulk free-energy described by Oseen and Frank was assumed to be irrelevant, particularly for the conditions under which the effect of saddle-splay on 5CB has been mostly studied (that is, large bulk samples confined in geometries without curvature). Of course, these elastic constants, however, start to play a larger role particularly if the LC is confined spherically [40, 58, 198] or cylindrically.

For both chromonic LC cases, Davidson et al. [58, 196] and Nayani et al. [195] showed through a series of POM experiments and free energy calculations that due to the extraordinarily high value of the saddle-splay constant (K_{24}) a distortion that contains saddle-splay can actually help lower the total free energy cost. Since having a twist deformation is quite inexpensive (less than 1 pN) the nematic phase will prefer to adopt a twisted director field along the curved areas in its confinement rather than any other deformation (e.g. splay or bend). Note that technically this should only happen if the confined LC, like the chromonics mentioned, has a twist constant considerably lower than its saddle splay constant (i.e ($\pm$ $K_{24} > K_2$) [195]. While this is not true for 5CB, recall that the saddle-splay constant when 5CB is confined in 2 μm - 4 μm diameter cylinders with planar anchoring has not been extensively studied yet. Additionally, the POM data shown previously indicates that during encapsulation via electrospinning the 5CB director field can form local regions of twist.

A filament containing five local twists (Fig. 6.7) examined via the way Nayani et al. [195] examined their DSCG filled capillaries (roughly 20 to 100 times wider than the electrospun fibers) shows strikingly similar optical features. The same director twist occurring in their capillaries is likely to also be forming around the black lines seen in my 5CB-PVP fibers. Nayani et al.

[195] and others [58, 195, 196, 199] have confirmed that complimentary interference colors will emerge in areas of confined chromonic LCs where the twist reverses handedness. When observed between crossed polarizers, with one polarizers offset from its regular orientation at 90° to the other (Fig. 6.8), the presence of these complimentary interference colors indicates that the director field on each side of the back line twists in an opposite direction in the cylinder. This forms a left-handed and right-handed twist. However, there is no preference for either left or right [196].

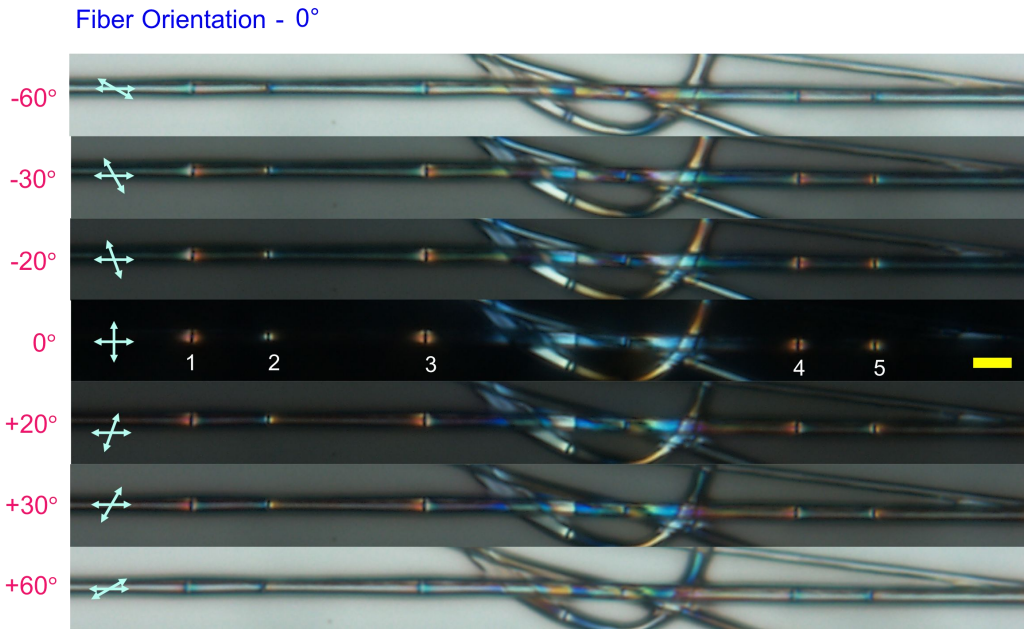

Fig. 6.7 – If an aligned 5CB-PVP fiber is kept at the 90° orientation between crossed polarizers in POM, and only the top polarizer (the analyzer) is rotated back and forth, the handedness of the director twist can be qualitatively determined. A single non-beaded 5CB filled PVP fiber, approximately 3 μm thick, has 5 twisted spots. Each black vertical line perpendicular to the fiber has a bright spot surrounding it. Spot 1 between crossed polarizers at 0° is bright red, while spot 2 has a white background. When the analyzer is turned clockwise or counterclockwise by up to 60° the interference colors on each side of the black defect line shift towards longer and shorter wavelengths on either side of the black line. This shows that the director field is twisted around the black lines with opposite handedness on each side of the line. Scale bars: 10 μm

Additionally, there is no strict condition that requires that any type of twists be found in the cylindrically confined chromonic LC, and according to Nayani et al., since the calculated free energy does not change when the sign is inverted, it means that there is an equal probability of finding just as many areas that are left twisting as there is finding those that twist oppositely. When turning the analyzer between +60° and -60° the illuminated defect spots in the filament shown in Fig. 6.7 all change from showing a single interference color to showing alternating colors on each side of the black line. Spots 1, 3, and 4 start off having symmetrical bright orange-red spots and once the analyzer is turned to 60°, the bright spots all become asymmetrical; one side showing red interference and the other side of the defect wall showing cyan. Spots 2 and 4, on the other hand, start off white and end in showing the blue-yellow pair.

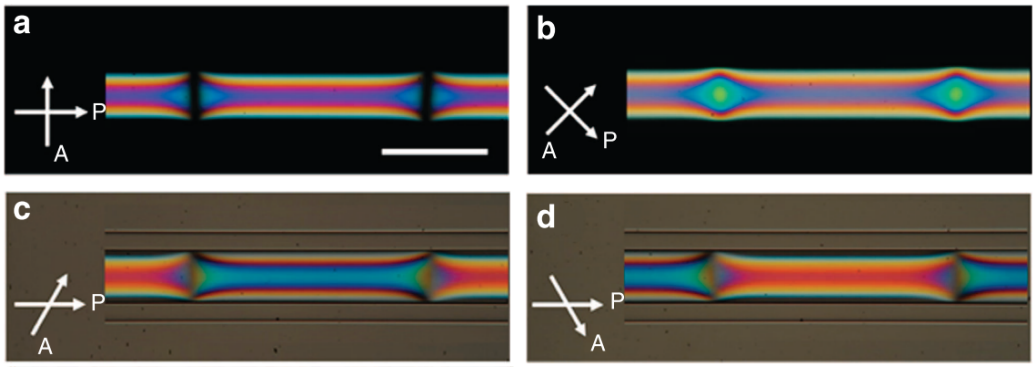

Fig. 6.8 – The images above from Nayani et al.'s study [195] show that when a cylindrical capillary filled with an achiral chromonic nematic LC (DSCG in water) is examined between crossed polarizers (P-polarizer, A-analyzer) through the POM, and the analyzer is rotated, the LC shows complementary changes in interference colors in adjacent regions. This indicates the presence of left and right handed twists, respectively in the director field of the regions. In (a) and (b) the capillaries are examined with the analyzer crossed 90° to the polarizer, and in (c) and (d) the analyzer is crossed at $\pm 60°$ to the analyzer. Images (a) and (c) show how the twist appears in the capillary when it is separated by black lines (similar to what was seen in the fibers of Fig. 6.5 and Fig. 6.7). Scale bar: 100μm (These images were adapted from ref. [195] (Fig. 4), with permission from the Nature Publishing Group under the license: CC BY 4.0)

Although further experiments to determine what types of bright spots were forming inside the fibers, whether they were walls or point defects (as per Wang et al. [200]), and check whether their morphology could be influencing the 5CB director to adopt local twists, were not performed, the POM evidence thus far obtained showing that these features can exist in the non-beaded 5CB-PVP electrospun fibers is enough for asking the question: If several areas in the fibers can have chiral symmetry breaking of the director, then can these areas influence how the scattering of the fiber mats, and also filaments, respond to volatile organic compounds (VOCs)? This question is finally explored in the next section, with the more quantitative gas sensing analysis continued in ch. 7.

6.4 The fiber mats respond to VOCs through a phase transition

To recap the study by Reyes et al. [70], several types of 5CB-PVP fiber mats were electrospun and exposed to a VOC (here, toluene vapors) to see whether the LC confined in the fiber mats would respond, and to determine how visibly detectable the response was without the use of optical or other electronic equipment. Ultimately, we saw that exposing the fiber mats to toluene vapor resulted in an immediate decrease in fiber mat brightness between crossed polarizers, associated with the nematic to isotropic transition of the 5CB in the fibers. The reduction in brightness was completely reversible once the VOC was taken away, and it usually took less than 10 seconds for the original mat birefringence to return. Microscopically, the transition between nematic phase to the isotropic phase, and back, of the 5CB was also seen to occur within the exposed area in this time frame (Fig. 6.9).

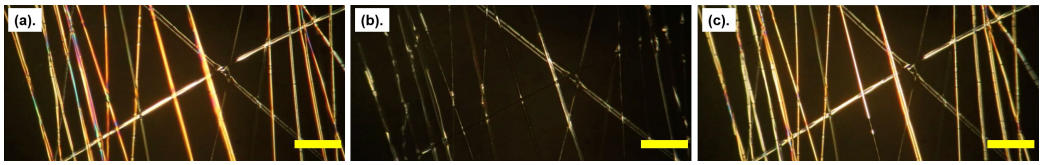

Fig. 6.9 – An area containing non-beaded 5CB-PVP fibers responding to toluene vapors in ambient air seen between crossed polarizers via the POM. Non-aligned, non-beaded and originally birefringent PVP fibers containing 5CB (a) were exposed to toluene vapors generated using the macro-sensing setup (shown in sec. 3.2.1) (b).When the toluene vapors are removed, the 5CB nematic phase returns (c). The experiment went on a few seconds longer than shown in (c). On average, it takes about 5 seconds for the original state in (a) to return completely. This time dependence is further discussed in ch. 7. Scale bars: 80 μm (This image was originally shown in ref. [70] (Fig. 4), and adapted here with permission from Taylor & Francis under the license: CC BY-NC-ND 4.0.)

Moreover, while it was confirmed that both aligned and random, free-hanging and non-freely hanging, beaded and non-beaded 5CB filled PVP fiber mats were able to respond to the toluene vapors, two categories - the beaded fiber mats, and the non-beaded aligned fiber mats seemed to have two different sets of visual responses. The beaded fiber mats, when exposed to vapors, showed scattering responses that were visible without the need for polarizers and illumination for contrast enhancement. The potential reason why has partially to do with the sheaths of the individual beaded fibers being able to reversibly deform each time they were exposed to the gas, and is discussed in further detail in sec. 6.4.2.

Meanwhile, the non-beaded aligned LC-PVP fibers appeared to show two types of scattering responses (a fast and a slow one) occurring simultaneously while exposed to the gas. However, only one of these two responses seemed to be clearly visible only when the fiber mat was oriented near 0° to the bottom polarizer. When the aligned fiber mat was oriented 45° (maximum brightness for the uniformly aligned LC director, as explained in sections 6.2 and 6.2.1), both of the responses overlapping one another were seen to occur. The major qualitative difference between the two responses in these aligned mats seen was that they exhibit different delay in both starting and disappearing; that is one response would be seen to occur a second or two faster before the second one started, and when the original ground state scattering of the mat was returning, one response would linger for a few seconds after the other fully disappeared.

6.4.1 Non-beaded & aligned mats show two responses to VOCs

An example of the aligned fiber mat responding with two changes in brightness is shown in Fig. 6.10. This image is similar to the one discussed in ref. [83], but not exactly the same as these were taken from another sample exposed to the vapors using the same technique.[†] The top row images (a - e) show the aligned fiber mat oriented parallel to the bottom polarizer (or, at 0°) as it is being exposed to toluene vapors. Additionally, in each of the top row images, the approximate area of the scattering response observed, relative to the size of the entire mat of the glass slide, is outlined in cyan. The non-outlined images of the responding mat is shown as

[†]The results regarding the two scattering responses observed in these types of fiber mats published in ref. [83] used the updated darker macroscopic polarizers, while previously in ref. [70] poorer quality polarizers (that allowed a greater amount of ambient light to filter through) had been used. The results from ref. [70] were confirmed to be reproducible in the later paper, however, even when the newer polarizers were used.

insets at the top right corner for reference. The bottom row images (f - j) show the aligned fiber mat being exposed to the same amount of vapors as in the top row, when the mat is aligned for maximum brightness at 45°. In both cases the toluene vapors are being actively generated using the microfluidics gas sensing setup previously discussed in sec. 3.2.1.

Starting from the first row images, the vapor exposure tube emitting toluene vapors is held a few centimeters away from the surface of the fiber mat on the glass slide and a reduction in nearly half of the mat's original scattering is instantly seen. This reduction in scattering is the result of the 5CB nematic phase transitioning to the isotropic phase in the individual fibers (a microscopic view of how this usually appears was shown in Fig. 6.9 using randomly oriented non-beaded fibers). Since the electrospun PVP fiber mat without the LC filling lacks high birefringence and cannot change the light polarization as much as the LC filled fiber mats (discussed in relation to Fig. 6.1), once the 5CB nematic phase in the exposed fibers clears to its isotropic state, the only contribution to the birefringence in that area of the mat will be the very weak one from their polymer sheaths. Thus, the mat appears darker in that exposed area than other parts of the fiber mat that were not exposed vapors. This is the sensing response seen.

The reduced brightness observed in certain areas of the mat that are exposed to vapors does not always remain segregated to those parts, however. Sometimes when one corner of the mat is exposed, the response seen appears to extend across a long distance over the mat. As shown in image (c) of Fig. 6.10,] when the exposure tube was taken away from the mat, and the vapor delivery stopped, the response appeared to take over a wider area of the mat compared to how it originally looked in image (a).

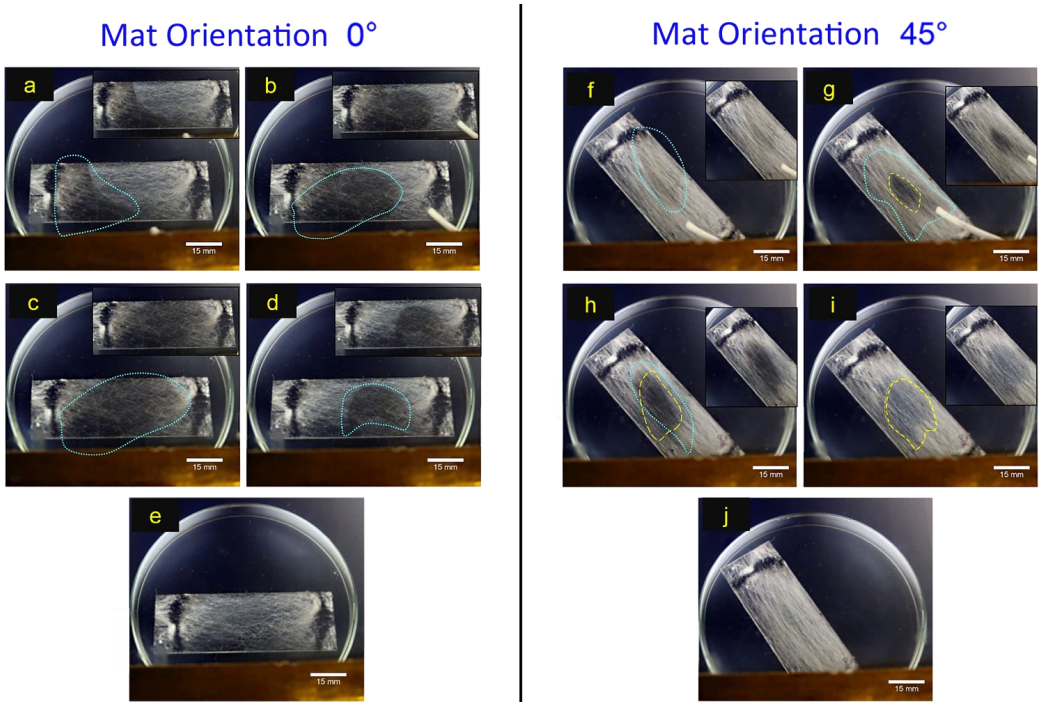

Fig. 6.10 – Two macroscopic responses seen in an aligned and non-beaded 5CB-PVP fiber mat while exposed to toluene vapors via the non-enclosed method (sec. 3.2.1). The aligned fiber mat was oriented in two directions: 0° (a-e), and 45° (f-j), while exposed to vapors between crossed polarizers. In (a - b) the mat is exposed to vapors roughly 5 cm away and the mat shows an immediate decrease in brightness (cyan outline). In (c-d) the exposure tube has been taken away, but the response still lingers until reaching its ground state (e). At an orientation of 45° (the brightest state) during exposure a second response (yellow outline) emerges later (f-h) and dissipates last (j). Images of the responses without the outlines are also shown in the top right. White scale bars: 15 mm

The reason is likely that for this series of macroscopic vapor exposure tests, the fiber mats were exposed to a concentration of toluene vapors in a ventilated fume-hood which had constant air flow. Since the polymer sheaths are porous to toluene vapors (but do not dissolve), and with help from the circulating air in the fume hood, the vapors can easily spread over multiple areas of a single mat and trigger the nematic clearing several centimeters away from the initially exposed location. Finally, it is not until a few seconds later that the original brightness of the mat, corresponding to when the nematic phase reappears in the individual fibers, finally starts to return (Fig. 6.10d). The original ground state of the mat returns a few more seconds later (Fig. 6.10e). In total, it takes less than about 8 seconds for the whole sensing process, from the time of initial vapor exposure to the loss and return of the original fiber mat brightness, to complete in this mat.

As mentioned earlier, the interesting quality about this aligned mat in Fig. 6.10 is that a second delayed response appears to be happening simultaneously if the mat is oriented 45° to the polarizers during vapor exposure, or while the first visible response (outlined in cyan) when the mat is oriented at 0°, is still present. Images (g - i) show two outlines indicating where the two responses (cyan - the first, and yellow - the second) overlap. Finally, it appears as though the second response is the last of the two to fully disappear (Fig. 6.10i). This means, however, that since the second response leaves after the first, if the mat positioned at 45° is turned back

to its original 0° position (as shown in the top row images), this lingering second response will not be visible.

Since the visibility of these two responses appeared to depend on how the aligned mat was oriented to the polarizers, it was initially believed for a while that the confined 5CB in the fibers actually underwent two types of transitions during toluene vapor exposure. Given the recent studies mentioned earlier about how nematic LC phases comprised of achiral molecules could have directors that adopt asymmetrical twist configurations with wall defects when cylindrically confined [58, 195, 196, 199, 201], and a recent report by Marco Bedolla-Pantoja and Nicholas Abbott [80] describing how thin films of confined 5CB could undergo an anchoring change from planar to homeotropic alignment when exposed to low concentrations of toluene vapors, it seemed plausible that perhaps one of the changes seen in the aligned mats (outlined in cyan - Fig.6.10) was in fact due to an anchoring transition taking place. The later occurring transition that seemed to linger longer, and also start later (outlined in yellow - Fig.6.10) could then actually be the rest of the non-twisted uniformly aligned 5CB director in the fibers clearing to the isotropic phase.

Are director twists responsible for the double response in aligned 5CB-PVP fiber mats?

To recap, the initial idea was that since the bright defect-like spots shown in Fig. 6.5 and in Fig. 6.6 appeared often throughout many of the electrospun fibers, and since these spots (most of the time) appeared to consist of very short but clear parts containing director twists, during VOC exposure, the first scattering response seen was thought to have been due to these specific areas experiencing an untwisting of the director before undergoing a phase transition later. The second more contrasted response seen occurring slightly later and lingering for a longer time was then thought to be the actual clearing of the nematic phase. The reason why this was first hypothesized came from the results of the study by Marco Bedolla-Pantoja and Nicholas Abbott [80]. They revealed that very low concentrations of toluene vapor are actually enough to trigger a hybrid 5CB director to undergo an anchoring change to adopt a uniform director throughout the bulk.

To first achieve the hybrid director in a sample of 5CB, a director that starts off as planar against one surface and progressively realigns to homeotropic towards the opposite surface, Bedolla-Pantoja and Abbott created epoxy based microscopic wells in glass slides that could contain very thin, precisely confined films of 5CB. The films of 5CB were in contact with 3 entities - the glass on the bottom (which imparts planar alignment), the epoxy walls on the sides (planar alignment), and the open air at the top (homeotropic alignment [202, 203]). Since these thin films are elastically strained to start off with, their director being deformed in the bulk since it is confined against different interfaces, when exposed to toluene vapors, the director along the glass surface (with lower anchoring energy) will prefer to adopt the homeotropic alignment (the same as the air interface) *before* the bulk nematic phase transitions to the isotropic. This is significant because their finding indicates that confined 5CB with a non-uniform director can show two types of responses to VOCs (the director becoming uniform through an anchoring transition, and the nematic-isotropic phase transition).

In our case, the lines in the fibers which originate during the electrospinning process[‡] are related to short regions nearby to adopting a twisted director configuration. This is not the same as the hybrid director seen in the films previously described, but similar, in that both are examples of a deformed director field. The majority of the LC in the fibers containing a uniformly aligned planar director, and the presence of these local "spots" where the twisted director is present (due to the tight 2μm - 4μm wide cylindrical confinement) could, therefore, cause the 5CB to be elastically strained enough to exhibit these two forms of responses during vapor exposure as well. Moreover, the reason why these two responses could only be visible for the aligned non-beaded fiber mats, it was originally thought, was as follows.

Since many of the LC-fibers have a uniformly aligned planar director along the fiber lengths, apart from the presence of the non-extinguishing bright spots which are constant at all rotations, if the fibers are oriented in non-right angles to the crossed polarizers then their cores will exhibit some level of birefringence that will increase the overall brightness of the mat as a whole. This is why if the randomly aligned LC-fiber mats are rotated between crossed polarizers they do not have different ground states of scattering; the base brightness overall is already the highest it can be with all the fibers randomly oriented over each other (Fig. 6.1b). However, if most or all, of the fibers are aligned in one general direction, and this mat is oriented at the right-angles of the crossed-polarizers, then the uniformly planar aligned director in those aligned fibers will become extinct. They will not contribute to the brightness of the aligned mat in this orientation.

Of course, not all of the fibers end up exactly aligned during electrospinning as desired. This means that whatever brightness of the mat does emerge when the aligned mat is rotated to the darkest orientations will mainly be due to the birefringence of these unaligned fibers, plus whatever small birefringence the polymer sheath imparts from being stretched, and the non-extinguishing bright defects. Therefore, the aligned mat has two main levels of brightness visible, the minimum at 90° or 0°, and the maximum, when the mat is oriented at 45°. The anchoring change would only mainly be visible when the mat is at the orientation with the lowest brightness because this response would then be highly contrasted against the majority of the fibers which are aligned to have decreased brightness to start off with. At 45° the mat shows its maximum birefringence effect so it would make sense that the first response is not visible (Fig. 6.10f) until the later response (the nematic clearing) optically provides a higher contrast for the first response to get noticed since the phase transition reduces the fiber mat scattering substantially as well (Fig. 6.10g). This seemed to be the most plausible explanation at the time.

However, if these points containing director twists were truly the source of a scattering response due to an anchoring change during gas sensing, and if it is true that in order to see this change we need to have non-beaded fibers oriented in an aligned manner in order to see it, then one way to prove this would be to attempt to reproduce the two scattering responses in other types of LC-fiber mats using an external stimulus other than organic vapors.

So far we had identified that during gas sensing experiments, the toluene vapors are absorbed by the fiber sheaths and enable the nematic-isotropic phase transition by lowering the transition temperature of 5CB from its pure bulk value (roughly 35°C) to room temperature [70]. The toluene vapors do not heat the sample to reach 35°C for the nematic to clear, rather they act

[‡]Exactly how? and why? are still two questions that could be topics for future research. All that is presently known is that several of these types of defect walls tend to be present throughout several fiber cores in the LC-fiber mats produced, are stable (unless the sample is exposed to external stimuli), and appear in random locations in the fiber cores. A recent report on coaxially electrospinning MBBA (another nematic LC compound, CAS #: 26227-73-6) with PVP has also shown POM images of fibers having these defects as well [204].

as impurities for the director and disrupt the molecular ordering. This reduction of order, in turn, causes a lowering of the clearing point and we see the transition to the isotropic at room temperature.

Additionally, Fig. 6.11 shows that if randomly oriented beaded fibers containing 5CB and the nematic mixture E7 are heated to three temperatures, the double response is seen to occur at least for the 5CB sample, at 38°C (cyan dot indicating the first scattering change seen, yellow dot: the second scattering change). Therefore, were the first hypothesis (stating that a low level of ground state scattering is necessary to see the fast response) correct, we would not have observed a response occur in a randomly oriented sample with a higher level of scattering present than the aligned mats.

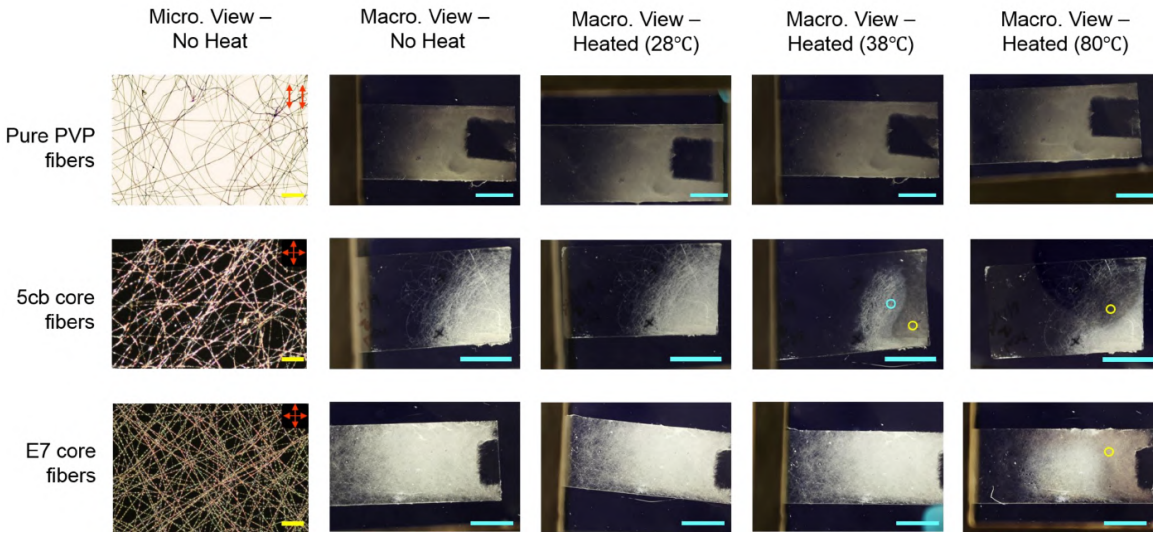

Fig. 6.11 – Three electrospun fiber mats, one containing just PVP fibers, and two containing 5CB and E7 in the fiber cores were first heated on a hotplate placed next to the macroscopic polarizer and light box setup. The mats were heated at each temperature (28°C, 38°C, and 80°C) for about 10 seconds then immediately transferred to between the crossed polarizers to see if any changes in scattering (similar to the toluene vapor responses) were observed. The pure PVP fiber mat showed no response at all after heating it to 80°C. The 5CB mat showed the double response as seen before in Fig. 6.10 occurring at 38°C (cyan - first response, yellow - second). At 38°C only the second response appeared. All responses simultaneously occurred as the samples were being heated. The E7 sample only showed one response at 80°C. Scale bars: 10 mm (light blue), 100 μm (yellow)

Second, clearly the two responses are visible for a beaded sample, so it means that defects seen in the non-beaded samples may not be necessary to induce the double response. Some of the beaded fibers only show these wall defects on the non-beaded sections, and some beaded fiber mats do not show these types of defects at all.

Third, the two responses emerged while heating the sample above the bulk clearing temperature of 5CB, it should have happened at a lower temperature distinct from the phase transition temperature. Fourth, because E7 has a higher clearing temperature (closer to 60°C) fibers containing this LC should not respond to a temperature lower than this value (unless if there is an impurity like significant excess solvent or something else in the cores) which when heated here did not.

While the double responses occurring in the aligned fibers do not negate the existence of defects and local areas in the cores with a twisted director field, the defects and twists do not suggest that an anchoring change is responsible for one of the two forms of scattering observed in Fig. 6.10 and Fig. 6.11. What is more likely is that both responses are actually stem from the 5CB clearing response from the nematic to the isotropic phase.

The main difference in why we see two types of scattering responses is that, one, because of the difference in the ground state scattering that the aligned samples can give when rotated a certain way, and two, not all sections of the fibers are clearing to the isotropic at once. For the beaded fibers, the non-beaded sections have less LC volume than the beaded sections so they will clear first. It will take a bit more vapor exposure fully clear the beads, and also maintaining the direction of the exposure tube steady so that previously cleared non-beaded sections do not rebuild the nematic phase once the vapor evaporates (discussed more in ch. 7).

Additionally, not all non-beaded fibers are the exactly the same thickness and they may have variations in core filling as well. The first macroscopic response seen at the lowest base scattering may just be due to the least filled sections clearing first. Microscopically, these were not able to be distinguished because in order to pinpoint the lowest fractions of toluene vapors that could induce a response in the 5CB cores short segments of the fibers at very high magnifications needed observation. Thus, correlating the macroscopically observed double responses (seen for a wide area of several cm^2) with what was observed in a minute area (a few hundred μm^2) in a few fibers was not feasible.

Last, the positioning of the exposure tube over the mat in these experiments with the Fluigent unit generated vapors, and the air currents from the fume hood dispersing the vapor, will cause some fiber sections to experience a slightly higher dose than other areas. This will initiate clearing in selective areas earlier than in others. It is only when the exposure tube is held at the same location for more about 4 to 5 seconds that a full clearing of that location (a strongly contrast response) will be noticeable.

6.4.2 Beaded mats respond macroscopically (polarizers not necessary)

While the previous section details the unexpected appearance of two types of responses seen in aligned, non-beaded fiber mats during toluene vapor exposure, the method through which the scattering responses were seen was largely avoided. Why did we need to insert these fiber mats between crossed-polarizers in order to see the responses in the first place? Can we not see the responses occurring with just unpolarized ambient lighting? The answer to the last question is no. Unfortunately, one aspect that may be necessary to improve in these types of fiber mats, depending on the intended application, has to do with enhancing the contrast visibility of the scattering responses when the mats are being exposed to VOCs without needing the polarizing films and a back light.

So far, only the beaded LC-fiber mats, produced in either humid conditions (above 30% RH, but below 60% RH) or with higher LC flow rate, can be exposed to toluene vapors and display scattering responses that do not require optical polarizers for these responses to be seen (Fig. 6.12). In other words, these responses are visible in ambient room lighting using the "naked eye."

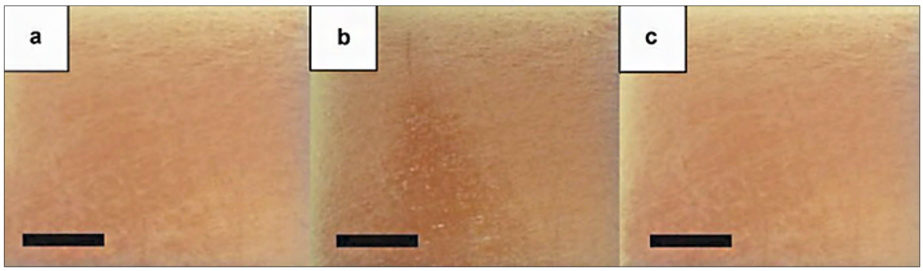

Fig. 6.12 – A beaded fiber mat was exposed to toluene vapors in ambient air using the non-enclosed method, and showed visible changes in mat scattering without the need for optical equipment to view the responses. These three screen shots were originally used in Ref. [70], Fig. 8(a-c), and are re-used here with permission from Taylor & Francis under the license: CC BY-NC-ND 4.0. The fiber mat in (a-c) was electrospun in an atmosphere containing 25% relative humidity, and beaded fibers were created by increasing the core flow rate such that it was slightly higher than that of the polymer solution rate. The images show a zoomed-in section of the fiber mat over the glass slide placed over a red background. When the sample is exposed to toluene vapors, the center portion becomes transparent and shows the contrasting background underneath (b). When the toluene vapors are removed the original scattering of the fiber mat returns as it was in (a). Scale bars: 10 mm

While Fig. 6.10, Fig. 6.9 and Fig. 6.11 show that during heating and also during VOC exposure, the LC encapsulated in the PVP polymer fibers is definitely necessary to allow the responses to be observed, from Fig.6.12 we know that to be able to visualize the responses macroscopically and in ambient lighting, the best option is to have a mat comprised of beaded LC filled fibers as opposed to one containing only just non-beaded filaments.

The reason why can be attributed to the overall volume increase and the greater variation of director orientation that the beaded fiber mats have, as opposed to the non-beaded fiber mats. Recall that sec. 4.3.2 hypothesized that two filaments, one beaded and one non-beaded, could have an LC core volume difference of at least 5:1 (the larger value for the beaded fiber) based on actual SEM measurements of several fiber widths and their cross-sectional diameters. Although the calculation assumed that the beaded fiber would have beaded sections that were all the same size, and that they have thinner polymer sheaths than those of the non-beaded sections and the non-beaded fiber, this estimate seems plausible in supporting why the visibility of the scattering responses is more apparent. With more LC in the fiber present, and differences in sheath thickness throughout the beaded morphology, the overall mat will scatter more strongly. So when the LC clears, the scattering loss from these fibers turning isotropic is more noticeable in ambient lighting.

A drawback of this beaded fiber mat type, however, as discussed earlier in ch. 4 on ideal coaxial LC-fiber formation, is that the beaded sections can be prone to rupture and leak more easily due to their thinner sheath overall, compared to that of the non-beaded filled fibers. Likewise, another drawback is that the more LC is present, the longer it may take for the beaded sections containing LC to fully transition to the isotropic phase (ch. 7 discusses this point in more detail). This means then that, potentially, the onset scattering response, as well as the relaxation back to the original scattering state can be delayed, and the threshold can increase. Moreover, with increased exposure time necessary for these fibers with greater LC volume to fully clear, the risk that the polymer sheaths comprising the integrity of the fibers can irreversibly deform (or degrade) grows higher with repeated use.

A closer look at the sheath of beaded fibers

These last points regarding sheath deformation and prolonged relaxation time, respectively, were further examined using the POM by focusing on what happens to two beaded fibers containing 5CB while they are exposed to toluene vapors. To address the latter point first, consider Fig. 6.13. There we see that it can take as much as 18 seconds (last image in part a) for the original birefringence of these fibers to return after the 5CB within both completely clear to the isotropic state.

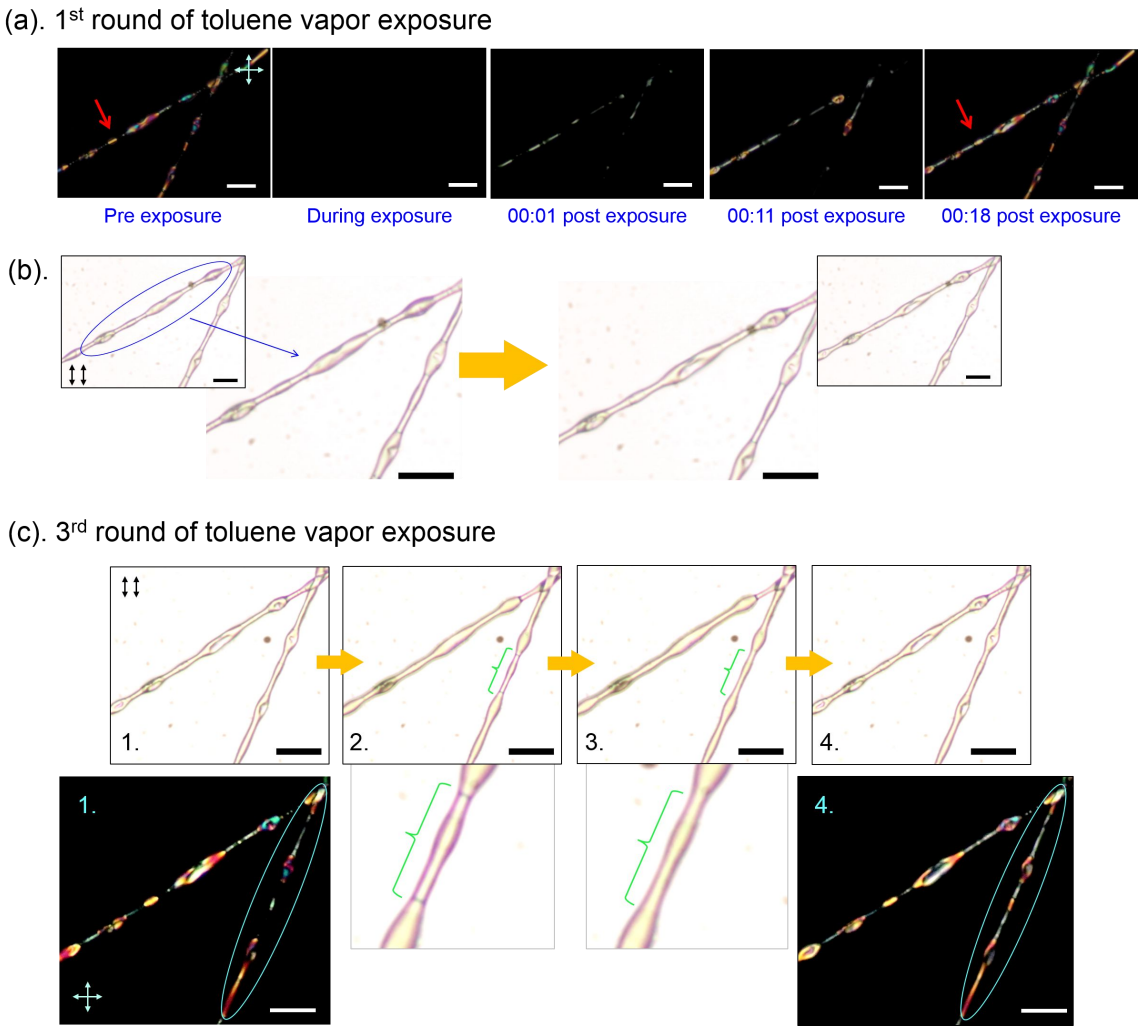

Fig. 6.13 – A 5CB-PVP fiber mat containing beaded fibers were exposed to toluene vapors using the macroscopic exposure method from sec. 3.2.1 while on the stage of the POM. See main text for details. Scale bars: 20μm

Compared to the non-beaded 5CB filled fibers which took, in total, less than 10 seconds to clear and return to the nematic phase, the transition observed here was significantly delayed during this first round of vapor exposure. This is also despite the fact that before exposure (first image in Fig. 6.13a) the beaded fibers were confirmed to have discontinuous filling.

To summarize the results shown in Fig. 6.13, two fibers were focused on to observe any changes to the polymer sheath. In left most image of Fig. 6.13(a), before exposure, the 5CB

filled fibers were birefringent but had some gaps ($\geq$3 μm wide) in the filling (red arrow points to the area). During exposure in Fig. 6.13(a) the nematic proceeded to fully clear to the isotropic state, and once the vapors were removed it took roughly 18 seconds for the original scattering to return. However, when the nematic phase reformed, some 5CB from the section above where the red arrow is pointing actually flowed into the gaps that were present before VOC exposure (right most image in Fig. 6.13(a)). A portion of the left-most beaded fiber gains birefringence, developing gray interference color, when before it was black.

This flow of LC was also accompanied by a swelling of the beaded fiber sheath during exposure, left image in Fig. 6.13(b). It swells during exposure (shown in Fig. 6.13(b) and in image 2 of Fig. 6.13(c)), and de-swells once the nematic phase returns. With repeated exposure, the de-swelling process is also accompanied by a permanent semi-flattening of the beaded sections (Fig. 6.13(c) showing that when the LC moves from a beaded section, it leaves behind volume without LC in the bead that immediately flattens once the fibers release the absorbed vapors. This was easily visible on the 3rd round of exposure where the right most fiber in Fig. 6.13(c)) showed that these air gaps merge (2, 3) in plane polarized light, and the 5CB is forced to fill up the entire fiber after relaxing.

Ultimately, this series of experiments for these two beaded filaments show that if large gaps in the fibers are present, the VOC molecules entering the fibers can cause them to swell and cause the LC to move upon relaxation. When the VOC escapes through the pores of the fibers, the sheath deforms and pushes the LC from the sections with more volume into the gaps with little or none.

A question that remains for possibly future explorations, however, is how large do those gaps have to be for the 5CB to be forced to move throughout the filaments during gas sensing experiments? Clearly a factor that influences the situation is if the fibers are exposed for a certain amount of time, as shown in Fig. 6.13(c) in images 2 and 3, where the endpoints of two gaps in one fiber happened to be visible under plane polarized light and appeared to merge under prolonged vapor exposure. When the vapors were removed and the nematic phase reformed, that fiber no longer had gaps throughout its length (6.13(c), image 4). It did, however, have a few defect lines present though. While it is difficult to say whether these tiny defect lines appearing in the fibers are actually tiny air gaps or indeed defects in the nematic phase, because first, they are not even a micron long, and second, they have birefringent LC fluid immediately surrounding them, from the investigations discussed throughout this section that they do not seem to have any significant role in influencing the optical responses seen.

On the other hand, air gaps in the fibers, at least for the beaded ones, that are wider than a micron long can potentially influence the responsivity to VOCs. To summarize, the air gaps in the fibers can allow the LC to flow within the fibers when they are repeatedly exposed to vapors, and this flow can cause the collapse of sections of the polymer sheath. This definitely contributes to the eventual degradation of the fiber mat, and also how the scattering responses are perceived. If there are no air gaps in the fibers, movement of the LC throughout the fiber lengths is not expected to occur. However, it is true that if the fibers are beaded, they will likely have more LC core volume than those which are non-beaded, and they should take longer to respond.

This also depends on the concentration of the vapor that is delivered as well. In this section, all of the fibers and fiber mats were exposed to toluene vapor concentrations that were quite high (the estimated amount was at least 57 μM, or about 1400 ppm). The next chapter discusses

whether the fiber mats are responsive to lower concentrations, and whether time delays in response were visible for different sections containing beads or not.

7 The VOC responsivity threshold of 5CB-PVP fiber mats

7.1 Results overview & recap

The last three chapters discussed the following:

- the importance of key parameters affecting the coaxial electrospinning process for creating "ideal" (non-leaking, and non-meshed) LC-PVP microfiber mats
- how the miscibility of the LC with a polymer solution's solvent can completely disrupt the spinning process and fiber formation
- how the unique optical properties of well formed LC-fiber mats (with different fiber morphologies and mat alignments) enable us to see their responses to VOCs at room temperature with and without polarizers

In particular sec. 6.4 of ch. 6 revealed that the response of LC filled beaded and non-beaded fiber mats, with fibers oriented in different directions (aligned and random), responded to toluene vapors by undergoing a nematic to isotropic phase transition. This was made possible by the toluene vapors absorbing into the fiber sheaths and essentially lowering the nematic-isotropic clearing temperature of the confined 5CB down to room temperature [70]. Macroscopically, this transition is qualitatively visible as a reduction in overall mat brightness when the fiber cores cleared to the isotropic state at the microscopic level. Once the vapors were directed away from the mat, the original appearance the mat had, prior to exposure, returned after several seconds. For the beaded fiber mats, prolonged or repeated exposure to the same high concentrations of toluene vapors irreversibly caused the polymer sheaths to sink in at some beaded areas. This then enabled the 5CB confined within to move throughout the filament. Seeing this happen further underscored the importance of achieving uniforming LC core filling within the filaments, as the timing of how visible changes developed in response to VOC exposure (like the double responses discussed for the aligned mats) can be influenced by these morphological changes in both core filling and sheath structure.

Additionally, these responses were also shown to be non-selective and non-specific to toluene vapors. When 5CB and E7 filled fiber mats were heated above room temperature to their bulk clearing points (near 35°, and 60°, respectively), the mats each displayed similar responses to those observed when the mats were exposed to toluene gas. However, changes in mat appearance were clearly the result of LC confined within the fiber cores. When sets of pure PVP electrospun fiber mats were heated at the same clearing temperatures and exposed to the same concentrations of toluene vapor, they did not reveal any responses. Polymer sheath structures alone are not enough to make the proposed non-electronic flexible textile gas sensor.

This chapter continues the analysis of the 5CB-PVP fiber mat responses to toluene vapors by demonstrating two ways in which quantitative values of their sensitivity to the vapors

can be found. Moreover I will discuss the advantages and disadvantages of using both, and disagreements that results of both approaches show and what can be done to improve them. Next, an explanation to an observation that was brought up in last chapter – the idea that multiple responses observed in LC-fiber mats are due to certain sections of fibers undergoing the nematic to isotropic phase transition faster than others (especially more pronounced for beaded filaments) – will be confirmed here. Finally, the last section of this chapter is dedicated to discussing ways in which the 5CB-PVP fiber mat sensors can be improved to be more chemically selective and sensitive to other VOCs.

7.2 Micromolar or Parts-per-million? A note on the units used here

Before continuing the discussion on the ways in which the minimum threshold concentrations of toluene vapor exposed to LC-PVP fibers can be determined both microscopically and macroscopically, I will just say some words about the units of vapor concentration I chose to use for my results. Although unconventional when describing concentrations of gases, I chose to use the units of micromolar (μM) because it is an accepted SI (International System of Units) unit which describes most accurately the concentration of toluene vapors I generated and passed through my syringe-aluminum-gas-cell system (described in sec. 3.2.2). Unlike the non-SI unit often used (and misused) notation of "parts-per-", the base unit of molarity is unambiguous and cannot be misinterpreted in its meaning. The statements below briefly describe the issue with using "parts-per-" notation and how it can be easily misinterpreted by researchers in both academia and in industry.

In September 1999, Brian Petley submitted a report to the IUPAP (International Union of Pure and Applied Physicists) General Assembly summarizing one of the most pressing issues on the minds of the IUPAC (International Union of Pure and Applied Chemists) Interdivisional Committee on Nomenclature and Symbols: "A continued source of annoyance to unit purists has been the continued use of percent, ppm, ppb, and ppt. There is also the general problem of conveying large or small values of dimensionless quantities in conversation. This has been raised over a number of years at the CCU [The Consultative Committee for Units]." [205]. At the end of the meeting while many members agreed that a change in how very small unitless numerical fractions were described, they seemed to equally disagree on what to replace the "parts-per-" notation with. Percent, although also not part of the SI, was decided to be kept as it has already become customary in many disciplines to use (sometimes incorrectly used in describing concentrations as well - e.g. "1% solution" is assumed to mean "1 mass unit per 100 volume units" for example).

The root of this ongoing problem with using the "parts-per-" notation for denoting fractions that are considered micro- (10^{-6}), nano- (10^{-9}), pico- (10^{-12}), or even femto- (10^{-15}) is that the body responsible for organizing the SI (the General Conference on Weights and Measures) never, officially, authorized any type of units to describe dimensionless quantities to begin with [206–208]. While the conference agrees that it is acceptable to add prefixes in front of symbols as an alternative to using scientific notation (e.g. 1 μm instead of 1×10^{-6} m), and that certain same-unit per same-unit fractions* can have symbols to represent them (e.g. refractive index

*These are often referred to as "concentration units", but actually are not if they measure the same type of quantity. In other words, 0.5 mmol/mol should be referred to as a "mole fraction" because it denotes a ratio

(n) - the speed of light in a vacuum divided by the speed of light in a medium), there is no consensus as of yet how to call fractions derived from very small quantities without having to resort to saying, or writing, values with many leading zeros after the decimal point.

Although the act of introducing the terms parts-per-million (ppm), parts-per-billion (ppb), and parts-per-trillion (ppt) was well intentioned for enabling more succinct discussions of very small value fractions, the trouble with becoming accustomed to using them to describe fractions is hardly that they sound odd to "unit purists", but that they can convey erroneous information on how certain measurements should be made. This in turn can have unwanted practical consequences. For example, researchers in atmospheric science communities have found that using ppm to (incorrectly) denote a concentration can be easily misunderstood by others to mean either mass mixing fractions, volume fractions, or even mass concentrations [209]. The ambiguity can really be enormous, and even if commonly practiced within sub-fields, for researchers working interdisciplinarily (more usual these days [210]) it becomes increasingly difficult to understand what actual measurement the abbreviation implies. A quantity like "5 ppm" reported as is can either refer to "5 μg/g" (a mass fraction) , "5 μL/L" (a volume fraction), or even "5 mg/L" (a concentration - which is still questionable because it assumes that the density of the liquid is exactly always 1.0 g/mL, which even for water, changes with the temperature).

For these reasons, as mentioned earlier, when discussing all vapor concentrations and sensitivity thresholds in this chapter I will use the concentration units of molarity: moles of vaporized VOC per liter of air, so that it is unambiguous as to how much actual vapor content there was for a given volume. As shown in Table 7.1, the various PELs (permissible exposure limits) reported in ppm for toluene vapors designated by OSHA (The Occupational Safety and Health Administration) and NIOSH (The National Institute for Occupational Safety and Health) of the United States generally correspond to very very low true concentrations (here shown in μM). OSHA and NIOSH make equivalent 1 ppm of toluene to 3.77 $mg_{toluene}/m^3_{air}$ (or roughly, 1 $mg/m^3 = 0.27$ ppm) [211, 212]. Setting aside that from a dimensional standpoint this equivalence of ppm to mg/m^3 (a concentration) is improper, if this equivalency is taken as convention, then it means all of the measurements in studies which are compared to it must not only be converted to these same concentration units, but also the methods in which those concentration values were acquired should be in agreement with those used by NIOSH (or another health agency reporting exposure limit values).

between milli-moles of something to the total moles present in something else. It can also be converted to mol.%, but still remains a dimensionless value. However, many researchers would refer, or have referred, to mol% as a unit of "molar concentration." A unit of molar concentration is defined as the ratio between the number of moles per total volume present. The same is true for vol.% and wt.% which are not true concentrations either, but fractions of quantities [209].

Tab. 7.1 – U.S. OSHA and NIOSH determined exposure limits to toluene vapors, divided by profession for OSHA, in non-SI units of parts-per-million (ppm) and SI units of micromolar (μM). The red outlined areas indicate the values in μM which will be referred to in the text. † - TWA is the "time weighted average" exposure value and refers to the maximum amount of exposure which is acceptable for a person working an average 8 hour day in the presence of the VOC. (‡) - PEL is the "permissible exposure limit" of which the TWA and any other maximum exposure limits (like short term 10 or 15 min., or the ceiling limit) are a part of. See refs. [211, 212] for more information.

NIOSH	150 ppm (15 min.) = 6.1 µM (15 min.)			
		In General Industry	In Construction Industry	In Shipyard Employment
OSHA	PEL (µM)‡	• 8.1 = TWA† • 12.2 Ceiling • 20.2 (10 min.)	8.1 = TWA†	8.1 = TWA†
	PEL (ppm)	• 200 = TWA† • 300 Ceiling • 500 (10 min.)	200 = TWA†	200 = TWA†

For instance, confusion can arise from the following situation: if I am told that the PEL (permissible exposure limit) for toluene vapor is 500 ppm and I create a solution that is comprised of 500 $\mu L_{toluene(liq.)}/L_{air}$, and my sensor exposed to this mixture tests positive for detecting it, I would assume that my sensor was successful in detecting the regulated PEL for toluene vapor. However, because the information that 1 ppm of toluene implies 3.77 mg/m^3 was overlooked, and because I had interpreted the volume as the volume of liquid to be evaporated, which is the only volume I can correctly measure, upon further analysis I could find that perhaps my sensor would not work as effectively if I convert both $mg_{toluene}/m^3_{air}$ and $\mu L_{toluene}/L_{air}$ to the same concentration units of molarity (M). Indeed 500 $\mu L_{toluene(liq.)}/1L_{air}$) is equivalent to about 4,700 μM, while 500 ppm is actually equivalent to about 20.2 μM (if the conversion by the mentioned agencies is used: 1 mg/m^3 = 0.27 ppm), which is a very significant difference.

After taking a closer look at how toluene exposure limit values, at least for OSHA, were determined, I discovered that at least 4 methods were employed: toluene vapor capture by typical charcoal tubes, by modified brand-name carbon charcoal tubes (Anasorb747), by 3M brand vapor diffusion monitor badges (films that absorb vapors diffused into them through time), and by SKC brand vapor diffusion monitor badges (filled with a foam disc and sorbent charcoal) [213]. In the analysis procedure, the vapors absorbed by the contents of each device were extracted using a desorption solvent comprised of a 60:40 (by volume) mixture of DMF:CS_2 (carbon disulfide) plus 1 mL of internal standard solvent (ethylbenzene). Here, the internal standard solvent was necessary because once the desorption solvent was allowed to extract all the toluene absorbed by the charcoal contents from the devices, this mixture was separated using gas chromatography. Using the chromatograms showing the separated organic solvent peaks, and calibration curves showing the peak areas versus the concentration of toluene, the concentration of absorbed toluene vapors from each device could be found in $\mu g_{toluene}$ / $L_{airsampled}$ multiplied by a desorption efficiency fraction (unitless) previously found [213].

Rather than leaving the concentration units as is, however, OSHA protocol advises to further convert this to mg/m^3 and then to ppm by multiplying the mg/m^3 value to the molar volume of toluene at 1 atm and 25°C and dividing by the molar mass of toluene. Eventually, this creates a proper fraction for using the ppm notation, but it is of relevance to state that certain

assumptions are made. The OSHA protocol explicitly states: "if the sampling site temperature is not provided, assume that it is 22.2°C (295.4°K, 72°F). If the sampling site atmospheric pressure is not given, calculate an approximate value based on the sampling site elevation" [213]. Thus, since assumptions can be made in acquiring this ppm value, if another researcher (unfamiliar with the OSHA protocol) attempts to compare their ppm values to the OSHA converted one, the comparison may not reliable, since the ppm values were not acquired the same way. As seen from Table 7.2 no study actually determined VOC exposure values using either of the methods which the government agencies used in their testing of chemical sensors.

To further explain, Table 7.2 describes the sensitivities of four LC based gas sensing devices proposed by researchers who reported their values in terms of ppm. In some instances, researchers reported their values and compared them with the lower VOC exposure limits recommended by government agencies, without mentioning how they arrived to their values. Without this information, it is difficult to compare the values even if they are reported using the same ppm units. As in the example above, using different methods to arrive to ppm does make a difference in the meaning of the concentrations if they are then reconverted to other less ambiguous units. By converting both the VOC exposure limits reported by the agencies, and the threshold detection levels found for the sensors proposed to true concentration units (whether mg/m^3 or mols/L) and eliminating the ambiguity presented from using "parts-per-" notation, a clearer picture emerges as to how well these current LC based sensors can work, and how much more room they have for improvement.

This criticism is also applicable to the LC-fiber sensors I have presented in my own work. Furthermore, as will be shown in the following sections, determining how to best measure the sensitivity of individual fibers (as well as the average sensitivity of several fibers grouped together) when exposed to variable amounts of organic (mostly toluene) vapors has been a challenge. For the most part, many of the threshold toluene vapor concentrations of the fiber mats found need further optimization so that they can be considered sensitive enough for responding below the limits imposed by OSHA or NIOSH, for example.

Tab. 7.2 – The VOC detection thresholds in ppm and μM units for new types of LC-VOC sensors are shown from various studies. Some studies reported how their ppm values were obtained, others did not. Some also compare their values to the acceptable values, in ppm, to those acquired from government health agencies (thresholds for toluene vapor, from Table 7.1), while some do not. Thus, there can be ambiguity in evaluating how well, or how poor, the proposed devices are at detecting certain VOC concentrations since the exposure limits they were compared to were determined using different methods. References for the studies: #1 - [63], #2 - [214], #3 - [77], #4 - [80]. References for the NIOSH testing methods: row 1 - [215, 216], row 4 -[213, 215, 217].

Study #	Ref.	VOC response type	Device Sensitivity			NIOSH exposure limits (µM)	NIOSH method for measuring exposure limits
			Reported threshold value (ppm)	Method for measuring reported value	Converted value (µM)		
1	Dickert et al. 1992	Change in N* pitch causes change in reflected wavelength	(a). 200 ppm methylcyclohexane (b). 500 ppm methane	un-specified for both	(a). 8.2 µM methylcyclohexane (b). 20.5 µM methane [converted using NIOSH guidelines]	(a). 16.4 µM methylcyclohexane (b). 8.2 µM methane	(a). by charcoal sampling and GC (gas chromatography) testing (b). By silica tube sampling and GC testing
2	Cadwell et al. 2006	$N_{homeotropic} \rightarrow N_{planar}$ anchoring transition shows change in birefringence	(a). 10 ppm DMMP (b). 900 ppm DMMP	(a). tank containing pre-mixed gas was ordered (no further analysis was stated) (b). un-specified	Uncertain how to convert without standard guidelines - can be µg/g, µL/L, µmol/mol...etc.	none	none
3	Bungabong et al. 2010	same as study #2	0.006 ppm DMMP	Mixing various concs. Of DMMP liquid in N_2 gas, extracting vapors headspace, and testing by GC	Uncertain how to convert without standard guidelines - can be µg/g, µL/L, µmol/mol...etc.	none	none
4	Bedolla-Pantoja et al. 2016	$N_{hybrid} \rightarrow N_{homeotropic}$ anchoring transition shows change in birefringence	316 ppm toluene	flooding a chamber containing the LC detector with toluene vapors from an evacuated toluene liquid resevoir and finding the pressure difference	13 µM	6.1 µM (15 min. exposure)	by charcoal sampling and GC testing, and FTIR spectroscopy

7.3 The sensitivity of non-contained LC-fiber mats exposed to toluene vapors measured by the Dräger method in open air

In section 6.4.2 of the previous chapter, the unique optical effects (i.e. birefringence, interference colors, twists, and enhanced mat scattering) which the 5CB core imparts to individual electrospun PVP fibers, and how these traits could be exploited for gas sensing with toluene vapors, as an example VOC, were first introduced. When mats containing non-beaded and beaded fibers were exposed to toluene vapors using the microfluidics pressure based flow control unit using the setup in Fig. 3.8 (ch. 3) various types of optical responses were observed. However, although these responses appeared to occur uniformly across the mat, there is more to the story - reconsider the responses of two beaded fibers (Fig. 6.13, ch. 6). These two fibers showed that the beaded sections of the filaments appeared to form irreversible indentations after repeated exposures to the toluene vapors. These indentations led to the subsequent flow of LC from the beaded parts throughout air gaps present within the fibers. From this series of experiments I found it was clear that the beaded sections and the non-beaded sections of the LC-fibers respond slightly differently to concentrated toluene vapors. Moreover, in addition to influencing the indentations formed in the fiber sheaths, the differences in sheath thickness from these two sections impact the concentration of vapors that each section responds to as well.

But can a relative value of the toluene concentration in the air around the mat during toluene vapor exposure using the method described in ch. 3 be estimated? For quick reference, Fig. 7.1(a) repeats a diagram of how the mechanism for generating vapors for the macroscopic sensing setup looks like. The problem with trying to determine the concentration of toluene vapor emitted by the tube outlet in real-time, or being sucked into the tube outlet in the vial head-space before reaching the fiber mat, is that it is unknown for sure how much air is passing through the vial head-space at any given moment. In other words, the flow rate of air passing through is unknown, even if the vapor pressure of the liquid toluene itself in the vial (because it is not subjected to a vacuum, or is over pressurized) stays relatively constant.

7.3.1 Responses from a non-beaded, aligned fiber mat

From Raoult's and Dalton's Laws, we know that the total vapor pressure (V) for a mixture of two volatile liquids is the sum of each liquid's vapor pressure (P) multiplied by the mole fraction (n) of each [i.e. $V = (P_{liq.1} \cdot n_{liq.1}) + (P_{liq.2} \cdot n_{liq.2})$] [218, 219]. And although a higher partial pressure of a gas over a liquid means that more gas molecules should be able to dissolve in that liquid (Henry's Law [220]), for the case of the toluene vapors generated by the method shown in Fig. 7.1(a) figuring out the fraction of air and toluene molecules above the toluene liquid in the vial is not straightforward. First, air (a mixture of several gases) which can dissolve into the toluene is used, and, second, that air passing through into the vial is not equilibrated under a constant pressure. The laws mentioned above only apply when the gases are at equilibrium over a liquid.

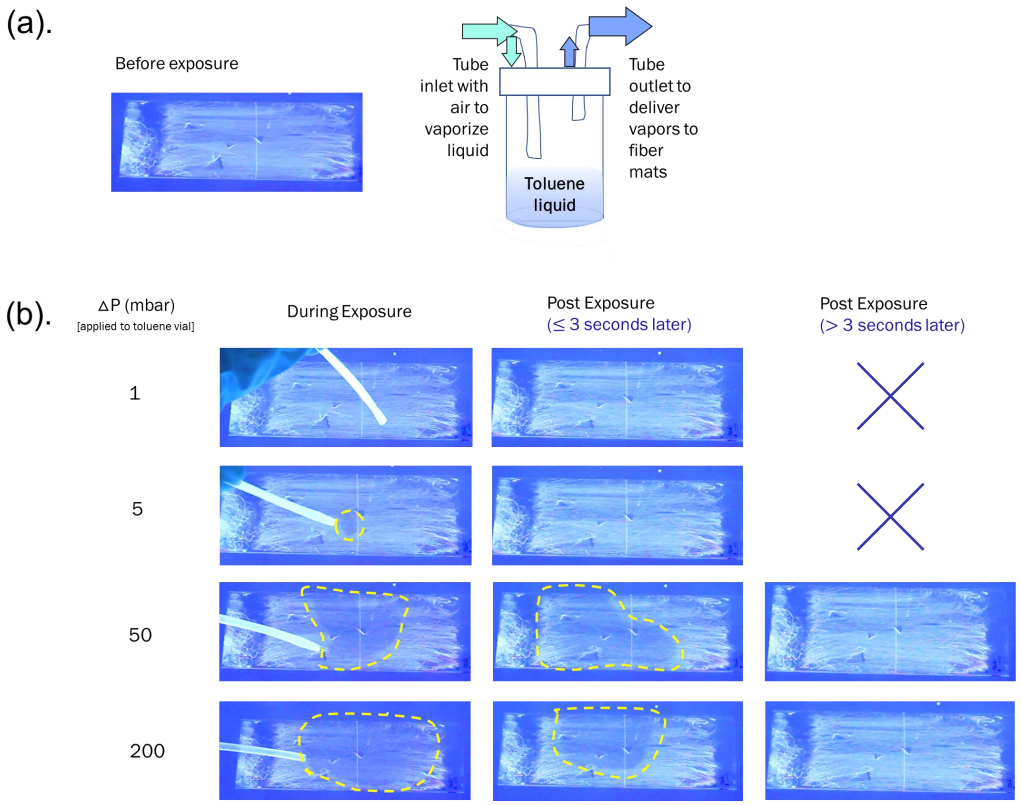

Fig. 7.1 – Air is flowed into a vial containing toluene liquid to distribute various amounts of toluene vapor towards a LC-filled aligned, non-beaded fiber mat. The process on an old aligned mat discussed in ref. [70] is shown in (a); the setup having been discussed in sec. 3.2.1. The application of various differential pressures (1, 5, 50, 200 mbar) to the vial containing liquid toluene results in different quantities of toluene vapor extracted using the vapor exposure tube. The fiber mat takes up the size of a typical microscopy glass slide (26 mm x 75 mm).

From the experiments in Fig. 7.1(b) (seen through the previous crossed polarizer setup), changing the pressure drop airflow inserted into the vial leads to a change in the scattering responses observed when the mat is exposed to the emitted vapors. Clearly, while the vapor pressure of the toluene may be constant, increasing the air flow inserted into the vial contributed to a higher flow of toluene vapors forced out of the liquid below and sucked into the outlet exposure tube. Lowering the applied pressures results in weaker flow of toluene vapors extracted that reduce the scattering mat responses in the aligned fiber mat (yellow outlines in 7.1b). The time which the lowered scattering responses remain before the mat returns to its original state also changes. Although the poor polarizers reduced the contrast of the responses, as shown in other examples having darker backgrounds, the polarizers were switched in later studies and the sensing responses were still fully visible. These experiments above show that scattering responses become macroscopically visible when vapors are generated from at least 5 mbar applied to the vial.

Moreover, if air would just flow out of the exposure tube, rather than having it connected to the vial with toluene, and expose the LC-fiber mat to this, then no scattering responses are visible either microscopically or macroscopically as seen above. Additionally, if sufficient water vapor from the air would have diluted the amount of toluene vapors gathered in the vial, then

the scattering responses of the fiber mat when exposed to the vapors should have decreased in spread and visibility, but they did not and the opposite occurred.

For this reason, it is more likely that the flow of air acts as a carrier that picks up higher amounts of toluene vapor that sits above the liquid to transport them over to the fiber mat. The flow rate of the toluene vapor within the tube outlet increases when the applied pressure to the vial from the inlet increases. If the vapor concentration flowing out of the outlet tube is high enough, such that it does not get drastically diluted by the surrounding ambient air of the fumehood before reaching the fiber mat's surface, then a response will be seen. Thus, when exposing the fiber mats to toluene vapors in an unenclosed manner (as in Fig. 7.1, there will always be a difference between the concentration of toluene vapors present in the headspace of the vial holding the toluene liquid, and the concentration which the mat finally experiences. The concentration that the mat experiences depends on how much the surrounding air dilutes the vapors that the exposure tube from the vial outlet delivers.

Given the complications in trying to get concentration values for the vapors that the mat was exposed to using the macroscopic sensing method from above, the short-term toluene sampling tubes and sampling pump by Dräger were employed to obtain a semi-quantitative approximation of how much vapor the fiber mats could be experiencing if placed very close (within 3 cm - 4 cm) to the tip of the exposure tube outlet (Fig. 7.2). The sampling tubes are each filled with a reactive resin that give a colorimetric response proportional to the amount of the target gas sucked in by the sampling pump.

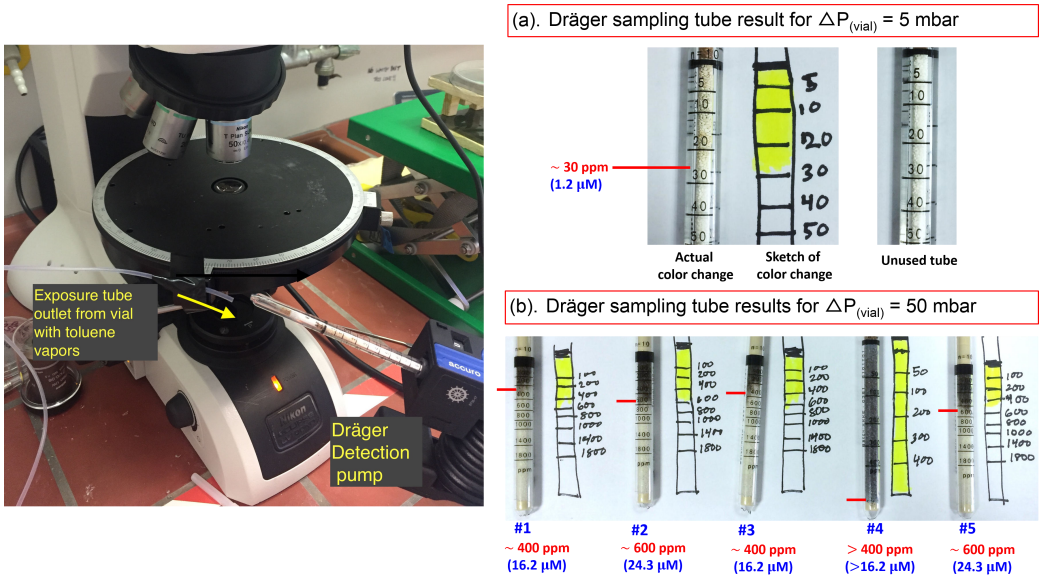

Fig. 7.2 – Using short-term toluene sampling tubes by Dräger to quantify the immediate concentrations of toluene vapor emitted from the exposure tube applied to the LC-fiber mats. This was performed using the sensing method for observing macroscopic scattering changes described in sec.3.2.1.

For detecting toluene vapors, the resins in the tubes are embedded with either iodine pentoxide (I_2O_5), or selenium dioxide (SeO_2), plus trace amounts of sulfuric acid, and the reactions with the toluene gas (C_7H_8(gas)) go as follows (with a more detailed evaluation given in sec. 7.3.4 as to the reliability of the results achieved): C_7H_8(gas) is mixed with I_2O_5 and H_2SO_4 to give

I_2 (which is a light brown color), or C_7H_8(gas) is mixed with SeO_2 and H_2SO_4 to give a Se (selenium) product that is violet) [221]. No explanation was given as to why Dräger decided to use selenium dioxide for detecting higher concentrations of toluene vapors in their sampling tubes with a higher sensing range, but it may be mostly because the toluene may be less reactive with selenium dioxide than it is with the iodine pentoxide, so higher concentrations of it are necessary to start the reaction. Thus, they decided to put this mixture into the tubes which detect higher concentrations of toluene, rather than the lower threshold ones.

In any case, the photograph on the left side of Fig. 7.2 showing the exposure tube mounted next to the stage of the POM shows the relative close proximity to the exposure tube at which I measured the concentration of toluene vapors being emitted using the Dräger sampling tube and pump device. Fig. 7.2(a-b) show the actual results, and my sketch representations, of the concentrations of toluene vapors detected from the exposure tube when I increased the amount of pressure flowing through the toluene vials from 5 mbar to 50 mbar. As seen for the 5 mbar case, the unopened and unused testing tube on the right side shows a completely white resin body, and on the left side the top of the tube has been discolored to light a brown color until roughly the 25 ppm mark (indicating that the reaction with iodine pentoxide has to form iodine has occurred for that toluene vapor concentration). For better clarity, I sketched out the range that was discolored in the tube, and I conservatively estimated that no more than 30 ppm (1.2 μM[†]) of toluene vapors must have reacted with the tubes' contents, if the sampling technique I used according to Dräger is correct.

The 50 mbar case in Fig. 7.2(b), shows that the process was reproducible and repeated several times for each applied pressure value. Here, four tubes with concentration limits from 100 ppm to 1800 ppm appeared to show levels of reactivity until the 400 ppm to 600 ppm marks (red). If a tube that has a testing range from 50 ppm to 400 ppm was used for sampling, however, the entire tube becomes discolored (tube # 4), thus leading me to believe that the best estimate of the concentration of vapors emitted at this pressure difference was probably between 400 ppm - 600 ppm (16.2 μM - 24.3 μM). Given the result of tubes #3 and # 5, I would more liberally say that the concentration of vapors is closer to 500 ppm (or, 20 μM) at this pressure difference, but the range is more appropriate given the qualitative nature of the experimental process. Applying this method for retrieving estimated toluene vapor concentrations for three more applied pressure values gives the following results compiled in Table 7.3.

[†]1 ppm = 3.8 mg/m^3 by Dräger's specifications [221].

Tab. 7.3 – Estimated concentrations of toluene vapors emitted by the exposure tube from the setup shown in Fig. 7.2(a) (and in Fig. 3.8) using the Dräger short-term tube and pump sampling method. Th pressure difference (ΔP) refers to the extra amount of air that was flowed through the headspace of the vial containing toluene liquid at the bottom. Again, this air flow was controlled by the microfluidics flow control unit previously described in ch. 3. The concentration values shown correspond to the color indicated limits of where the absorbed vapors reacted with the resins in the Dräger tubes. If the colorimetric readout appeared to fall between concentration values indicated on the tubes, such as for the 50 mbar case described in Fig. 7.2(b), then a range of concentration values was reported to illustrate the uncertainty in the measurement. All concentration values were rounded up to the next integer.

Applied ΔP_{tovial} (mbar)	**Dräger readout conc. (ppm)**	**Converted Dräger conc. (μM)**
5	30	2
25	50 - 100	2 - 4
50	400 - 600	16 - 24
200	1400 - 1800	57 - 73

Furthermore, assuming that the conservative estimations shown in Table 7.3 are accurate for detecting the amount of toluene vapors expelled very close to the tip of the exposure tube, then if we compare the results to how the previous non-beaded, aligned 5CB-PVP fiber mat responded to the vapors in Fig. 7.1(b), then it would seem like our mat is sensitive to at least 2 μM (30 ppm) of toluene vapors. To put this value of 2 μM in perspective one can consider that, compared to the recommended exposure limits to toluene vapors suggested in Table 7.3, this value is about six times lower than the NIOSH recommended 15 minute exposure limit to toluene of 6.1 μM. But just how much would the sensitivity threshold for beaded fibers change when exposed to vapors generated from these pressure differences?

7.3.2 Responses from a single beaded fiber

Figure 7.3, Fig. 7.4, and Fig. 7.5 show how a single beaded filament responded to the toluene vapors generated using the exposure method shown in 7.1(a). Note that this section of fiber displayed in the three figures (Fig. 7.3 - Fig. 7.5) belongs to one of the two long fibers that were studied previously in Fig. 6.13 of the previous chapter, and the approximate width ratio of the beaded sections to the non-beaded sections is 5.5 μm : 3.2 μm. As expected from the qualitative results seen in ch. 6.4, the beaded sections of the fiber take longer to clear than the non-beaded sections do.

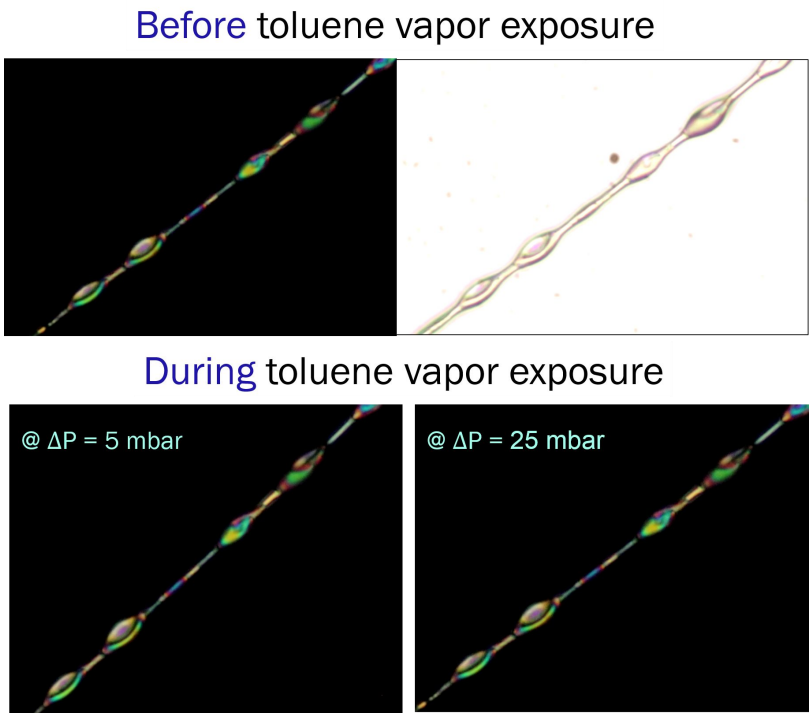

Fig. 7.3 – A beaded fiber exposed to vapors emitted from 5 mbar and 25 mbar of air flowing through a vial containing toluene liquid (the vial setup shown previously in Fig. 7.1a). The beaded fiber, which has non-beaded sections that are roughly 3.2 μm wide and beaded sections that are 5.5 μm, does not appear to show signs of clearing from vapors emerging from these applied pressures. The crossed polarizer image of the fiber and its corresponding plane polarized light image before vapor exposure are shown.

Likewise, after the entire fiber clears to the isotropic state, once the exposure tube is immediately taken away, the non-beaded sections are the first to reassemble the nematic phase first. This process is most evidently displayed in Fig. 7.4, for instance, where the same fiber is exposed to the vapors generated from flowing 45 mbar of air through the toluene vial. Although when exposed to vapors generated with 25 mbar air applied, and lower, for longer than 3 seconds no clearing or changes in birefringence were observed (Fig. 7.3), at 45 mbar and higher, the responses began to show a clear time dependence.

If the fiber is first exposed to the toluene vapors emitted from the exposure tube for less than 3 seconds, the sections that immediately clear are those in between the beaded portions of the fiber (Fig. 7.4a). Moreover, if one looks closely at this crossed POM image in Fig. 7.4(a) and

compare it to the corresponding plane polarized light image in Fig. 7.3(before vapor exposure) one can see that the non-beaded section above the second to last bead (yellow outline in 7.4(a)) did not actually clear either just like the rest of the beaded sections in the image. However, the beads here are about twice the width of the rest of the non-beaded sections, and this section that did not immediately clear was definitely was not the same size as the beads present. Referring back to the POM image taken in plane polarized light we see that this section does bulge out a bit more than the rest of the non-beaded parts of the fiber, thus, it most likely has more core filling than the other areas.

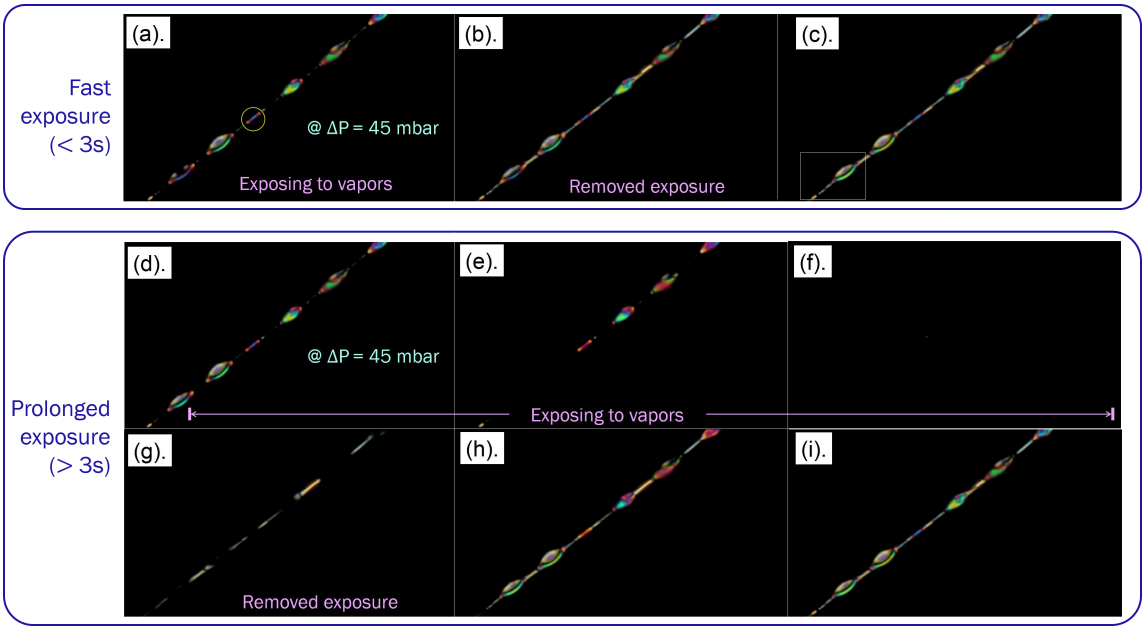

Fig. 7.4 – The same beaded fiber from Fig. 7.3 is exposed to vapors emitted from 45 mbar of air flowing through a vial containing toluene liquid. Here, we see that exposing the beaded fiber for a slightly longer period of time (after 3 seconds) helps to finish clearing the LC volume present in the entire fiber. However, exposing the fiber for less than 3 seconds or so, only results in the clearing of the non-beaded sections first. Slightly wider non-beaded sections (yellow outline in (a)), but with not quite the same size as the beads also delay in clearing as well. After completely clearing, the nematic ordering returns first in the non-beaded sections, followed by the beaded sections.

Actually, the more important reason as to why this tiny feature is relevant is because it serves as evidence that even though many of the non-beaded segments clear immediately upon vapor exposure (if concentrated enough), there is the possibility that some of these areas may not. This instance is one example for supporting the argument made in sec. 6.4.1 which stated that the double scattering responses observed in the non-beaded aligned fiber mats is likely due to the fact that not all of the sections of the filaments (despite lacking large modulations in width like beaded filaments) do not transition to the isotropic phase at the same time during exposure. Once the exposure tube is removed, the non-beaded sections which previously cleared immediately return to their original birefringent state in Fig. 7.4(c). Additionally, one beaded part shown in the lower left corner of this image (white outline) was also observed to regain additional interference colors. In this case, it seems as though this one bead of the filament

shown actually did appear to partially clear during the first exposure. However, that part of the bead that did clear was a part in the center which happened to be indented.

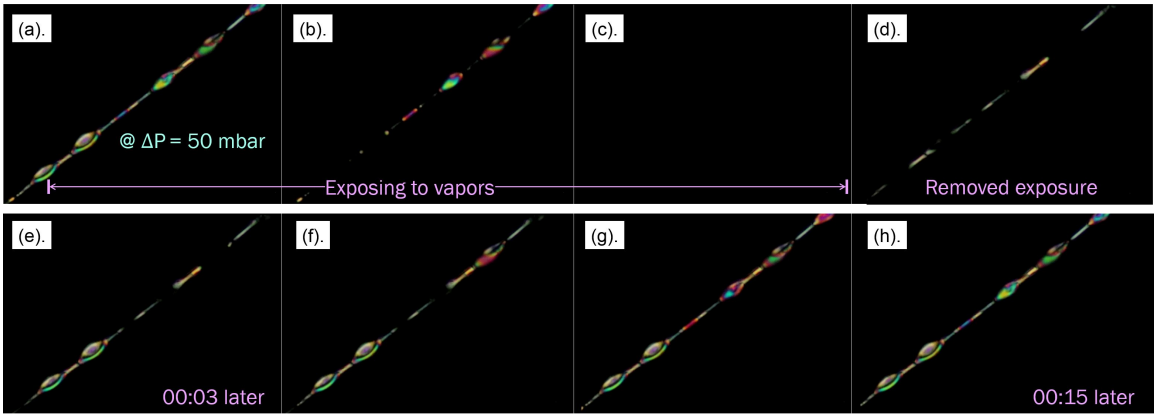

Fig. 7.5 – The same beaded fiber from Fig. 7.3is exposed to vapors emitted from 50 mbar of air flowing through a vial containing toluene liquid. As with Fig. 7.4, but more clearly here, exposing the beaded fiber until it clears shows that the clearing process is not uniform for all sections of the beaded fiber. Moreover once the exposure is removed, (d), the return of the nematic phase is instant for the non-beaded sections containing less LC volume, then the flattened beads show birefringence returning (e) some seconds after. And finally, after about 15 seconds the full birefringence from the non-flattened beads (the top 3 in (f-h)) return to their original state.

Furthermore, while we may be inclined to think that the images shown in Fig. 7.4(a-c) suggest that a higher concentration of vapors in the air is necessary to clear the entire fiber to the isotropic state, the images (d-i) in the same figure below shows that exposing the fiber for a slightly longer period of time (about 5 seconds longer) under the same amount of vapor flow causes the entire fiber to clear. This is even though it also takes a few more seconds for the fiber to return to its original nematic state in the end. When exposed to the vapors generated at the 50 mbar level, the beaded sections of the filament are shown to take between 3 and 15 seconds before fully returning to their original birefringent state (Fig.7.5e-h).

To summarize these findings, the schematic in Fig. 7.6 illustrates the areas of a beaded 5CB filled fiber (with two types of bead morphologies, and a LC twist spot) that are most likely to clear to the isotropic state first during exposure to toluene vapors. Note that the presence of a local "bright spot" twist in the LC director field of a certain area in the fiber (beaded or not) can help speed up the response time for that area when exposed to vapors. This is because, following the discussion of the nematic 5CB elastic energy in the fibers in sec. 6.4, the director field has become twisted due to the confinement geometry of the sheath. In order to relieve its distortion while exposed to VOCs, this part is likeliest to react first in disassembling the nematic phase to reach its minimum free energy. Recall that for elastically strained partially confined thin films of 5CB exposed to toluene vapors in Bedolla-Pantoja and Abbott's case this led to an anchoring change to homeotropic alignment [80], while in our case, because of the non-uniformities in confinement it leads to non-uniform clearing of LC filled fiber sections during vapor exposure.

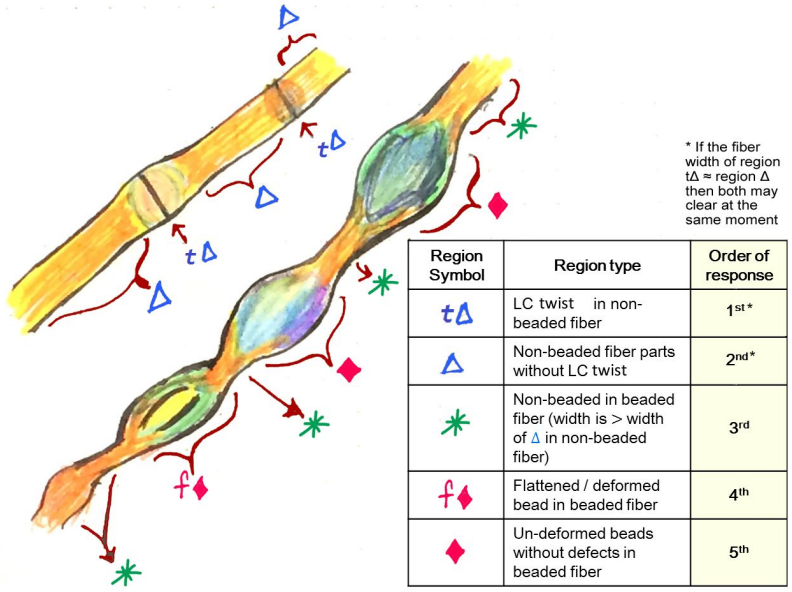

* If the fiber width of region tΔ ≈ region Δ then both may clear at the same moment

Region Symbol	Region type	Order of response
tΔ	LC twist in non-beaded fiber	1st*
Δ	Non-beaded fiber parts without LC twist	2nd*
✳	Non-beaded in beaded fiber (width is > width of Δ in non-beaded fiber)	3rd
f♦	Flattened / deformed bead in beaded fiber	4th
♦	Un-deformed beads without defects in beaded fiber	5th

Fig. 7.6 – Schematic showing the sequence of clearing in LC filled fiber sections when exposed to toluene vapors. The sketch differentiates regions by symbol in two types of fibers, beaded and non-beaded. It also takes into consideration that if the walls dividing the areas of twist or deformed "flattened" beads are present, then the influence that the VOC has on disturbing the nematic order will be greater, thus it will respond faster than the other non-deformed beaded sections in the fiber. For the first two regions shown in the non-beaded fiber, locations with twists clear faster than those areas without any. However, if the volume of both of these regions is the same, and both regions show the same interference colors and birefringence both will will clear at the same moment. This diagram also assumes that the fibers are exposed to equal amounts of vapor at the same time, and there are no concentration gradients where more vapor has accumulated on one end.

7.3.3 The threshold sensitivities of non-beaded fiber mats & beaded fibers

Finally, if I apply the Dräger tube determined concentrations found in the previous section for the vapors generated from the applied pressure differences to the toluene vial in Table 7.3 to this case of the beaded fiber exposed in Fig. 7.3 - Fig.7.5, we find that this filament appears to respond the quickest when exposed to vapors from the 45 mbar - 50 mbar air flow applied to the vial, corresponding to a threshold between 16 μM - 24 μM. While this sensitivity threshold is significantly higher than that one seen for the non-beaded fiber mat shown in sec. 7.3.1 (corresponding to 2 μM), two important points must be considered when comparing these results. The first has to do with the quality of threshold response observed in the non-beaded fiber mat, and the second has to do with differences in fiber morphologies for the two cases.

First, the non-beaded fiber mat exposed to the vapors generated at 5 mbar applied pressure to the toluene vial did not macroscopically show a widespread response throughout the entire mat that was capable of lasting for even 3 seconds after the exposure tube was taken away (Fig. 7.1). In fact, the response was so limited to just the very part of the mat directly under the area of the tube that it would be largely unnoticeable if it was not actively searched for. Thus, it is questionable that in an applied "real-world" scenario that this low, but very localized, and largely unnoticeable visual response would be of substantial use. Onto the second point:

since the response for the 5 mbar case was so short-lived, and since a corresponding microscopic observation for at least one non-beaded filament directly underneath the exposure tube was not performed, we do not know for certain that the entire fibers in this particular spot that showed the brief scattering response completely cleared. From the supplemental videos supplied to ref. [70], showing the microscopic responses of non-beaded aligned fibers partially clearing at a very high concentration of toluene vapors generated from 200 mbar of applied air flow to the toluene vial, we do know that the clearing of entire fiber lengths is not immediate. It is not an overestimation to assume that during exposure to vapors generated from a much lower applied air flow will result in the same effect occurring. Even more so since the vapors transmitted to the mat will be of a lower concentration.

Additionally, from how the single beaded fiber shown above behaves during vapor exposure, non-beaded sections in the fiber will generally clear first before the beaded sections which have a greater LC volume, however, this does not mean that all non-beaded sections will behave the same way. As seen in Fig. 7.4(a), not all sections that were considered "non-beaded" cleared at the same time. Although the beaded sections in the fiber were indeed twice as wide (roughly 6 μm) compared to the non-beaded segments (3 μm), for that one yellow outlined section in Fig. 7.4(a), the section did not need to have as much LC volume as the 6 μm wide sections to delay in responding, it was only just 1 μm or 2 μm wider than the rest of the non-beaded sections which did clear at the same time. Thus, it is possible that minor modulations in fiber thickness can exist in what we call the "non-beaded" fibers as well. These can cause delays in observing entire fibers respond to VOCs because different sections of the fiber (depending on the sheath morphology, and whether there are bright twist spots or the other director distortions in the LC core) can respond at different moments (Fig. 7.6). Therefore, stating a single threshold for the fiber responsivity is not entirely representative of how the entire filament, or the mat, for that matter, behaves.

Moreover, short breaks in LC filling such as the one example shown in Fig.7.7 from fibers without significant beading in the mat can also occur. Images of two fibers, one showing gaps in the LC core (green arrows), and another showing a continuous LC core, under crossed polarizers with the analyzer 10° and 50° to the polarizer are shown in indicate that twists separated by black walls in a continuous LC core are different from gaps in LC core filling. While it is possible that some of these segments in the fibers may be able to clear at lower VOC concentrations than others, to suggest a flat value of 2 μM based on an observed small scattering change is probably inaccurate. Therefore, the sensitivity threshold for the fibers and mat, when measured using this method should consider the concentration at which most of the fibers reduce in birefringence, and the concentration at which a large area of scattering away from the site of exposure is macroscopically observable. Thus, a more conservative estimate of the lowest toluene concentrations that the non-beaded fibers are sensitive to, as measured using the Dräger method, can be noted as certainly between 2 μM - 16 μM. For the beaded fibers the lowest threshold of sensitivity should be at least from 16 μM - 24 μM.

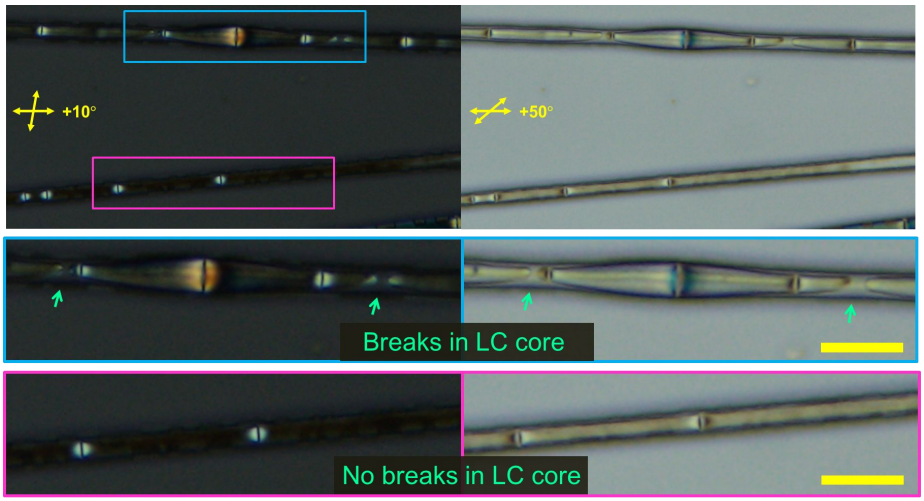

Fig. 7.7 – Partially crossed polarizer images side-by-side (left: analyzer turned 10° to the polarizer, right: analyzer turned 50° to the polarizer) showing two example fiber sections that have breaks in LC filling (blue outline) and that do not (purple outline). The closeups of the two fibers are shown in the corresponding blue and purple boxes. In particular, the bottom non-beaded fiber shows an LC core that is continuous without gaps, but which does contain 2 walls separating LC twist regions with the same handedness. Thus, small twists in the LC core are distinguishable from gaps in the filling. Scale bars: 12 μm

7.3.4 Analysis of the reliability of Dräger tubes for determining vapor concentrations

Since the concentrations listed in Table 7.3 were used in the previous sections to determine approximate sensitivity thresholds for the beaded and non-beaded LC-fiber mats to toluene vapors, a brief evaluation of the Dräger semi-qualitative VOC concentration testing method is warranted. Although the process of pumping in vapors being created in situ from the exposure tube was carried out multiple times for each pressure value applied to the vial containing toluene liquid (Fig. 7.1a), and the colorimetric readouts on the tubes were largely reproducible, apart from the errors possible in misinterpreting the readouts (Fig. 7.2), there is some issue with the way the reaction in the tubes progresses. The Dräger tube method for determining VOC concentrations from known vapors relies on the premise that if VOC specific glass tubes with a scale of concentration values (in ppm) and containing different reactive resins inside, are attached to a hand-held suction pump, then depending on how much vapor is pumped to activate the tubes, the vapors will react proportionately with the concentration of resins inside [221]. The concentration of the vapors that reacts with the resins will then directly correspond to a level of color change and concentration value marked on the tube. Of course, increasing the intake of vapors into the tube will increase the colorimetric response in the tube, but this is why the number of strokes needed to pump in the vapors are specified on the tubes to make sure the readout is calibrated.

According to the tubes for sensing toluene vapors, the two types of reactions which can take place between the toluene vapors ($C_7H_{8(gas)}$) mentioned in sec. 7.3.1 can be either reductions of iodine pentoxide or selenium dioxide with trace amounts of sulfuric acid. Recall the reactions (provided by Dräger which are actually incomplete, but were provided in their manual [221] as

follows) :

$C_7H_{8(gas)} + I_2O_5 + H_2SO_4 \longrightarrow I_2$ (light brown), or
$C_7H_{8(gas)} + SeO_2 + H_2SO_4 \longrightarrow$ Se product (violet) .

Upon giving reaction with iodine pentoxide a closer inspection, the issue is not whether they will not run to completion or not, but as I will discuss below, it is clearly non-selective and does not require the specific presence of toluene molecules to initiate.

The reason why can be found in literature [222, 223] by looking at the reaction between iodine and benzene. It is well understood that the iodination of benzene is difficult to achieve because reactions which require the breaking of double bonds inside aromatic rings are very unfavorable, despite benzene, here, being a nucleophile (abundant in π electrons and willing to donate them to electrophiles). Two ways to circumvent this are to use either a substituted benzene ring with a nucleophilic group attached (phenol for instance) which can give off the electrons instead, or to use a very strong electrophile (deficient in electrons) that can react with the benzene. Iodine (I_2) is not one of these very strong electrophiles, and so if the reaction must occur with a non-substituted benzene, an oxidizer like a Lewis acid (which can accept electrons by giving up H^+ ions) is necessary. The acid (which can be sulfuric acid (H_2SO_4) or nitric acid (HNO_3) makes sure that once iodine and benzene react, one of the products formed (HI) does not react with the other desired product (iodobenzene) and decompose it back down to the starting benzene and iodine reactants again.

The reason why this is relevant here is because compared to pure iodine, iodine pentoxide (I_2O_5), is a much stronger electrophile and more electronegative than iodine itself, thus making it more reactive with an aromatic compound to start off with. However, like the case with pure iodine and benzene, a strong oxidizer like sulfuric acid is necessary for product stabilization. Therefore, what most likely occurs within the tubes containing both iodine pentoxide and the sulfuric acid is that iodine pentoxide reacts with the toluene vapors pumped in and while this reaction does not yield a color sensitive product, whatever intermediates are formed are immediately stabilized by sulfuric acid and the remainder of the unreacted iodine pentoxide is reduced back to iodine, the latter which gives the color. The reason why this method, although it works, is non-selective lies at the very start of the process. Since iodine pentoxide is so reactive, it is known to be able to oxidize many types of molecules from carbon monoxide to substituted aromatics (e.g. toluene, ethyl benzene, xylenes) and even acetylene, vinyl chloride and carbon disulfide [224].

Of these compounds it reacts with, the reaction with carbon monoxide to produce carbon dioxide and iodine has been widely recognized as one of the first implemented for carbon monoxide detectors as early as 1919; known as the "Hoolambite" reaction after its founders: Hoover and Lamb [225, 226]. The "Hoolambite" reaction also used H_2SO_4 as a stabilizer for the remaining iodine pentoxide, and this allowed for its reduction back down to the brown tinted iodine. Overall, the lack of specificity for specifically detecting toluene vapors (or even carbon monoxide) using this type of reaction in detection tubes in the words of McKee and McConnaughey from ref.[226] cannot be better stated: "...the iodine pentoxide and dichromate oxidation-reduction reactions are nonspecific, although the sensitivities of indication are different for different compounds. For instance, I_2O_5 plus fuming sulfuric acid gives a stain of 14.5 mm for 50 ppm benzene using one pump stroke, 10.5 mm for toluene, and 7.5 mm for xylene. But

if these three compounds were together in a mixture, using detector tubes, there is no way of telling what the concentration of each is in the mixture."

While it seems as though even the Dräger VOC concentration testing method also suffers from the issue of non-specificity, which is described in the brief review of gas sensing technologies in sec. 2.3, this is quite common to encounter with many sensors. While the response may be clear for detecting one specific compound if already suspected, if a compound is not suspected before testing or if there is a mixture of several compounds, the sensor may give an erroneous response. Two positive outcomes from using the Dräger method for my case, however, are that: first, it gives some sense of what vapor concentrations are being emitted at the very end tip of the outlet tube from my first sensing setup using the vial in Fig. 7.1(a) that was meant for observing the macroscale scattering responses, and second, this method provides a better estimation of toluene vapor exposure than the very crudely estimated upper limit proposed previously in my first paper [70].

At the time, an upper limit concentration of about 3% toluene was proposed, which in retrospect, means a fairly high (and physically dangerous) amount of toluene vapor concentration. The lower explosive limit for this VOC is 1% saturation in air, and the upper limit is 7% [227], so this means that if a 3% vapor saturation were met it would be enough toluene vapor in the air to sustain its combustion in air if a spark or flame were presented. Additionally, less than 1% of the air saturated in vapor is enough to cause health affects. Clearly, the fiber mats must have been responsive to vapor concentrations less than this 3%, but at the time of reporting we did not have a method for estimating the values. At the very least this method by Dräger has provided some more realistic estimations of what concentrations the fiber mats could have been responsive to, and if anything are actually overestimates, given that the fume hood in which the samples were tested in was actively circulating the air.

Given that air circulation of the vapors was occurring this offered an opportunity to attempt the next approach of attempting to find the toluene vapor concentrations at which the LC-fiber mats were responsive to. The improvement proposed was to pre-mix known concentrations of toluene vapors separately and deliver them to an enclosed gas tight and non-reactive aluminum holding cell that contained the fiber mats. The vapor could then be held at equilibrium, and then released or evacuated out once the fibers had responded. Close-up areas of the individual fibers, at the micron level, that responded to the vapors inserted could also be recorded through the microscope at the same time. The next section discusses how the data was analyzed for this method and what the results were.

7.4 The collective sensitivity of a fiber mat with beaded & non-beaded fibers

The second method used for attempting to obtain reliable toluene vapor sensitivity thresholds for the 5CB-PVP fiber mats, relied on tracking the decreasing brightness levels in several fibers at once as their 5CB cores underwent clearing from the nematic phase. Unlike in sections 6.4.1 and 6.4.2, where the macroscopic scattering changes of the fiber mats were discussed qualitatively, for tracking how individual fiber sections responded, the POM and a cell for maintaining the fibers under constant exposure was necessary. Recall this is the same setup originally described in sec. 3.2.2, and shown in Fig. 3.9. Of course since the window of the cell (Fig. 3.10(a),

Tab. 7.4 – Known concentrations of toluene vapors (in μM) were mixed in ambient air by evaporating various microliter volumes of toluene liquid in a gastight one liter syringe barrel (the method described in sec. 3.2.2). Each volume was pipetted 7 times (using the same pipette that was used for mixing the gas) and the masses were averaged. The standard deviations for all of the masses ranged in between 6.0×10^{-3} and 6×10^{-5}. According to ref. [228] the density of pure toluene should be 0.8627 g/mL at 25°C and at 1 atm, so the corresponding concentrations for toluene with this density evaporated from the volumes indicated with this theoretical value are shown in the "expected toluene vapor conc." column. They are shown as a reference to indicate how much of an upper error in the concentrations created using this method of in-house vapor generation can occur (the "Actual" column), assuming the best case scenario that pipettes with the best precision are used to disperse the liquid toluene. All concentrations shown were rounded up to the next integer. Once the targeted toluene vapor-air mixture had been prepared, it was transferred through the gas tight cell containing the LC-fiber mat positioned in the POM.

Toluene$_{liq.}$ vol. (μL)	**Toluene$_{liq.}$ avg. mass (mg)**	**Actual Toluene vapor conc. mixed (μM)**	**Expected toluene vapor conc. (μM)**
05	5.1	56	47
10	9.6	105	94
15	14.9	162	141
20	28.4	309	188
50	52.5	570	469
90	98.6	1071	844

sec. 3.2.2) is only about 2 cm in diameter and smaller than an entire microscope slide, which a typical electrospun LC-fiber mat usually takes up (7.5 cm x 2.6 cm), the area investigated in the POM will not represent the clearing pattern of the entire mat. However, at least the area will be an average representation of several fibers that are: (1). randomly arranged, (2). interacting with one another (filaments over and under), and (3). varying in size (if contain both beaded and non-beaded filaments).

While sec. 3.2.2 described how the known concentrations of toluene vapors were mixed, Table 7.4 describes which mixtures were made using the microliter evaporation method before flooding the gas cell containing the fiber mat. Recall that the entire gas cell setup (i.e. fiber-mat-holding-cell, inlet/outlet tubing, connection to the syringe or Tedlar bag, and valves) where the mixed gas passes through does not have an inner volume greater than 20 mL. This means that since I had mixed a liter of toluene gas separately, and given that the setup which I intended to transfer it through had a substantially smaller volume, the sensing cell holding the fiber mat became flooded with vapors relatively quickly. Additionally, upon closing and opening the valves on either end of the cell I noted that there were no pressure differences present which could further alter either the concentration of vapors inserted, or the morphology of the fibers in the mat. One other aspect that I noticed after acquiring the "actual" concentrations of toluene vapor, shown in Table 7.4, is that even though calibrated pipettes were used, the concentrations mixed always overshot the "expected" concentration values.

Furthermore, Fig. 7.8 gives a summary of how the analysis of the filmed responses proceeded . By using the green filter (sec. 3.2.2) to simplify the optical response by restricting it to the birefringence effect for a single wavelength, only the illuminated cores of the fibers were isolated

using binary thresholding techniques in ImageJ. Thus, the analysis was narrowed down to only the 5CB-filled cores. Such techniques are often applied to videos recorded through the confocal microscope that track the interaction of fluorescently marked proteins moving through cells [229].

In this case, the videos retrieved from the vapor exposure experiments can be reconverted into batches of images called "stacks" (typically hundreds or thousands of frames long) and then appropriately condensed. The thresholding and isolation analysis to find the mean-gray value changes of the pixels corresponding to the LC filled parts can be done at once (although it is usually rather time consuming). The steps taken in order to extract the relative brightness data from the recorded fiber images during gas sensing can be briefly described as follows, and correspond to the images (a-g) shown in Fig. 7.8:

- Choosing the fiber area region of interest (ROI) for brightness tracking through plane polarized light and through crossed polarizers (a-b)
- Applying the green filter over the polarizer to normalize the wavelength of light passing through the fiber sample (c)
- Running the experiment - allowing the toluene vapors to interact with the fiber mat in the cell while filming how the area (c) changes in brightness over time, converting each color frame from the video to a gray scale frame by extracting only the green channel color values (d)[‡]
- Discriminating all gray values in the stack of frames (which indicate LC brightness) from the black background using a threshold fitting that covers all the filaments (e). and which also converts the selected areas into several smaller ROIs for measuring (f)
- Last, applying this mask of ROIs over the gray scale images (from d) to analyze each highlighted ROI section of the filaments individually. Analyzing each ROI section using other plugins in ImageJ will allow one to obtain the mean and modal gray values (Note: image (g) shows the mask of ROIs created placed over on the unprocessed POM image (c) to illustrate that the ROIs retrieved after the thresholding process should match almost exactly to the original birefringent areas seen)
- Finally, if some of the frames retrieved from the experimental video at the step in (c) appear to be shifted and the mask of ROIs generated later on do not seem to align perfectly as in the close up shown for image (g), the intermediate step of applying a "drift correction" algorithm over the stack of frames should be applied before the gray scale green channel extraction.[§]

[‡]This step is done automatically using a script I programmed for Image J.

[§]A video explaining how this entire procedure is applied to a video containing changes in fiber brightness upon exposure will be made available in conjunction with any peer-reviewed articles published.

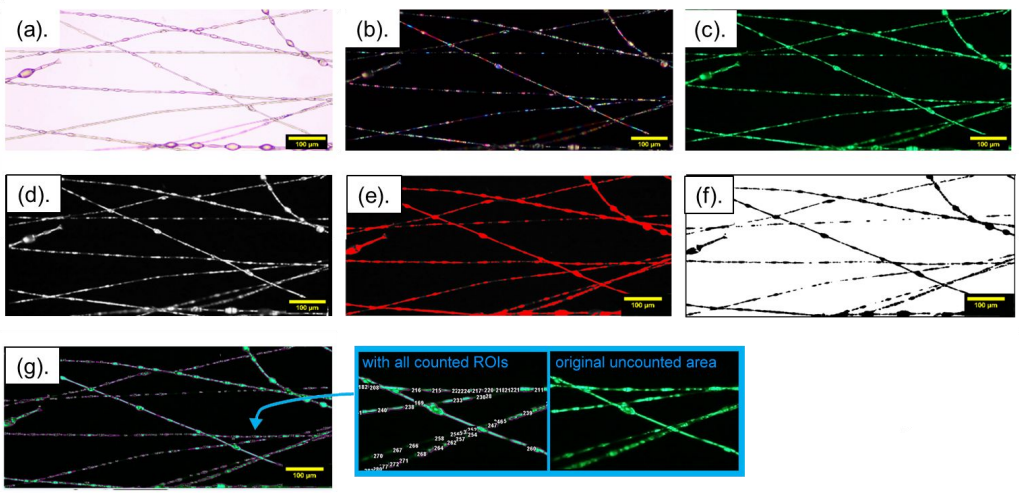

Fig. 7.8 – Process of how the mean gray value differences in an area of fibers were tracked during toluene vapor exposure in the microscopic based sensing setup introduced in sec. 3.2.2. See main text above for detailed explanations for the significance of these isolated images. Scale bars: 100 μm

After extracting all of the mean gray values from the segmented ROIs in the frames of data following the procedure above (usually the number of values accumulated per frame tends to be on the order of 300 - 500), these values were again averaged to get an overall mean gray value for that particular frame (corresponding to the time at which the fibers had been exposed to vapors in the cell up to that point). I assume that the gray values from each frame followed a normal distribution because in addition to acquiring a mean value of brightness intensity for each frame, I also acquired the statistical median value for the data.

As described by Leys et al. [230] many outliers in data are incorrectly eliminated by researchers because they often assume that values outside the mean $\pm$ 3 standard deviations are significant outliers, when in reality they may not be. This is because the mean value of a sample set, like the standard deviation, is subject to error as well. In other words this means that one or two large values averaged in the data set can skew the mean value found either too far left or too far right. Very small and very large values skew the data distribution such that it no longer is uniform. Thus, applying the outlier exclusion practice stated above (finding the mean $\pm$ 3 standard deviations) for this data is not applicable. In my case, no outliers were removed because all fell within the median $\pm$ 3 standard deviations, the median being less affected by very large or very small values in the sample because they automatically get placed to the far left and right of the data while being ordered, leaving the center values unaffected [230].

The plot and corresponding POM frames for the response to the 1071 μM exposure trial in Fig. 7.9 together quantitatively and qualitatively describe the rate of overall fiber mat clearing observed to each vapor concentration in the gas cell. To show the relative decreases in LC brightness in the plot, Eqn. 7.1 was used where I_{max} refers to the maximum mean gray brightness intensity value found for the fiber sections seen in the entire isolated frame (before vapor exposure), I_{expt} is the mean gray value acquired for the entire frame while the experiment

was taking place, and I_{rel} refers to the fraction of mean gray brightness intensity relative to the I_{max} that was originally found.

$$I_{rel} = I_{expt}/I_{max} \tag{7.1}$$

Ultimately, it is these values for I_{rel} versus the first 6-9 minutes of the experiments that are plotted in Fig. 7.9. Thus, if the particular area of fibers observed in the frame starts off at 100% brightness (corresponding to an average gray intensity value of 427 counts) after half a minute of exposing the area to a toluene concentration of ~1070 μM, the average frame brightness will drop to 214 counts (or, roughly 50 % of what the starting scattering brightness was).

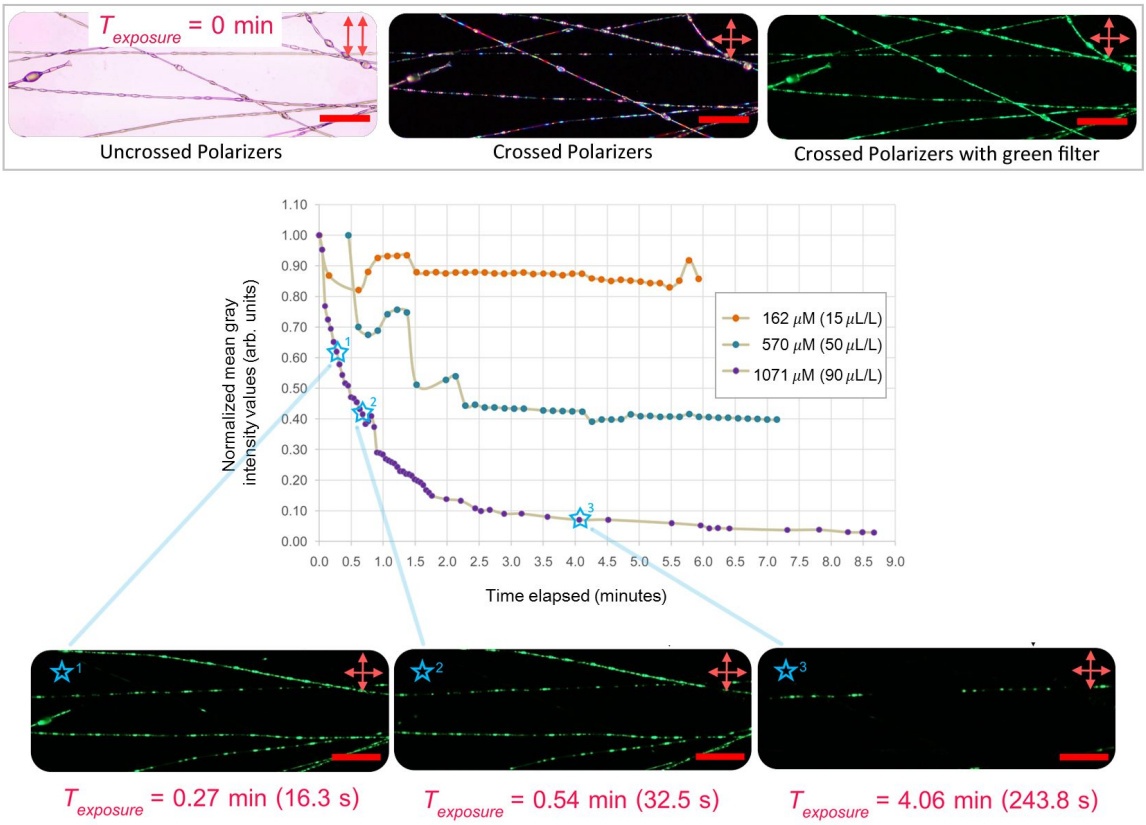

Fig. 7.9 – Screen shots of the area of fibers examined through the POM (with plane polarized light, cross polarizers, and with green filter) before toluene vapor exposure are shown in the gray outline at $T_{exposure} = 0$ minutes. The plot below shows the changes in normalized mean gray values that represent LC brightness intensity of the same fiber area during exposure to three pre-mixed concentrations of toluene gas using the cell-containment method (sec. 3.2.2). Each gas concentration (in μM) corresponds to the volume of toluene liquid (in μL) evaporated in a liter of ambient air prior delivery to the fiber mat. Although the experiments were conducted for longer than 9 minutes, the brightness intensity changes that occurred within the first 6-9 minutes of exposure were most relevant for observing the threshold sensitivity of the fiber mat. Select frames of the mat after exposure to roughly 1071μM of vapor at 0.27, 0.54, and 4.06 minutes illustrate how the LC core cleared (blue $\star^1$, $\star^2$, and $\star^3$).

Finally, although the reverse process, i.e the return of the LC core's nematic state after clearing in the fibers, was recorded it was not plotted for the graphs shown because I found out that the speed at which the fiber mat returned to its original state can be altered greatly. If active suction of the vapors was applied directly to the outlet of the gas cell, any lingering vapors absorbed and

not released by the polymer sheath once the outlets were opened could be immediately removed. This meant that the original brightness intensity and birefringence of the observed area could return in a manner of seconds. However, if active suction was not employed and the fiber mat was allowed to relax steadily, releasing the remaining vapors absorbed into the sheath on its own in the cell, then there was no guarantee that all the fiber segments in the mat would return to their original birefringence.

Earlier experiments without using active suction on the cell to remove the vapors showed that the swelling and eventual degradation of the fiber sheaths by meshing caused the birefringence of the LC cores to lower. In previous sessions, once vapor exposure was stopped, the valves on either side of the containment cell containing the exposed LC-fiber mat would be opened to allow the excess vapors in the mat to siphon out and mix with the atmospheric air. In retrospect, active suction should have been employed at the beginning of the trials using the cell to assist the evacuation of the toluene vapors as the vapor density of toluene is about three times as much as that of air (3.2 to 1.0(air)). Thus, like hydrocarbon based vapors such as propane and hydrogen sulfide, in the right atmospheric conditions it can aggregate towards the bottom of enclosures creating a gradient and making it difficult to ventilate completely.

Although the vapor density of air is assumed to be 1, it is often a bit higher since water vapor is often in the atmosphere. Although toluene vapor dispersed in an open space may mix with water vapor saturated air in a uniform manner and significant concentration gradients would not be expected to develop, in this case my expectation that dense toluene vapors saturated in an enclosure having less than 20 cm^3 space would evacuate uniformly without causing significant degradation to porous polymer fibers was rather short sighted. Diffusion from this containment cell would surely take longer, and moreover the chance that re-condensing vapors within the cell into the mat would eventually lead to fiber LC leakage (Fig. 7.10) should have been considered.

Note that in Fig. 7.10 among the first areas to respond first to the vapors are not LC-core filled regions of the fibers themselves but the meshed regions in between the fibers that have leaked out LC. Then the filaments with the thinnest LC cores start to clear along with regions containing isolated brights spot of twist. The meshing that can occur between fibers kept inside of the gas cell after exposure without actively removing the vapors through suction was not noticed at first, however, since it was thought that any significant vapor condensation would become macroscopically visible through the viewing window. However, for exposure trials conducted on subsequent fiber mats later this aspect was corrected and the cell containing the fiber mat was aired out sufficiently after the end of each exposure round.

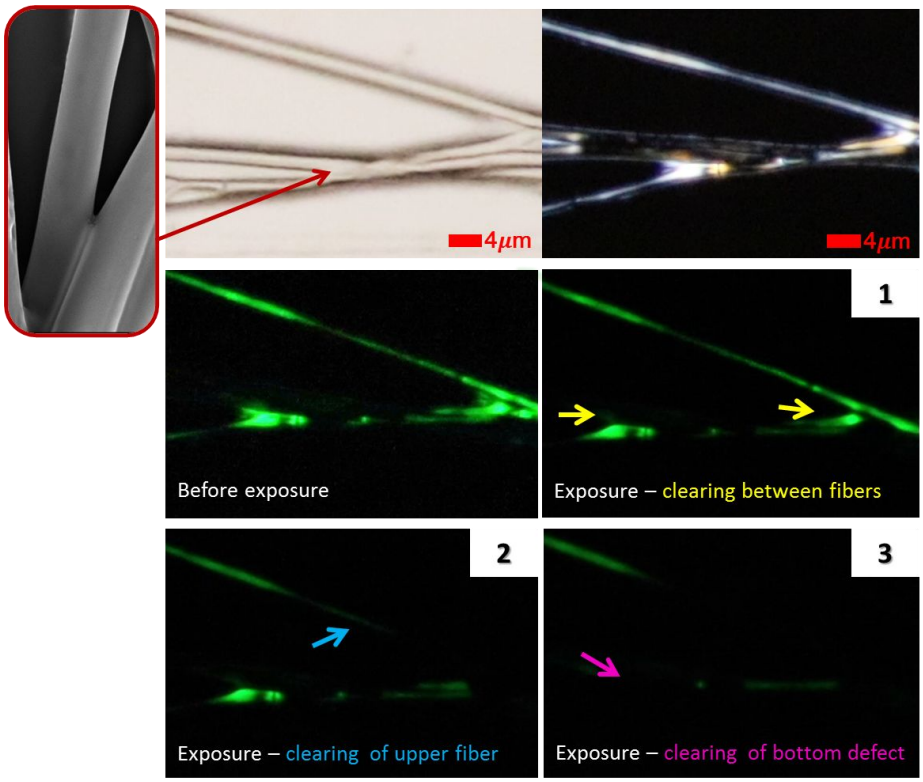

Fig. 7.10 – Region of LC-filled fibers which started to mesh and leak LC after repeated rounds of toluene vapor exposure in the containment cell. This fiber mat was continuously exposed to vapors without the realization that condensed vapors absorbed into the polymer sheaths were causing the mat to degrade. It was found that vapor evacuation from the cell using active suction is more beneficial to preserving the exposed mats than allowing the cell to release vapors by diffusion alone.

7.4.1 Tracking LC-fiber clearing versus exposure time

Returning the focus back to Fig. 7.9, however, some important points to consider from this plot are that: (1). although the area as a whole clears gradually, higher concentrations of vapors affect the fibers in a shorter period of time than the lower concentrations, and (2). the non-uniformity of the LC cores clearing is most visible when the mats are exposed to lower vapor concentrations.

Exposure to higher gas concentrations causes faster LC-fiber clearing

For the first point, this is expected largely because of the polymer sheath. In a sample area containing beaded as well non-beaded LC filled fibers we know from previous results (sec. 4.3.2) that the sheath thickness is thinner at the beads compared to the more cylindrical segments. This means that higher volumes of LC are likely to be contained in the beaded features than for the latter. Moreover, the thinness of the sheath at the beads mean that they can be easily deformed (dented inwards) after repeated rounds of vapor exposure (sec. 6.4.2) and cause the LC within to relocate throughout the fiber length (or worse, leak out). At higher exposure concentration the deformation of the filaments from the fibers swelling also becomes more likely, with the

beaded fibers being the most vulnerable from the thin sheath at these points. Recall also from Fig. 7.6 above, that local regions of twist in LC core, or deformation of the sheath enclosing the core also influence the clearing after the repetitive exposure rounds. While a beaded section having more LC usually takes a few seconds longer to clear entirely than a non-beaded section in the same fiber, if the beaded section becomes deformed (flattened or biconcave) after an exposure round then it will reduce in volume as well. The next exposure round then will result in this flattened bead responding faster than another non-deformed beaded section, and moreover, depending on just how much the bead was flattened it could up responding just as fast as the non-beaded segments in the fiber.

While liquid toluene cannot dissolve PVP with a molar mass of 1×10^6 g/mol, it does cause the polymer in powder form to gel considerably at least in solution (Fig. 7.11). The gelation of PVP in liquid toluene at room temperature, and at elevated temperature (40°C), is visible with as little as 1% by mass of the powder in the liquid. Dissolving 10% by mass of PVP in toluene is not feasible either, and as shown in Fig. 7.11, if the vial is tilted such that more solvent is separated from the polymer, we see that the gelled PVP does not flow and appears tacky sticking to the bottom of the vial. In fact, for PVP of this molar mass only about 0.16% by mass can homogeneously dissolve in toluene liquid without gelling (in my experiment I used a mass of 0.75 mg polymer in 479.8 mg of toluene).

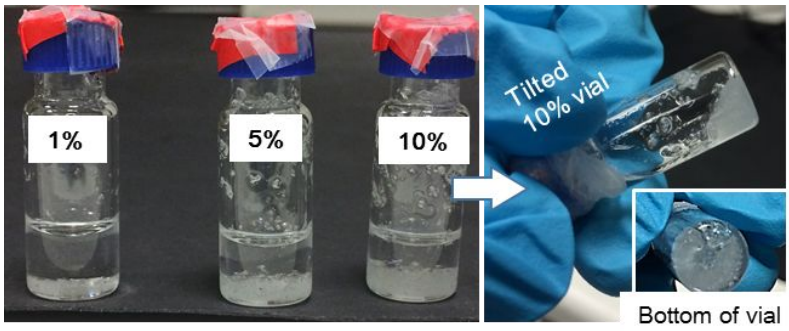

Fig. 7.11 – Different mass fractions of PVP (molar mass: 1×10^6 g/mol) in toluene showing that while this polymer is insoluble in this solvent it does gel. In tilting the vial containing the 10% mass fraction of PVP we see how the gelled porous mass separates and sticks to the bottom of the container.

Since the polymer does visibly swell in liquid toluene, it is not unreasonable to assume that repeated trials of vapor exposure at high concentrations (particularly if 200 mbar applied to a vial containing the solvent does closely correspond to a concentration between 50 - 73 μM, Table 7.3) will cause the thinnest sections of the sheath to start irreversibly gelling. This may contribute to the formation of a more porous interface against the LC confined core to form. After the gel shown for the 10% by mass PVP-toluene mixture in Fig. 7.11 was extracted and dried at room temperature for overnight in a desiccator it showed a stiff, porous PVP film. Thus, higher concentrations of VOC exposure, through the consequences of the sheath deforming faster by becoming porous and gelling, and the non-uniformity of the sheath thickness to start off with within the coaxial filaments, will cause quicker clearing of the confined LC.

Bright-dark modulations on the way to clearing cause jumps in brightness intensity

This brings me to addressing the second most interesting aspect shown in Fig. 7.9, which is that after using this vapor exposure method the non-uniformity in LC clearing is most visible when the fiber mats are exposed to concentrations of toluene vapors below 1071 μM. Note that for the green and orange curves, they first never reach the lowest brightness possible (0%) and instead the values plateau at either 40% brightness (green curve) or at ~85% brightness (orange curve). Second, there are jumps in the brightness intensity values which are especially noticeable for green curve after roughly 1.2 minutes and 2 minutes of exposure. What could explain these features? First of all, for both cases we first have to remember that what is measured is the average percent of LC brightness remaining after exposing several fiber sections, both beaded and non-beaded inside the containment cell, *not* the percent of LC brightness intensity that remains after exposing a single fiber. This means that the final plotted response curves are the average of responses detected from roughly 13 to 20 different fibers observed through the viewing window in the cell.

The concentrations of toluene vapors mixed below roughly 1000 μM are simply too low to finish clearing the LC-cores of many of the fiber sections in this area. Though the vapors are held at equilibrium inside the cell for the same amount of time for every exposure round, it seems as though the clearing of the LC cores can stabilize at intermediate points (such as 40%, or 85%) and the remaining concentration of vapors saturating the inside of the cell are not enough to cause the remaining birefringent areas to respond. One issue could be that these lower concentrations of vapor contained in the cell are not being absorbed completely through all of the fiber sheaths present, and that perhaps most of the filaments are only experiencing superficial surface adsorption of the vapor molecules instead. Previously, there have been reports which have used electrospun PVP fibers as both VOC SAW (surface acoustic wave) [231] and ion capture sensors for dyes [232], where both types of devices were shown to have high sensitivity for surface adsorption due to their mesoporosity. However, the signals detected for both types of sensors upon exposure were not optically visible, and no mention was made as to how much exposure to the targets was necessary in order for the inner bulk of the fibers to become saturated.

Additionally, though I was not able to finish testing this theory at the time, but perhaps exposing these lower concentrations of toluene gas to sparser fiber areas would help in concentrating the distribution of vapor molecules to fewer fiber sections, thus causing an increased clearing rate and more noticeable response threshold. The drawback with this approach though would be that the response threshold found, though lower, would not be representative of how a typically spun, non-sparse LC-fiber mat would perform. Finally, we should consider that since some fibers in an area intersect one another, perhaps these intersections are contributing a more complex change in birefringence, depending on whether the fibers cross largely parallel (birefringence adding) or perpendicular (birefringence subtracting). Therefore, during vapor exposure trials even if one section of the intersecting fiber clears, the fiber below may delay in clearing, or may not clear at all, and depending on the configuration, this may result to a brightness decrease or increase.

Next, the jumps in brightness intensity seen for the green curve in the plot of Fig. 7.9, which occurred twice before the clearing flat lined at 40%, should be considered. Note that the jumps were also initially visible for the orange curve before the mat began to stabilize at 85% brightness intensity, but they were most prominent during the exposure to the middle toluene concentration. One trivial explanation based on what was observed was that in the first 2 minutes of vapor exposure, again, not all the fiber areas finished clearing at once, with some areas delaying by as

much as a minute. However, this explanation does not satisfy all observations witnessed during the sensing experiments. In addition to seeing that not all the fiber areas cleared at once, the following was also observed: some fiber sections appeared to clear completely (appearing black), then after a few seconds returned in birefringence (appearing bright green), and then finally cleared for sure (black). Additionally, sometimes this phenomenon occurred in the same location, and sometimes it occurred at another location of the same fiber (where first one section turned black, then some distance away the fiber increased in brightness, and then finally became black there). These features observed are likely related to the jumps in brightness intensity detected.

For the first version of the feature observed - where the brightness intensity drops, then increases, and drops again in the same location, the explanation can be sought in the fact that the original sample birefringence may have been so high that it produced interference color beyond the first order. If a quartz wedge compensator, used for analyzing birefringent samples at a 45° angle through crossed polarizers, is illuminated with 3 types of monochromatic light (wavelengths corresponding to red, green, and blue), the quartz wedge will show a series of colored and non-colored stripes ("fringes") that align perpendicularly to the long axis of the wedge (Fig. 7.12). Unlike a single wavelength retardation plate (like the λ one) used to analyze the director of the LC-fibers in ch. 6, the quartz wedge compensator is rectangular slab of cut quartz with varying thickness used for viewing a sample through up to 4 orders of retardation (between 500 to 2000 nm) [233]. If illuminated with short monochromatic wavelengths of light (like blue, 450 nm), it will produce more bands than that if illuminated with longer monochromatic wavelengths (red, 670 nm). Although every black fringe and bright fringe will correspond to an integer multiplied by λ and every black fringe will correspond to every $1/2$ integer multiplied by λ, of course a higher starting λ used will increase the optical path difference for every fringe accordingly. Likewise, if the quartz wedge is illuminated with unpolarized white light then the interference colors of the Michel-Lévy chart (Fig. 6.4) will be reproduced.

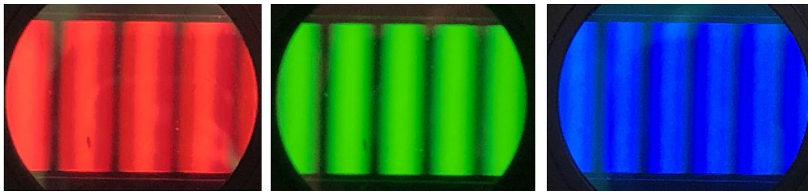

Fig. 7.12 – The appearance of bright-dark modulating fringes (or stripes) when a quartz wedge compensator is illuminated with monochromatic light of red ($\lambda = 670$ nm), green (540 nm) and blue (450 nm). The optical path differences for every black fringe will correspond to: 0λ, 1λ, 2λ...etc., while every bright fringe will correspond to: $\lambda/2$, $3\lambda/2$, $5\lambda/2$...etc. Thus, the distance between two maxima, or between two minima, will become wider when light with a larger λ is used.

For this case, since green monochromatic light was used to image the sample, it's possible that the bright-dark modulation seen before the LC in the fiber section really cleared, could be due to the initial birefringence being high enough to produce second-order interference, corresponding to the second fringe in a wedge plate. As toluene is introduced, it initially disturbs the nematic order without fully removing the nematic phase, resulting in a decreased value of the nematic order parameter S, which yields a lower value of birefringence Δn, and thus lower retardation for the same thickness. If the retardation starts at the second-order maximum, the brightness can thus initially decrease as Δn decreases, but then the brightness again increases, as the

retardation reaches the first-order maximum, before finally the transition to the isotropic state is reached and no birefringence remains.

Another plausible explanation, in particular for the bright-dark modulations being observed in separate locations of the fiber length, is centered on what was previously seen for the beaded fibers in Fig. 6.13 of sec. 6.4.2 – the clearing of certain sections in a fiber causes the movement of LC core in the filaments. While one section clears and swells with vapor absorbed, another section of the LC core some distance away, in the same fiber, merges with the LC content adjacent to it. If this occurs for more than one section filmed, then it will contribute to jumps being observed in the fiber mat brightness until the mat reaches an equilibrium point. It is especially noticeable during lower concentrations of exposure because the absorption of the vapors by all the fiber sections is lower and various LC core sections have more time to merge. After reaching equilibrium, where no area is responding anymore, then whatever fiber sections did previously clear will start becoming birefringent again once the vapors are allowed to leave the gas cell.

Ultimately, from the plot shown in Fig. 7.9 the sensitivity of the fiber mat starts when it is exposed to roughly 162 μM toluene vapors (created from evaporating 15 μL of toluene liquid in a one liter space filled with ambient air). A more prominent response is detected during exposure to slightly more than twice this concentration, at 570 μM of toluene vapor (50 μL evaporated in one liter of air), and the fastest clearing rate for all fibers is achieved at the 1000 μM level. Although compared to the results discussed for the Dräger determined sensitivity thresholds these concentration values are more than 10 times higher, these two sets of results should be treated as measuring different aspects of the LC-fiber mat sensitivity.

7.5 Reconciling threshold sensitivities from two methods of VOC exposure

As was noticed earlier, the sensitivity thresholds seen for the LC-fiber mats tested using the macroscopic sensing method plus the Dräger tubes and the sensitivity thresholds acquired from testing the mats using the containment-cell-method plus microscopic observation do not match up. Specifically, for the latter method, exposing a mat contained in the cell to a vapor mixture with concentration lower than roughly 162 μM (taking into account the error possible from using volumetric pipettes, Table 7.4) does not cause a change to occur in the mat area discussed for Fig. 7.9, either with green filter added or not. However, from previous experimental trials of gas sensing described in [83], it was seen that if a mat containing solely non-beaded fibers was exposed to slightly lower concentrations of vapors (95 μM, made by mixing 10 μL toluene in 1 L_{air}) then very small decreases in brightness were observed. These small areas that cleared in the case of ref. [83] were primarily made possible by the sheath degradation that had occurred for these samples, plus the fact that the fibers were thin to begin to with. Those samples had been tested before it was noticed that fiber sheath degradation (i.e. Fig. 7.10) was occurring from allowing the fiber mat to remain in the gas cell without actively siphoning out excess vapors post exposure trials. Thus, it was still questionable as to whether these early observations were reliable for noting the threshold response. For this reason, these experiments were then repeated again. Without taking those experiments into account though, and just the results shown from the previous sections, Fig. 7.13 compares the results of the threshold sensitivities acquired from

using both detection methods applied to fiber mats containing both beaded and non-beaded filaments.

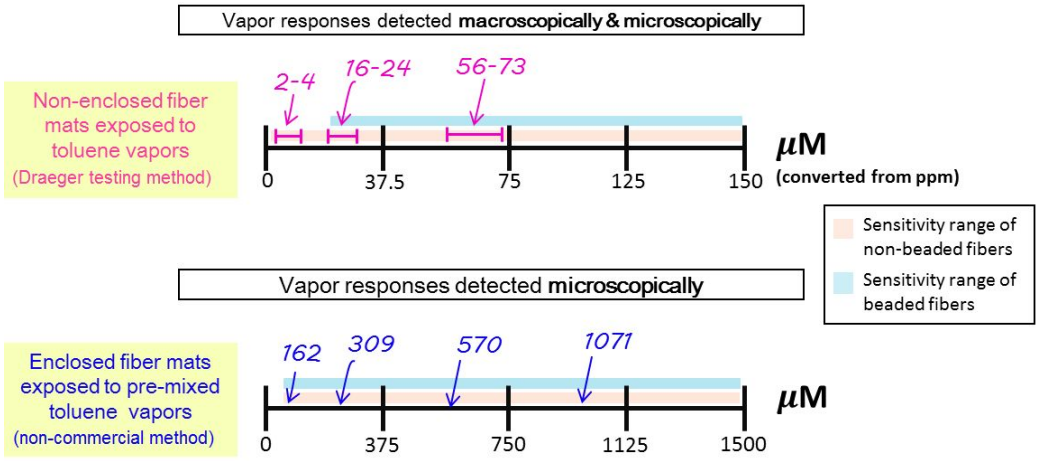

Fig. 7.13 – Summary of toluene vapor sensitivity threshold results observed for non-beaded and beaded 5CB-PVP fiber mats using two methods for sensing.

Although it appears as though the fiber mats are responsive to very low concentrations of toluene vapor when exposed to vapors generated in real-time (the macroscopically visible scattering responses), and that this directly conflicts with the very high concentrations I needed to mix in order to see microscopic responses through the containment cell, I believe that both results are useful and are not wrong. In the end, the results of these techniques cannot be directly compared. Not only were two very separate techniques used to observe the responses of the fiber mats (contained versus dispersed gas exposure), but we also know now that fiber mats containing beaded sections and non-beaded sections respond at slightly different rates and any gaps in core filling can promote LC movement within the fiber cores during exposure.

Ultimately, it's safe to say that the containment-cell is best suited for discovering how the mats work as a passive sensor over time. For discovering how the mat scattering response develops macroscopically in ambient air very quickly, the method of exposing the mats freely when not enclosed is better. Further improvements though in controlling how the threshold responses from both methods are measured are needed before the specificity of the fiber mats to other vapors can be addressed.

7.5.1 Recommendations for improving methods of exposure & verifying vapor sensitivity thresholds

The following suggestions should be implemented for improving the certainty of the VOC threshold responses detected for the LC-fiber mats, when tested using the two methods.

Recommendation #1 for method: Non-contained fiber mat exposure to VOCs in ambient air for macroscopic analysis (from sec. 7.3)

Rather than directly exposing the fiber mats to the gases emitted directly from the exposure tube in Fig. 7.1(a), the gases generated should be collected and analyzed for their concentration first. Since applying different pressure differences (5 mbar - 200 mbar) to the vial inlet clearly generates different concentrations of vapor that are transported out of the exposure tube, each

concentration can be separately collected into a an inert Tedlar sampling bag for analysis. The Tedlar bags come in pre-defined volume sizes (1L, 2L or 10L) and so noting the time it takes to fill up one bag using the vapors generated from the vial in real-time can also help in finding the rate at which the vapors are flowing out. To find the accurate quantity of the gas that was contained spectroscopic analysis should be used.

Once a Tedlar bag with the unknown gas concentration acquired using the Fluigent unit is filled, a small sample of that gas can be removed and flowed through a desorbent mixture (mentioned in the text surrounding Table 7.2) that OSHA and NIOSH use for desorbing the gases absorbed into charcoal based commercial sensors conventionally used for vapor testing. This entire mixture can then be run on a GC-MS (gas chromatography-mass spectrometer) so that the components may be separated by mass and retention time. According to the chromatograms observed in [213] for OSHA's detection of toluene vapors desorbed in the liquid mixture containing carbon disulfide, DMF and ethylbenzene (internal standard for the GC) the retention time of toluene was constant at roughly 5.2 min. Of course, since a GC curve reports abundance peaks (arb. units) for each component that are a function of the time the experiment is run, a calibration curve for toluene in order find the relationship between peak area and concentration (in μ/L) would first need to be performed.

With the GC based toluene calibration curve, and the chromatograms for each vapor sample collected in the Tedlar bags it would then be possible to correlate the toluene peak areas to the proper concentration. Moreover, it would then be possible to precisely quantify the concentration of vapor emitted from the vials from the Fluigent unit, and the rate which it flows during the application of various applied pressure values.

Additionally, in isolating the vapors generated from the vial in the Tedlar bags, it would make exposing the LC-fiber mats easier and more reliable since the concentration of these contained vapors would already have been characterized. An exposure tube could be attached to the outlet of the bag, and the bag squeezed to force out the gas. Though the responses initially noted would correspond to the specific concentration in the bag, two issues to consider are that the fiber samples would no longer be exposed to continuously generated gas and once the gas dissipates, the concentration values would drop significantly.

Recommendation #2 for method: Contained fiber mats exposed to pre-mixed gases for microscopic analysis (from sec. 7.4)

The same approach can be taken as above in using a mixture for flowing the pre-mixed gas and then characterizing this mixture to separate the components using the GC-MS. However, this would only succeed in getting half of the problem solved because although the concentration of the pre-mixed gas would be known, there would still be the question as to how much of this gas the fiber mat inside its small enclosure would experience. To answer this, one could apply the same charcoal or modified carbon sorbent materials used by NIOSH and OSHA inside of the gas cell and flow the pre-mixed vapors through. Then the desorbing process would be essentially the same as their methods [213, 215, 234] used to validate the concentrations detected from the VOC sensors they used.

While it is tempting to think that using the desorbent method for isolating the VOC or toluene molecules absorbed could work for directly dissolving the fiber mats, recall that the PVP and the LC are not volatile components and thus running this mixture through the GC will most

likely cause the device to malfunction. Moreover, even if they could be analyzed together using liquid chromatography techniques, as are used for investigating non-volatile biological matter [235], the ionization peaks in the output chromatogram showing 5CB, PVP, toluene, and the internal solvent together will require far more effort to differentiate and is more prone to error.

Another idea that could be implemented, if using the latter point is unfeasible, is to revise the connections to the containment cell such that on one end it is directly connected to a reservoir containing the liquid to be vaporized and transmitted to the fiber mat with a pressure gauge is inserted. This setup would then follow that of Bedolla-Pantoja and Abbott's shown in ref. [80]. The liquid to be evaporated could be degassed separately, attached to the main line of the cell and blocked off until ready to be used. The entire gas cell could then be evacuated, and the pressure difference caused from opening the valve to the liquid reservoir as the vapors pass through the cell would correspond to the partial pressure of the gas. This can then be related to the number of moles of the compound directly present in the exposed area.

Recommendation #3: Analysis is better suited to thin, not thick, fiber mats

Last, for best observing the changes in brightness intensity microscopically it is better to use fiber mats that do not have many layers or are not excessively thick. Even though ref. [83] notes that differences exist in the time it takes for scattering responses observed macroscopically in thicker fiber mats to appear and dissipate, observing these types of mats microscopically can become problematic for another reason. If many fibers are layered over one area, obtaining the focus of each filament's core will be more difficult as it will be intertwined with that of the other fibers causing some parts of it to become more blurry than others. With some parts of the fiber being blurry, uncertainty is added to the amount of thresholding that should be done for the analysis (Fig. 7.8) in order to isolate the LC core filled areas. With many fibers we have many polymer-air and polymer-liquid crystal interfaces, each of which gives rise to scattering. Thus, a thick mat has a background of scattering that reduces the precision of the analysis.

While the issue of fiber mat thickness was not explored in detail for determining its impact on raising the sensing threshold detected at this time, it seems like this issue addresses points more related to the design and implementation of the final sensor, which although outside the scope of this thesis, could be explored further in the future. It may be particularly interesting as well to combine this investigation with the exploration of how different LC-fiber mat configurations electrospun by tuning the collectors can also contribute to changes in threshold sensitivity. However, before these more applied aspects can be explored, it is clear that not only the sensitivity threshold data needs to be further confirmed, perhaps by using the spectroscopic methods that previous organizations have used in addition to the methods presented here, but also that the confinement of the LC within the fibers needs to have more robust polymer sheaths. The latter is especially crucial in order to avoid fiber buckling and degradation after multiple rounds of vapor exposure, which can also impact the sensitivity data obtained.

8 Conclusions & Outlook

While a cursory glance at the structure may give the impression that this thesis is quite broad in scope (with topics ranging from electrospinning, to phase separation, to liquid crystal optics, and gas sensing) all these facets had to be taken into consideration for explaining the end results. In this sense, while broad themes are discussed, they are very specifically used to address a single focus: the challenges and advantages of using a very specialized type of anisotropic self-assembled material (liquid crystals) combined with a niche fiber spinning method (electrospinning) to make a functional gas sensing textile for easy integration.

8.1 A summary of the main results

Ultimately, what was found throughout the course of this work is that, first, if coaxially electrospinning with multiple fluids, the variables affecting fiber formation should be carefully re-prioritized for every new LC-polymer solution system. This means that not only can the misciblity, or immiscibility, of the polymer solution with the LC phase be important, but the ambient conditions as well which can influence the phase separation of the two during spinning. Second, the confinement of the LC within the fibers will determine how the mat optically responds to gases and the fiber morphological structure (whether it is beaded or non-beaded) will dictate how the LC is confined. The confined LC phase within a polymer fiber, having no birefringence of its own, will impart this attribute to make the fiber mat scatter more strongly than an unfilled mat. This new form factor will allow the responsivity of the LC to gases and heat to be detectable macroscopically. However, how the individual LC filled fibers in a mat respond will depend largely on how the LC is confined, If the polymer sheath adopts a beaded morphology, the responses can be slightly delayed compared to the non-beaded sections of the fiber.

If the filled fibers contain LC director defects, or areas where there is a twisted director field, these will respond faster. Air gaps within the fiber cores will also contribute to the movement of LC sections within the cores, and may cause fiber swelling and deformations in the sheath to irreversibly occur. All of these attributes describing the filling of the LC within the fibers will contribute to mats formed from these filaments responding to heat, and gas exposure non-uniformly. Thus, determining a strict threshold of sensitivity for these mats to VOCs is not a trivial process as the LC confinement impacts how the fiber is perceived (birefringence), and the fiber morphology impacts the LC confinement.

Finally, how the fiber mats are exposed to gases for detection plays an important role in how the responses can be visualized. If exposed using highly localized streams of continuously flowing gas, then changes in the overall scattering of the mat will be readily visible. If exposed using broad streams of diluted gas and allowed to sit until equilibrated, then individual fiber cores responding section by section can be observed. Sensitivities acquired from both methods of testing, however, should be considered separately for attaining separate goals (sensors that react

passively over time versus sensors that respond immediately to direct flows of gas). Last, in order to further improve measurements made regarding the sensitivity of the fibers spectroscopic techniques, such as GC-MS, should be used in tandem with the sensing methods described in ch. 7 for confirming values.

8.2 Recommendations for better fiber formation & gas sensing

8.2.1 Changing the polymer sheath & spinning method

Since the degradation of the PVP polymer sheath impacts the confinement of the LC, as well as the threshold sensitivity to VOCs, alternatives to using it are necessary for improving the long-term stability of the electrospun LC-fiber mat (particularly, if employed in highly humid environments).

There are some constraints on choosing a polymer however. A polymer must:

- it must be non-crystallizing/atactic (so that it does not optically interfere with distinguishing the level of LC confinement within post electrospinning)
- cannot be soluble in the target gas (PVP is not readily dissolved in toluene, but can gel)
- be electrospinnable into micron-size (or larger) fibers, and be resistant to swelling in water.

Although the polymer can be a co-polymer, given the phase separation that occurs with 5CB and ethanol found, the addition of other monomer sections that can potentially give rise to unfavorable separations, or precipitations, during electrospinning should be limited. Although LC electrospinning with polystyrene has been attempted it has not been explored in enough detail, and shown in Fig. 4.6 on pg. 58 is at least one instance where the Taylor cone partially solidified when polystyrene in DMF was attempted to be spun with 5CB.

One recommendation may be that polycaprolactone may be able to satisfy the requirement of atacticty needed [236], however, it may not be able to form the 4μm sized (or larger diameter) filaments desired [237]. One other positive aspect about this polymer is that if it is melt electrospun it can make filaments with diameters as large as 33 μm wide [238], and likewise, depending on how the polymer melt is cooled during extrusion, fiber mats created from this biodegradable polymer may be able to withstand significant exposure to humid environments [239].

Employing another polymer and another facile spinning technique (compared to the conventional ones such as wet and melt spinning which traditionally require several more industrial components) like melt electrospinning may alleviate the issues of ambient water condensation, LC-solvent miscibility, and the requirements for polymer atacticity and large diameter encountered here while encapsulating 5CB. Moreover, as melt electrospinning is gaining popularity for use in designing well aligned tissue scaffolds in the biomaterials community more polymers that amorphous which can easily degrade are being spun: polyurethane, poly(methyl methacrylate), and atactic polypropylene, to name a few [4, 240].

Moreover as of 2011 melt electrospinning has also been combined with 3D printing ventures to create highly stackable three dimensional fiber based structures with very defined resolution [241]. These developments open up novel avenues for further exploring the encapsulation of LC

phases within the textile format not only limited to creating unique responsive materials, but also for fundamental studies concerning LC director confinement, in both uniformly aligned or deformed ways, and defect formation.

8.2.2 A selective sensor made from fibers encapsulating different LCs

While the opportunity to optimize the selectivity of the 5CB-PVP fiber mats to various VOCs was missed here, an interesting aspect was noticed in conjunction to observing the macroscale qualitative responses of various LC filled PVP fiber mats to heat (related to Fig. 6.11 on pg. 129). Compared to the 5CB-PVP fiber mats, ROTN-403 filled fiber mats containing some chiral dopant do not readily respond to similar concentrations of acetone vapors. The scattering responses observed for ROTN filled mats spun for roughly the same time, and which qualitatively have similar amounts of fiber distribution as those of the 5CB filled mats, are either very faint or not visible at all.

This may suggest that, in addition to attempting electrospin LC fibers containing an LC with an agent that could alter the LC anchoring upon VOC exposure (just as Abbott's group had done in the past by using perchlorate salts in nematic phases that selectively bonded to organophosphonate group containing VOCs), combining various LC filled fiber mats into an array-like format and exposing this collective group to target gases may also be a way of differentiating selectivity based on the response patterns seen in the group. Moreover, the exploration of how the sensitivity of the fiber mats to certain vapor concentrations can be tuned by adding different amounts, or types of, chiral dopants to the nematic LCs (in addition to adding selective reflection to the mats) can also be advantageous. Altering the assembly of combined LC filled fiber mats in different configurations and seeing how the visual scattering responses to gases may be changed or tuned is also another avenue that can be explored.

Ultimately, there are many opportunities and challenges for continuing LC-fiber encapsulation research. And, indeed, while LC phases are confined within polymer fibers, the potential uses for advanced materials developed from these structures (as those who will likely improve upon them in the future) will probably not be confined to just one field or discipline either.

Bibliography

[1]W. Gilbert. *De Magnete, Magneticisque Corporibus, et de Magno Magnete Tellure (On the Magnet and Magnetic Bodies, and on That Great Magnet the Earth)*. London: Londini, 1600 (cited on pg. 1).

[2]N. Tucker and J. Stanger. "The History of the Science and Technology of Electrospinning from 1600 to 1995". In: *J. Eng. Fiber. Fabr.* 7 (2012), pp. 63–73 (cited on pg. 1).

[3]C. J. Luo et al. "Electrospinning versus fibre production methods: from specifics to technological convergence". In: *Chem. Soc. Rev.* 41.13 (2012), p. 4708 (cited on pg. 1).

[4]Y. Kadomae et al. "Relation between tacticity and fiber diameter in melt-electrospinning of polypropylene". In: *Fibers Polym.* 10.3 (2009), pp. 275–279 (cited on pgs. 1, 168).

[5]D. H. Reneker and A. L. Yarin. "Electrospinning jets and polymer nanofibers". In: *Polymer* 49.10 (2008), pp. 2387–2425 (cited on pgs. 1, 8, 9, 47, 53, 54).

[6]M. M. Hohman et al. "Electrospinning and electrically forced jets. II. Applications". In: *Phys. Fluids* 13.8 (2001), pp. 2221–2236 (cited on pgs. 1, 9).

[7]M. M. Hohman et al. "Electrospinning and electrically forced jets. I. Stability theory". In: *Phys. Fluids* 13.8 (2001), p. 2201 (cited on pgs. 1, 9).

[8]Revolution Fibres. *Seta (TM) Filtration*. `https://www.revolutionfibres.com/products/seta-filter-system/`. 2018 (cited on pg. 1).

[9]The Electrospinning Company. *Mimetix Scaffolds*. `https://www.electrospinning.co.uk/3d-cell-culture/mimetix-scaffolds/`. 2018 (cited on pg. 1).

[10]L. Lejček et al. "Commemorative plaque of Prof. Friedrich Reinitzer installed in Prague". In: *Liq. Cryst. Today* 26.3 (2017), pp. 66–68 (cited on pg. 1).

[11]D. Dunmur and T. Sluckin. *Soap, Science and FlatScreen TVs*. New York: Oxford University Press, 2011 (cited on pgs. 2, 13, 15).

[12]I. Dierking. *Textures of Liquid Crystals*. Darmstadt: Wiley-VCH Verlag GmbH & Co. KGaA, 2003 (cited on pgs. 3, 12–15, 63).

[13]J. B. Fenn et al. "Electrospray ionization for mass spectrometry of large biomolecules". In: *Science* 246.4926 (1989), pp. 64–71 (cited on pg. 5).

[14]J. K. Ziemer et al. "Colloid micro-newton thrusters for the space technology 7 mission". In: *IEEE Aerosp. Conf. Proc.* 2010 (cited on pg. 5).

[15]D. Krejci and P. Lozano. "Space Propulsion Technology for Small Spacecraft". In: *Proc. IEEE* 106.3 (2018), pp. 362–378 (cited on pg. 5).

[16]National Aeronautics and Space Administration (NASA). *Next Space Technologies for Exploration Partnerships (NextSTEP) Projects*. https://www.nasa.gov/feature/next-space-technologies-for-exploration-partnerships-nextstep-projects. 2015 (cited on pg. 5).

[17]F. Zhou et al. "Mass production of nanofibre assemblies by electrostatic spinning". In: *Polym. Int.* 58.4 (2009), pp. 331–342 (cited on pgs. 5, 35).

[18]R. Gopal et al. "Electrospun nanofibrous filtration membrane". In: *J. Memb. Sci.* 281.1-2 (2006), pp. 581–586 (cited on pg. 5).

[19]J. Sharma et al. *Multifunctional Nanofibers towards Active Biomedical Therapeutics*. Vol. 7. 2. 2015, pp. 186–219 (cited on pg. 5).

[20]T. Maver et al. "Combining 3D printing and electrospinning for preparation of pain-relieving wound-dressing materials". In: *J. Sol-Gel Sci. Technol.* 88.1 (2018), pp. 33–48 (cited on pg. 5).

[21]A. Andrady. *Science and technology of polymer nanofibers*. Hoboken: John Wiley & Sons, Inc., 2008, pp. 1–424 (cited on pgs. 5, 8–10, 37, 50).

[22]P.-G. de Gennes et al. *Capillarity and Wetting Phenomena*. New York, NY: Springer New York, 2004 (cited on pg. 7).

[23]J. Plateau. *Statique Experimentale et Theorique des Liquids Soumis aux Seules Forces Moleculaire (Vol.2)*. Paris, France: Gauthiers-Villars Paris, 1873 (cited on pg. 7).

[24]Lord Rayleigh. "On The Instability Of Jets". In: *Proceedings of the London Mathematical Society* s1-10.1 (1878), pp. 4–13. eprint: https://londmathsoc.onlinelibrary.wiley.com/doi/pdf/10.1112/plms/s1-10.1.4 (cited on pg. 7).

[25]Lord Rayleigh. "XVI. On the instability of a cylinder of viscous liquid under capillary force". In: *Philos. Mag* 34.207 (1892), pp. 145–154 (cited on pg. 7).

[26]B. Bugarski et al. "Effect of electrode geometry and charge on the production of polymer microbeads by electrostatics". In: *Can. J. Chem. Eng.* 72.3 (1994), pp. 517–521 (cited on pg. 7).

[27]D. H. Reneker and I. Chun. "Nanometre diameter fibres of polymer, produced by electrospinning". In: *Nanotechnology* 7.3 (1996), pp. 216–223 (cited on pg. 8).

[28]G. Taylor. "Disintegration of Water Drops in an Electric Field". In: *Proc. R. Soc. A Math. Phys. Eng. Sci.* 280.1382 (1964), pp. 383–397 (cited on pgs. 8, 47, 50, 54).

[29]G. Taylor. "Electrically Driven Jets". In: *Proc. R. Soc. A Math. Phys. Eng. Sci.* 313.1515 (1969), pp. 453–475 (cited on pgs. 8, 54).

[30]Lord Rayleigh. "XX. On the equilibrium of liquid conducting masses charged with electricity". In: *Philos. Mag. Ser. 5* 14.87 (1882), pp. 184–186 (cited on pg. 8).

[31]H. Xu and D. H. Reneker. "Characterization of Electrospinning Jets Using Interference Color Technique The Origin of the Interference Color on a Cylindrical Jet". In: *Polym. Nanofibers* 918 (2006), pp. 21–35 (cited on pg. 8).

[32]A. L. Yarin et al. "Bending instability in electrospinning of nanofibers". In: *J. Appl. Phys.* 89.5 (2001), pp. 3018–3026 (cited on pgs. 9, 47, 50, 68).

[33]Guillaume Riboux et al. "Whipping instability characterization of an electrified visco-capillary jet". In: *J. Fluid Mech.* 671 (2011), pp. 226–253 (cited on pg. 9).

[34]A. Holzmeister et al. "Barb formation in electrospinning: Experimental and theoretical investigations". In: *Polymer.* 51.12 (2010), pp. 2769–2778 (cited on pg. 10).

[35]S. Agarwal et al. "Characterization of spinning solutions and fibers". In: *Electrospinning A Pract. Guid. to Nanofibers*. Berlin: Walter de Gruyter GmbH, 2016, pp. 40–60 (cited on pg. 10).

[36]Z.-M. Huang et al. "A review on polymer nanofibers by electrospinning and their applications in nanocomposites". In: *Compos. Sci. Technol.* 63.15 (2003), pp. 2223–2253 (cited on pg. 10).

[37]T. Subbiah et al. "Electrospinning of nanofibers". In: *J. Appl. Polym. Sci.* 96.2 (2005), pp. 557–569 (cited on pg. 10).

[38]V. Kleivaitė and R. Milašius. "Electrospinning – 100 Years of Investigations and Still Open Questions of Web Structure Estimination". In: *Autex Res. J.* 0.0 (2018) (cited on pg. 10).

[39]O. Akampumuza et al. "Raising Nanofiber Output: The Progress, Mechanisms, Challenges, and Reasons for the Pursuit". In: *Macromol. Mater. Eng.* 303.1 (2018), p. 1700269 (cited on pg. 10).

[40]M. Urbanski et al. "Liquid crystals in micron-scale droplets, shells and fibers". In: *J. Phys. Condens. Matter* 29.13 (2017), p. 133003 (cited on pgs. 10, 13–15, 23, 24, 26, 58, 121).

[41]C. L. Casper et al. "Controlling Surface Morphology of Electrospun Polystyrene Fibers: Effect of Humidity and Molecular Weight in the Electrospinning Process". In: *Macromolecules* 37.2 (2004), pp. 573–578 (cited on pgs. 11, 35, 37, 74, 75).

[42]P. Lu and Y. Xia. "Maneuvering the Internal Porosity and Surface Morphology of Electrospun Polystyrene Yarns by Controlling the Solvent and Relative Humidity". In: *Langmuir* 29.23 (2013), pp. 7070–7078 (cited on pgs. 11, 35, 75).

[43]D. K. Kim and J. P. F. Lagerwall. "Influence of Wetting on Morphology and Core Content in Electrospun Core–Sheath Fibers". In: *ACS Appl. Mater. Interfaces* 6.18 (2014), pp. 16441–16447 (cited on pgs. 11, 48).

[44]S. Koombhongse et al. "Flat polymer ribbons and other shapes by electrospinning". In: *J. Polym. Sci. Part B Polym. Phys.* 39.21 (2001), pp. 2598–2606 (cited on pgs. 11, 48, 53, 54, 70).

[45]P. J. Collings and M. Hird. *Introduction to Liquid Crystals*. London: Taylor & Francis, 1997 (cited on pg. 11).

[46]J. N. Israelachvili and D. J. Mitchell. "A model for the packing of lipids in bilayer membranes". In: *BBA - Biomembr.* 389.1 (1975), pp. 13–19 (cited on pg. 12).

[47]C.C. Mueller-Goymann. "Physicochemical characterization of colloidal drug delivery systems such as reverse micelles, vesicles, liquid crystals and nanoparticles for topical administration". In: *Eur. J. Pharm. Biopharm.* 58.2 (2004), pp. 343–356 (cited on pg. 12).

[48]G. Ao et al. "Cholesteric and nematic liquid crystalline phase behavior of double-stranded DNA stabilized single-walled carbon nanotube dispersions". In: *ACS Nano* 5.2 (2011), pp. 1450–1458 (cited on pg. 12).

[49]M. Kleman and O. Lavrentovich. *Soft Matter Physics, An Introduction*. New York: Springer-Verlag, 2003 (cited on pg. 13).

[50]J. P. F. Lagerwall and G. Scalia. "A new era for liquid crystal research: Applications of liquid crystals in soft matter nano-, bio- and microtechnology". In: *Curr. Appl. Phys.* 12.6 (2012), pp. 1387–1412 (cited on pg. 13).

[51]J. P. Sethna. "Order Parameters, Broken Symmetry, and Topology". In: *Lect. Sci. Complex.* Ed. by Lynn Nadel and Daniel L. Stein. Addison-Wesley Publishing Company, Inc, 1992, pp. 243–288. arXiv: 9204009 [cond-mat] (cited on pg. 14).

[52]G. R. Luckhurst and R. N. Yeates. "Negative Order Parameters For Nematic Liquid Crystals?" In: *Mol. Cryst. Liq. Cryst.* 34.2 (1976), pp. 57–61 (cited on pg. 14).

[53]J. Viamontes et al. "Orientational order parameter of the nematic liquid crystalline phase of F -actin". In: *Phys. Rev. E - Stat. Nonlinear, Soft Matter Phys.* 73.6 (2006), pp. 1–10 (cited on pg. 14).

[54]D. Mistry et al. "Coincident Molecular Auxeticity and Negative Order Parameter in a Liquid Crystal Elastomer". In: *Arxiv.org* (2018), pp. 1–11. arXiv: 1807.03608 (cited on pg. 14).

[55]M. Kleman and O. Lavrentovich. "The Order Parameter: Amplitude and Phase". In: *Soft Matter Physics, An Introd.* New York: Springer-Verlag, 2003. Chap. 3, pp. 76–98 (cited on pg. 14).

[56]S. Chandrasekhar and N. V. Madhusudana. "Spectroscopy of Liquid Crystals". In: *Appl. Spectrosc. Rev.* 6.2 (1972), pp. 189–311 (cited on pg. 14).

[57]N. V. Madhusudana and R. Pratibha. "Elasticity and orientational order in some cyanobiphenyls. Part IV. Reanalysis of the data". In: *Mol. Cryst. Liq. Cryst.* 89.1-4 (1982), pp. 249–257 (cited on pgs. 16, 121).

[58]Z. S. Davidson. "Assembly, elasticity and structure of lyotropic chromonic liquid crystals and disorderd colloids". PhD thesis. University of Pennsylvania, 2017 (cited on pgs. 16, 121, 122, 127).

[59]M. Kleman and O. Lavrentovich. "Surface Anchoring in Nematic Liquid Crystals". In: *Soft Matter Physics, An Introd.* New York: Springer-Verlag, 2003. Chap. 13, pp. 492–495 (cited on pg. 17).

[60]D. W. Green et al. "Mechanical properties of wood." In: *Wood Handb. Wood as an Eng. Mater.* Madison: USDA Forest Service, Forest Products Laboratory, 1999. General technical report FPL, 1999. Chap. 4, pp. 4.1–4.45 (cited on pg. 17).

[61]D. J. David and E. E. Hardy. *Organic Vapor Detection with Liquid Crystals*. 1977 (cited on pg. 23).

[62]J. E. Jacobs. *Liquid Crystal Gas Analyzer*. 1975 (cited on pg. 23).

[63]F.L. Dickert et al. "Molecular recognition of organic solvents and ammonia: shapes and donor properties as sensor effects". In: *Sensors Actuators B Chem.* 6.1-3 (1992), pp. 25–28 (cited on pgs. 23, 26, 140).

[64]F. L. Dickert et al. "Cholesteric liquid crystals for solvent vapour detection - Elimination of cross sensitivity by band shape analysis and pattern recognition". In: *Fresenius. J. Anal. Chem.* 350.10-11 (1994), pp. 577–581 (cited on pgs. 23, 24, 26).

[65]J. Clements et al. "Novel, self-organising materials for use in gas sensor arrays: beating the humidity problem." In: *Sensors Actuators B Chem.* 47.1-3 (1998), pp. 37–42 (cited on pg. 23).

[66]D. A. Winterbottom et al. "Cholesteric liquid crystals for detection of organic vapours". In: *Sensors Actuators B Chem.* 90.1-3 (2003), pp. 52–57 (cited on pg. 23).

[67]J. P. F. Lagerwall et al. "Coaxial electrospinning of microfibres with liquid crystal in the core". In: *Chem. Commun.* 42 (2008), p. 5420 (cited on pg. 23).

[68]E. A. Buyuktanir et al. "Self-assembled, optically responsive nematic liquid crystal/polymer core-shell fibers: Formation and characterization". In: *Polymer* 51.21 (2010), pp. 4823–4830 (cited on pg. 23).

[69]D. K. Kim et al. "Liquid crystal functionalization of electrospun polymer fibers". In: *J. Polym. Sci. Part B Polym. Phys.* 51.11 (2013), pp. 855–867 (cited on pgs. 23, 24, 26, 29).

[70]C. G. Reyes et al. "Non-electronic gas sensors from electrospun mats of liquid crystal core fibres for detecting volatile organic compounds at room temperature". In: *Liq. Cryst.* 43.13-15 (2016), pp. 1986–2001 (cited on pgs. 23, 24, 26, 29, 30, 32, 38, 43, 70, 76, 123, 124, 128, 131, 135, 142, 150, 153).

[71]X. Liu et al. "A Survey on Gas Sensing Technology". In: *Sensors* 12.7 (2012), pp. 9635–9665 (cited on pg. 24).

[72]G. F. Fine et al. "Metal Oxide Semi-Conductor Gas Sensors in Environmental Monitoring". In: *Sensors* 10.6 (2010), pp. 5469–5502 (cited on pg. 24).

[73]V. E. Bochenkov and G. B. Sergeev. "Sensitivity , Selectivity , and Stability of Gas-Sensitive Metal-Oxide Nanostructures". In: *Met. Oxide Nano-structures Their Appl.* Ed. by Ahmad Umar and Yoon-Bong Hahn. Vol. 3. American Scientific Publishers, 2010. Chap. 2, pp. 31–52 (cited on pg. 24).

[74]N. Yamazoe. "New approaches for improving semiconductor gas sensors". In: *Sensors Actuators B Chem.* 5.1-4 (1991), pp. 7–19 (cited on pg. 24).

[75]H. Yoon and J. Jang. "Conducting-Polymer Nanomaterials for High-Performance Sensor Applications: Issues and Challenges". In: *Adv. Funct. Mater.* 19.10 (2009), pp. 1567–1576 (cited on pg. 24).

[76]C. B. Jacobs et al. "Review: Carbon nanotube based electrochemical sensors for biomolecules". In: *Anal. Chim. Acta* 662.2 (2010), pp. 105–127 (cited on pg. 24).

[77]M. L. Bungabong et al. "Using copper perchlorate doped liquid crystals for the detection of organophosphonate vapor". In: *Sensors Actuators B Chem.* 148.2 (2010), pp. 420–426 (cited on pgs. 24, 140).

[78]J. T. Hunter and N. L. Abbott. "Dynamics of the chemo-optical response of supported films of nematic liquid crystals". In: *Sensors Actuators B Chem.* 183 (2013), pp. 71–80 (cited on pgs. 24, 25).

[79]K. D. Cadwell et al. "Detection of organophosphorous nerve agents using liquid crystals supported on chemically functionalized surfaces". In: *Sensors Actuators B Chem.* 128.1 (2007), pp. 91–98 (cited on pgs. 24, 25).

[80]M. A. Bedolla-Pantoja and N. L. Abbott. "Surface-Controlled Orientational Transitions in Elastically Strained Films of Liquid Crystal That Are Triggered by Vapors of Toluene". In: *ACS Appl. Mater. Interfaces* 8.20 (2016), pp. 13114–13122 (cited on pgs. 24, 25, 127, 140, 148, 166).

[81]C. Chang et al. "Optical detection of organic vapors using cholesteric liquid crystals". In: *Appl. Phys. Lett.* 99.7 (2011), p. 073504 (cited on pg. 24).

[82]Y. Han et al. "Optical monitoring of gases with cholesteric liquid crystals". In: *J. Am. Chem. Soc.* 132.9 (2010), pp. 2961–2967 (cited on pgs. 24–26).

[83]C. G. Reyes and J. P. F. Lagerwall. "Advancing flexible volatile compound sensors using liquid crystals encapsulated in polymer fibers". In: vol. 10555. 2018, pp. 10555 –10555 –14 (cited on pgs. 24, 26, 39, 124, 163, 166).

[84]C. Ataman et al. "A robust platform for textile integrated gas sensors". In: *Sensors Actuators, B Chem.* 177 (2013), pp. 1053–1061 (cited on pg. 24).

[85]A. Frutiger et al. "Capacitive Soft Strain Sensors via Multicore-Shell Fiber Printing". In: *Adv. Mater.* 27.15 (2015), pp. 2440–2446 (cited on pg. 24).

[86]S. Yao and Y. Zhu. "Nanomaterial-Enabled Stretchable Conductors: Strategies, Materials and Devices". In: *Adv. Mater.* 27.9 (2015), pp. 1480–1511 (cited on pg. 24).

[87]J Courbat et al. "Foil level packaging of a chemical gas sensor". In: *J. Micromechanics Microengineering* 20.5 (2010), p. 055026 (cited on pg. 24).

[88]D. Vilela et al. "Flexible sensors for biomedical technology". In: *Lab Chip* 16 (2016), pp. 402–408 (cited on pg. 24).

[89]K.-L. Yang et al. "Mechanistic Study of the Anchoring Behavior of Liquid Crystals Supported on Metal Salts and Their Orientational Responses to Dimethyl Methylphosphonate". In: *J. Phys. Chem. B* 108.52 (2004), pp. 20180–20186 (cited on pg. 25).

[90]A. Sen and B. R. Acharya. "Alignment of nematic liquid crystals at inorganic salt-liquid crystal interfaces". In: *Liq. Cryst.* 38.4 (2011), pp. 495–506 (cited on pg. 25).

[91]L. T. Roling et al. "Towards first-principles molecular design of liquid crystal-based chemoresponsive systems". In: *Nat. Commun.* 7 (2016), p. 13338 (cited on pg. 25).

[92]A. Saha et al. "Irreversible visual sensing of humidity using a cholesteric liquid crystal." In: *Chem. Commun. (Camb).* 48.38 (2012), pp. 4579–81 (cited on pg. 25).

[93]N. Herzer et al. "Printable Optical Sensors Based on H-Bonded Supramolecular Cholesteric Liquid Crystal Networks". In: *J. Am. Chem. Soc.* 134.18 (2012), pp. 7608–7611 (cited on pg. 25).

[94]F. Haaf et al. "Polymers of N-Vinylpyrrolidone: Synthesis, Characterization and uses". In: *Polym. J.* 17.1 (1985), pp. 143–152 (cited on pgs. 28, 51, 82).

[95]D. Li and Y. Xia. "Fabrication of titania nanofibers by electrospinning". In: *Nano Lett.* 3.4 (2003), pp. 555–560 (cited on pg. 29).

[96]E. Enz and J. P. F. Lagerwall. "Electrospun microfibres with temperature sensitive iridescence from encapsulated cholesteric liquid crystal". In: *J. Mater. Chem.* 20.33 (2010), p. 6866 (cited on pg. 29).

[97]E. Enz. "Electrospun Polymer - Liquid Crystal Composite Fibres". PhD thesis. Martin-Luther-Universit at Halle-Wittenberg, 2013, pp. 1–147 (cited on pgs. 31, 63, 88).

[98]A. Sharma and J. P. F. Lagerwall. "Electrospun Composite Liquid Crystal Elastomer Fibers". In: *Materials (Basel).* 11.3 (2018), p. 393 (cited on pg. 32).

[99]W. Zeng et al. "Characterization of syringe-pump-driven versus pressure-driven microfluidic flows". In: *2015 International Conference on Fluid Power and Mechatronics (FPM)*. 2015, pp. 711–715 (cited on pg. 34).

[100]C. G. Reyes and M. W. Frey. "Morphological traits essential to electrospun and grafted Nylon-6 nanofiber membranes for capturing submicron simulated exhaled breath aerosols". In: *J. Appl. Polym. Sci.* 134.17 (2017), pp. 1–15 (cited on pg. 35).

[101]D. Yang et al. "Electrospun Nanofibrous Membranes: A Novel Solid Substrate for Microfluidic Immunoassays for HIV". In: *Adv. Mater.* 20.24 (2008), pp. 4770–4775 (cited on pg. 35).

[102]G. Scalia et al. "Morphology and core continuity of liquid-crystal functionalized, coaxially electrospun fiber mats tuned via the polymer sheath solution". In: *Macromol. Mater. Eng.* 298.5 (2013), pp. 583–589 (cited on pgs. 35, 36).

[103]L. Natarajan et al. "Surface morphology of electrospun PLA fibers: mechanisms of pore formation". In: *RSC Adv.* 4.83 (2014), pp. 44082–44088 (cited on pg. 35).

[104]X. F. Wu et al. "Modeling of solvent evaporation from polymer jets in electrospinning". In: *Appl. Phys. Lett.* 98.22 (2011), pp. 2014–2017 (cited on pgs. 36, 37).

[105]A. Greiner and J. H. Wendorff. "Electrospinning: A Fascinating Method for the Preparation of Ultrathin Fibers". In: *Angew. Chemie Int. Ed.* 46.30 (2007), pp. 5670–5703 (cited on pg. 37).

[106]S. Megelski et al. "Micro- and nanostructured surface morphology on electrospun polymer fibers". In: *Macromolecules* 35.22 (2002), pp. 8456–8466 (cited on pgs. 37, 51, 74).

[107]National Institute for Occupational Safety and Health. "N,N-Dimethylformamide (DMF) - NIOSH pocket guide to chemical hazards". In: *DHHS Publ.* no. 2005-149 (2005) (cited on pg. 37).

[108]D. Ambrose and C. H. S. Sprake. "Thermodynamic properties of organic oxygen compounds XXV. Vapour pressures and normal boiling temperatures of aliphatic alcohols". In: *J. Chem. Thermodyn.* 2.5 (1970), pp. 631–645 (cited on pg. 37).

[109]National Institute for Occupational Safety and Health. "Ethanol - NIOSH pocket guide to chemical hazards". In: *DHHS Publ.* no 2005-149 (2005) (cited on pg. 37).

[110]J. S. Kiurski et al. "Indoor air quality investigation from screen printing industry". In: *Renew. Sustain. Energy Rev.* 28 (2013), pp. 224–231 (cited on pg. 37).

[111]M. Yan et al. "Emission of volatile organic compounds from new furniture products and its impact on human health". In: *Hum. Ecol. Risk Assess. An Int. J.* 7039 (2018), pp. 1–21 (cited on pg. 37).

[112]M. Fries et al. "Airborne exposures associated with the typical use of an aerosol brake cleaner during vehicle repair work". In: *J. Occup. Environ. Hyg.* 15.7 (2018), pp. 531–540 (cited on pg. 37).

[113]L. Kopelovich et al. "Screening-level human health risk assessment of toluene and dibutyl phthalate in nail lacquers". In: *Food Chem. Toxicol.* 81 (2015), pp. 46–53 (cited on pg. 37).

[114]V. M. Pak et al. "Occupational Chemical Exposures Among Cosmetologists: Risk of Reproductive Disorders". In: *Workplace Health Saf.* 61.12 (2013), pp. 522–528. arXiv: NIHMS150003 (cited on pg. 37).

[115]F. Yavari et al. "Effect of acute exposure to toluene on cortical excitability, neuroplasticity, and motor learning in healthy humans." In: *Arch. Toxicol.* 92.10 (2018), pp. 3149–3162 (cited on pg. 37).

[116]B. Barua and M. C. Saha. "Investigation on jet stability, fiber diameter, and tensile properties of electrospun polyacrylonitrile nanofibrous yarns". In: *J. Appl. Polym. Sci.* 132.18 (2015), n/a–n/a (cited on pgs. 47, 54, 55).

[117]L. M. Bellan et al. "Direct measurement of fluid velocity in an electrospinning jet using particle image velocimetry". In: *J. Appl. Phys.* 102.9 (2007) (cited on pg. 47).

[118]J. J. Feng. "Stretching of a straight electrically charged viscoelastic jet". In: *J. Nonnewton. Fluid Mech.* 116.1 (2003), pp. 55–70 (cited on pg. 47).

[119]A. V. Bazilevsky et al. "Co-electrospinning of Core-Shell Fibers Using a Single-Nozzle Technique". In: *Langmuir* 23.5 (2007), pp. 2311–2314 (cited on pg. 48).

[120]T. Kiatyongchai et al. "Coaxial electrospinning and release characteristics of cellulose acetate-gelatin blend encapsulating a model drug". In: *J. Appl. Polym. Sci.* 131.8 (2014), pp. 1–9. arXiv: 1512.00567 (cited on pg. 48).

[121]J. Fernández de la Mora. "The Fluid Dynamics of Taylor Cones". In: *Annu. Rev. Fluid Mech.* 39.1 (2007), pp. 217–243 (cited on pg. 50).

[122]A. V. Subbotin and A. N. Semenov. "Electrohydrodynamics of stationary cone-jet streaming". In: *Proc. R. Soc. A Math. Phys. Eng. Sci.* 471.2182 (2015), p. 20150290 (cited on pg. 50).

[123]M. Teodorescu and M. Bercea. "Poly(vinylpyrrolidone) – A Versatile Polymer for Biomedical and Beyond Medical Applications". In: *Polym. Plast. Technol. Eng.* 54.9 (2015), pp. 923–943 (cited on pgs. 51, 76, 82).

[124]R. S. Porter and J. F. Johnson. "The entanglement concept in polymer systems". In: *Chem. Rev.* 66.1 (1966), pp. 1–27 (cited on pg. 51).

[125]L. Huang et al. "Controlling electrospun nanofiber morphology and mechanical properties using humidity". In: *J. Polym. Sci. Part B Polym. Phys.* 49.24 (2011), pp. 1734–1744 (cited on pg. 51).

[126]A. Jaworek. "Micro- and nanoparticle production by electrospraying". In: *Powder Technol.* 176.1 (2007), pp. 18–35 (cited on pgs. 52, 71).

[127]T. Ostapenko et al. "Filaments formed in the hexagonal columnar liquid crystal phase of star-shaped oligobenzoates". In: *Liq. Cryst.* 40.3 (2013), pp. 345–353 (cited on pg. 52).

[128]D. H. Reneker et al. "Nanofiber garlands of polycaprolactone by electrospinning". In: *Polymer (Guildf).* 43.25 (2002), pp. 6785–6794 (cited on pg. 53).

[129]J. Zelany. "The electrical discharge from liquid points, and a hydrostatic method of measuring the electric intensity at their surfaces". In: *Phys. Rev.* 3.2 (1914), pp. 69–91 (cited on pg. 54).

[130]V. E. Kalayci et al. "Charge consequences in electrospun polyacrylonitrile (PAN) nanofibers". In: *Polymer (Guildf).* 46.18 (2005), pp. 7191–7200 (cited on pg. 54).

[131]D. Cheng et al. "A sensing device using liquid crystal in a micropillar array supporting structure". In: *J. Microelectromechanical Syst.* 18.5 (2009), pp. 973–982 (cited on pg. 60).

[132]I. S. Heo and S. Y. Park. "Smart shell membrane prepared by microfluidics with reactive nematic liquid crystal mixture". In: *Sensors Actuators, B Chem.* 251 (2017), pp. 658–666 (cited on pg. 60).

[133]T. Sumiyoshi et al. "Vacuum-deposited films of mesogen of 4-Cyano-4"-pentyl-p-terphenyl: their electronic spectra and molecular aggregate structures". In: *Thin Solid Films* 370.1 (2000), pp. 285–293 (cited on pg. 60).

[134]S. Schymura. "Liquid Crystalline Carbon Nanotube Suspensions - From Unique Challenges to Unique Properties". PhD thesis. 2013, p. 128 (cited on pgs. 60, 88).

[135]A. S. Utada et al. "Dripping to jetting transitions in coflowing liquid streams". In: *Phys. Rev. Lett.* 99.9 (2007), pp. 1–4. arXiv: `arXiv:1011.1669v3` (cited on pg. 62).

[136]S. A. Theron et al. "Experimental investigation of the governing parameters in the electrospinning of polymer solutions". In: *Polymer (Guildf).* 45.6 (2004), pp. 2017–2030 (cited on pg. 69).

[137]C. J. Thompson et al. "Effects of parameters on nanofiber diameter determined from electrospinning model". In: *Polymer* 48.23 (2007), pp. 6913–6922 (cited on pg. 69).

[138]X. X. He et al. "Near-Field Electrospinning: Progress and Applications". In: *J. Phys. Chem. C* 121.16 (2017), pp. 8663–8678 (cited on pg. 69).

[139]R. Festag et al. "Effects of molecular entanglements during electrospray of high molecular weight polymers". In: *J. Am. Soc. Mass Spectrom.* 9.4 (1998), pp. 299–304 (cited on pg. 71).

[140]Suresh L. Shenoy et al. "Role of chain entanglements on fiber formation during electrospinning of polymer solutions: Good solvent, non-specific polymer-polymer interaction limit". In: *Polymer* 46.10 (2005), pp. 3372–3384 (cited on pgs. 71, 73, 76).

[141]F. Bueche. "Viscosity, self-diffusion, and allied effects in solid polymers". In: *J. Chem. Phys.* 20.12 (1952), pp. 1959–1964 (cited on pgs. 71, 72).

[142]F. Bueche. "Viscosity of polymers in concentrated solution". In: *J. Chem. Phys.* 25.3 (1956), pp. 599–600 (cited on pgs. 71, 72).

[143]W. Graessley. *The Entanglement Concept In Polymer Rheology*. Berlin: Springer-Verlag, 1974. Chap. Chapters 5, p. 179 (cited on pgs. 71, 72).

[144]L. J. Fetters et al. "Connection between Polymer Molecular Weight, Density, Chain Dimensions, and Melt Viscoelastic Properties". In: *Macromolecules* 27.17 (1994), pp. 4639–4647 (cited on pgs. 71–73, 76).

[145]J.D. Ferry. *Viscoelastic Properties of Polymers*. 3rd ed. New York: Wiley-VCH, 1980. Chap. (10) - Mol, p. 641 (cited on pgs. 71, 72).

[146]R. H. Colby et al. "Melt Viscosity-Molecular Weight Relationship for Linear Polymers". In: *Macromolecules* 20.9 (1987), pp. 2226–2237 (cited on pgs. 71, 72).

[147]J. R. Dorgan et al. "Melt rheology of poly(lactic acid): Entanglement and chain architecture effects". In: *J. Rheol. (N. Y. N. Y).* 43.5 (1999), pp. 1141–1155 (cited on pg. 71).

[148]M. Hu et al. "Linear Rheological Response of a Series of Densely Branched Brush Polymers". In: *Macromolecules* 44.17 (2011), pp. 6935–6943 (cited on pg. 71).

[149]S. Nouri et al. "Effect of chemical and physical branching on rheological behavior of polylactide". In: *J. Rheol. (N. Y. N. Y).* 59.4 (2015), pp. 1045–1063 (cited on pg. 71).

[150]M. G. McKee et al. "Correlations of Solution Rheology with Electrospun Fiber Formation of Linear and Branched Polyesters". In: *Macromolecules* 37.5 (2004), pp. 1760–1767 (cited on pg. 72).

[151]T. McLeish. "Tube theory of entangled polymer dynamics". In: *Adv. Phys.* 51.6 (2002), pp. 1379–1527 (cited on pg. 72).

[152]R. G. Larson et al. "Definitions of entanglement spacing and time constants in the tube model". In: *J. Rheol. (N. Y. N. Y).* 47.3 (2003), pp. 809–818 (cited on pgs. 72, 73, 76).

[153]J.M Dealy and R. G. Larson. *Structure & rheology of molten polymers: From structure to flow behaviour and back again*. Munich: Hanser Publishers, 2006 (cited on pg. 72).

[154]P. G. de Gennes. "Reptation of a Polymer Chain in the Presence of Fixed Obstacles". In: *J. Chem. Phys.* 55.2 (1971), pp. 572–579 (cited on pg. 72).

[155]M. Doi and S. F. Edwards. *The Theory of Polymer Dynamics*. Oxford University Press, 1986 (cited on pg. 72).

[156]B. Torres and N. J. Pinto. "Ultrafine fibers of polystyrene dissolved in tetrahydrofuran prepared using the electrospinning method". In: *Proceeding Natl. Conf. Undergrad. Res.* (2001), pp. 15–17 (cited on pg. 74).

[157]S. Chuangchote et al. "Electrospinning of poly(vinyl pyrrolidone): Effects of solvents on electrospinnability for the fabrication of poly(p -phenylene vinylene) and TiO 2 nanofibers". In: *J. Appl. Polym. Sci.* 114.5 (2009), pp. 2777–2791 (cited on pgs. 75, 76).

[158]M. Miftahul et al. "Scaling law on particle-to-fiber formation during electrospinning". In: *Polymer (Guildf).* 50.20 (2009), pp. 4935–4943 (cited on pg. 75).

[159]S. Mitra et al. "Hydrogel nanoparticles made of cross-linked polyvinylpyrrolidone". In: *Dekker Encycl. Nanosci. Nanotechnol.* Ed. by J.A. Schwartz et al. Boca Raton: CRC Press - Taylor & Francis Group, 2004. Chap. Volume 3, pp. 1546–1547 (cited on pg. 76).

[160]J. H. Chai and Q. S. Wu. "Electrospinning preparation and electrical and biological properties of ferrocene/poly(vinylpyrrolidone) composite nanofibers". In: *Beilstein J. Nanotechnol.* 4.1 (2013), pp. 189–197 (cited on pg. 76).

[161]L. J. Fetters et al. "Chain dimensions and entanglement spacings in dense macromolecular systems". In: *J. Polym. Sci. Part B Polym. Phys.* 37.10 (1999), pp. 1023–1033 (cited on pg. 76).

[162]S. De Vrieze et al. "The effect of temperature and humidity on electrospinning". In: *J. Mater. Sci.* 44.5 (2009), pp. 1357–1362 (cited on pg. 77).

[163]D. Peeters and P. Huyskens. "Endothermicity or exothermicity of water/alcohol mixtures". In: *J. Mol. Struct.* 300.C (1993), pp. 539–550 (cited on pg. 79).

[164]P. L. Huyskens. "Mobile and static molecular disorder in liquids". In: *J. Mol. Struct.* 274.C (1992), pp. 223–246 (cited on pg. 79).

[165]C. K. Law et al. "Alcohol droplet vaporization in humid air". In: *Int. J. Heat Mass Transf.* 30.7 (1987), pp. 1435–1443 (cited on pgs. 79, 87).

[166]B. Smith. *Infrared Spectral Interpretation - A Systematic Approach*. Boca Raton: CRC Press - Taylor & Francis Group, 1998 (cited on pg. 81).

[167]B. C. Smith. "Alcohols — The Rest of the Story". In: *Spectroscopy* 32.4 (2017), pp. 19–23 (cited on pg. 81).

[168]S. Bhattacharya et al. "Plasticization of poly(vinylpyrrolidone) thin films under ambient humidity: Insight from single-molecule tracer diffusion dynamics". In: *J. Phys. Chem. B* 117.25 (2013), pp. 7771–7782 (cited on pg. 82).

[169]B. C. Smith. "An IR Spectral Interpretation Potpourri : Carbohydrates and Alkynes". In: *Spectroscopy* 32.7 (2017), pp. 18–24 (cited on pg. 82).

[170]P. Griffiths and J. de Haseth. *Fourier Transform Infrared Spectrometry*. 2nd ed. New York: Wiley-VCH, 2007 (cited on pg. 82).

[171]C. Reichardt. "(7.4) Empircal parameters of solvent polarity from spectroscopic measurements". In: *Solvents Solvent Eff. Org. Chem.* 3rd ed. Marburg: Wiley, 2003. Chap. Appendix, pp. 411–443 (cited on pg. 89).

[172]J. Deschamps et al. "Vapor pressure and density of thermotropic liquid crystals: MBBA, 5CB, and novel fluorinated mesogens". In: *J. Phys. Chem. B* 112.13 (2008), pp. 3918–3926 (cited on pg. 94).

[173]Henke. S Kadlec. P and Z. Bubník. "Properties of ethanol and ethanol-water solutions: tables and equations". In: *Sugar Ind.* 135.10 (2010), pp. 607–613 (cited on pg. 94).

[174]N.S. Osborne et al. "The density and thermal expansion of ethyl alcohol and its mixtures with water". In: *Bull. U.S. Bur. Stand.* 9.197 (1913), pp. 0–2 (cited on pg. 94).

[175]J. Yamamoto and H. Tanaka. "Transparent nematic phase in a liquid-crystal-based microemulsion". In: *Nature* 409.6818 (2001), pp. 321–325 (cited on pg. 95).

[176]L. A. Serrano et al. "Phase behaviour and applications of a binary liquid mixture of methanol and a thermotropic liquid crystal". In: *Soft Matter* 14.22 (2018), pp. 4615–4620 (cited on pg. 96).

[177]T. Araki and H. Tanaka. "Nematohydrodynamic effects on the phase separation of a symmetric mixture of an isotropic liquid and a liquid crystal". In: *Phys. Rev. Lett.* 93.1 (2004), pp. 015702–1 (cited on pg. 99).

[178]T. Araki and H. Tanaka. "Stripe pattern formation in phase separation accompanying orientational ordering under an external field". In: *J. Phys. Condens. Matter* 18.22 (2006) (cited on pg. 99).

[179]Y. Lansac et al. "Dynamics of phase separation in mesomorphic mixtures". In: *Liq. Cryst.* 18.6 (1995), pp. 829–837 (cited on pg. 99).

[180]A. Ten Bosch. "Spinodal decomposition in liquid crystalline materials". In: *J. Phys. II* 1.8 (1991), pp. 949–958 (cited on pg. 99).

[181]P. S. Drzaic. "Liquid Crystal/Polymer Phase Separation". In: *Liq. Cryst. Dispersions*. Singapore: World Scientific Publishing Co. Pte. Ltd., 1995. Chap. 2, pp. 75–97 (cited on pg. 99).

[182]H. W. Chiu and T. Kyu. "Spatio-temporal growth of nematic domains in liquid crystal polymer mixtures". In: *J. Chem. Phys.* 110.12 (1999), pp. 5998–6006 (cited on pg. 99).

[183]J. W. Gibbs. "On the equilibrium of heterogeneous substances". In: *Am. J. Sci.* s3-16.96 (1878), pp. 441–458. arXiv: arXiv:1011.1669v3 (cited on pg. 101).

[184]J. Thomson. "A quantitative investigation of certain relations between the gaseous, the liquid, and the solid states of water-substance". In: *Proc. R. Soc.* 22 (1873), pp. 27–36 (cited on pg. 101).

[185]R. Brown. "XXVII. A brief account of microscopical observations made in the months of June, July and August 1827, on the particles contained in the pollen of plants; and on the general existence of active molecules in organic and inorganic bodies". In: *Philos. Mag.* 4.21 (1828), pp. 161–173 (cited on pg. 103).

[186]P. Atkins and J. de Paula. "Diffusion". In: *Atkins' Phys. Chem.* 7th ed. Oxford: Oxford University Press, 2002. Chap. 24, pp. 842–854 (cited on pg. 104).

[187]E. P. Favvas and A. C. Mitropoulos. "What is spinodal decomposition?" In: *J. Eng. Sci. Technol. Rev.* 1.1 (2008), pp. 25–27 (cited on pg. 105).

[188]D. G. Clerc and D. A. Cleary. "Spinodal Decomposition as an Interesting Example of the Application of Several Thermodynamic Principles". In: *J. Chem. Educ.* 72.2 (1995), p. 112 (cited on pg. 105).

[189]J. W. Cahn. "Phase separation by spinodal decomposition in isotropic systems". In: *J. Chem. Phys.* 42.1 (1965), pp. 93–99 (cited on pg. 106).

[190]H. Tanaka. "Viscoelastic phase separation". In: *J. Phys. Condens. Matter* 12.15 (2000), R207–R264 (cited on pg. 106).

[191]V. Tomar et al. "Morphological transitions in liquid crystal nanodroplets". In: *Soft Matter* 8.33 (2012), pp. 8679–8689 (cited on pg. 107).

[192]H. Kakooei and M. Normohammadi. "Asbestos Exposure among Construction Workers During Demolition of Old Houses in Tehran, Iran". In: *Ind. Health* 52.1 (2014), pp. 71–77 (cited on pg. 114).

[193]Jun Li et al. "High temperature-gradient refractive index liquid crystals". In: *Opt. Express* 12.9 (2004), pp. 2002–2010 (cited on pg. 118).

[194]R. P. Pan et al. "Temperature-dependent optical constants and birefringence of nematic liquid crystal 5CB in the terahertz frequency range". In: *J. Appl. Phys.* 103.9 (2008) (cited on pg. 118).

[195]K. Nayani et al. "Spontaneous emergence of chirality in achiral lyotropic chromonic liquid crystals confined to cylinders". In: *Nat. Commun.* 6 (2015), pp. 1–7 (cited on pgs. 119, 121–123, 127).

[196]Z. S. Davidson et al. "Chiral structures and defects of lyotropic chromonic liquid crystals induced by saddle-splay elasticity". In: *Phys. Rev. E* 91.5 (2015), pp. 1–5. eprint: arXiv:1504.03619v1 (cited on pgs. 119, 121, 122, 127).

[197]A. A. Joshi et al. "Measuring liquid crystal elastic constants with free energy perturbations". In: *Soft Matter* 10.6 (2014), pp. 882–893 (cited on pg. 121).

[198]J. Noh. "Tuning Self-Assembly in Liquid Crystal shells: from Interfacial- to Polymer-stabilization". PhD thesis. University of Luxembourg, 2018 (cited on pg. 121).

[199]J. Fu et al. "Spontaneous emergence of twist and the formation of a monodomain in lyotropic chromonic liquid crystals confined to capillaries". In: *NPG Asia Mater.* 9.6 (2017), e393 (cited on pgs. 122, 127).

[200]X. Wang et al. "Topological defects in liquid crystals as templates for molecular self-assembly". In: *Nat. Mater.* 15.1 (2015), pp. 106–112 (cited on pg. 123).

[201]T. C. Lubensky. "Confined chromonics and viral membranes". In: *Mol. Cryst. Liq. Cryst.* 646.1 (2017), pp. 235–241 (cited on pg. 127).

[202]H. Ramezani-Dakhel et al. "Understanding atomic-scale behavior of liquid crystals at aqueous interfaces". In: *J. Chem. Theory Comput.* 13.1 (2017), pp. 237–244 (cited on pg. 127).

[203]M. P. Valignat et al. "Wetting and Anchoring of a Nematic Liquid Crystal on a Rough Surface". In: *Phys. Rev. Lett.* 77.10 (1996), pp. 1994–1997 (cited on pg. 127).

[204]M. J. Bertocchi et al. "Electrospun Polymer Fibers Containing a Liquid Crystal Core: Insights into Semiflexible Confinement". In: *J. Phys. Chem. C* 122.29 (2018), pp. 16964–16971 (cited on pg. 128).

[205]B. Petley. *Report to the 1999 IUPAP General Assembly IU14 . IUPAC Interdivisional Committee on Nomenclature and Symbols (IDCNS)*. Tech. rep. IUPAC, 1999, pp. 1–15 (cited on pg. 136).

[206]I. Mills. "The Units ppm, ppb, and ppt". In: *Chem. Int.* 36.2 (2014), pp. 23–24 (cited on pg. 136).

[207]Kuchitsu K. Mills I., Cvitas T., Homann K., Kallay N. *Quantities, Units and Symbols in Physical Chemistry, International Union of Pure and Applied Chemistry*. 2nd ed. Oxford: Blackwell Scientific Publications, 1993 (cited on pg. 136).

[208]BIPM. "Unit of electric current (ampere)". In: *SI Broch. Int. Syst. Units [8th Ed. 2006; Updat. 2014]*. 8th ed. 2006, Section 2.1.1.4 (cited on pg. 136).

[209]S. E. Schwartz and P. Warneck. "Units for use in Atmospheric Chemistry". In: *Pure Appl. Chem.* 67.8/9 (1995), pp. 1377–1406 (cited on pg. 137).

[210]A. L. Porter and I. Rafols. "Is science becoming more interdisciplinary? Measuring and mapping six research fields over time". In: *Scientometrics* 81.3 (2009), pp. 719–745 (cited on pg. 137).

[211]United States Dept. of Labor (OSHA). *OSHA || Toluene - Occupational Exposure Limits*. https://www.osha.gov/SLTC/emergencypreparedness/guides/earthquakes.html. 2017 (cited on pgs. 137, 138).

[212]The National Institute for Occupational Safety and Health (NIOSH) and Centers for Disease Control (CDC). *Toluene*. https://www.cdc.gov/niosh/npg/npgd0619.html{%}0ASynonyms, urldate = 2018-01-01. 2018 (cited on pgs. 137, 138).

[213]C. J. Elskamp. *Toluene (Organic Method Analysis #111)*. https://www.osha.gov/dts/sltc/methods/organic/org111/org111.pdf. Salt Lake City, 1998 (cited on pgs. 138–140, 165).

[214]K. D. Cadwell et al. "Infrared spectroscopy of competitive interactions between liquid crystals, metal salts, and dimethyl methylphosphonate at surfaces." In: *J. Phys. Chem. B* 110.51 (2006), pp. 26081–8 (cited on pg. 140).

[215]The National Institute for Occupational Safety and Health (NIOSH) and Centers for Disease Control (CDC). *Aromatic Hydrocarbons (Organic Method Analysis #1501)*. `https://www.cdc.gov/niosh/docs/2003-154/pdfs/1501.pdf`. 2003 (cited on pgs. 140, 165).

[216]The National Institute for Occupational Safety and Health (NIOSH) and Centers for Disease Control (CDC). *Methanol (Organic Method Analysis #2000)*. `https://www.cdc.gov/niosh/docs/2003-154/pdfs/2000.pdf`. 1998 (cited on pg. 140).

[217]The National Institute for Occupational Safety and Health (NIOSH) and Centers for Disease Control (CDC). *Organic and Inorganic Gases By Extractive Ftir Spectrometry (Organic Method Analysis #3800)*. `https://www.cdc.gov/niosh/docs/2003-154/pdfs/3800.pdf`. 2003 (cited on pg. 140).

[218]J. Dalton. "Essay IV. On the expansion of elastic fluids by heat". In: *Mem. Lit. Philos. Soc. Manchester* 5 (1802), 595–602 (see pg. 600) (cited on pg. 141).

[219]F. M. Raoult. "Loi générale des tensions de vapeur des dissolvants (General law of vapor pressures of solvents)". In: *Comptes rendus* 104 (1886), pp. 1430–1433 (cited on pg. 141).

[220]W. Henry. "Experiments on the Quantity of Gases Absorbed by Water, at Different Temperatures, and under Different Pressures". In: *Philos. Trans. R. Soc. London* 93 (1803), pp. 29–274 (cited on pg. 141).

[221]Drager Safety AG & Co. *Draeger-Tubes & CMS-Handbook: Soil, Water, and Air Investigations as well as Technical Gas Analysis*. 16th ed. 2011, pp. 259–260 (cited on pgs. 144, 151).

[222]L. C. Brazdil et al. "Kinetics of aromatic iodination reactions using iodine, diiodine pentoxide and sulfuric acid in acetic acid". In: *J. Chem. Soc. Perkin Trans. 2* 4 (1998), pp. 933–936 (cited on pg. 152).

[223]H. Suzuki et al. "The Direct Iodination of Polyalkylbenzenes Bearing Bulky Groups')". In: *Bull. Chem. Soc. Jpn.* 39.1 (1966), pp. 28–131 (cited on pg. 152).

[224]J. P. Lodge. "Direct reading colorimetric indicators". In: *Methods air Sampl. Anal.* Ed. by J. P. Lodge. 3rd ed. Routledge, 2017. Chap. 27, p. 784 (cited on pg. 152).

[225]B. Lamb and A. W. Phillips. "The solubility of iodine pentoxide in sulfuric acid". In: *J. Am. Chem. Soc.* 45.1 (1923), pp. 108–112 (cited on pg. 152).

[226]E. S. Mckee and P. W. McConnaughey. "Detector Tubes". In: *Sampl. calibration Atmos. Meas. A Symp. Spons. by ASTM Comm. D-22 Sampl. Anal. Atmos.* Ed. by John Keenan Taylor. Boulder: ASTM, 1985, p. 225 (cited on pg. 152).

[227]The National Institute for Occupational Safety and Health (NIOSH) and Centers for Disease Control (CDC). *Toluene - Immediately Dangerous to Life or Health Concentrations (IDLH) May 1994*. `https://www.cdc.gov/niosh/idlh/108883.html`. 1994 (cited on pg. 153).

[228]M. O. Mclinden and J. D Splett. "A liquid density standard over wide ranges of temperature and pressure based on toluene". In: *J. Res. Natl. Inst. Stand. Technol.* 113.1 (2008), pp. 29–67 (cited on pg. 154).

[229]M. Kang et al. "Live imaging, identifying, and tracking single cells in complex populations in vivo and ex vivo." In: *Methods Mol. Biol.* 1052 (2013), pp. 109–23 (cited on pg. 155).

[230]C. Leys et al. "Detecting outliers: Do not use standard deviation around the mean, use absolute deviation around the median". In: *J. Exp. Soc. Psychol.* 49.4 (2013), pp. 764–766 (cited on pg. 156).

[231]D. Matatagui et al. "Real-Time Characterization of Electrospun PVP Nanofibers as Sensitive Layer of a Surface Acoustic Wave Device for Gas Detection". In: *J. Nanomater.* 2014 (2014), pp. 1–8 (cited on pg. 161).

[232]A. Taha et al. "Preparation and application of amino functionalized mesoporous nanofiber membrane via electrospinning for adsorption of Cr3+from aqueous solution". In: *J. Environ. Sci.* 24.4 (2012), pp. 610–616 (cited on pg. 161).

[233]M. W. Davidson. *The Quartz Wedge Compensator*. olympus-lifescience.com/en/microscope-resource/primer/techniques/polarized/quartzwedge/. 2000 (cited on pg. 162).

[234]The National Institute for Occupational Safety (CDC) et al. *(Organic Method Analysis #4000)*. https://www.cdc.gov/niosh/docs/2003-154/pdfs/4000.pdf. 1994 (cited on pg. 165).

[235]J. Pitt. "Principles and applications of liquid chromatography-mass spectrometry in clinical biochemistry." In: *Clin. Biochem. Rev.* 30.1 (2009), pp. 19–34 (cited on pg. 166).

[236]A. Bahareh et al. "Poly (ϵ-caprolactone) fiber: an overview". In: *J. Eng. Fiber. Fabr.* 9.3 (2014), pp. 74–90 (cited on pg. 168).

[237]R. Ghobeira et al. "Wide-ranging diameter scale of random and highly aligned PCL fibers electrospun using controlled working parameters". In: *Polymer (Guildf).* 157 (2018), pp. 19–31 (cited on pg. 168).

[238]N. Detta et al. "Melt electrospinning of polycaprolactone and its blends with poly(ethylene glycol)". In: *Polym. Int.* 59.11 (2010), pp. 1558–1562 (cited on pg. 168).

[239]S. Liao et al. "Effect of humidity on melt electrospun polycaprolactone scaffolds". In: *BioNanoMaterials* 17.3-4 (2016), pp. 173–178 (cited on pg. 168).

[240]T. D. Brown et al. "Melt electrospinning today: An opportune time for an emerging polymer process". In: *Prog. Polym. Sci.* 56 (2016), pp. 116–166 (cited on pg. 168).

[241]Toby D. Brown et al. "Direct writing by way of melt electrospinning". In: *Adv. Mater.* 23.47 (2011), pp. 5651–5657. arXiv: arXiv:1011.1669v3 (cited on pg. 168).